Unravelling stereodynamic effects in the scattering of NO(X)

Max McCrea

University College
University of Oxford

A thesis submitted for the degree of
Doctor of Philosophy

Trinity 2025

Abstract

If humanity is to truly master chemistry, it must be able to understand the processes linking reactants to products. One way to exert control over collisional chemical reactions is by having the ability to choose the geometry of the reactants before the collision. Hence, it is vital that significant study is put into theoretical and experimental work in the field of stereodynamics that can facilitate the prediction of the effects of this control. Here, work is presented which aims to further this cause through studies of inelastic scattering of the molecule NO(X), which uses electric and magnetic fields to orient either one or both collision partners before the collision.

On the experimental side, progress towards an experiment in which NO(X, $j = 1/2f$) collides with a symmetric top molecule, such as ND_3 or CH_3F, in a specific quantum state in conditions in which both molecules are oriented by a single electric field. This experiment will make use of the double hexapole which has been designed and tested, with those results presented here. Theory to understand how these molecules may orient in an electric field strong enough to orient NO(X, $j = 1/2f$) is also shown. New data analysis methods are also discussed which may be used to extract stereodynamic quantities from 3D velocity map imaging scattering data, the format in which experimental data will be collected when studying the NO(X) + symmetric top molecule system.

Two studies are also shown which look closely at the theory behind these stereodynamic effects, allowing characterisation. This theory is first displayed by using electric fields to orient a $^2\Pi$ molecule (such as NO(X)) in a collision with a rare gas atom, or an unoriented molecule, with some examples shown to display the power of the formalism and the insights it can provide. After this, the theory is expanded to a system in which a $^2\Pi$ molecule is oriented by an electric field and it collides with another molecule whose angular momentum is oriented by a magnetic field. Quantum mechanical scattering calculations are then presented to illustrate the utility of this theory, helping to provide insights into the potential energy surfaces involved in the scattering and the properties of resonances seen in low energy scattering.

Unravelling stereodynamic effects in the scattering of NO(X)

Max McCrea

University College

University of Oxford

A thesis submitted for the degree of

Doctor of Philosophy

Trinity 2025

Acknowledgements

Firstly, I must thank my supervisor, Prof Mark Brouard. I'm not sure that I was personally ideally suited to the world of research, and it is only through his patience and guidance that I have made it here at all. But beyond that, there is one key undervalued trait which Mark possesses which has been my vital to whatever success I've had. Four years of a DPhil is a long period of time to submit to, and the reality is that there was no way I would have been able to complete this had Mark not been a kind and generous person. I think I probably I owe him quite a few Friday evening pints by now.

They other key reason I've made it to this point is the rest of the Brouard group. I have met some amazing people, all of whom have inspired me in their own way. Firstly I have to give my warmest thanks to Dr Josh Featherstone. We went through quite a lot of emotions trying our hearts out to get that dastardly experiment to work, and finally, just as he was leaving, scattering finally occurred. There were times in those first three years I thought I would never be able to finish, but Josh's always upbeat outward personality always helped to pick me up (and of course, where would I be now if I hadn't picked up a few of the computational skills he possesses). He is an excellent friend and I look forward to a trip to Canada in the future...

Secondly - Dr Elena Castellani. Although I did not work directly with Elena during DPhil, her immense energy always cut through when I was lacking it, particularly in those dark times in my first and second year where nothing seemed to work. She is always kind and, probably to her own detriment, puts others before herself. It was always fun to talk music, and even though I perhaps don't support her goal for universal communism, politics. Every group needs an Elena - someone who works damn hard and makes everyone feel valued. She's a wonderful person and needs to know that.

Next, Matt Strutton. I must admit, after spending close to two years working on the hexapole together with Josh, I was somewhat apprehensive when Matt started working with in the tail-end of his Part II. I needn't have been. Matt has the gifts of being immensely intelligent and more naturally inclined to practical work than I am, but at no point as he been anything other than immensely supportive. I've come to rely on him more and more as someone who can check whether I'm being mad or not (it's worrying how often I am), and as someone whose first

response to any difficult situation is kindness. I should also very definitely say thank you to him and Augustine for letting me stay at theirs when I needed to towards the end of my final year.

The next member of the group I want to single out is Dr Joseph McManus. Sometimes I don't understand Joe - he has more energy than I think I've seen in any other human being (apart from perhaps me as a small child). I think that I've discovered that I value this sort of energy in people. It drives things to get done, it drives me to get things done and it pushes me to do things I might have been reticent to do otherwise. There's no doubt you've contributed a get-up-and-go attribute since you joined the hexapole, which has helped to get me where I am experimentally, and will hopefully get you and Matt to some exciting experimental results. The other thing about Joe, in simple terms, is that he's just a really nice guy. Simple as that.

Finally, Alex Crosby has been our Part II this year. I see a lot of me in him. I think he needs to believe in himself more. There is absolutely no doubt though that he made my final year of my DPhil a richer experience and his company was always appreciated.

I also want to thank all the other members of the group during my DPhil: Kieran Cheung, Leo Jia, Dr Martin Lam, Yuanyuan Pu, Jerry Chou, Dr Felicia Green, Natasha Smith, Yuting Su, Anya Eyres, Milan Patel, Ciara Hodgkinson, Mukhtar Quaraishi, Freddie Scowen, Frank Kan, Harryson Skelly, Dario Ruiz, and, yes, even Daniel Bein. Outside the group, but still at Oxford, I also want to thank Dr Michael Burt for his help early on in training me in YAG lasers, and the many members of the NDMS programme grant who have helped me along the way, including, but not limited to: Prof Stuart Mackenzie (I've enjoyed all those dinners we seem to have mysteriously been put next to each other), Prof Claire Vallance, Prof Ken McKendrick, Prof Matt Costen, Dr Martin Fournier (who I must thank for increasing our signal by about ten-fold), Dr Chris Robertson, Dr Peter Watson, Dr (now Prof) Patrick Robertson, Dr Christain Haakansson, Philip Pearcy and Alex Butler.

My thanks must also go to other collaborators: Javier Aoiz, Pablo Jambrina, Helen Chadwick, Gil Alexandrowicz and Dmitri Babikov.

My thanks must also go to everyone in the workshops, both mechanical and electronic, particularly Andy Green and Philip Hurst, to whom I gave a lot of work.

Away from the world of academia, there is one person who I could not have finished this DPhil without. Bobby, we may no longer be together, but I will never forget all the support you gave me while I was despairing over this that and the other. It will always be appreciated. I must also thank my parents for their encouragement, and my brother for refusing to ever let me pay for things and for letting me have his car. I also want to thank my grandparents, whose visits could often be an escape which would ground me back in the real world again.

My undergraduate friends: Rachel, Kenzie, Adam, Maddie and Miki also must be thanked for their optimism - perhaps particularly Adam, whose tales of woe when we were living together often made me feel things weren't so bad.

It is in places like this where you are supposed to have something profound to end on. Alas, I'm not sure I possess the words, so I'll end with my mantra for the last four years: 'Don't give up. REFUSE TO LOSE.'

Abstract

If humanity is to truly master chemistry, it must be able to understand the processes linking reactants to products. One way to exert control over collisional chemical reactions is by having the ability to choose the geometry of the reactants before the collision. Hence, it is vital that significant study is put into theoretical and experimental work in the field of stereodynamics that can facilitate the prediction of the effects of this control. Here, work is presented which aims to further this cause through studies of inelastic scattering of the molecule NO(X), which uses electric and magnetic fields to orient either one or both collision partners before the collision.

On the experimental side, progress towards an experiment in which NO(X, $j = 1/2f$) collides with a symmetric top molecule, such as ND_3 or CH_3F, in a specific quantum state in conditions in which both molecules are oriented by a single electric field. This experiment will make use of the double hexapole which has been designed and tested, with those results presented here. Theory to understand how these molecules may orient in an electric field strong enough to orient NO(X, $j = 1/2f$) is also shown. New data analysis methods are also discussed which may be used to extract stereodynamic quantities from 3D velocity map imaging scattering data, the format in which experimental data will be collected when studying the NO(X) + symmetric top molecule system.

Two studies are also shown which look closely at the theory behind these stereodynamic effects, allowing characterisation. This theory is first displayed by using electric fields to orient a $^2\Pi$ molecule (such as NO(X)) in a collision with a rare gas atom, or an unoriented molecule, with some examples shown to display the power of the formalism and the insights it can provide. After this, the theory is expanded to a system in which a $^2\Pi$ molecule is oriented by an electric field and it collides with another molecule whose angular momentum is oriented by a magnetic field. Quantum mechanical scattering calculations are then presented to illustrate the utility of this theory, helping to provide insights into the potential energy surfaces involved in the scattering and the properties of resonances seen in low energy scattering.

Contents

List of Abbreviations

PES . . . . . Potential Energy Surface

LAB . . . . . Laboratory

COM . . . . . Centre-Of-Mass

DCS . . . . . Differential Cross Section

ICS . . . . . Integral Cross Section

PDF . . . . . Probability Density Function

PDDCS . . . . Polarisation-Dependent Differential Cross Section

QCT . . . . . Quasi-Classical Trajectories

TDSE . . . . . Time-Dependent Schrödinger Equation

TISE . . . . . Time-Independent Schrödinger Equation

CC . . . . . Close-Coupled

3D . . . . . Three Dimensional

REMPI . . . . Resonance-Enhanced Multiphoton Ionisation

VMI . . . . . Velocity Map Imaging

ToF . . . . . Time-of-Flight

CMOS . . . . . Complementary Metal Oxide Superconductor

CCD . . . . . Charge-Coupled Device

iCCD . . . . . Intensified Charge-Coupled Device

2D . . . . . Two Dimensional

PImMS . . . . Pixel Imaging Mass Spectrometry

PMT . . . . . Photomultiplier Tube

DC . . . . . Direct Current

PEISI . . . . . Post Extraction Inversion Slice Imaging

PEDA . . . . . Post Extraction Differential Acceleration

QM . . . . . Quantum Mechanical

QQT . . . . . Quasi-Quantum Treatment

1 Introduction

Contents

1.1 Chemical Control and Reactant Geometry

One of the central aims of chemistry is to be able to understand, and therefore predict, the processes that underlie chemical reactions. This aim arises from mankind's natural tendency to want to shape its environment to make survival easier. If a chemical reaction is understood and predictable, then there is the possibility of control. If a reaction can be controlled, such that a specific outcome can be preferred or so that a reaction occurs more quickly, this may reduce waste and lost time when producing desired compounds. This compound could be desired for new technologies, or for healthcare purposes, or for a smorgasbord of other societal

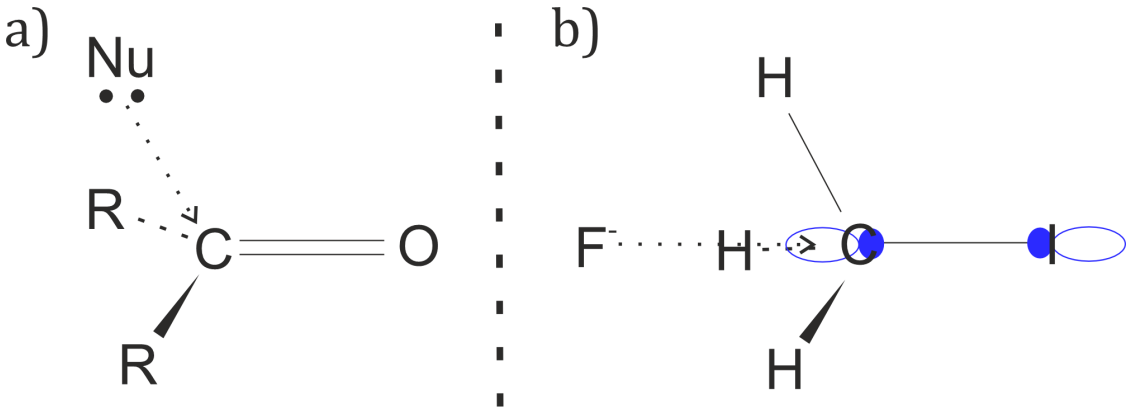

Figure 1.1: Two examples of the importance of reactant geometry. A depiction of a) the Bürgi-Dunitz angle for nucleophilic addition into a carbonyl bond and b) an SN2 reaction in which iodine is substituted with fluorine, where the fluoride ion must attack from a specific geometry to find the σ^* orbital of the C-I bond.

functions. Hence, the ability to have total control (or as much as is reasonably achievable) of chemical reactions is the key societal function of the chemist.

While there are many potential approaches to obtain control over a reaction, one of the most powerful is to ensure that the two colliding molecules are in a specific geometry that enables the desired outcome. The concept that the arrangement of atoms in space is crucial in deciding the outcome of a collision is not a new one. For example: a simple SN2 reaction between a F^- ion and a CH_3I molecule[1–3]. CH_3I has a tetrahedral molecular geometry, with the sp^3 hybrid orbitals interacting with a 5p orbital on I to produce a σ bond. An antibonding σ^* orbital would also be formed with density on either side of the bond. The F^- ion requires access to the σ^* orbital on the carbon end of the C-I bond to ensure that bond's breakage, and to then form a new C-F bond[4–6]. Hence, the chemical reaction is only likely if the CH_3I molecule is oriented such that the I points in away from the incoming F^- ion. One could conclude, that if the chemist had the ability to orient the CH_3I molecule before the collision, they would be massively able to increase the rate of reaction. In fact, in the similar example of abstraction of iodine from CH_3I by rubidium, reactivity ratios between cases in which CH_3I oriented such that rubidium hits either end of the molecule can be a factor of three[7].

Organic chemistry is littered with examples of the importance of molecular geometry to the collision outcome. Another famous example is that of carbonyl bonds undergoing nucleophilic addition more favourably when the nucleophile collides at the Bürgi-Dunitz angle of around 107° to the C=O bond axis [8, 9].

In the field of chemical kinetics, these 'steric effects' are well known. The formulation of simple collision theory, a basic model to predict chemical reaction rates, requires the addition of a 'steric factor' when one or both reactants is a molecular species[10, 11]. This factor is included to recognise that not all collisions with enough kinetic energy to produce a reaction will result in said reaction, as some, if not most, collisions do not have the correct geometry to react. This was recognised in the development of the angular-dependent line-of-centres model, which uses an energy barrier to reaction which is a function of the geometry of the colliders[12].

1.1.1 Reaction Dynamics and Potential Energy Surfaces

The role of chemical reaction dynamics is to study reactions at the molecular level, divining more granular information about the process than can be achieved through the bulk study of kinetics. Hence, the dynamicist plays an integral role in unravelling the intricacies of 'steric effects' and how they might be harnessed for the benefit of a synthetic chemist. Those dynamicists that investigate these steric effects work in the field of stereodynamics, which aims to provide deeper understanding of the fundamentals of these effects.

The most powerful tool to understand how a reaction occurs is its Potential Energy Surface(s) (PES). Within the Born-Oppenheimer approximation[13], these surfaces provide a map detailing the forces the molecules experience at all possible geometries during a collision. By propagating a trajectory using these forces, one can, classically, obtain information about how the reaction takes place. If one propagates many trajectories with different initial molecular geometries, one can obtain a picture of the steric preferences of the collision.

Of course, on a single molecule level, there is only so much that may be gained from a classical interpretation of a collision (also known as a scattering event),

particularly if the collision is at low energy. Alternatively, by propagating a wavefunction along the surface, a more accurate quantum mechanical picture of a chemical reaction can be obtained. However, due to the probabilistic nature of quantum mechanics, building up an intuitive picture of steric preference from these sorts of calculations is more complex. One of the aims of this thesis is to go some way to provide answers for how this can be achieved, and to provide ways of calculating parameters with clear physical interpretations which describe steric preferences simply.

PESs may be calculated for simple systems by computationally expensive electronic structure theory methods[14, 15]. One could make the argument that if these surfaces can be calculated, and we can propagate wavefunctions on these surfaces, then these are solved problems. However, this is only a half picture. These electronic structure theory methods are imperfect, and as the systems of interest grow in size to become more relevant to real world problems, both the PES calculation and the wavefunction propagation techniques become less and less feasible[16, 17], and hence more and more approximate methods must be employed.

With this backdrop, the role of the experimentalist is two-fold. Firstly, they interrogate the accuracy of the calculated PESs, by performing experiments that test different parts of the surface. This ensures that whatever serious, or less serious, imperfections in the surface may be resolved to ensure greater accuracy. Secondly, they perform experiments on systems which the theoretician finds challenging to perform accurate calculations on, proving their inadequacies, and laying out the challenge for more accurate, more efficient computation. Experimentally, one of the aims of this thesis is to lay the groundwork for an experiment investigating the stereodynamics of a collision between NO and a symmetric top molecule - a system which, at the collision energies to be studied, cannot be analysed with exact quantum mechanical calculations, due to its complexity. Hence, the experiment will lay down the gauntlet to the theoreticians to devise methods that can reproduce the results efficiently and accurately.

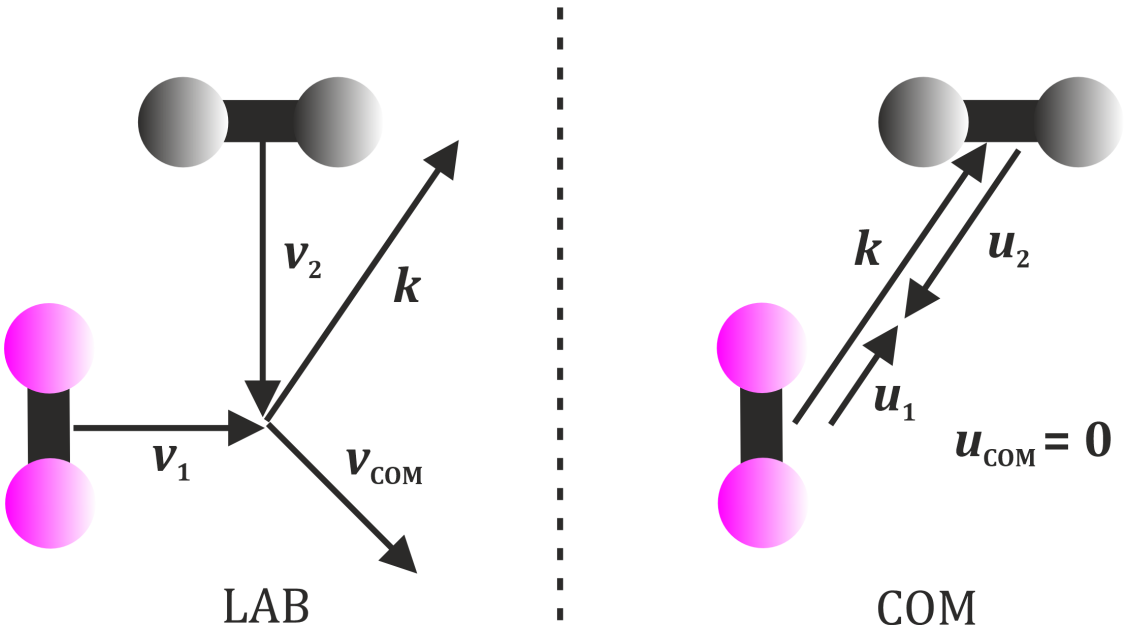

Figure 1.2: A schematic displaying what is meant by the laboratory (LAB) frame and the COM frame. The relative velocity vector remains unchanged. $\boldsymbol{u}_{\mathrm{COM}}$ is the velocity of the COM in the COM frame, which, by definition, must be zero.

1.1.2 The Centre-of-Mass Frame

Before moving on to how one might mathematically represent stereodynamics, it is important to first understand one concept. Collisions in this thesis will generally be discussed in a frame of reference in which the two collision partners are initially moving along a single axis. Generally, of course, this is not the case. Collisions can happen at any angle between the velocities of the two partners. However, by changing the reference frame, any collision can be considered as having initial motion along a single axis.

This frame is known as the centre-of-mass (COM) frame[18]. Beginning with the geometry as it is seen in the laboratory, which will henceforth be called the LAB frame, if the velocity of the COM of the system, $\boldsymbol{v}_{\mathrm{COM}}$ is subtracted from the velocities of the individual collision partners, then their motion lies directly along the relative velocity vector, $\boldsymbol{k}$. As the total linear momentum of the system must be conserved, $\boldsymbol{v}_{\mathrm{COM}}$ must be unchanged by the collision. Hence, subtracting $\boldsymbol{v}_{\mathrm{COM}}$ from the LAB frame velocities fixes the position of the COM both before and after the collision. Velocities in the COM frame are often denoted by the symbol

$\boldsymbol{u}_x$ where x represents a label for a given collision partner. Note that the relative velocity vector may be defined in terms of the COM frame or LAB frame velocities

$$\boldsymbol{k} = \boldsymbol{v}_1 - \boldsymbol{v}_2 = \boldsymbol{u}_1 - \boldsymbol{u}_2 \,. \tag{1.1}$$

where the labels 1 and 2 refer to the two collision partners.

In the COM frame, assuming no preference for the direction of scattering, the products would then have COM frame velocities that point in all directions from the origin. In the LAB frame, these vectors would then have the fixed vector $\boldsymbol{v}_{\mathrm{COM}}$ added to it, meaning most, if not all products, are scattered around the direction of $\boldsymbol{v}_{\mathrm{COM}}$.

1.1.3 Vector Correlations

One of the most convenient ways of expressing stereodynamic properties is via vector correlations. By expressing reactant and product geometries as polarised vectors, mathematical descriptions describing how changing the degree of initial polarisation of these vectors changes the collision with reference to an unpolarised system, or how the collision induces product polarisation.

Polarisation comes in two forms, orientation and alignment[19]. Orientation describes the likelihood of a vector being polarised in a particular direction, over a direction antiparallel to it. An example of this might be a thumbs up sign and a thumbs down sign. With the thumbs up, the thumb is oriented upwards, while in the thumbs down, the thumb is oriented downwards. Upon alignment, the vector can directed in one direction, or its antiparallel, but not perpendicularly. An example of this might be a symmetric stick placed vertically. As the stick is symmetric, it is impossible to say that it is oriented upwards or downwards. However, it is clearly not directed horizontally. Hence, the stick is aligned vertically.

For a molecule-molecule collision, there are a wide variety of vectors that could be polarised[20]. The most intuitive example is the symmetry axis of the molecule. This scenario involves placing the geometry of the molecule such that a given axis points in a specific direction (or its opposite in the case of alignment). This is not full control of the geometry of the molecule, as rotation about this symmetry axis

is freely allowed. A second vector perpendicular to the symmetry axis would also need to be controlled to determine the position of all atoms. This polarisation of a symmetry axis could occur in either or both molecules. These vectors are usually denoted by the letter $\boldsymbol{r}$, followed by a subscript denoting the molecule polarised.

Secondly, the angular momentum of a molecule may be polarised. This angular momentum may be intrinsic as in the case of an open shell molecule, or may be produced due to the rotation of the molecule before the collision. While this is less intuitive than axis polarisation, it can have profound effects on the scattering. It should be noted that there is an intimate link between axis polarisation and angular momentum polarisation when the latter is induced by rotation. In a closed shell diatomic, an orientation in angular momentum must produce an alignment of a symmetry axis. This polarisation could again occur separately in each molecule, and the vectors are denoted by $\boldsymbol{j}$, followed by the molecule identifying subscript.

All vectors relating to the products are denoted with a prime after the vector (e.g. $\boldsymbol{r}'_{\mathrm{A}}$). It is worth noting that, due to the principle of microscopic reversibility[21], measuring the polarisation of the products of a collision is equivalent to measuring the effect of polarisation of the reactants in the backward reaction.

Two other vectors are often involved in stereodynamical measurements. These are the initial relative velocity vector, $\boldsymbol{k}$, and the final relative velocity vector, $\boldsymbol{k}'$. This allows understanding of the effect of polarisation relative to a direction of approach and scattering, which makes for significantly more simple interpretation. Vector correlations are then denoted with hyphens. For example, if one were measuring the correlation between polarising the symmetry axis of molecule A, $\boldsymbol{r}_{\mathrm{A}}$, and the measured induced polarisation in the angular momentum of molecule B, $\boldsymbol{j}'_{\mathrm{B}}$, all relative to the initial and final relative velocity vectors, then the correlation examined is denoted $\boldsymbol{r}_{\mathrm{A}} - \boldsymbol{k} - \boldsymbol{k}' - \boldsymbol{j}'_{\mathrm{B}}$.

The most extensively studied correlation is that between $\boldsymbol{k}$ and $\boldsymbol{k}'$. A correlation between two vectors simply produces a probablity as a function of the angle between them. This angle is known as the scattering angle, θ. The scattering angular distribution $P(\theta)$ is then directly proportional to a property known as the

differential cross section (DCS). The differential cross section is defined relative to the integral cross section (ICS), such that[18]

$$\sigma = \int_0^{2\pi} \int_0^{\pi} \frac{\mathrm{d}\sigma}{\mathrm{d}\omega}(\theta) \sin\theta \mathrm{d}\theta \mathrm{d}\phi \tag{1.2}$$

where σ is the ICS, $[\mathrm{d}\sigma/\mathrm{d}\omega](\theta)$ is the DCS and ω is the solid angle defined as $\mathrm{d}\omega = \sin\theta \mathrm{d}\theta \mathrm{d}\phi$. The ICS is defined in terms of a variable known as the opacity function. This describes how the probability of a given outcome of a collision changes with the distance between the centres-of-mass (COMs) of the two molecules perpendicular to $\boldsymbol{k}$. This variable is known as the impact parameter, and is given by the letter b. Hence, the opacity function is denoted $P(b)$. Thus, taking into account the Jacobian related to the increasing circumference of a circle surrounding the COM of one of the molecules, the ICS can be defined classically as

$$\sigma = 2\pi \int_0^{b_{\max}} P(b) b \mathrm{d}b \,. \tag{1.3}$$

where $b_{\max}$ is the maximum value of the impact parameter for which scattering takes place.

Having defined the ICS, it becomes simple to define the DCS in terms of the scattering probability distribution, $P(\theta)$, as

$$\frac{\mathrm{d}\sigma}{\mathrm{d}\omega}(\theta) = \frac{\sigma}{2\pi} P(\theta) \,. \tag{1.4}$$

1.1.4 The Scattering Frame

Before including any more than two vectors, it is helpful to define a new frame of reference, known as the scattering frame. In it, the z-axis is defined to be parallel with $\boldsymbol{k}$. $\boldsymbol{k}'$ is then defined to point in the $+xz$ plane and the y-axis is chosen to give a right-handed coordinate system (see Figure 1.3)[22, 23]. Defining any polarisation beyond the relative velocity vectors in this frame allows it to be defined relative to the scattering plane, ensuring each and every direction of polarisation is unique relative to the directions of approach and scattering.

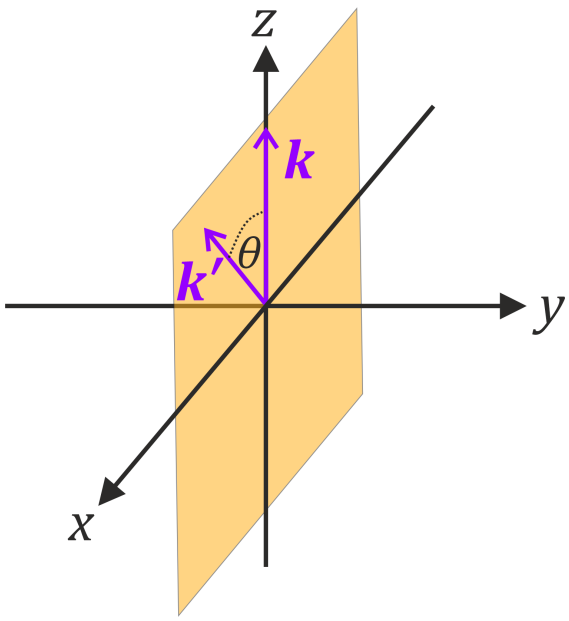

Figure 1.3: A diagram showing what is meant by the scattering frame. $\boldsymbol{k}$ and $\boldsymbol{k}'$ define the xz (scattering) plane, and the y-axis is chosen to produce a right-handed coordinate system.

1.1.5 Multipolar Expansions

Hence, now one can define a third vector $\boldsymbol{x}$, which is correlated with $\boldsymbol{k}$ and $\boldsymbol{k}'$. $\boldsymbol{x}$ will have an angular distribution defined by the polar and azimuthal angles, θ_x and ϕ_x, in the scattering frame. Classically, at a given scattering angle, θ, $\boldsymbol{x}$ has a distribution, $P(\theta_x, \phi_x|\theta)$, which may be given as a multipole expansion[23–27]

$$P(\theta_x, \phi_x|\theta) = \sum_{k=0}^{\infty} \frac{2k+1}{4\pi} \sum_{q=-k}^{k} a_q^{(k)}(\theta) C_{kq}^*(\theta_x, \phi_x) \tag{1.5}$$

where the distribution has been expanded in terms of the modified spherical harmonics, defined in terms of the regular spherical harmonics by $C_{kq}(\theta_x, \phi_x) = \sqrt{4\pi/(2k+1)} Y_q^{(k)}(\theta_x, \phi_x)$, and where $a_q^{(k)}(\theta)$ are the expansion coefficients at each value of the scattering angle given by

$$a_q^{(k)}(\theta) = \int_0^{2\pi} \int_{-1}^{1} P(\theta_x, \phi_x|\theta) C_{kq}(\theta_x, \phi_x) \mathrm{d}\cos\theta_x \mathrm{d}\phi_x \,. \tag{1.6}$$

The probability density function (PDF) linking all three vectors may be given similarly by[28]

$$P(\theta, \theta_x, \phi_x) = \sum_{k=0}^{\infty} \frac{2k+1}{4\pi} \sum_{q=-k}^{k} \left[X_q^{(k)}(\theta)\right]^* C_{kq}(\theta_x, \phi_x) \tag{1.7}$$

where

$$X_q^{(k)}(\theta) = \int_0^{2\pi} \int_{-1}^{1} P(\theta, \theta_x, \phi_x) C_{kq}(\theta_x, \phi_x) \mathrm{d}\cos\theta_x \mathrm{d}\phi_x \,. \tag{1.8}$$

Hence, the scattering angular distribution, parametrically dependent on θ_x and ϕ_x can be found by integrating the full PDF multiplied by the angular distribution of the vector[28]

$$P(\theta|\theta_x, \phi_x) = 4\pi \int_0^{2\pi} \int_{-1}^{1} P(\theta, \theta_x, \phi_x) P(\theta_x, \phi_x|\theta) \mathrm{d}\cos\theta_x \mathrm{d}\phi_x \,. \tag{1.9}$$

Inserting the expressions for $P(\theta, \theta_x, \phi_x)$ and $P(\theta_x, \phi_x|\theta)$, one obtains

$$P(\theta|\theta_x, \phi_x) = \sum_{k=0}^{\infty} (2k+1) \sum_{q=-k}^{k} \left[X_q^{(k)}(\theta)\right]^* a_q^{(k)}(\theta) \tag{1.10}$$

which is then directly proportional to the DCS. The normalisation is chosen such that

$$\frac{\mathrm{d}\sigma}{\mathrm{d}\omega}(\theta|\theta_x, \phi_x) = \frac{\sigma_{\mathrm{iso}}}{2\pi} P(\theta|\theta_x, \phi_x) \tag{1.11}$$

where σ_{iso} is the ICS averaged over all polarisations of $\boldsymbol{x}$.

Assuming a preparation of polarisation before collision, $P(\theta_x, \phi_x)$ will have no parametric dependence on θ. Hence, $a_q^{(k)}$ loses its dependence on θ. These three different PDFs in Eqs. (1.5), (1.7) and (1.10) all have their uses depending on the situation. If one would like to know how the scattering changes with reactant polarisation, Eq. (1.10) is useful. If instead, one is interested in the polarisation of the products at a given scattering angle, Eq. (1.5) is most helpful. Finally, if one is interested in how all vectors interact together, Eq. (1.7) is required.

The expansion moment $X_q^{(k)}(\theta)$ is known as a polarisation-dependent differential cross section (PDDCS)[29]. The monopole moment $X_0^{(0)}(\theta)$ is simply the scattering angular distribution with no polarisation. Further moments provide corrections to the angular distribution depending on the distribution of $\boldsymbol{x}$. PDDCSs are often

denoted with a prefix detailing which vector is influencing the DCS through its polarisation. Therefore, in this case, it would be an $\boldsymbol{x}$-PDDCS.

1.2 Scattering Amplitudes

Everything that has been discussed so far has been a highly classical picture of scattering and vector correlations. However, the get the most accurate picture of steric effects in scattering, an understanding of the quantum mechanical picture of scattering is required.

In quantum scattering, the most important quantity is known as the scattering amplitude, $f_\Omega(\theta)$. The scattering amplitude is the amplitude of the outgoing spherical wave for a given final state, depending on the initial state[30]. These initial and final states are represented here by the subscript Ω. The state-to-state differential cross section is then given by the simple equation[31]

$$\frac{\mathrm{d}\sigma_\Omega}{\mathrm{d}\omega}(\theta) = |f_\Omega(\theta)|^2 \,. \tag{1.12}$$

The scattering amplitudes may be used, once calculated, to extract stereodynamic properties of the collision[22, 23, 28, 32].

1.3 Aims and Outline of Thesis

The field of stereodynamics has come a long way from its inception in the 1960s with the early experiments using electric fields to orient small molecules in reactions with alkali metals[7, 33, 34]. These experiments might now be described as crude due to their lack of state selectivity and poorly controlled conditions. Since then, experiments have now moved towards seeking greater control over the reaction conditions, and to obtaining results in finer detail. The use of hexapoles[35, 36], Stark and Zeeman decelerators[37, 38], and new laser-based detection techniques[39, 40] have all facilitated this change.

The next stage for the field is to reincorporate elements of complexity that in recent decades have been neglected in the search for finer control, while retaining

the new techniques developed to facilitate that control. Instead of analysing atoms scattering off diatoms in ever finer detail, efforts are being made to increase the relevance of the systems studied to the wider endeavour of chemical research[41]. These efforts pushing systems to greater number of atoms, for example diatoms scattering off symmetric tops[42] and the beginnings of work towards polarisation of both molecules before collision[43, 44].

All work in this thesis is toward a single goal, namely the progression of the study of stereodynamics to systems in which both colliders are polarised. This thesis tackles this issue on two fronts. Firstly, apparatus essential to the experimental study of the scattering symmetric top molecules is designed and tested. This is an essential step on the road towards using electric fields to orient both colliders - in this case NO(X) and a symmetric top - simultaneously prior to collision. Additionally, data analysis methods are tested for the switch to 3D imaging required for that system.

Secondly, theory is devised to characterise and evaluate how symmetry axis orientation in an electric field affects the outcome of a collision, discovering how the scattering amplitudes may be used to calculate the vector correlations in that scenario. This is then also extended to a situation in which the collision partner has its angular momentum polarised before the collision. A couple of theoretical studies are then presented to display that the theory works, what orienting both molecules may achieve and also to show what might be possible to observe in an experiment.

The outline of the rest of this thesis is, therefore, as follows. Firstly, all the relevant experimental methods shall be discussed. Following this, experimental advancements towards the oriented scattering of NO(X) with a symmetric top molecule are shown. Subsequently, some data analysis methods are devised and tested for the data likely to be collected in future experiments. Next, a general formalism for the characterisation of the stereodynamics of bond axis orientation of a molecule in a $^2\Pi$ electronic state is shown. Finally, this is then extended to the system of NO(X) + H_2 in which the latter has its angular momentum oriented by a magnetic field.

2
Theoretical Methods

Contents

This chapter describes the different theoretical considerations for the calculation of scattering amplitudes. These can then used for the evaluation of stereodynamic properties.

2.1 Potential Energy Surfaces

There are two types of system for which calculated PESs are used in this thesis. These are: a $^2\Pi$ diatom with a rare gas atom, and a $^2\Pi$ diatom with a $^1\Sigma$ diatom. In both cases there are two near-degenerate PESs which both contribute to the scattering. In the case of a $^2\Pi$ diatom with a rare gas atom, where there is a plane of symmetry through all three atoms, the two PESs are labelled A' and A'' in the C_s point group[45]. If a specific linear combination of the two electronic states is taken,

one can produce a potential energy matrix in the basis of $\pm|\Lambda|$ (or equivalently $\pm|\Omega|$) states. The diagonal terms are the 'sum' PES[45]

$$V_{\text{sum}}(R,\theta) = \frac{1}{2}\left[V_{A''}(R,\theta) + V_{A'}(R,\theta)\right] \tag{2.1}$$

where θ is the angle between the bond axis of the molecule and the vector $\boldsymbol{R}$, which connects the centres-of-mass of the diatom and atom, and has a magnitude given by R. The off-diagonal terms are the 'difference' PES

$$V_{\text{diff}}(R,\theta) = \frac{1}{2}\left[V_{A''}(R,\theta) - V_{A'}(R,\theta)\right] \tag{2.2}$$

In a pure Hund's case (a) situation where the $|\Omega| = 1/2$ and $3/2$ spin-orbit manifolds are completely separated, the sum potential governs spin-orbit conserving collisions, while spin-orbit changing collisions are governed by the difference potential[45, 46].

When the rare gas is replaced with a diatomic molecule, the planar symmetry is generally lost. This has implications. Firstly, the surfaces can no longer be labelled A' and A'', and so are instead labelled 1 and 2 respectively. Secondly, the off-diagonal terms become given by[47]

$$V_{\text{o}}(R,\theta_1,\theta_2,\phi) = \frac{1}{2}\left[V_2(R,\theta_1,\theta_2,\phi) - V_1(R,\theta_1,\theta_2,\phi)\right] e^{\pm 2\gamma} \tag{2.3}$$

where θ_1 and θ_2 are the polar angles of the two diatoms, ϕ is the azimuthal angle of the $^1\Sigma$ molecule relative to the plane defined by the $^2\Pi$ molecule and the COM of the $^1\Sigma$ molecule, and γ is the angle linking states 1 and 2 to the degenerate Π_x and Π_y states, which depends non-trivially on the intermolecular geometry. The diagonal terms are given identically to the sum potential

$$V_{\text{d}}(R,\theta_1,\theta_2,\phi) = \frac{1}{2}\left[V_2(R,\theta_1,\theta_2,\phi) + V_1(R,\theta_1,\theta_2,\phi)\right] . \tag{2.4}$$

Despite the differences with the atom + diatom case, it remains true that the spin-orbit conserving collisions are driven by the diagonal potential and the off-diagonal potential governs the spin-orbit changing collisions in pure Hund's case (a)[42].

2.2 Scattering Theory

This section will discuss a variety of different methods that may be used to derive scattering quantities which may in turn be used to derive stereodynamic quantities.

2.2.1 Quasi-Classical Trajectories

Quasi-Classical Trajectories (QCT) is a method that propagates classical trajectories on a PES using Hamilton's equations of motion. Developed by Karplus *et al.*[48], it introduces a quantum mechanical effect, quantisation, by binning the final energies of the internal states into the quantum mechanical states. Initial internal energies are also chosen to match with a given internal energy quantum state.

By calculating the scattering angle, and binning that into small bins for each final state, one can calculate the scattering angular distribution by

$$P(\theta)\sin\theta \approx \frac{N_\theta}{N} \tag{2.5}$$

where N_θ is the number of trajectories scattered into a bin centred at a scattering angle θ for the given final state, and N is the total number of trajectories. By calculating the impact parameter for each trajectory and binning them, the integral cross section may be calculated from

$$\sigma = 2\pi \int_0^{b_{\max}} P(b) b \mathrm{d}b \;\approx 2\pi \sum_i \frac{N_i}{N} \Delta b \tag{2.6}$$

where i is an index corresponding to a bin of impact parameters, N_i is the number of trajectories scattered into the chosen final in bin i, and Δb is the width of the bin. Note that the distribution of impact parameters is chosen in the simulation such that the probability for any trajectory to have an impact parameter b is $P(b) \propto b$. This accounts for the increasing circumference of a circle around the COM of one molecule.

To obtain $k \neq 0$ terms in the expansion in Eq. (1.10), one can weight trajectories based on their initial geometries to agree with a chosen distribution to produce a polarisation of a vector as per Eq. (1.5). $P(\theta)$ then becomes

$$P(\theta)\sin\theta \approx \frac{\sum_N W_\theta}{\sum_N W_N} \tag{2.7}$$

where W_θ is the weight of a trajectory into the chosen final state at a scattering angle of θ (those not scattered into θ or into a different state have $W_\theta = 0$) and W_N is the weight of every trajectory regardless of final state or scattering angle.

From the different oriented angular distributions, linear combinations can be taken to obtain values for different $X_q^{(k)}$ moments. Alternatively, one may simply extract these moments by evaluating the expectation value of the bipolar harmonics describing the relationship between the scattering angle and the direction of vector $\boldsymbol{x}$[25, 29], or by calculating $P(\theta, \theta_x, \phi_x)$ and finding it's expectation value.

As the trajectories in QCT simply follow classical mechanics, they are often quantitively and qualitatively inaccurate. However, where there are parallels between more accurate results and QCT methods allows discernment of which effects are classical in origin, and which are not. QCT is particularly poor at lower collision energies[49] and in systems in which the internal energy states are widely spaced energetically, leading to very wide bins[50]. This is because in both of these cases, these collisions are intrinsically quantum mechanical in character.

There are a wide range of studies that make use of this method for both inelastic[51–55] and reactive[25, 56–61] scattering. QCT was recently used to elucidate mechanistic insights in scattering of ^{13}CO with ^{12}CO[62].

2.2.2 Quantum Mechanical Scattering Calculations

To improve the veracity of the calculations, the best option is to perform full quantum mechanical scattering calculations. These can come in two varieties. Firstly, one can propagate a wavepacket over the PES surface according to the Time-Dependent Schrödinger Equation (TDSE)[63–67]. The second option is to solve the Time-Independent Schrödinger Equation (TISE) for a stationary scattering state, which asymptotically represents the molecules in their initial and final states.

While the first of these is used and has its advantages - most obviously providing information about how the scattering event evolves over time - it is the latter

that is more commonly used due to simplicity if simply the connection between the initial and final states is desired.

The incident wave of the scattering event is simply a plane wave. After the scattering event has taken place, this wave will be replaced by two components, a transmitted plane wave which is unaltered from the incident wave, and a scattered wave, which is more complicated in shape, but has the form of an outgoing spherical wave in the asymptotic regime. The amplitude of this spherical wave can vary with angle. A function that permits this shape and remains an eigenfunction of the TISE is[30]

$$\psi_{\text{scattered}} = f_k(\theta, \phi)\frac{e^{ikr}}{r} \tag{2.8}$$

where k is the initial wavevector given by $k = \sqrt{2\mu E_{\text{coll}}}/\hbar$, with μ as the reduced mass of the system, and E_{coll} is the collision energy. The collision energy in turn is given by $E_{\text{coll}} = \mu v_{\text{rel}}^2/2$, where v_{rel} is the relative velocity, to avoid confusion with the wavevector. The angularly dependent quantity represented by $f_k(\theta, \phi)$ is known as the scattering amplitude. In practice, due to the azimuthal symmetry about the relative velocity vector of a scattering process, the scattering amplitude is only dependent on the scattering angle $f_k(\theta, \phi) \rightarrow f_k(\theta)$. Perhaps unsurprisingly, the scattering amplitude has a intimate relationship with the DCS given by

$$\frac{\mathrm{d}\sigma}{\mathrm{d}\omega}(\theta) = |f_k(\theta)|^2 \tag{2.9}$$

from which the ICS can be found by integration.

In inelastic scattering, which all examples in this thesis are, one must consider the initial and final states of the molecule. The molecules must each exist in a given internal energy state asymptotically before the scattering process takes place. Each possible combination of internal energy states is known as an entrance channel. Equally, each possible combination of internal energy states in the products is known as an exit channel. Note that these channels do not have to be energetically accessible asymptotically to be important in a scattering calculation; during the scattering process those channels above this threshold may come down in energy

and become involved. These channels that cannot be accessed asymptotically are known as closed channels, and those that are accessible are open channels.

The scattering amplitude is defined for a specific entrance and exit channel. For example, if scattering molecules A and B are initially in state $|j_{\mathrm{A/B}}, m_{\mathrm{A/B}}\rangle$ and finally in state $|j'_{\mathrm{A/B}}, m'_{\mathrm{A/B}}\rangle$, then the scattering amplitude will be indexed in terms of these channels: $f_{j_{\mathrm{A}}m_{\mathrm{A}}j_{\mathrm{B}}m_{\mathrm{B}}j'_{\mathrm{A}}m'_{\mathrm{A}}j'_{\mathrm{B}}m'_{\mathrm{B}}}(\theta)$. The complex square of this scattering amplitude gives the state-to-state differential cross section.

Calculating the Scattering Amplitude

It is clear then that the next step must be to be able to calculate the scattering amplitude. However, before diving into that, it is important that one other quantity is discussed. Namely, the scattering matrix, $\boldsymbol{S}$.

The scattering operator acts on the initial asymptotic wavefunction to give the final asymptotic wavefunction and is therefore defined

$$\hat{S}|\psi_{\mathrm{ent}}^{J_{\mathrm{TOT}}}\rangle = |\psi_{\mathrm{exit}}^{J_{\mathrm{TOT}}}\rangle \tag{2.10}$$

where the subscripts 'ent' and 'exit' refer to entrance and exit channels. Hence $\boldsymbol{S}$, made up of the matrix elements of the scattering operator, represents the probability amplitude of one entrance channel being transformed into a given exit channel. The transition matrix, $\boldsymbol{T}$, is defined as $\mathbf{1} - \boldsymbol{S}$. Often, using $\boldsymbol{T}$ is more convenient for brevity. This section shall now focus on how the transition matrix (and hence the scattering matrix) may be obtained, and then what information may be gleamed from it.

For any process, the total angular momentum, J_{TOT}, consisting of the molecules individual angular momenta, and the orbital angular momentum of the system, must be conserved. Hence, when analysing a scattering problem, one can decompose the wavefunctions into an expansion of so-called 'partial waves', each with a unique value of J_{TOT}, and treat each value of J_{TOT} independently.

Hence, we can rewrite the wavefunction of the entrance channel and exit channels as an expansion in terms of J_{TOT}

$$\psi(r,\theta,\hat{\mathbf{\Omega}}) = \sum_{J_{\mathrm{TOT}}} \psi^{J_{\mathrm{TOT}}}(r,\theta,\hat{\mathbf{\Omega}})\,. \tag{2.11}$$

where $\hat{\mathbf{\Omega}}$ represents the coordinates required to define the relative orientations of the two molecules.

This may be further expanded to give[31, 68]

$$\psi^{J_{\mathrm{TOT}}}(r,\theta,\hat{\mathbf{\Omega}}) = \sum_{\substack{j_1' j_2' \\ j_{12}' l'}} r^{-1} u^{J_{\mathrm{TOT}} j_1 j_2 j_{12} l}_{j_1' j_2' j_{12}' l'}(r) \mathscr{Y}^{J_{\mathrm{TOT}} M}_{j_1' j_2' j_{12}' l'}(\theta,\hat{\mathbf{\Omega}}) \tag{2.12}$$

where M is the magnetic projection number of J_{TOT}, j_x is the rotational quantum number of molecule x, j_{12} is the coupled rotational angular momentum of the two molecules, l is the orbital angular momentum and a prime denotes the products. The functions $\mathscr{Y}^{J_{\mathrm{TOT}} M}_{j_1 j_2 j_{12} l}(r,\theta)$ may be defined in terms of the spherical harmonics by

$$\begin{aligned}\mathscr{Y}^{J_{\mathrm{TOT}} M}_{j_1 j_2 j_{12} l}(\theta,\hat{\mathbf{\Omega}}) = \sum_{m_l m_{12}} & \langle l m_l, j_{12} m_{12} | J_{\mathrm{TOT}} M \rangle Y^{(l)}_m(\theta,0) \\ & \sum_{m_1 m_2} \langle j_1 m_1, j_2, m_2 | j_{12} m_{12} \rangle Y^{(j_1)}_{m_1}(\hat{\mathbf{\Omega}}_1) Y^{(j_2)}_{m_2}(\hat{\mathbf{\Omega}}_2)\end{aligned} \tag{2.13}$$

where m_l is the magnetic projection number of l, $\hat{\mathbf{\Omega}}_x$ represents the relevant orientation angles for molecule x, and $\langle .., ..|..\rangle$ is a Clebsch-Gordan angular momentum coupling coefficient.

Upon applying the Hamiltonian to the wavefunction at a given J_{TOT}, the TISE must be obeyed:

$$\hat{H}\psi^{J_{\mathrm{TOT}}}(r,\theta,\hat{\mathbf{\Omega}}) = E\psi^{J_{\mathrm{TOT}}}(r,\theta,\hat{\mathbf{\Omega}}) \tag{2.14}$$

where E is the translational energy plus the asymptotic rotational energy.

The Hamiltonian for the system is given by

$$\hat{H} = \hat{H}_{\mathrm{rot}} - \frac{\hbar^2}{2\mu}\nabla_r^2 + \hat{H}_{\mathrm{orb}} + V(r,\hat{\mathbf{\Omega}}) \tag{2.15}$$

where

$$\hat{H}_{\rm rot} Y_m^{(j)}(\hat{\mathbf{\Omega}}) = \frac{\hbar^2}{2I} j(j+1) Y_m^{(j)}(\hat{\mathbf{\Omega}}) \tag{2.16}$$

and

$$\hat{H}_{\rm orb} Y_{m_l}^{(l)}(\theta, 0) = \frac{\hbar^2}{2\mu r^2} l(l+1) Y_{m_l}^{(l)}(\theta, 0)\,. \tag{2.17}$$

Inserting Eq. (2.12) into Eq. (2.14), multiplying by $[\mathscr{Y}^{J_{\rm TOT}M}_{j_1'' j_2'' j_{12}'' l''}(\theta, \hat{\mathbf{\Omega}})]^*$ and then integrating over all angles, returns the close-coupled (CC) equations

$$\begin{aligned}\frac{\hbar^2}{2\mu}\left[-\frac{\mathrm{d}^2}{\mathrm{d}r^2} + \frac{l'(l'+1)}{r^2} - k^2_{j_1' j_2' j_1 j_2}\right] u^{J_{\rm TOT} j_1 j_2 j_{12} l}_{j_1' j_2' j_{12}' l'}(r) \\ + \sum_{\substack{j_1'' j_2'' \\ j_{12}'' l''}} \langle j_1'' j_2'' j_{12}'' l'' | \hat{V} | j_1' j_2' j_{12}' l' \rangle u^{J_{\rm TOT} j_1 j_2 j_{12} l}_{j_1'' j_2'' j_{12}'' l''}(r) = 0\end{aligned} \tag{2.18}$$

where $\langle j_1'' j_2'' j_{12}'' l'' | \hat{V} | j_1' j_2' j_{12}' l' \rangle$ is a potential coupling matrix element given by

$$\langle j_1'' j_2'' j_{12}'' l'' | \hat{V} | j_1' j_2' j_{12}' l' \rangle = \int\int [\mathscr{Y}^{J_{\rm TOT}M}_{j_1'' j_2'' j_{12}'' l''}(\theta, \hat{\mathbf{\Omega}})]^* \hat{V} \mathscr{Y}^{J_{\rm TOT}M}_{j_1' j_2' j_{12}' l'}(\theta, \hat{\mathbf{\Omega}}) \mathrm{d}\cos\theta \mathrm{d}\hat{\mathbf{\Omega}}\,. \tag{2.19}$$

and $k_{j_1' j_2' j_1 j_2}$ is a wavevector given by

$$k_{j_1' j_2' j_1 j_2} = \sqrt{\frac{2\mu}{\hbar^2}\left(E_{\rm coll} + E_{j_1 j_2} - E_{j_1' j_2'}\right)} \tag{2.20}$$

where $E_{j_1 j_2}$ is the rotational energy of the system with rotational quantum numbers j_1 and j_2.

Once the CC equations have been solved for $u^{J_{\rm TOT} j_1 j_2 j_{12} l}_{j_1' j_2' j_{12}' l'}(r)$, the scattering amplitude may be formulated from the transition matrix.

By comparing the asymptotic wavefunctions of the entrance and exit channels to those obtained one can obtain values for the transition matrix, and hence the scattering matrix. This asymptotic wavefunction may be given by[31]

$$\begin{aligned}\lim_{r\to\infty} \psi^{J_{\rm TOT}}(r, \theta, \hat{\mathbf{\Omega}}) = j_l(k_{j_1 j_2 j_1 j_2} r) \mathscr{Y}^{J_{\rm TOT}M}_{j_1 j_2 j_{12} l}(\theta, \hat{\mathbf{\Omega}}) \\ + \sum_{\substack{j_1' j_2' \\ j_{12}' l'}} \frac{i^{l'-l+1}}{2} h_l^{(1)}(k_{j_1' j_2' j_1 j_2} r) \mathscr{Y}^{J_{\rm TOT}M}_{j_1' j_2' j_{12}' l'}(\theta, \hat{\mathbf{\Omega}}) T^{J_{\rm TOT}M}_{j_1 j_2 j_{12} l j_1' j_2' j_{12}' l'}\end{aligned} \tag{2.21}$$

where $j_l(k_{j_1j_2j_1j_2}r)$ is a Spherical Bessel function of the first kind and $h_l^{(1)}(k_{j_1j_2j_1j_2}r)$ is a Spherical Hankel function of the first kind[69]. The first term in this expansion corresponds to the ingoing wave and the latter part refers to the outgoing wave.

Once the transition and scattering matrices have been established, the scattering amplitudes may be calculated according to[31, 70]

$$f_{j_1m_1j_2m_2j_1'm_1'j_2'm_2'}(\theta) = \frac{i\sqrt{\pi}}{k_{j_1j_2j_1j_2}} \sum_{\substack{JMl \\ m_{12}l'm_l' \\ j_{12}'m_{12}'}} \sqrt{2l+1}\langle l'm_l', j_{12}'m_{12}'|JM\rangle\langle l0, j_{12}m_{12}|JM\rangle$$
$$\langle j_1'm_1', j_2', m_2'|j_{12}'m_{12}'\rangle\langle j_1m_1, j_2, m_2|j_{12}m_{12}\rangle T^{J_{\mathrm{TOT}}M}_{j_1j_2j_{12}lj_1'j_2'j_{12}'l'} Y^{(l')}_{m_l'}(\theta, 0)\,. \tag{2.22}$$

Once the scattering amplitudes have been obtained it is possible to calculate any observable relevant to the scattering. However, the theory to do this for stereodynamic quantities has not been fully established in all cases. This is one of the aims of this thesis.

Integral cross sections from a given set of rotational states j_1 and j_2 to a set of rotational stats j_1' and j_2' averaged over initial m_1 and m_2 states and summed over final m_1' and m_2' states may be determined by

$$\sigma = \frac{\pi}{k^2_{j_1j_2j_1j_2}(2j_1+1)(2j_2+1)} \sum_{\substack{J_{\mathrm{TOT}}Ml \\ j_{12}l'j_{12}'}} |T^{J_{\mathrm{TOT}}M}_{j_1j_2j_{12}lj_1'j_2'j_{12}'l'}|^2\,. \tag{2.23}$$

The opacity function for the transition as a function of J_{TOT}, $P(J_{\mathrm{TOT}})$, may then be given by

$$P(J_{\mathrm{TOT}}) = \frac{1}{2J_{\mathrm{TOT}}+1} \sum_{\substack{Ml \\ j_{12}l'j_{12}'}} |T^{J_{\mathrm{TOT}}M}_{j_1j_2j_{12}lj_1'j_2'j_{12}'l'}|^2 \tag{2.24}$$

and hence the partial cross section, the contribution to the ICS for each value of J_{TOT}, is given by

$$\sigma_{J_{\mathrm{TOT}}} = \frac{\pi(2J_{\mathrm{TOT}}+1)}{k^2_{j_1j_2j_1j_2}(2j_1+1)(2j_2+1)} P(J_{\mathrm{TOT}})\,. \tag{2.25}$$

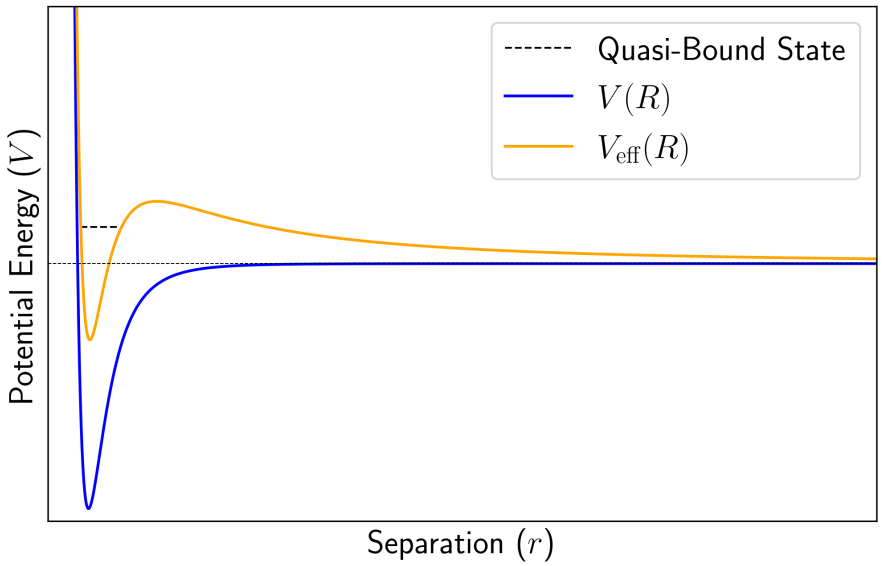

Figure 2.1: A depiction of a quasi-bound state formed in the effective potential $V_{\text{eff}}(R)$ between the repulsive wall and the centrifugal barrier.

Scattering Resonances

When one plots an ICS as a function of the collision energy - a plot known as an excitation function - signifiant structure may be found at low energies. This structure, characterised by sharp peaks, can be explained in terms of scattering resonances[71]. The use of the word resonant suggests an energy matching and this is precisely what occurs. A quasi-bound state exists somewhere along the reaction coordinate of the PES. When a collision takes place at exactly the right energy, and at the right value of l, the orbital angular momentum, a resonance can take place with the quasi-bound state.

The quasi-bound state forms between the repulsive wall of the PES and the centrifugal barrier, a peak in the effective potential, $V_{\text{eff}}(R)$, brought about by the orbital motion of the particles about the reaction coordinate[72, 73]:

$$V_{\text{eff}}(R) = V(R) + \frac{l(l+1)}{2\mu R^2} \tag{2.26}$$

where $V(R)$ is the interaction potential and μ is the reduced mass. This is illustrated in Figure 2.1.

When the resonance takes place, the molecule may remain in the quasi-bound state for some time, before tunnelling out into a particular exit channel. This exit channel will, therefore, have a very large cross section as the probability of an elastic collision following the formation of the quasi-bound state is reduced due to the difficulty escaping the quasi-bound state in the entrance channel.

There are two types of scattering resonance relevant to this thesis: shape and Feshbach. In a shape resonance, the quasi-bound state is formed in the scattering state connecting the entrance and exit channels. Hence, if one were to plot the radial distribution function of the wavefunction, one would find a sharp peak in that channel for a given value of l and r while in the quasi-bound state, before then decaying. However, it would not decay to zero, as the channel is the exit, and must therefore be present in the asymptotic regime. In the case of a Feshbach resonance, the quasi-bound state is found in a scattering state linking the entrance and some other channel[74]. Typically, this other channel is closed. As it is closed, there is no possibility of this channel being present asymptotically, hence the scattering state must link to the exit channel. The resonant channel's radial distribution function will in this case, again show a large peak in the region of the quasi-bound state, but will then decay to zero and large separation.

In fact, in a Feshbach resonance, the quasi-bound state may actually be a bound state in the potential energy well of the closed channel's PES. There is no need for a centrifugal barrier as the wall of the well can begin above the incident energy.

2.2.3 Mixed Quantum/Classical Theory

In addition QCT, there are a plethora of alternative approximate methods to obtain the scattering amplitudes with differing degrees of accuracy, including, but not limited to, the Fraunhofer model[75, 76] and Stolte's Quasi-Quantum Treatment[77].

A new, highly promising, approximate method for calculating the scattering matrix, and hence scattering amplitudes has been developed by Babikov and coworkers[78–81] and has been applied to both system with an open-shell nature[82] and those including an inversion splitting in a symmetric top molecule[83].

The method works by treating the translational motion of the scattering process completely classically, while treating the rotational degrees of freedom completely quantum mechanically. A single trajectory is then calculated at integer values of l, analogous to the partial wave expansion in J_{TOT} in quantum mechanical equations. By calculating the probability amplitude of forming a given product rotational state for each value of l, one can construct the scattering matrix and hence the scattering amplitudes.

This method has been shown to accurately approximate quantum scattering results for both integral and differential cross sections [81, 84].While developments are being made toward stereodynamical quantities being derived from this theory, there is yet more progress required. The software is also currently limited to integer values of j, preventing usage for systems containing open shell NO(X). Hence, this method is not used in this thesis.

2.3 HIBRIDON Calculations

HIBRIDON[85] is a suite of codes that solves the close-coupled equations for inelastic scattering problems with a given input PES. It is used throughout this thesis for that purpose.

Steps must be taken to ensure convergence of these calculations. Firstly, values of R_{start} and R_{end}, the values of R which mark the boundaries between which the scattering wavefunction is calculated, must be chosen such that the entire scattering process occurs within the range. Hence, care is taken to ensure the calculation has converged by adjusting these parameters, ensuring R_{start} lies within the classical turning point, and that the calculation changes only negligibly with increasing R_{end}. Secondly, the spacing of grid points along the distance R must be small enough to ensure adequate wavefunction propagation. Thirdly, enough partial waves, each with a different value of J_{TOT}, must be included; as an expansion with diminishing contributions as J_{TOT} increases, only a certain number are required before numerical convergence is reached. Finally, the basis set chosen must be large

enough to capture all significant effects. It is necessary to include channels that are asymptotically closed, as they may still contribute during the scattering process.

Hence, great care is taken to ensure that partial cross sections have decreased to 0 and stayed there (suggesting no more partial waves are required), calculations are checked by attempting similar calculations with smaller grid spacings, to ascertain if this has converged.

2.4 Conclusions

In this chapter, theory relevant to the computational scattering calculations shown in this thesis was displayed. The role of the near-degenerate PESs was described, before a discussion of QCT, quantum scattering theory and a brief description of an exciting new model of scattering, the mixed quantum/classical theory, was given. An overview of how quantum scattering calculations were performed using HIBRIDON for this thesis was then provided.

3
Experimental Methods

Contents

3.1 Introduction

The work described in this thesis utilises the crossed molecular beam method[86] for studying the properties of molecular collisions. The development of this method, refined and popularised by Dudley Herschbach and Y.T. Lee in the 1960s[87, 88],

contributed to the award of the 1986 Nobel Prize in Chemistry to the aforementioned pair, along with John Polanyi. This method involves two collimated beams of atoms, molecules or ions which cross each other. In the overlap volume of the two beams, their constituents collide. Then, after the collision, the products are detected to calculate cross sections.

Early experiments were blunt instruments with little to no control of the initial quantum states of the molecules, at what energy they collide or which products were detected. The development of molecular beams formed via supersonic expansion[89–92] has provided the ability to produce much colder beams, reducing the spread of internal energy states of the reactants. Further state control has been achieved using the Stark[35, 37] and Zeeman[38, 93] effects, optical methods[94, 95], as well as velocity selectors[96].

State selective detection has become a crucial part of many crossed molecular beam experiments. These methods include Laser Induced Fluorescence[97] and Resonance-Enhanced Multi-Photon Ionisation[98] (REMPI) (see Section 3.2.3).

This chapter describes some of the key experimental concepts as well as the experimental setup involved in this thesis.

3.2 Experimental Concepts

3.2.1 Vacuum Chambers

Gas phase dynamics experiments are almost universally carried out in either ultra-high vacuum (below 1×10^{-8} mbar), or in very high vacuum conditions (below 1×10^{-6} mbar). This is to allow a long enough mean free path to ensure that the only collisions taking place are those to be studied. These conditions are most usually produced in stainless steel vacuum chambers. These can then be pumped by roughing pumps, capable of producing pressures in the region of 1×10^{-3} mbar at the lowest. Traditionally, these have been oil-based Rotary Vane Pumps, although in many cases, due to the desire to prevent oil from entering the vacuum and due to their more energy efficient nature, these are being replaced by dry pumps, such as Scroll Pumps. Once a low enough pressure has been produced in the chamber,

a turbomolecular pump, fixed to the chamber and through which the roughing pumps are connected, may be switched on. These act more like compressors, essentially pushing gas out of the chamber, and are able to achieve pressures below 1×10^{-6} mbar, or as low as 1×10^{-9} mbar, depending on the pump and the quality of the seals in connections between vacuum chamber components.

3.2.2 Molecular Beams

Molecular beams can be produced in many ways, but by far the most common way is through the use of pulsed valves. These have a small opening (nozzle) which is periodically opened for a very short period of time. As the gas behind the valve is at pressures of greater than 1 bar, and the other side of the valve is at vacuum, with pressures on the order of 1×10^{-7} mbar or lower, the gas is forced through the nozzle in a supersonic expansion. As part of this expansion, much of the internal energy is converted into directed translational energy, producing a rotationally cold directed beam with a relatively narrow velocity distribution. The beam can then be collimated using a skimmer: a curved, hollow cone-like object which sits with the thin end towards the nozzle of the valve. If the skimmer is situated such that it catches the zone of silence of the supersonic expansion, it will not only ensure that the beam is collimated, but also that the coldest part of the beam is selected.

The velocity of a molecular beam may be approximated by the result obtained in a perfect gas upon an ideal expansion, which is given by[99]

$$v = \sqrt{\frac{2R}{M_{\mathrm{W}}}\left(\frac{\gamma}{\gamma - 1}\right)T} \tag{3.1}$$

where R is the molar gas constant, M_{W} is the molecular weight of the molecule, T is the temperature, and γ is the ratio of the heat capacities at fixed pressure and volume, C_p/C_V.

3.2.3 Resonance-Enhanced Multi-Photon Ionisation

Resonance-Enhanced Multi-Photon Ionisation (REMPI) is a laser-based technique used to ionise a single rovibrational state of a molecule[18]. The first step is to use

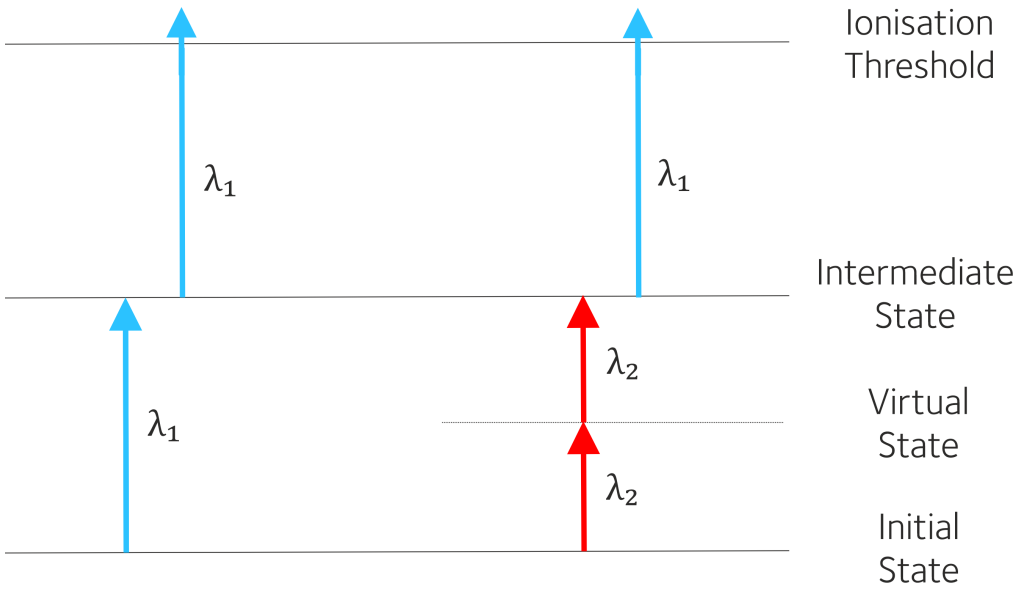

Figure 3.1: A schematic of two REMPI schemes for a hypothetical molecule. On the left hand side is a $(1+1)$ REMPI scheme, in which one photon is required to excite to the resonant intermediate state, and then one photon of the same wavelength is required to ionise. On the right hand side is a $(2+1')$ REMPI scheme, using two photons of one wavelength reach the intermediate state, and then using a photon of another wavelength to achieve ionisation.

a single wavelength of light to excite the molecule to an intermediate electronic state which is resonant with the photon energy of the light used. As the resonance significantly increases the transition probability, only a rovibrational state with the correct energy to facilitate the resonance will be excited. This first step may be a one, two or more photon process, but the sensitivity of the technique decreases significantly with each photon required. Once excited to the intermediate state, more photons (usually only one to maximise sensitivity) are then used to ionise the excited molecule. These processes can be labelled using the notation $(a+b)$, where a is the number of photons required for the excitation to the intermediate state, and b is the number of photons required for the post-excitation ionisation. A prime may be added after b to describe a process in which photons of different energy are used for the excitation and ionisation processes.

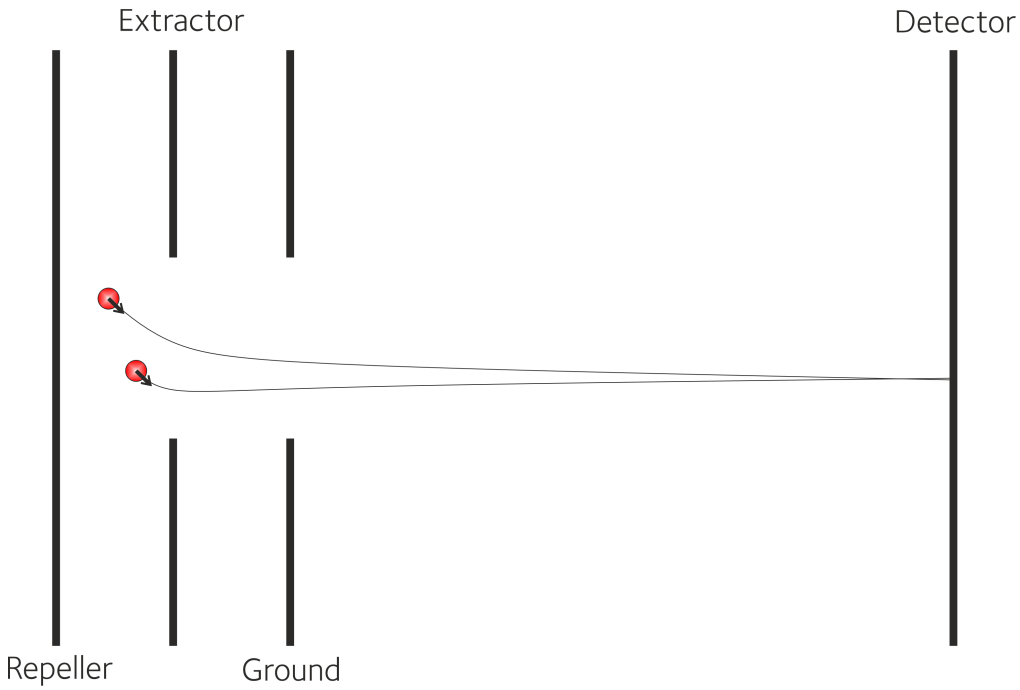

Figure 3.2: A schematic displaying the principle of velocity map imaging. Two ions with the same velocity but different initial positions are focussed onto the same position on a two-dimensional detector.

3.2.4 Velocity Map Imaging

Velocity map[40] ion imaging[39] (VMI) is a technique in which ions produced in the interaction region are focussed onto a position sensitive detector using electrostatic lenses. The ions are focussed such that their position upon impact with the detector depends only on their velocity upon either ionisation or the imposition of the electric field, if ionisation is not required. In an idealised situation, this occurs without regard to the initial position of the ions, although in practice there can be some effects if the ions detected are produced over a wide area. The time of arrival of the ions at the detector should also only be dependent on their initial velocity in the Time-of-Flight (ToF) direction, assuming a single ion mass. Therefore, it is possible to retrieve full 3D velocity distributions for the process using this method, as has been shown before in a variety of different ways[100–103].

The most common position sensitive detector used in these sorts of experiment is composed of two Microchannel Plates (MCPs) and a phosphor screen. MCPs consist of arrays of small tubes at a small angle from the surface normal. In the

dual MCP setup, these tubes are rotated 180° to each other from one plate to the other, forming a chevron shape. When an ion moves towards the detector and enters one of these channels, it will hit the wall due to the angle on the channel. This impact will produce a cloud of electrons. If an electric field is applied across the MCPs, the electrons are accelerated through the channels. Due to the chevron shape, the electrons are certain to hit the walls again of the channel in the second MCP, further amplifying the number of electrons. After exiting the second MCP, these electrons are then accelerated onto the phosphor screen, which acts as a scintillator, producing light in the position of the electrons' impact, which may then be detected by a camera.

In the most basic version of VMI, a three-plate Wiley-McLaren[104] setup is used. The first of these plates, which is known as the repeller, sits behind the nascent ions and provides an accelerating force along the ToF tube. The second electrode is known as the extractor. This electrode sits a little beyond the nascent ions along the ToF tube. It has a circular hole in the middle of it, and a lower voltage is applied to it than the repeller. Its role is to focus the ions to create the velocity-mapping effect. Finally, there is a ground plate which, after extraction, creates a field-free region into which the ion cloud may expand as it travels down the ToF tube. This expansion allows the image to grow larger on the detector, increasing velocity resolution by helping to separate out events on the detector, and increasing the number of pixels activated on the camera.

3.2.5 Cameras

The introduction and subsequent development of Complementary Metal Oxide Semiconductor (CMOS) sensors has largely caused them to supersede the traditional intensified charge-coupled device (iCCD) cameras that have been used in this field before. All cameras used in this thesis are CMOS cameras. These can range from frame-based cameras, suitable for 2D imaging, through to those that are designed to capture events recorded, rather than a whole frame. This second form of camera can be used as fast imaging cameras, with enough time resolution to record 3D

(x, y, t) data. The advantage of using these cameras over other methods to collect 3D VMI information is that they can work with high count rates, as would be likely for a cross beam molecular scattering experiment.

PImMS

The Pixel Imaging Mass Spectrometry (PImMS)[105–107] camera series uses CMOS technology to produce time-stamping, event-based cameras, which record data with full (x, y, t) coordinates. The PImMS1 camera provides a 72×72 pixel array with a time-stamping resolution of 12.5 ns. The second generation PImMS2 camera has a 324×324 pixel array, which is much more practical for the requirements of the experiment, but has a time-stamping resolution of 25 ns.

TimePix3Cam

The Timepix3 camera[108–110] is another fast imaging camera. This camera has technologically superseded the PImMS cameras, but are much less easy to come by. It comes with a 256×256 pixel array, with a time-stamping resolution of 1.56 ns, which is an order of magnitude better than the PImMS cameras.

3.2.6 Photomultiplier Tubes

A Photomultiplier Tube (PMT) is a device used to detect light with a high degree of sensitivity and a high time resolution. Light enters the PMT and hits a photocathode, which through the photoelectron effect, causes the emission of a photoelectron. After the photocathode lies a series of electrodes known as dynodes. Each successive dynode is held at a potential somewhat above the previous one. Hence, the photoelecton is accelerated towards the first dynode. This causes emission of more electrons by the process of secondary emission, which are then accelerated onto the next dynode. This process continues down the chain of dynodes, amplifying the number of electrons by a very large factor, often by 10^8 times. After the final dynode, the electrons are further accelerated onto an anode, which produces a detectable current.

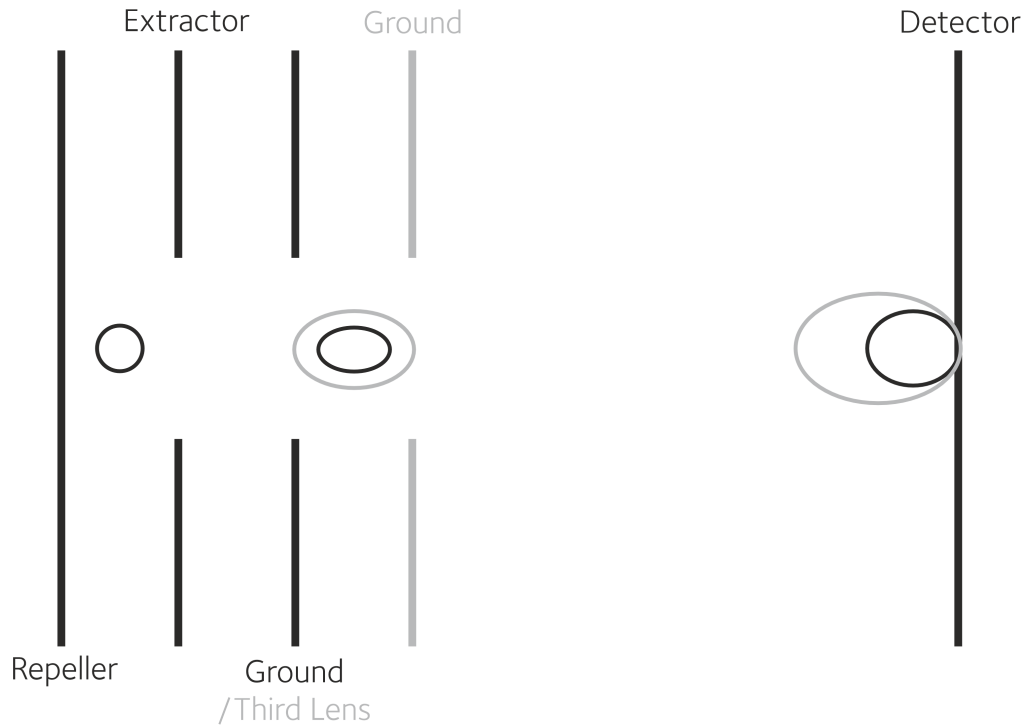

Figure 3.3: A schematic showing the difference that adding an extra lens into the ion optic setup can allow the ion cloud to expand more than with a conventional Wiley-McLaren setup. Changes in the DC slicing setup from a standard VMI setup are shown in grey.

While a PMT has an excellent time resolution, it has no spatial resolution. Therefore, its usage is restricted to the measurement of ToF peaks and for use in REMPI spectra, in which a REMPI process occurs and the resulting ions are detected by an MCP detector, with the intensity of the light produced recorded by the PMT. By varying the wavelength of the excitation laser, one can obtain a set of peaks for each rotational state present.

3.2.7 Direct Current Slice Imaging

In general, the Wiley-McLaren setup does not give a wide enough ToF peak to allow a PImMS2 camera or sometimes even a Timepix3 camera to obtain enough slices to provide enough resolution along the ToF axis to be useful. The limited time resolution of a P47 phosphor screen (rise time of approximately 7 ns) could also inhibit the resolution for a small duration of ion cloud. Hence, it is necessary to stretch out the ion cloud along this axis.

In theory, one could reduce the voltages in concert on the repeller and extractor, and the reduced acceleration caused by the smaller electric field gradient should allow for greater expansion of the ion cloud as it travels down the ToF tube. One could also extend the ToF tube to obtain a similar effect. However, this expansion will also occur in the plane of the detector, which may cause it to exceed the size of the detector. This can be resolved by extending the extraction region, allowing for lower electric field gradients, reducing the acceleration while not significantly changing the velocity of the ions in the ToF region. As was shown by Townsend *et al.*[111] and Lin *et al.*[112], this can be achieved by adding in electrodes between the extractor and the ground plate in a process know as direct current (DC) slice imaging. By carefully adjusting the voltages on the electrodes, one can retain velocity mapping capability while extending the width of the ToF peak. The more electrodes that are added, the potential for greater time extension increases, while also increasing the volume the nascent ions may inhabit initially while retaining velocity-mapping capability.

This method has traditionally facilitated the collection of a 'central slice'[113–115]. In that case, after the ion cloud has been temporally extended, the detector or camera is gated to only capture the centre of the ToF peak, such that only those ions scattered perpendicular to the plane of the detector are captured. It is also possible to vary the timing of the gate, and therefore obtain slices through the ion cloud. This method does have the disadvantages of both having a slower data collection rate than fast imaging cameras, and being susceptible to differences between slices being caused by drifting experimental parameters, rather than simply due to inherent scattering effects.

3.2.8 Post-Extraction Inversion Slice Imaging

The Post-Extraction Inversion Slice Imaging (PEISI)[116] method extends the capabilities of the DC slice imaging to allow significantly greater extension of the ion cloud along the ToF axis. It is based on Post-Extraction Differential Acceleration (PEDA)[117]: a technique used in mass spectrometry to reduce the width of ToF peaks. In that method, a pulsed voltage is applied to an electrode after extraction,

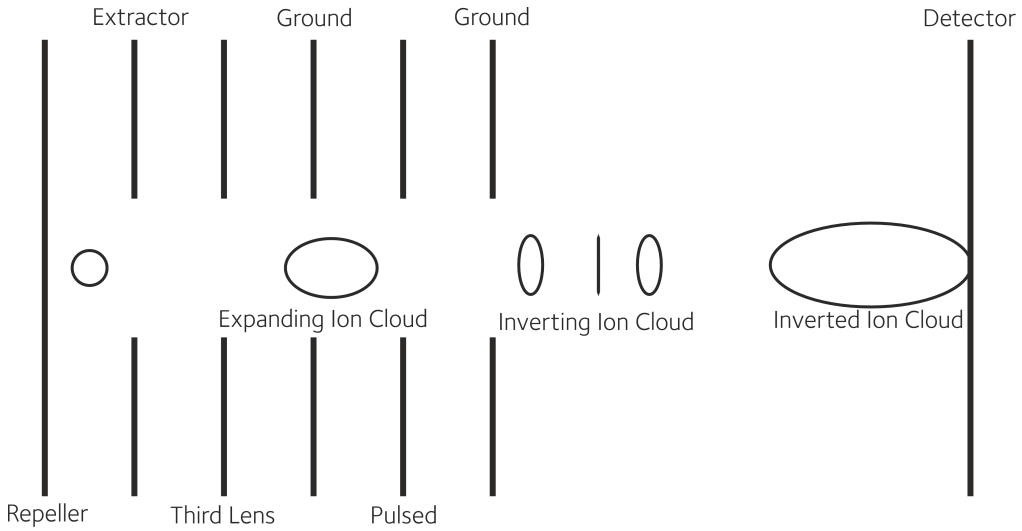

Figure 3.4: A schematic displaying the principle of PEISI. The ion cloud initially expands through the extraction region, before inverting after travelling past the pulsed plate. After inversion, the cloud expands rapidly along the time-of-flight direction until detection.

but before the ions pass the ground electrode. This causes the ions to experience a force, accelerating them down the ToF tube. Those ions at the back of the ion cloud (those with initially the most negative velocities along the ToF axis) are accelerated more than those at the front of the ion cloud. This causes the ion cloud to contract along the ToF axis, with the aim, in the case of PEDA, of focussing the ions temporally at the point they hit the detector.

In PEISI, this principle is taken one step further. If the voltage applied is significantly greater than that applied in PEDA, the ion cloud will not only contract, but fully invert along the ToF axis. After inversion, the ion cloud will then continue to extend along the time-of-flight axis. This is illustrated in Figure 3.4. This process allows the ion cloud to be temporally extensive enough to be able to collect a significant number of slices, even from a PImMS2 camera. Although initially demonstrated in the context of photodissociation, this method has also been tested on a scattering system and shown to work in principle[118].

3.3 Experimental Apparatus

The experimental apparatus about which the majority of this thesis relates is a crossed molecular beam machine. A General valve is used to produce a molecular beam of NO at 10 Hz, which is then skimmed by two successive skimmers. This collimated beam then passes through a 2 m long hexapole, six rods of alternating positive and negative potential in an hexagonal arrangement, which focusses and state selects the $j = 1/2f$ state of NO into an interaction region.

Another molecular beam lies at 90° to the first beam, running at 5 Hz. This halving of the frequency allows every other repetition to be a background measurement, which can then be subtracted. Historically, this beam has been a rare gas beam. This rare gas beam was produced from a home-built Jordan valve through a skimmer straight into the interaction region. As part of the work that went into this thesis, this molecular beam arm was redesigned, to facilitate the production of a symmetric top molecular beam, requiring a double hexapole for state selection, for more details on this, see Chapter 4.

The two molecular beams meet in the centre of the interaction region. Here they encounter two laser beams, which propagate in the same plane as the molecular beam, but are rotated 135° anticlockwise from the propagation direction of the molecular beams. The first laser beam is produced by a Sirah Cobra Stretch dye laser, pumped by 355 nm light obtained as the third harmonic of a 1064 nm Continuum Powerlite Nd:YAG laser. The dye laser uses Coumarin 450 dye to produce tunable light of around 452 nm, which is then frequency doubled using a BBO crystal to produce tunable radiation of around 226 nm. The second laser beam takes the remaining second harmonic of the Nd:YAG laser at 532 nm, and frequency doubles that to give radiation of 266 nm. These lasers carry out a $(1 + 1')$ REMPI scheme of NO(X)[119]. The tunable beam allows for state selective excitation of the transition NO(A-X). The 266 nm beam has a much greater fluence (it has an energy of roughly 30 mJ per pulse compared to 20 μJ per pulse for the 226 nm beam when in a normal running configuration), and thus the ionisation process is more likely in the region of the second laser beam, allowing greater definition of the detection

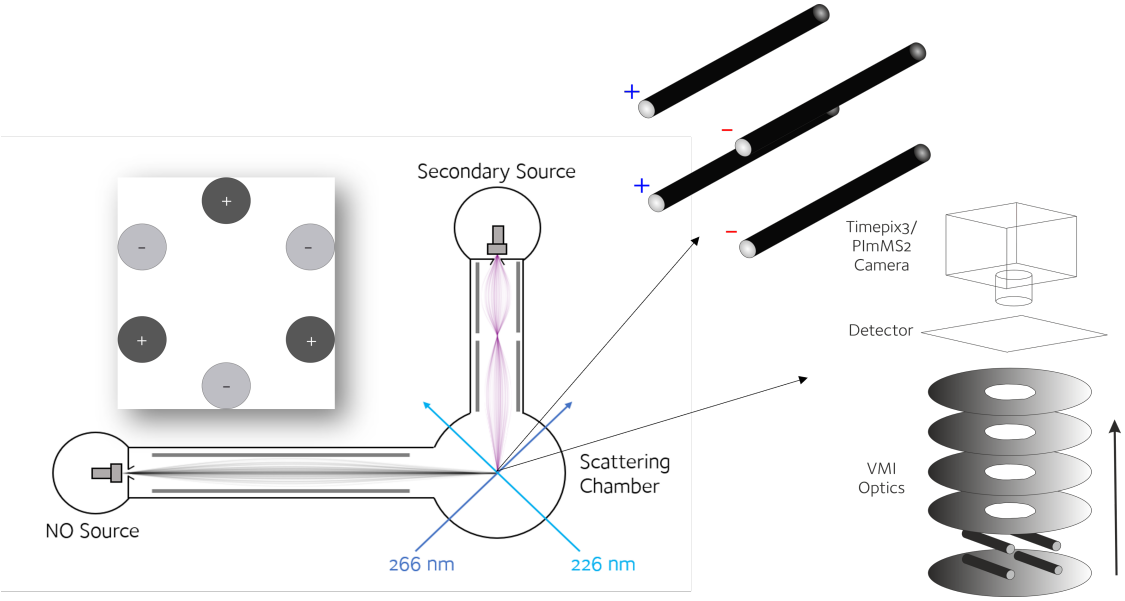

Figure 3.5: A schematic of the experimental apparatus described in this thesis. An NO beam, focussed and state selected by a hexapole (inset top left) is crossed with a symmetric top beam focussed and state selected by a double hexapole. In the interaction region lies 4 rods, producing a dipolar static electric field which orients the two molecules prior to collision. A 226 nm laser beam is used to excite the chosen product rotational state of NO(X), and a 266 nm laser beam ionises the products. After ionisation, the voltages are switched on the rods to velocity-mapping voltages, and the ions undergo VMI. Upon lighting up the detector, a PImMS2 camera, or a Timepix3 camera may be used to collect 3D VMI data. A frame-based CMOS camera may also be used to capture 2D VMI data.

region compared to if the second laser beam were absent. Its usage gives a large increase in signal over the 226 nm beam alone, as long as the fluence of the 226 nm light is not increased significantly from the normal configuration.

If, instead, detection of $NH_3(\tilde{X})$ or $ND_3(\tilde{X})$ is desired, the Nd:YAG laser is only frequency doubled, and the 532 nm light is used to pump the dye laser. DCM laser dye is then used to produce tunable light in the region of $624 - 644$ nm, before it is then frequency doubled by a KDP crystal to produce $312 - 322$ nm radiation. This is then focussed into the interaction region using a 50 cm lens. This facilitates a $(2+1)$ REMPI scheme[120]. This method does not require the use of a second laser.

In this region also lies a set of velocity-mapping ion optics, which can either be a 3-plate Wiley-McLaren, DC slice imaging or PEISI setup. These accelerate the ions produced via REMPI onto a dual-MCP detector with a P47 phosphor

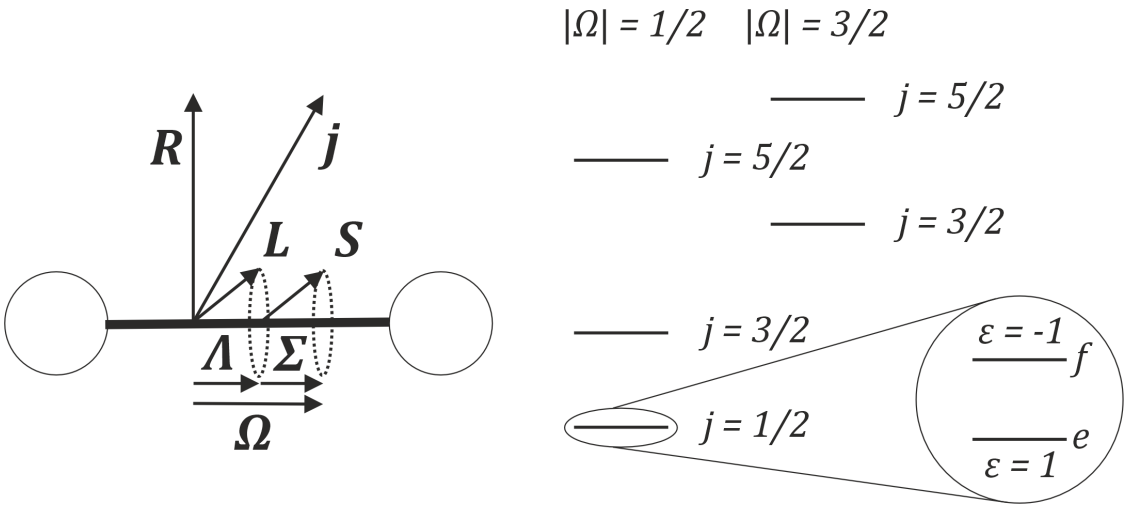

Figure 3.6: A diagram displaying the angular momentum coupling scheme for Hund's case (a) along with the energy levels produced. If the spin-orbit coupling constant, $A_0 < 0$, then the $|\Omega| = 3/2$ manifold will sit below the $|\Omega| = 1/2$ manifold energetically.

screen. Situated above this is a Basler ace U acA1920-40um CMOS camera, which captures an image of the detector. A PImMS2 or Timepix3 camera may also be used as the camera if time-stamping capability is required.

3.4 Spectroscopy of NO(X)

One of the key molecules studied in this thesis is NO in its $X^2\Pi$ ground state. Hence, it is useful to understand its rotational structure and some of its electronic spectroscopy.

NO has the ground state electronic configuration

$$1\sigma^2 2\sigma^2 3\sigma^2 4\sigma^2 1\pi^4 5\sigma^2 2\pi^1$$

and thus has an unpaired electron in what is a π^* orbital. This therefore gives it an orbital angular momentum of $\boldsymbol{L}$ which gives a projection $\Lambda = \pm 1$ onto the internuclear axis. The unpaired electron also gives rise to a spin angular momentum $\boldsymbol{S}$, whose projection onto the nuclear axis is given by $\Sigma = \pm\frac{1}{2}$. These then couple to give a total electronic angular momentum projection, Ω, where $\boldsymbol{\Omega} = \boldsymbol{\Lambda} + \boldsymbol{\Sigma}$.

For low rotational states of NO(X), the angular momentum coupling is well described by Hund's case (a). In this angular momentum coupling scheme, the

coupling between the nuclear rotation angular momentum $\boldsymbol{R}$ and the electronic angular momentum represented by $\boldsymbol{\Omega}$ is very weak, and the electronic angular momentum is coupled strongly to the internuclear axis. Hence, $\boldsymbol{\Omega}$ is well defined, and the total angular momentum is given by $\boldsymbol{j} = \boldsymbol{R} + \boldsymbol{\Omega}$. This gives states similar to symmetric tops, with a defined j (with half-integer values), m (from $-j$ to j in integer steps) and projection onto a body-fixed axis, Ω (with values $|\Omega| = 1/2, 3/2$).

To determine the energy of the states of NO(X) one must not only consider the nuclear rotation, but also spin-orbit coupling. The Hamiltonian considering these two factors is then

$$\hat{H} = \hat{H}_{\text{rot}} + \hat{H}_{\text{SO}} = B_v \boldsymbol{R}^2 + A_v \boldsymbol{L} \cdot \boldsymbol{S} \tag{3.2}$$

where, for the $v = 0$ vibrational ground state, $A_0 = 123.14\,\text{cm}^{-1}$ and $B_0 = 1.6961\,\text{cm}^{-1}$ [121] are the spin-orbit constant and rotational constant respectively. Hence, the rotational energy of the vibrational ground state (which is henceforth assumed) is given by

$$E(j) = B_0 \left[\left(j - \frac{1}{2} \right) \left(j + \frac{3}{2} \right) \pm \frac{1}{2} X \right] \tag{3.3}$$

with

$$X = \left[4 \left(j + \frac{1}{2} \right)^2 + Y \left(Y - 4 \right) \right]^{\frac{1}{2}} \tag{3.4}$$

$$Y = \frac{A_0}{B_0} \,. \tag{3.5}$$

Energy levels corresponding to a negative sign in Eq. 3.3 are denoted F_1, while those with a poistive sign are denoted F_2. At low j, when Hund's case (a) is most closely followed, the F_1 levels are associated with states with $|\Omega| = 1/2$, and the F_2 levels are associated with states with $|\Omega| = 3/2$. The F_1 and F_2 levels are manifolds of rotational levels with increasing j, but with differing spin-orbit effects.

The symmetric top-like states denoted by $|j, \Omega, m\rangle$ do not have a well defined parity with respect to inversion, and so are not eigenstates of the Hamiltonian. This is resolved by taking a linear combination of these states such that

$$|j, \Omega, m, \epsilon\rangle = \sqrt{\frac{1}{2}} \left(|j, \bar{\Omega}, m\rangle + \epsilon |j, -\bar{\Omega}, m\rangle \right) \,, \tag{3.6}$$

where the notation $\bar{\Omega} = |\Omega|$ is used (and will be used henceforth throughout this thesis) and $\epsilon = \pm 1$, are eigenstates of the Hamiltonian. The inversion parity of these states is given by $p = (-1)^{j-\epsilon/2}$[46]. The states for a single (j, $\bar{\Omega}$, m) but different values of ϵ are known as Λ-doublets. These states are split in energy. This splitting can be understood in terms of the decoupling of $\boldsymbol{L}$ from the internuclear axis with increasing j[122], or in terms of perturbation by the nearby $^2\Sigma^+$ A state[123]. The magnitude of this Λ-doublet splitting is given by[46]

$$E_{\Lambda,\bar{\Omega}=1/2} = p(j+1/2) \tag{3.7}$$

$$E_{\Lambda,\bar{\Omega}=3/2} = \frac{1}{Y}\left(2q + \frac{p}{Y}\right)\left(j-\frac{1}{2}\right)\left(j+\frac{1}{2}\right)\left(j+\frac{3}{2}\right) \tag{3.8}$$

where $p = 0.01172\,\mathrm{cm}^{-1}$ and $q = 6.7 \times 10^{-4}\,\mathrm{cm}^{-1}$[85]. The upper levels are denoted f and have $\epsilon = -1$, while the lower levels are known as e and have $\epsilon = 1$[124].

To grasp the spectroscopy of the NO(A-X) transition, which is pertinent to this thesis, we must also briefly discuss the energy levels present in NO(A). The energy levels once again fall into two manifolds labelled F_1 and F_2. These energy levels can be given by[125]

$$E_{F_1}(j) = B_v\left(j-\frac{1}{2}\right)\left(j+\frac{1}{2}\right) + \frac{1}{2}\gamma_v\left(j-\frac{1}{2}\right) \tag{3.9}$$

$$E_{F_2}(j) = B_v\left(j+\frac{1}{2}\right)\left(j+\frac{3}{2}\right) - \frac{1}{2}\gamma_v\left(j+\frac{3}{2}\right) \tag{3.10}$$

where B_v is the vibrational state dependent rotational constant for NO(A), and γ_v is the spin-rotation coupling constant. These equations can be reworked into a more helpful form by making the substitution $N = j - \frac{1}{2}$ for the F_1 levels and $N = j + \frac{1}{2}$ for the F_2 levels. This gives

$$E_{F_1}(j) = B_v N(N+1) + \frac{1}{2}\gamma_v N \tag{3.11}$$

$$E_{F_2}(j) = B_v N(N+1) - \frac{1}{2}\gamma_v\left(N+1\right) . \tag{3.12}$$

The advantage of this form is that one can straight away recognise that there are pairs of energy levels, one of label F_1 and one of F_2, which are separated by a value mediated by γ_v.

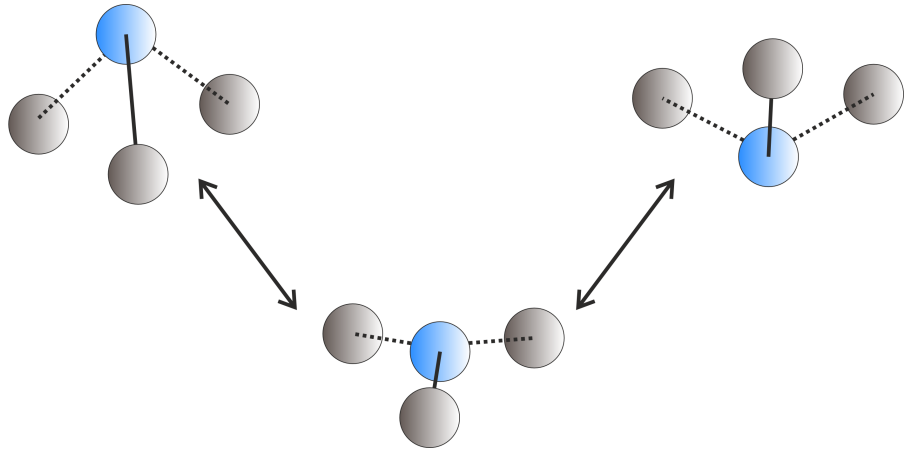

Figure 3.7: A cartoon displaying the umbrella vibrational mode of NH_3/ND_3, which leads to inversion. N atoms are depicted in blue and H/D atoms are shown in grey. The low energy of this vibrational mode (or equivalently the low barrier to inversion) allows coupling with the rotational states, producing a superposition of $\pm k$ states.

The rotational branches of the NO(A-X) can de described using the notation[122]

$$\Delta j_{x_\mathrm{f},x_\mathrm{i}}$$

where $\Delta j = -1, 0, 1$ are represented by the letters P, Q and R respectively, and x_i and x_f are the subscripts of the F_x levels for the initial and final states respectively. In the case $x_\mathrm{i} = x_\mathrm{f}$, only a single one of these values is shown (e.g. Q_{11} becomes Q_1).

The spin-rotation coupling constant, $\gamma_0 = -0.00268\,\mathrm{cm}^{-1}$[126], in NO(A) is significantly smaller than even the Λ-doublet splitting for NO(X). As the transition probed in this thesis is from $v = 0$ in the X state to $v = 0$ in the A state, the term containing γ_v can be neglected in Eqs. 3.11 and 3.12, and hence some of the branches coincide. These will be referred to as mixed branches, and are $Q_{21} + R_1$, $Q_1 + P_{21}$, $Q_2 + R_{12}$ and $Q_{12} + P_2$. Other branches shall be referred to as pure branches.

3.5 Spectroscopy of $NH_3(\tilde{X})$ and $ND_3(\tilde{X})$

One example of a symmetric top molecule is NH_3 and its isotopologue ND_3. As a molecule that features in this thesis, a description of its spectroscopy is given here.

NH_3 is a closed-shell symmetric top molecule with C_{3v} symmetry. However, it has a very low barrier to inversion, which can be easily overcome. Due to the

high frequency of inversion, spectroscopically, ammonia is usually interpreted as having D_{3h} symmetry. In it's A_1' electronic ground state, denoted ($\tilde{X}$), this coupling of states with the nitrogen above and below the plane of the hydrogens couples together the symmetric top states with $\pm k$. Hence, the rotational states available to ammonia can be described in terms of $|j,k,m\rangle$ states by[127]

$$|j,k,m,\epsilon\rangle = \frac{1}{\sqrt{2(1+\delta_{k0})}}\left(|j,k,m\rangle + \epsilon|j,-k,m\rangle\right) \tag{3.13}$$

where k is chosen to be non-negative, δ_{k0} is a Kronecker delta and $\epsilon = \pm 1$, except for $k = 0$, when $\epsilon = 1$. States with the same (j,k,m) but different values of ϵ are known as inversion doublets.

The energies of these states can then determined, using

$$E_{j,k,\epsilon} = B_v j(j+1) + (C_v - B_v)k^2 + \frac{1}{2}(-1)^j \epsilon E_{\text{inv}} \tag{3.14}$$

where B_v is the repeated rotational constant and C_v is the unique rotational constant for a given vibrational state, and E_{inv} is the energy splitting between the two inversion states which may be well approximated for the levels relevant to this thesis by[128]

$$E_{\text{inv}}\left(\text{cm}^{-1}\right) = 0.79347 - 0.005048j(j+1) + 0.00704k^2\,. \tag{3.15}$$

Rotational levels in $NH_3(\tilde{X})$ may be written in the format $j_k^{\pm}$ where the $\pm$ corresponds to the inversion symmetry of the vibrational wavefunctions for the given state. Those states with $-$ inversion symmetry are the upper inversion doublets, while those with $+$ inversion symmetry are the lower inversion doublets. This symmetry is related to the value of ϵ by the relation $\pm = -\epsilon(-1)^j$. Note that usually for NH_3 the states are written j_k^{ϵ}. This format is suitable for NH_3 as there is only one level for a given j for $k = 0$, namely j_0^+, as $\epsilon = 1$ always for $k = 0$. This is due to nuclear spin statistics as shall be seen shortly. However, for ND_3, the j_0 level is split into two components, both with $\epsilon = 1$. However, they still have different vibrational inversion symmetries, and so it makes sense to designate the

Symmetry	States	$g_{I,\mathrm{NH_3}}$	$g_{I,\mathrm{ND_3}}$
A_1	$k = 3n$ (if $k = 0$, $+/-$ state for j is even/odd)	0	10
A_2	$k = 3n$ (if $k = 0$, $+/-$ state for j is odd/even)	4	1
E	$k \neq 3n$	4	16

Table 3.1: Nuclear Spin Versions of NH_3 and ND_3, indicating which states are present for each version (where $n \in \mathbb{Z}^+$), and their nuclear spin degeneracies[133, 135].

levels with respect to this. Hence, what would have been known as j_0^+ under the other nomenclature, is here described as j_0^- for even j, and j_0^+ for odd j.

$ND_3(\tilde{X})$ shares many of the same properties as $NH_3(\tilde{X})$ in terms of its rotational wavefunctions. Due to the increased mass of deuterium in comparison to hydrogen, the tunnelling probability coupling together states with $\pm k$ is lower, and so the splitting between the inversion doublets is smaller. In this case, the splitting can be well approximated by[129]

$$E_{\mathrm{inv}}\left(\mathrm{cm}^{-1}\right) = 0.05308 - 0.0001708j(j+1) + 0.0002582k^2\,. \tag{3.16}$$

Nuclear Spin Statistics

Hydrogen is a fermion with nuclear spin, $I = 1/2$, while deuterium is a boson with nuclear spin $I = 1$. Nuclear spin wavefunctions with different symmetries can only be combined with certain rotational wavefunctions and still abide by the Pauli principle. For this section, NH_3 and ND_3 will be thought of as having D_3 symmetry to ensure that differences between inversion doublets can be taken into account[130].

ND_3 has 3 nuclear spin versions labelled A_1, A_2 and E[131], while NH_3 has only two, as there is no A_1 nuclear spin version[132]. This information is summarised in Table 3.1. One could define the labels of the nuclear spin modifications by the symmetries of the nuclear spin states or by the symmetries of the levels these spin states allow. In this case, they are labelled by the symmetries of the states they allow. The symmetries of the nuclear spin states are actually A_1 and E for NH_3[133, 134].

It should be noted that both inversion states with $k = 3, 6, 9...$ can have both A_1 and A_2 symmetry, corresponding to either $\epsilon = 1$ or $\epsilon = -1$, depending on the inversion state. Hence, the link between the inversion state label, $\pm$, and ϵ, $\pm = -\epsilon(-1)^j$, is broken. However, for NH_3, only the state in each inversion doublet

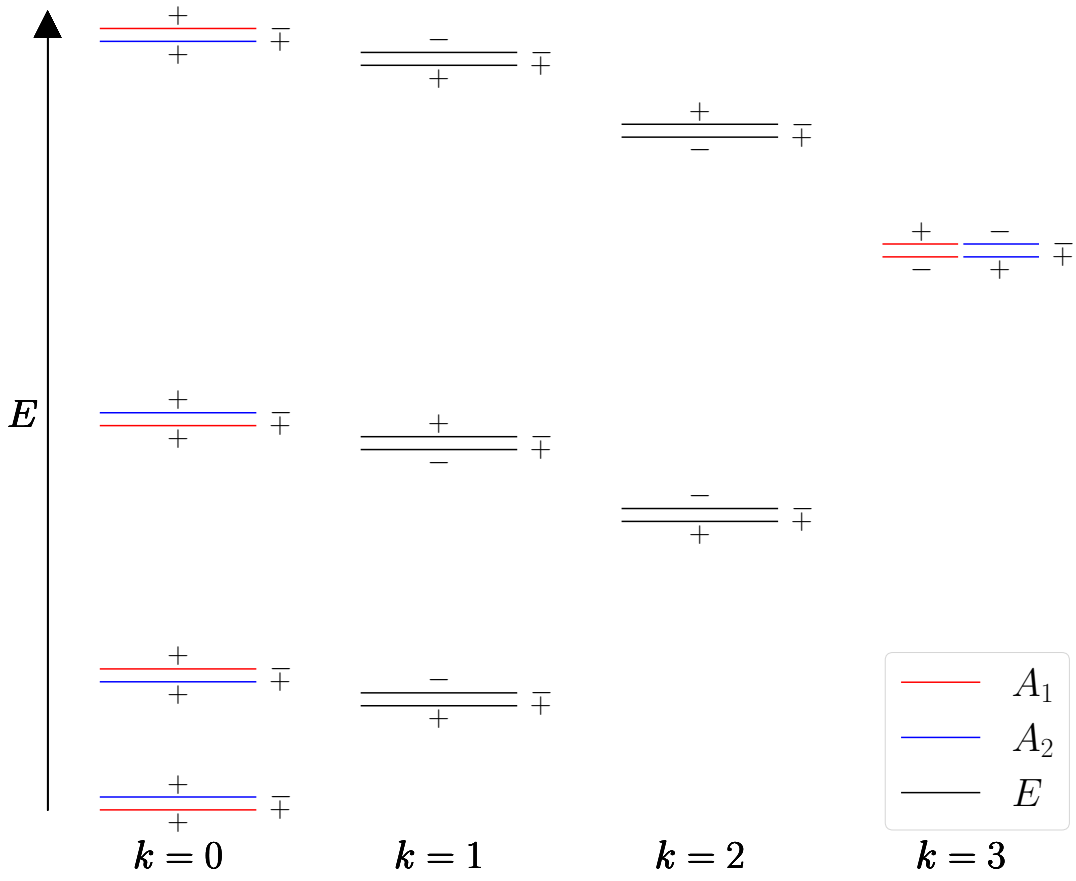

Figure 3.8: Energy levels of NH_3 and ND_3, indicating the levels that exist in each nuclear spin modification. Only the A_2 and E levels exist for NH_3. The inversion doubling is smaller in ND_3, but is exaggerated for clarity even with respect to NH_3. On the right hand side of each inversion doublet is the inversion symmetry of the vibrational wavefunctions. The value of ϵ is displayed above or below the levels.

with symmetry A_2 is allowed, because, ignoring the E nuclear spin state which is unsuitable, A_1 is the only nuclear spin state available, which can only give the required A_2 symmetry (due to Fermi-Dirac statistics) with an A_2 level. Therefore, for NH_3 the relationship between ϵ and the upper and lower components of the inversion doublet holds. However, in the case of ND_3, there are two relevant nuclear spin states, A_1 and A_2, allowing both values of ϵ for each inversion doublet (in different nuclear spin modifications). Hence, the relationship between ϵ and the upper and lower component of the inversion doublet breaks down. The corollary of this is that Eq. 3.14 only applies to $k = 0, 1, 2, 4, 5, 7, 8...$ for ND_3. In the case $k = 3, 6, 9...$ energies must be stated according to the inversion parity, rather than according to ϵ.

Transitions

In this thesis, electronic spectroscopy of NH_3/ND_3 will involve a two-photon resonant transition to the $\tilde{B}$ electronic state. All transitions from the $-$ inversion doublet will be to the $\tilde{B}$ electronic state in $v = 5$, while those from the $+$ inversion doublet will be to the $\tilde{B}$ electronic state in $v = 4$. The spectroscopic constants required for these two final states for both isotopologues can be found in reference [120]. Selection rules for these transitions are $\Delta j = 0, \pm 1, \pm 2$ and $\Delta k = 0, \pm 1, \pm 2$[136]. These transitions follow the notation

$$\Delta k \mathbf{\Delta} \boldsymbol{j} k_i(j_i)$$

where j_i and k_i are the values of j and k in the initial state. Δj values are given the labels O, P, Q, R and S for -2, -1, 0, $+1$ and $+2$ respectively. For Δk, the same letters are used but in lower case. Hence a transition from a 1_1 state to a 3_2 state would be denoted r**S**1(1).

3.6 Data Analysis Methods

In this section, some of the methods employed to analyse the experimental data found in this thesis will be explored. Firstly, the mathematics behind bond axis orientation will be discussed. Subsequently, a discussion of the Monte Carlo simulation of the experiment and how it has been used in data analysis will be found.

3.6.1 Bond Axis Orientation

If bond axis orientation before the collision is desired, a set of four rods on a rotatable base may be added to the collision region. These four rods are separated by 10 mm. Two of the rods are given a positive potential and two are given a negative potential, usually of ± 8 kV, producing an electric field in the centre of strength $9.2\,\mathrm{kVcm^{-1}}$. This field orients the NO molecule before the collision in the opposite direction to that which the field is oriented, which can be changed by rotating the base.

This electric field achieves orientation of the $j = 1/2f$ state of NO by producing a superposition with the $j = 1/2e$ state. Assuming the field is insufficiently strong to induce a superposition of j states, the wavefunction of NO in an electric field in the symmetric-top like wavefunction basis set, is given by

$$\Psi_{j,\bar{\Omega},m_E,E} = c_{\bar{\Omega}}\psi_{j,\bar{\Omega},m_E} + c_{-\bar{\Omega}}\psi_{j,-\bar{\Omega},m_E}\,. \tag{3.17}$$

When the molecule is placed into an electric field, the square of the perturbed wavefunction is proportional to the distribution of the electric dipole moment vector $\boldsymbol{\mu}$ about the electric field vector of the molecule, $\boldsymbol{E}$[137]

$$P\left(\cos\theta_{\mu E}\right) = 4\pi^2\left|\Psi_{j,\bar{\Omega},m,E}\right|^2\,. \tag{3.18}$$

After the insertion of Eq. 3.17, this becomes

$$\begin{aligned} P\left(\cos\theta_{\mu E}\right) = 4\pi^2[&c_{\bar{\Omega}}c^*_{\bar{\Omega}}|\psi_{j,\bar{\Omega},m_E}|^2 + \epsilon c_{\bar{\Omega}}c^*_{-\bar{\Omega}}\psi_{j,\bar{\Omega},m_E}\psi^*_{j,-\bar{\Omega},m_E} \\ &+ \epsilon c_{-\bar{\Omega}}c^*_{\bar{\Omega}}\psi_{j,-\bar{\Omega},m_E}\psi^*_{j,\bar{\Omega},m_E} + c_{-\bar{\Omega}}c^*_{-\bar{\Omega}}|\psi_{j,-\bar{\Omega},m_E}|^2]\,. \end{aligned} \tag{3.19}$$

A symmetric top wavefunction may be written in terms of a Wigner rotation matrix element

$$\psi_{j,\Omega,m_E} = \left(\frac{2j+1}{8\pi^2}\right)^{\frac{1}{2}} D^{j^*}_{m_E\Omega} = (-1)^{m_E-\Omega}\left(\frac{2j+1}{8\pi^2}\right)^{\frac{1}{2}} D^{J}_{-m_E-\Omega}\,. \tag{3.20}$$

Inserting Eq. 3.20 into Eq. 3.19, one obtains

$$\begin{aligned} P\left(\cos\theta_{\mu E}\right) = &\frac{2j+1}{2}\Big[\left(-1\right)^{m_E-\bar{\Omega}} c_{\bar{\Omega}}c^*_{\bar{\Omega}}D^j_{m_E\bar{\Omega}}D^j_{-m_E-\bar{\Omega}} + \left(-1\right)^{m_E+\bar{\Omega}} c_{-\bar{\Omega}}c^*_{-\bar{\Omega}}D^j_{m_E-\bar{\Omega}}D^j_{-m_E\bar{\Omega}} \\ &\epsilon\left(-1\right)^{m_E-\bar{\Omega}} c_{-\bar{\Omega}}c^*_{\bar{\Omega}}D^j_{-m_E-\bar{\Omega}}D^j_{m_E-\bar{\Omega}} + \epsilon\left(-1\right)^{m_E+\bar{\Omega}} c_{\bar{\Omega}}c^*_{-\bar{\Omega}}D^j_{-m_E\bar{\Omega}}D^j_{m_E\bar{\Omega}}\Big]\,. \end{aligned} \tag{3.21}$$

Products of Wigner rotation matrices can be written [125]

$$D^{J'}_{M'K'} D^{J''}_{M''K''} = \sum_k (2k+1) \begin{pmatrix} J' & J'' & k \\ M' & M'' & 0 \end{pmatrix} \begin{pmatrix} J' & J'' & k \\ K' & K'' & 0 \end{pmatrix} P_k(\cos\theta_{\mu E}) \,. \quad (3.22)$$

where (:::) is a Wigner 3j symbol. Using Eq. 3.22, the product Wigner rotation matrix elements in the third term inside the square brackets in Eq. 3.21 becomes

$$D^{j}_{-m_E-\bar{\Omega}} D^{j}_{m_E-\bar{\Omega}} = \sum_k (2k+1) \begin{pmatrix} j & j & k \\ -m_E & m_E & 0 \end{pmatrix} \begin{pmatrix} j & j & k \\ -\bar{\Omega} & -\bar{\Omega} & 0 \end{pmatrix} P_k(\cos\theta_{\mu E}) \quad (3.23)$$

where the second 3j symbol is identically 0. Analogously

$$D^{j}_{-m_E\bar{\Omega}} D^{j}_{m_E\bar{\Omega}} = \sum_k (2k+1) \begin{pmatrix} j & j & k \\ m_E & -m_E & 0 \end{pmatrix} \begin{pmatrix} j & j & k \\ \bar{\Omega} & \bar{\Omega} & 0 \end{pmatrix} P_k(\cos\theta_{\mu E}) \quad (3.24)$$

where the second 3j symbol is also identically 0. Hence

$$\psi_{j,\bar{\Omega},m_E} \psi^*_{j,-\bar{\Omega},m_E} = \psi_{j,-\bar{\Omega},m_E} \psi^*_{j,\bar{\Omega},m_E} = 0 \,. \quad (3.25)$$

Inserting Eqs. 3.22 and 3.25 into Eq. 3.21 and acknowledging that $(-1)^{m_E-\bar{\Omega}} = -(-1)^{m_E+\bar{\Omega}}$ for half-integer values of j, one finds

$$P(\cos\theta_{\mu E}) = \frac{2j+1}{2} (-1)^{m_E-\bar{\Omega}} \sum_k (2k+1) \begin{pmatrix} j & j & k \\ m_E & -m_E & 0 \end{pmatrix} \left[c_{\bar{\Omega}} c^*_{\bar{\Omega}} \begin{pmatrix} j & j & k \\ \bar{\Omega} & -\bar{\Omega} & 0 \end{pmatrix} - c_{-\bar{\Omega}} c^*_{-\bar{\Omega}} \begin{pmatrix} j & j & k \\ -\bar{\Omega} & \bar{\Omega} & 0 \end{pmatrix} \right] P_k(\cos\theta_{\mu E}) \,. \quad (3.26)$$

Using the identity

$$\begin{pmatrix} J_1 & J_2 & J_3 \\ M_1 & M_2 & M_3 \end{pmatrix} = (-1)^{J_1+J_2+J_3} \begin{pmatrix} J_2 & J_1 & J_3 \\ M_2 & M_1 & M_3 \end{pmatrix} \quad (3.27)$$

one can rewrite Eq. 3.26 as

$$P(\cos\theta_{\mu E}) = \frac{2j+1}{2} (-1)^{m_E-\bar{\Omega}} \sum_k (2k+1) \begin{pmatrix} j & j & k \\ m_E & -m_E & 0 \end{pmatrix} \begin{pmatrix} j & j & k \\ \bar{\Omega} & -\bar{\Omega} & 0 \end{pmatrix} \left[c_{\bar{\Omega}} c^*_{\bar{\Omega}} + (-1)^k c_{-\bar{\Omega}} c^*_{-\bar{\Omega}} \right] P_k(\cos\theta_{\mu E}) \,. \quad (3.28)$$

Converting into Clebsch-Gordan coefficients using the relationship

$$\begin{pmatrix} J_1 & J_2 & J_3 \\ m_1 & m_2 & m_3 \end{pmatrix} \equiv \frac{(-1)^{J_1-J_2-m_3}}{(2J_3+1)^{1/2}} \langle J_1 m_1, J_2, m_2 | J_3 - m_3 \rangle \tag{3.29}$$

one obtains

$$P(\cos\theta_{\mu E}) = \frac{2j+1}{2}(-1)^{m_E-\bar{\Omega}} \sum_k \langle j m_E, j - m_E | k 0 \rangle \langle j\bar{\Omega}, j - \bar{\Omega} | k 0 \rangle \left[c_{\bar{\Omega}} c^*_{\bar{\Omega}} + (-1)^k c_{-\bar{\Omega}} c^*_{-\bar{\Omega}} \right] P_k(\cos\theta_{\mu E}) \,. \tag{3.30}$$

One can now use the relationship

$$\langle J_1 m_1, J_2, m_2 | J_3 m_3 \rangle = (-1)^{J_1 - m_1} \left(\frac{2J_3+1}{2J_2+1} \right)^{1/2} \langle J_1, J_3 - m_3 | J_2 - m_2 \rangle \tag{3.31}$$

so that Eq. 3.30 may be rewritten

$$P(\cos\theta_{\mu E}) = \sum_k \frac{2k+1}{2} \langle j m_E, k 0 | j m_E \rangle \langle j\bar{\Omega}, k 0 | j\bar{\Omega} \rangle \left[c_{\bar{\Omega}} c^*_{\bar{\Omega}} + (-1)^k c_{-\bar{\Omega}} c^*_{-\bar{\Omega}} \right] P_k(\cos\theta_{\mu E}) \,. \tag{3.32}$$

If one were to write the expansion in Eq. 3.17 in the basis of the symmetry adapted wavefunctions of NO, one writes

$$\Psi_{j,\bar{\Omega},m_E,E} = \frac{1}{\sqrt{2}} \left(\alpha \psi_{j,\bar{\Omega},m_E,e} + \beta \psi_{j,\bar{\Omega},m_E,f} \right) \tag{3.33}$$

where α and β are chosen such that $\alpha^2 + \beta^2 = 2$ and hence $c_{\bar{\Omega}} = 1/\sqrt{2}(\alpha + \beta)$ and $c_{-\bar{\Omega}} = 1/\sqrt{2}(\alpha - \beta)$.

As the Hamiltonian matrix is real and its eigenvalues are non-degenerate, α, β, $c_{\bar{\Omega}}$ and $c_{-\bar{\Omega}}$ may be chosen to be real. Hence the term in the square brackets in Eq. 3.32 can be rewritten

$$c_{\bar{\Omega}} c^*_{\bar{\Omega}} + (-1)^k c_{-\bar{\Omega}} c^*_{-\bar{\Omega}} = \begin{cases} \frac{1}{2}(\alpha^2 + \beta^2) = 1 & \text{k even} \\ \alpha\beta & \text{k odd} \end{cases} \,. \tag{3.34}$$

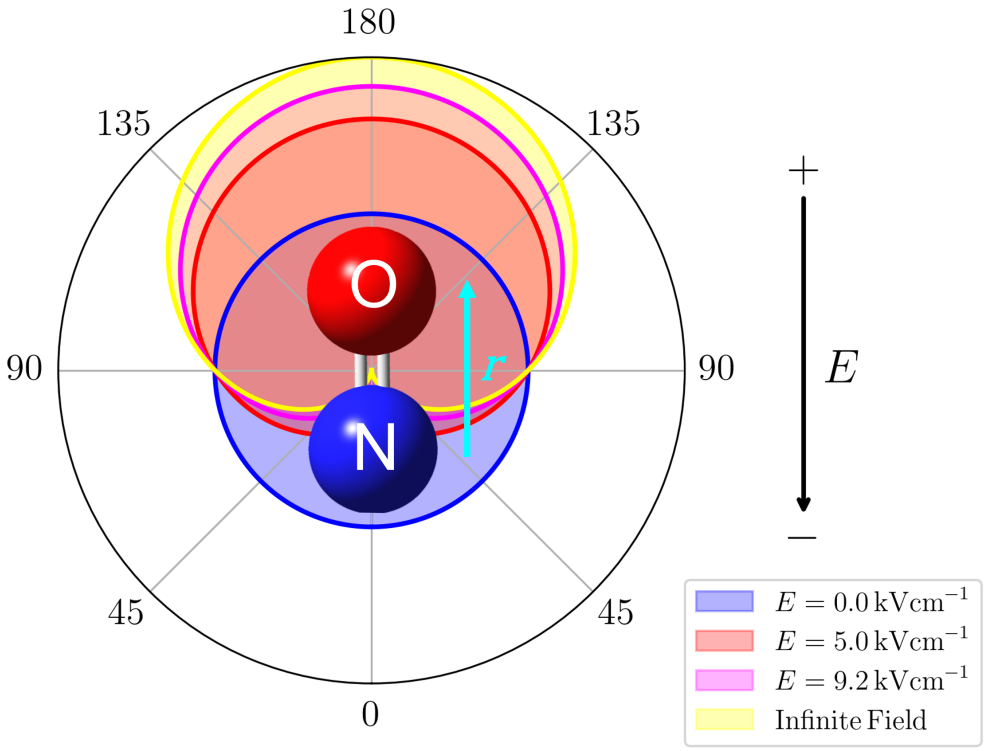

Figure 3.9: The bond axis distribution plot for a set of electric field strengths. Radius corresponds to probability of the bond axis vector, which is parallel to the dipole moment vector, being found at that angle. The usual experimental electric field is $9.2\,\mathrm{kVcm^{-1}}$.

Eq. 3.32 hence becomes

$$P\left(\cos\theta_{\mu E}\right) = \sum_k \frac{2k+1}{2} \mathcal{A}_0^{(k)} P_k(\cos\theta_{\mu E})\,. \tag{3.35}$$

where

$$\mathcal{A}_0^{(k)} = \begin{cases} \langle jm_E, k0|jm_E\rangle\langle j\bar{\Omega}, k0|j\bar{\Omega}\rangle & \text{k even} \\ \alpha\beta\langle jm_E, k0|jm_E\rangle\langle j\bar{\Omega}, k0|j\bar{\Omega}\rangle & \text{k odd} \end{cases} \tag{3.36}$$

and would classically be interpreted as the expectation value of the legendre polynomial

$$\mathcal{A}_0^{(k)} = \int_{-1}^{1} P(\cos\theta_{\mu E}) P_k(\cos\theta_{\mu E}) \mathrm{d}\cos\theta_{\mu E} = \langle P_k(\cos\theta_{\mu E})\rangle\,. \tag{3.37}$$

For an f Λ-doublet state, when $m_E > 0$, and $\alpha\beta < 0$, when $m_E < 0$, $\alpha\beta > 0$. Hence, if in the interaction region is an incoherent superposition of $\pm m_E$ states,

as would be the case after focussing through a hexapole, and noting that the first Clebsch-Gordan coefficient has the property

$$\langle j - m_E, k0 | j - m_E \rangle = \begin{cases} \langle j m_E, k0 | j m_E \rangle & \text{k even} \\ -\langle j m_E, k0 | j m_E \rangle & \text{k odd} \end{cases} , \tag{3.38}$$

the values of $\mathcal{A}_0^{(k)}$ are given by

$$\mathcal{A}_0^{(k)} = \begin{cases} \langle j\bar{m}_E, k0 | j\bar{m}_E \rangle \langle j\bar{\Omega}, k0 | j\bar{\Omega} \rangle & \text{k even} \\ -|\alpha\beta| \langle j\bar{m}_E, k0 | j\bar{m}_E \rangle \langle j\bar{\Omega}, k0 | j\bar{\Omega} \rangle & \text{k odd} \end{cases} . \tag{3.39}$$

For a $j = 1/2f$ state, this results in a bond axis distribution characterised by

$$P(\cos\theta_{\mu E}) = \frac{1}{2} \left[1 - |\alpha\beta| \cos\theta_{\mu E} \right] . \tag{3.40}$$

The values of α and β may be calculated using

$$\bar{\alpha} = \sqrt{1 - \frac{1}{\sqrt{1 + E_{\text{red}}^2}}}, \quad \bar{\beta} = \sqrt{1 + \frac{1}{\sqrt{1 + E_{\text{red}}^2}}} \tag{3.41}$$

where

$$E_{\text{red}} = \frac{2\bar{\kappa}\mu E}{E_\Lambda}, \quad \kappa = \frac{m_E \Omega}{j(j+1)} \tag{3.42}$$

and E_Λ is the Λ-doublet splitting. A visualisation of what this means for NO(X, $j = 1/2f$) is given in Figure 3.9.

3.6.2 Monte Carlo Simulation

One of the difficulties of analysing data from a crossed molecular beam experiment surrounds the flux-density transformation. In these experiments, collisions occur over a poorly defined time frame. Hence, product molecules are formed, and have time to move away from the formation location before detection. This causes a problem. Differential cross sections measure the differences in molecule flux at different scattering angles, whereas the detection system in the experimental apparatus measures the density of molecules at different angles.

As the centre-of-mass (COM) of the system is moving during the collision (*ie* the velocity of the COM, $v_{\mathrm{COM}} \neq 0$), after the collision has been completed, if the molecule is scattered in the same direction in the laboratory as the COM, their velocities will add together to give the product LAB frame NO velocity, v'_{NO}. However, if the molecule scatters in the opposite direction the COM frame NO velocity, u'_{NO} will be subtracted from v_{COM} to give v'_{NO}. Those molecules with a higher value of v'_{NO} (those scattered in the same direction as v_{COM}), will be more likely to have escaped the detection region, than those scattered elsewhere. If scattered into the LAB origin, where $v'_{\mathrm{NO}} = 0$, the molecule is not moving after the collision, and so has an exceptionally high likelihood of being detected. Hence, detection is biased towards regions in the ion image which correspond to low values of v'_{NO}.

To account for this detection of density, rather than flux, a flux-density transformation must be performed. One way of doing this transformation is by multiplying the whole image by v'_{NO}. However, this assumes that every single collision occurred with a given exact relative velocity, which will not be true, and also that the detection region is a sphere of decreasing detection probability, which is clearly not true given the shape of two overlapping cylindrical lasers is not spherical. A more accurate way of determining this transformation is through a Monte Carlo simulation of the experiment.

The Monte Carlo simulation of the experiment has been discussed in detail before[138, 139], and thus will only briefly be recapped here. Linear trajectories from two molecular beams are propagated into an interaction region, assuming they arrive at the same time in the same place. The location of the collision depends upon the angular distribution of the two beams.

If the collision is deemed to be after the time the laser fired, those trajectories are discounted. Then, a random scattering angle and a final rotational state of the NO molecule is applied. If another molecule is the scattering partner, rather than an atomic species, a separate random energy is applied to this molecule. This internal energy of the scattering partner is not quantised in the simulation. The

reason for this is the velocity resolution of the experiment. If it were possible to produce separate rings for each final kinetic energy of the product (and hence each final internal energy state of the scattering partner), it would be useful to include this quantisation in the simulation. It would facilitate the recovery of relative cross sections for each internal energy state. However, as the resolution of the experiment is insufficient to differentiate between many of the internal energy states for most molecules, it would be impossible to retrieve this information from the data. Hence, with that in mind, one thing that can be obtained is a product kinetic energy distribution (or equivalently an internal energy distribution of the scattering partner). For this to occur, no prior assumptions must be made with regard to the product kinetic energy distribution in the simulation. Hence, the internal energy states of the scattering partner must not be quantised.

Once the final kinetic energy of the NO molecule is determined, the probability of detection is determined. The two laser beams are described as having a normally distributed intensity profile across the beam. Hence, the relative probability of detection can be calculated using the perpendicular distances from the lines-of-centre of the two laser beams. This value is then used as the intensity of the detection at a point on the ion image determined by the product velocity and scattering angle. If a 3D set of ion images is required, the ToF of the ion may be used as a third coordinate. Trajectories continue to be run until the relative intensity across the whole image remains unchanged.

This provides an instrument function for the ion images, a sample of which can be seen in Figure 3.10. Here one can see that the Monte Carlo distribution captures the fact those molecules travelling more slowly, and therefore appear closer to the LAB origin will be preferentially detected. It also captures that those that are scattered with minimal velocity in the COM frame have a smaller circumference on which to form their ring of intensity. Hence, the centre of the image is more intense than positions toward the outside.

An instrument function like this may be used in one of two ways. One may simply divide the experimental ion image by the instrument function, leaving

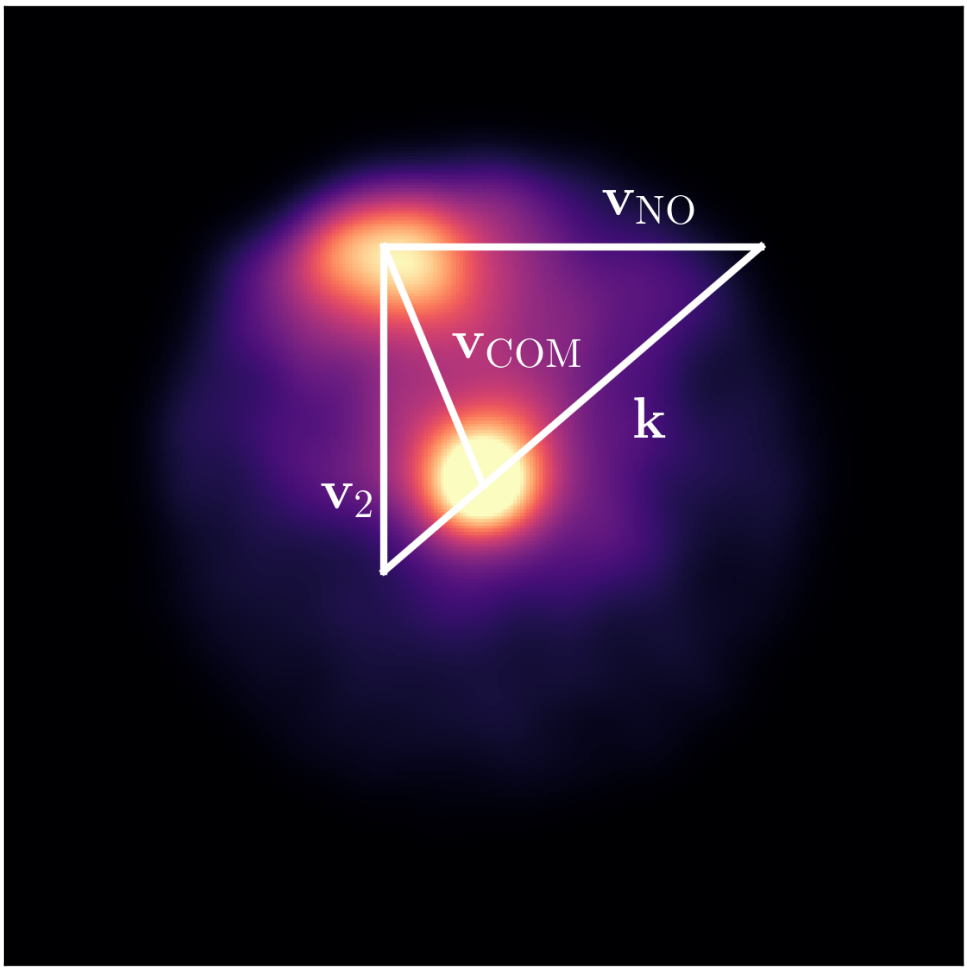

Figure 3.10: A sample simulated instrument function for a central slice of a 3D VMI experiment, assuming the internal energy states of the scattering partner are not quantised. A Newton Triangle is drawn on it, showing the LAB frame velocities of the NO molecule ($\boldsymbol{v}_{NO}$), the scattering partner ($\boldsymbol{v}_2$), and the centre-of-mass ($\boldsymbol{v}_{COM}$). The initial relative velocity vector is indicated by $\boldsymbol{k}$. The LAB origin is the top left corner of the triangle.

an image that should only contain the differential cross section (and any collision induced alignment effects, see Chapter 5). Alternatively, one can create a set of basis functions by convoluting the instrument function with the Legendre polynomials. These basis functions can then be fitted in a linear least squares manner to the experimental images to obtain the DCS.

3.7 Conclusion

An outline of the experimental methods used in this thesis have been provided here, including a description of the experimental apparatus. The established mathematics for bond axis orientation of a $^2\Pi$ molecules has also shown, and a description of the Monte Carlo simulation of the experiment was given.

4

Experimental Developments Towards NO(X) + Symmetric Top Scattering

Contents

4.1 Introduction

Experimentally, the aim of the work that is presented in this thesis was to prepare for an experiment in which state-selected NO(X) scatters with a state-selected

symmetric top molecule in a static electric field, resulting in a collision in which both molecules are oriented in space before the collision.

This will not be the first time symmetric top molecules have been studied in inelastic scattering studies. The first molecule likely to be used as the symmetric top molecule in the experiment is ND_3. There are many experimental[131, 140–145] and theoretical[146, 147] studies investigating the scattering of that molecule and perhaps even more for its isotopologue, NH_3[148–159]. Some of these studies use similar velocity map imaging techniques used in this apparatus[131, 140–143]. There is one experimental and theoretical study in which the scattering of NO(X) with ND_3 is investigated[42], in which the focus was on finding ICSs and DCSs over a very large range of energies. No studies thus far have focussed on the stereodynamics of these collisions.

The preparation for the intended experiment comes in two parts. Firstly, the mathematical framework has to be established to evaluate the Stark effect on symmetric tops in an hexapole field, and then its effect on orienting the molecule in the static electric field in the interaction region. Secondly, a double hexapole, which is to be used to state-select the symmetric top molecule, has to be designed and characterised.

Note that for the duration of this chapter, the quantum numbers j, k and m will be written as J, K, and M, to avoid confusion with the tensor order, k.

4.2 Hexapole Theory

The theory of hexapole state-selection for symmetric top molecules is well known[35, 160], and has not been expanded on here. However, to provide clarity, it is presented.

4.2.1 Stark Effects

The Stark effects for symmetric top molecules, including when inversion symmetry plays a role, such as for NH_3, will be presented in this section.

On application of an electric field along the z-axis (the space-fixed projection axis), the resulting perturbation to the Hamiltonian can be described by

$$H_{\text{Stark}} = -\boldsymbol{\mu} \cdot \boldsymbol{E} = -\mu |\boldsymbol{E}| \cos\theta = -\mu E D^1_{00}(\phi, \theta, \chi) \tag{4.1}$$

where $\boldsymbol{\mu}$ is the electric dipole moment of the molecule and $\mu = |\boldsymbol{\mu}|$, $E = |\boldsymbol{E}|$ is the electric field strength and $D^1_{00}(\phi, \theta, \chi)$ is a Wigner rotation D-matrix element, for which ϕ, θ and χ are the Euler angles connecting the space-fixed and body-fixed reference frames.

Symmetric Top Molecules

The rotational states of a symmetric top molecule in an a field-free environment can be described using three quantum numbers: J, K and M, where J is the total angular momentum quantum number, while K and M are the body-fixed and space-fixed angular momentum projection quantum numbers. These states shall henceforth be described as $|J, K, M\rangle$.

If the electric field is weak enough (the strength depends on the rotational constants of the molecule), the molecule can be treated as a single $|J, K, M\rangle$ (i.e. there is no state mixing). The first order Stark effect is given by[125]

$$\Delta E^{(1)} = -\mu E \langle J, K, M | D^1_{00} | J, K, M \rangle = -\frac{MK}{J(J+1)} \mu E = -\kappa \mu E \tag{4.2}$$

where

$$\kappa = \frac{MK}{J(J+1)}\,. \tag{4.3}$$

If the electric field in strong enough to begin to cause a non-negligible superposition of the $J' = J \pm 1$ states, a second order Stark effect of magnitude[125]

$$\Delta E^{(2)} = \frac{(\mu E)^2}{2B} \left[\frac{\left[J^2 - K^2\right]\left[J^2 - M^2\right]}{J^3 \left(2J+1\right)\left(2J-1\right)} - \frac{\left[(J+1)^2 - K^2\right]\left[(J+1)^2 - M^2\right]}{(J+1)^3 \left(2J+1\right)\left(2J+3\right)} \right] \tag{4.4}$$

where B is the repeated rotational constant of the molecule, will play a role. In all cases relevant to this thesis, these two terms will be sufficient to describe the Stark effects experienced.

Symmetric Top Molecules With Inversion Doubling

As described in the case of NH_3 and ND_3 in Section 3.5, a symmetric top with inversion doublets have symmetry adapted states of the form

$$|J,K,M,\epsilon\rangle = \frac{1}{\sqrt{2\left(1+\delta_{K0}\right)}}\left(|J,K,m\rangle + \epsilon|J,-K,M\rangle\right) \tag{4.5}$$

where δ_{k0} is a Kronecker delta and ϵ is a symmetry label.

The first order Stark effect in this system is identically 0 for all electric field strengths. This can be shown by expanding the matrix element using equation 4.5

$$\begin{aligned}\langle J,K,M,\epsilon|H_{\text{Stark}}|J,K,M,\epsilon\rangle = \\ \frac{-\mu E}{2\left(1+\delta_{K0}\right)}[\langle J,K,M|D^1_{00}|J,K,M\rangle + \epsilon\langle J,K,M|D^1_{00}|J,-K,M\rangle \\ + \epsilon\langle J,-K,M|D^1_{00}|J,K,M\rangle + \langle J,-K,M|D^1_{00}|J,-K,M\rangle].\end{aligned} \tag{4.6}$$

The second and third terms in the square brackets are identically 0. The first and last term, as in 4.2, are given by

$$\pm\kappa = \pm\frac{MK}{J\left(J+1\right)} \tag{4.7}$$

and hence they cancel out and give a first order Stark effect of 0 for all states.

A two state model, consisting of the two inversion doublets, captures most of the behaviour of these molecules in an electric field considered in this thesis.

If one calculates and diagonalises the Hamiltonian matrix for these two states, and then subsequently subtracts the field-free energies of the states, one can obtain an expression for the Stark energy of each state.

In the basis $\{|JKM1\rangle, |JKM-1\rangle\}$, the unperturbed Hamiltonian matrix is given by

$$\boldsymbol{H}_0 = \begin{pmatrix} E_{J,K,M,1} & 0 \\ 0 & E_{J,K,M,-1} \end{pmatrix}. \tag{4.8}$$

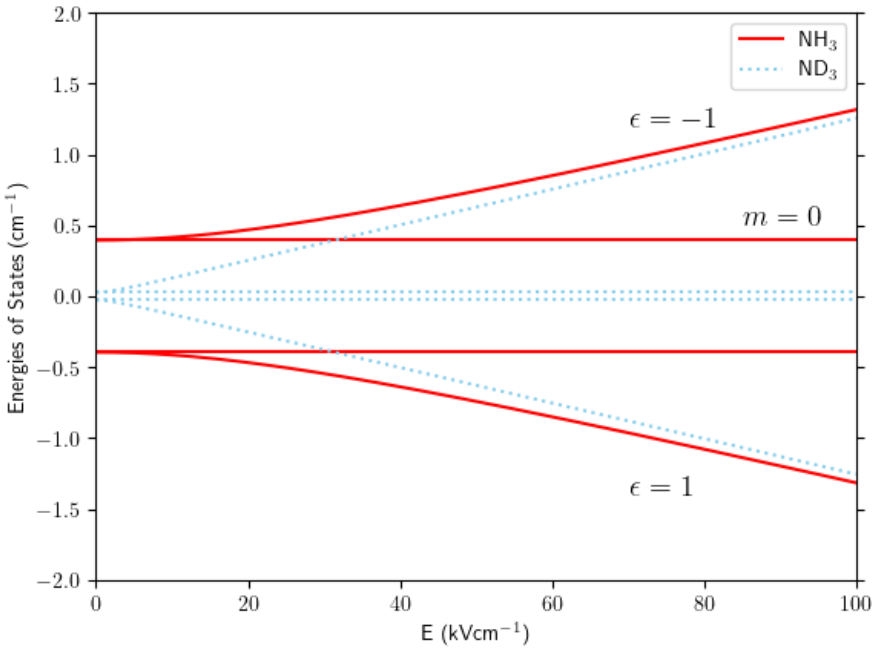

Figure 4.1: Energies of the inversion doublets for NH_3 and ND_3 in electric field strengths up to 100 kV cm^{-1}, assuming no mixing of J states.

If one works through the matrix elements of the Stark perturbation matrix in the same manner as in equation 4.6, one can obtain

$$\boldsymbol{H}_{\text{Stark}} = \begin{pmatrix} 0 & -\kappa\mu E \\ -\kappa\mu E & 0 \end{pmatrix}. \tag{4.9}$$

Using $\boldsymbol{H} = \boldsymbol{H}_0 + \boldsymbol{H}_{\text{Stark}}$, the eigenvalues of $\boldsymbol{H}$ may be determined. This returns an equation

$$E_\epsilon = \frac{E_{J,K,M,1} + E_{J,K,M,-1}}{2} + \epsilon\sqrt{\left(\frac{E_{\text{inv}}}{2}\right)^2 + (-\mu E\kappa)^2} \tag{4.10}$$

for the higher (E_+) and lower (E_-) energy states.

Subtracting the field-free energy reveals an expression for the Stark Energy[161]

$$E_{\text{Stark},\epsilon} = \epsilon\left(-\frac{E_{\text{inv}}}{2} + \sqrt{\left(\frac{E_{\text{inv}}}{2}\right)^2 + (\mu E\kappa)^2}\right). \tag{4.11}$$

The results of these equations are shown for the states present in $J = 1$ for NH_3 and ND_3 are shown in Figure 4.1. Eq. 4.11 is completely analogous to the Stark energies of the Λ-doublet states in a $^2\Pi$ state linear molecule. Replacing

the inversion splitting, E_{inv}, with the Λ-doublet splitting, E_Λ, and K with Ω, the Stark energies in this scenario may be written

$$E_{\text{Stark},\epsilon} = \epsilon \left(-\frac{E_\Lambda}{2} + \sqrt{\left(\frac{E_\Lambda}{2}\right)^2 + (\mu E \kappa)^2} \right) . \tag{4.12}$$

where

$$\kappa = \frac{M\Omega}{J\left(J+1\right)} . \tag{4.13}$$

Asymmetric Top Molecules

Asymmetric top molecules can be divided into four varieties, *a*-type, *b*-type and *c*-type, or some combination of the three[162]. a, b and c refer to the three axes of rotation with increasing moments of inertia. The type is determined by which axis the dipole moment points along. For example, if it points along axis c, then it will be a *c*-type.

Asymmetric top molecules in states with low values of J have wavefunctions similar to those of symmetric tops with inversion doubling. Hence, Eq. 4.11 acts as a good approximation to the Stark effect experienced by one of these states if the dipole moment is aligned with the axis of rotation with the smallest moment of inertia (an *a*-type). The value of the splitting (given in Eq. 4.11 as E_{inv}) may be calculated from the eigenvalues of the field-free Hamiltonian for an symmetric top. Matrix elements for this are given in Eq. 4.50. The Stark effects for an asymmetric top molecule that is *b*-type (e.g. water), or *c*-type may be found by matrix diagonalisation of the Hamiltonian using the matrix elements found in Appendix A.

4.2.2 Force in a Hexapole Field

The potential within an ideal hexapole is given by[35]

$$V\left(R,\phi\right) = V_0 \left(\frac{R}{R_0}\right)^3 \cos 3\phi \tag{4.14}$$

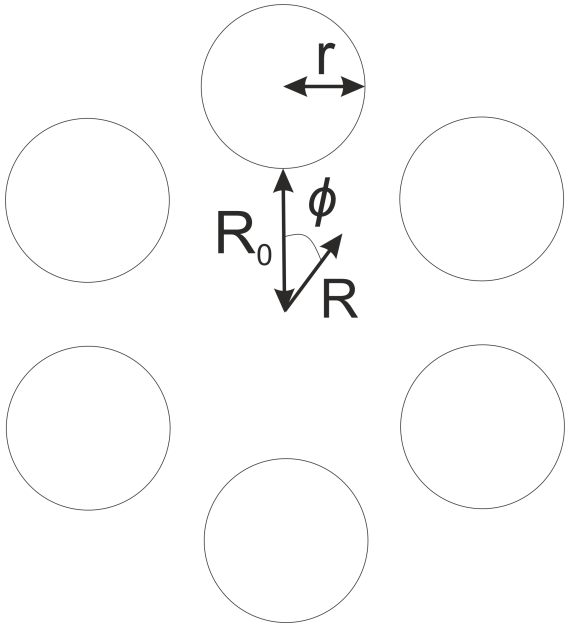

Figure 4.2: A schematic cross section of a hexapole showing the meaning of the internal radius R_0, as well as radius of the hexapole rods, r. A point with coordinates R and ϕ is also shown.

where V_0 is the absolute value of the potentials applied to the hexapole rods, R_0 is the inner radius of the hexapole, and R and ϕ are the radial and azimuthal components in cylindrical polar coordinates. The electric field strength vector is given by

$$\boldsymbol{E}(R) = -\nabla V \tag{4.15}$$

where, as usual for cylindrical coordinates, and excluding the longitudinal coordinate, upon which the potential does not depend[163]

$$\nabla = \hat{\boldsymbol{R}}\left(\frac{\partial}{\partial R}\right)_{\phi} + \hat{\boldsymbol{\phi}}\frac{1}{R}\left(\frac{\partial}{\partial \phi}\right)_{R} \tag{4.16}$$

and $\hat{\boldsymbol{R}}$ and $\hat{\boldsymbol{\phi}}$ are the unit vectors for the R and ϕ coordinates respectively. Therefore,

$$\boldsymbol{E}(R) = \left(-3V_0\frac{R^2}{R_0^3}\cos 3\phi\right)\hat{\boldsymbol{R}} + \left(-3V_0\frac{R^2}{R_0^3}\sin 3\phi\right)\hat{\boldsymbol{\phi}} \tag{4.17}$$

and

$$|\boldsymbol{E}(R)| = E(R) = 3V_0\frac{R^2}{R_0^3}. \tag{4.18}$$

The force applied by this electric field is then given by

$$F(R) = -\frac{dE_{\text{Stark}}}{dR} \tag{4.19}$$

and the differential of the field strength with respect to the radius is given by

$$\frac{dE}{dR} = 6V_0 \frac{R}{R_0^3}\,. \tag{4.20}$$

Symmetric Top Molecules

The force experienced by a symmetric top molecule can then be obtained by substituting first Eqs. 4.2 and 4.4, and then Eq. 4.20 into Eq. 4.19. This results in the expression

$$F(R) = \frac{6V_0\mu\kappa R}{R_0^3} - \frac{18V_0^2\mu^2}{B}\left(\frac{R}{R_0^2}\right)^3 L \tag{4.21}$$

where

$$L = \frac{\left[J^2 - K^2\right]\left[J^2 - M^2\right]}{J^3\left(2J+1\right)\left(2J-1\right)} - \frac{\left[\left(J+1\right)^2 - K^2\right]\left[\left(J+1\right)^2 - M^2\right]}{\left(J+1\right)^3\left(2J+1\right)\left(2J+3\right)}\,. \tag{4.22}$$

The first term in Eq. 4.21 is the first order Stark effect, while the second term is the second order Stark effect. Hence, if only the first order effects are required, the second term may be neglected.

Symmetric Top Molecules With Inversion Doubling

Using the Stark energy in Eq. 4.11, one can follow the same process to find the force in a hexapole electric field for a symmetric top with inversion doubling. After some rearrangement, this results in the expression

$$F(R) = \frac{\epsilon F_0}{\sqrt{1 + \left(\frac{E_{\text{inv}}}{F_0 R}\right)^2}} \tag{4.23}$$

where

$$F_0 = \frac{6V_0\mu|\kappa|R}{R_0^3}\,. \tag{4.24}$$

Therefore, for a $^2\Pi$ linear molecule in a hexapole field, the analogous equation is

$$F\left(R\right) = \frac{\epsilon F_0}{\sqrt{1+\left(\frac{E_\Lambda}{F_0 R}\right)^2}} \tag{4.25}$$

where F_0 may be expressed identically to Eq. 4.24, but where κ is now given by Eq. 4.13.

Asymmetric Top Molecules

As stated in Section 4.2.1, asymmetric tops in low j states share similar wavefunctions to symmetric tops with inversion doubling. Hence, Eq. 4.23, is a good approximation to the force experienced by these states, so long as the molecule is a-type. As in Section 4.2.1, the value of E_{inv} may be determined by matrix diagonalisation. For b- and c-types the Stark energies and hence gradients must be solved by this method at each time-step in the trajectory.

4.2.3 Trajectory Propagation

Once the force applied to the molecule is calculated, to produce a simulation of the effect of a hexapole on a molecular beam, one must be able to propagate trajectories of molecules along the hexapole.

Non-Linear Stark Effect

In the case of a non-linear Stark effect with respect to the radial displacement of the molecule within the hexapole, the trajectory may be calculated by iteratively solving the equations of motion, most pertinently

$$R(t+\Delta t) = R(t) + v_r(t)\Delta t + \frac{a_r(t)}{2}\Delta t^2 \tag{4.26}$$

and

$$v_r(t + \Delta t) = v_r(t) + a_r(t)\Delta t \tag{4.27}$$

where t is the time, v_r is the radial velocity, $a_r(t) = F(R(t))/M$ is the radial acceleration (where M is the mass of the molecule), and Δt is the time increment.

Linear Stark Effect

In the case of a symmetric top molecule in a weak enough electric field to avoid a significant superposition of j-states in the field, a linear Stark effect is observed. In this case, if $\kappa < 0$, the force applied resembles that of an harmonic oscillator. Harmonic motion allows facile trajectory calculation due to its predictability, allowing as large a time step as is desired. This motion is calculated using the equation[164]

$$R(t) = R(t = 0)\cos\left(\sqrt{C}t\right) + v_r(t = 0)\frac{1}{\sqrt{C}}\sin\left(\sqrt{C}t\right) \tag{4.28}$$

where

$$C = \frac{6V_0\mu|\kappa|}{MR_0^3}\,. \tag{4.29}$$

4.2.4 Hexapole Trajectory Simulation

A simulation was developed built around the equations given above to be able to predict the behaviour of symmetric top molecules through a hexapole. There are factors included in the simulation that are not necessarily simple to measure, such as the angular distribution of the beam as it enters the hexapole and the velocity of spread of the beam. These factors are therefore approximated. It is worth noting that for systems for which the Stark effect is very non-linear, the initial conditions can have significant effects on the voltages at which focussing occurs. For example, for a system with non-linear Stark effects, those molecules that enter the hexapole at a wider angle with respect to the line of centre will require a lower potential to be focussed than those at narrower angles. Hence, if the angular distribution is increased in width, the position of the focal points will move to lower voltages.

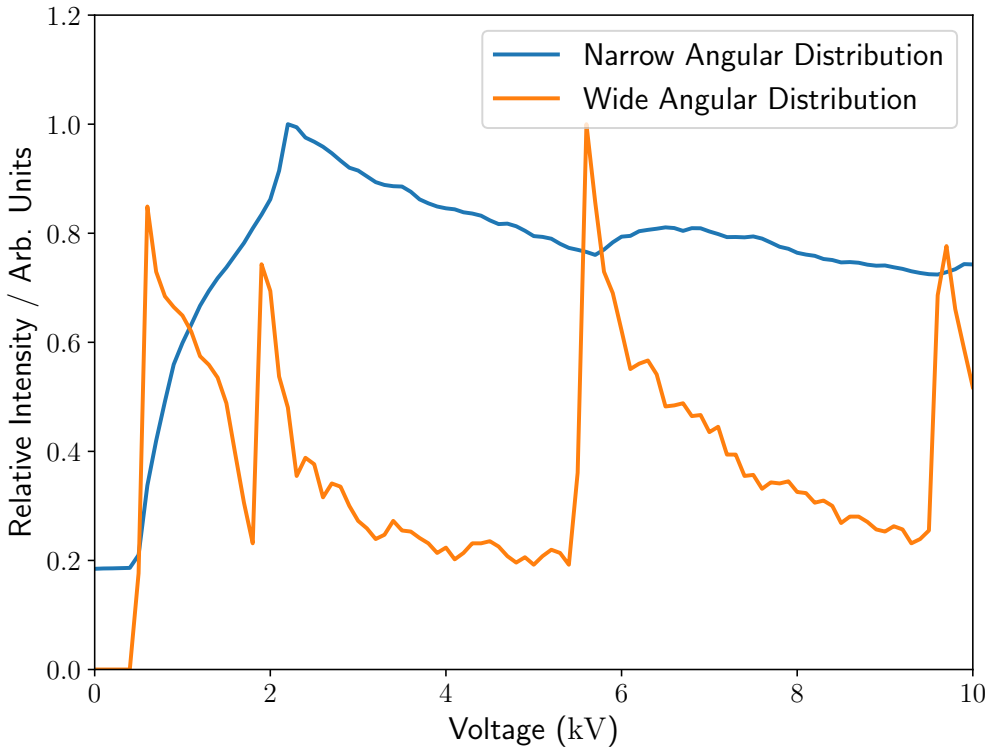

Figure 4.3: Two simulated tuning curves (transmission against voltage) for ND_3. One is simulated with a narrow angular distribution: a normal distribution with a standard deviation $\approx 0.17°$. The other is simulated with a wider angular distribution with standard deviation $\approx 0.69°$, but with an initial offset from the centre of the hexapoles of 0.5 mm. Both curves are normalised so that their maximum intensity is 1.

This is brought into stark focus by the simulated ND_3 tuning curves for the double hexapole, described in Section 4.4, shown in Figure 4.3. In this figure, transmission is shown against voltage for two normal angular distributions: one with a standard deviation of 0.17° and one with a standard deviation of 0.69°. The latter of these also initially has the molecules offset from the line of centre of the hexapoles by 0.5 mm. Although the molecules have the same velocity distribution, their angular distributions and starting positions vary. The narrow angular distribution produces a set of trajectories that never experience the linear Stark effect. Hence, there is hardly a focus point, with very similar transmissions across most of the voltage range. In the case of the wide angular distribution with an offset starting location, most of the molecules spend significant time in regions of the hexapoles in which they experience a linear Stark effect. Hence, these molecules oscillate in sine-like

curves, producing multiple foci for different numbers of oscillations. The fact these curves are so different highlights the importance of the initial conditions in the simulations. In many cases in this Chapter, the initial conditions are yet to be determined with great accuracy, limiting the quality of any simulations. This is more of an issue for molecules such as NH_3 and ND_3 than for NO, due to the inversion doubling being larger than the Λ-doublet splitting in NO. This increases the voltage at which the transition from non-linear to linear Stark effects take place.

The quality of the simulation was tested by measuring a voltage tuning curve, measuring the quantity of detected $(1 + 1')$ REMPI signal of NO(X, $j = 0.5f$) produced after the NO molecular beam travels through the 2 m long primary hexapole at a selection of voltages applied to the hexapole rods. The signal on the detector is captured by a PMT, and the corresponding peak integrated over to obtain an intensity. The results of this procedure and the simulation are shown in Figure 4.4. The simulation matches the experimental data exceptionally well, recreating the peak transmission voltage. Previous hexapole trajectory simulations carried out to represent this hexapole assumed harmonic motion, which this simulation does not. Given the experimental data collected matches the more accurate simulation, returning a peak intensity at ≈ 11kV, whereas harmonic motion returns an optimal voltage of ≈ 10 kV, it is inescapable to draw the conclusion that assuming harmonic motion is insufficient to describe the motion of NO in the hexapole.

4.3 Orientation Theory

The theory of bond axis orientation of a $^2\Pi$ molecule, assuming no mixing of J-states was presented in Section 3.6.1. The equations for the expansion coefficients in Eq. 3.39 also apply completely to a molecule with inversion doubling, replacing Ω with K, and evaluating $\bar{\alpha}$ and $\bar{\beta}$ using the inversion splitting, rather than the Λ-doublet splitting. In this section, this theory will be expanded upon to allow determination of the degree of orientation when more J-states are also included in the superposition in the electric field, and then going one step further and applying it to some asymmetric tops.

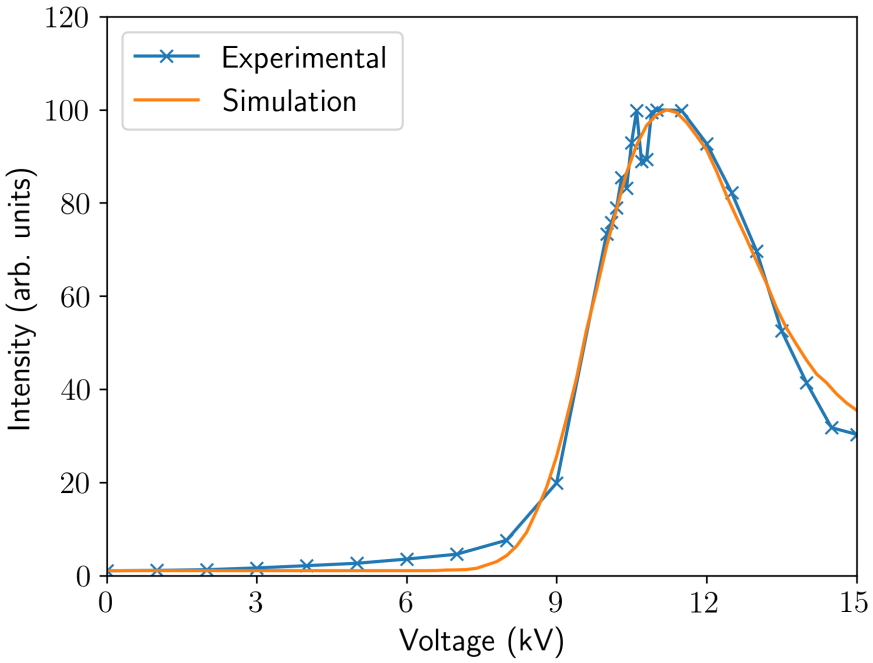

Figure 4.4: In blue: the $(1 + 1')$ REMPI signal obtained from NO(X, $j = 0.5$) after the NO molecular beam passes through the 2 m long primary hexapole held at potentials in the range 0-15 kV. In orange: the percentage transmission of NO(X, $j = 0.5f$) into the detection region from a trajectory simulation assuming a mean molecular beam velocity of 625 ms^{-1} with standard deviation of 35 ms^{-1}. The angular distribution from the normal is assumed to be uniform up to a maximum angle of 1.15°.

4.3.1 Symmetric Top Molecules

This simplest systems for this analysis are symmetric tops whose rotational states may be written as $|J, K, M\rangle$. For clarity, Eq. 3.35 is reprinted, which describes a Legendre polynomial expansion of the distribution of a dipole moment $\boldsymbol{\mu}$ of about the axis of a static electric field, $\boldsymbol{E}$

$$P\left(\cos\theta_{\mu E}\right) = \sum_{k} \frac{2k+1}{2} \mathcal{A}_0^{(k)} P_k(\cos\theta_{\mu E})\,. \tag{4.30}$$

The values of $\mathcal{A}_0^{(k)}$ in electric fields of insufficient strength to cause J-state mixing were determined by Choi and Bernstein[137] and are not repeated here. Bulthuis *et al.*[165] provided theory that included some J-states into this basis set. Their theory is presented in this section in a more explicit form, with details on how to calculate the degree of mixing of other J-states.

In an electric field, and neglecting hyperfine splitting, the wavefunction of the molecule in the electric field, Ψ_E may be described as an expansion of the field free wavefunctions, ψ_{JKM} with the same value of K and M as the initial state [165]

$$\Psi_E = \sum_{J=J_{\min}}^{\infty} c_J(J,K,M)\psi_{JKM}. \tag{4.31}$$

where $J_{\min}$ is the maximum value of $|K|$ and $|M|$.

A single ψ_{JKM} may be recast in terms of a Wigner rotation matrix element[125]:

$$\psi_{JKM} = \left(\frac{2J+1}{8\pi^2}\right)^{\frac{1}{2}} D^{J*}_{MK} = (-1)^{M-K}\left(\frac{2J+1}{8\pi^2}\right)^{\frac{1}{2}} D^{J}_{-M-K}. \tag{4.32}$$

Combining Equations 4.31 and 4.32 allows the evaluation $|\Psi_E|^2$ [137, 165]

$$4\pi^2|\Psi_E|^2 = P\left(\cos\theta_{\mu E}\right) = \frac{(-1)^{M-K}}{2}\sum_{J'J''} c_{J'}c_{J''}\left(2J'+1\right)^{\frac{1}{2}}\left(2J''+1\right)^{\frac{1}{2}} D^{J'}_{MK}D^{J''}_{-M-K}. \tag{4.33}$$

As in Eq. 3.22, the product of Wigner rotation matrix elements in equation 4.33 can be cast in terms of an expansion of the Legendre polynomials

$$D^{J'}_{MK}D^{J''}_{-M-K} = \sum_k (2k+1)\begin{pmatrix} J' & J'' & k \\ M & -M & 0 \end{pmatrix}\begin{pmatrix} J' & J'' & k \\ K & -K & 0 \end{pmatrix} P_k(\cos\theta_{\mu E}). \tag{4.34}$$

Converting into Clebsch-Gordan coefficients, using their properties of permutation and remembering that $(-1)^{M-K} = (-1)^{M+K}$ for $J, K \in \mathbb{Z}$, Eq. 4.35 becomes

$$D^{J'}_{MK}D^{J''}_{-M-K} = (-1)^{M-K}\sum_k \frac{2k+1}{2J''+1}\langle J'M, k0|J''M\rangle\langle J'K, k0|J''K\rangle P_k(\cos\theta_{\mu E})\,. \tag{4.35}$$

This in turn leads to Eq. 4.33 being rewritten as

$$P\left(\cos\theta_{\mu E}\right) = \sum_k \frac{2k+1}{2}\sum_{J'J''} c_{J'}c_{J''}\left(\frac{2J'+1}{2J''+1}\right)^{\frac{1}{2}} \langle J'M, k0|J''M\rangle\langle J'K, k0|J''K\rangle P_k(\cos\theta_{\mu E})\,. \tag{4.36}$$

By comparison with Eq. 4.30, the values of $\mathcal{A}_0^{(k)}$ may be determined as

$$\mathcal{A}_0^{(k)} = \sum_{J'J''} c_{J'} c_{J''} \left(\frac{2J'+1}{2J''+1}\right)^{\frac{1}{2}} \langle J'M, k0|J''M\rangle \langle J'K, k0|J''K\rangle \,. \tag{4.37}$$

The values of the expansion coefficients c_J may be calculated by diagonalising the matrix formed by the Hamiltonian operator, $\hat{H}$, which has elements given by[125, 166]

$$\begin{aligned} \langle J,K,M|\hat{H}|J,K,M\rangle &= E_{JKM} - \frac{MK}{J(J+1)}\mu E \\ \langle J+1,K,M|\hat{H}|J,K,M\rangle &= -\frac{\sqrt{(J+1)^2-K^2}\sqrt{(J+1)^2-M^2}}{(J+1)\sqrt{(2J+1)(2J+3)}}\mu E \,. \end{aligned} \tag{4.38}$$

where

$$E_{JKM} = BJ(J+1) + (A-B)K^2 \tag{4.39}$$

where B is the repeated rotational constant, and A is the non-repeated rotational constant.

4.3.2 Symmetric Top Molecules With Inversion Doubling

With inversion doubling, the $\pm K$ states (where $K > 0$) for a given J and K are superposed in a field-free scenario. This requires an extension of Bulthuis *et al.*'s[165] theory. In this case, the wavefunction in the electric field is given by

$$\Psi_E = \sum_J \left(c_{J,K}\psi_{J,K,M} + c_{J,-K}\psi_{J,-K,M}\right) \tag{4.40}$$

where $c_{J,K}$ are expansion coefficients for a given ψ_{JKM}. The distribution of $\boldsymbol{\mu}$ about $\boldsymbol{E}$, $P(\cos\theta_{\mu E}) = 4\pi^2|\Psi_E|^2$, is then

$$\begin{aligned} P(\cos\theta_{\mu E}) =& 4\pi^2 \sum_{J'J''} \Big[c_{J',K} c_{J'',K} \psi^*_{J',K,M}\psi_{J'',K,M} + c_{J',-K} c_{J'',K} \psi^*_{J',-K,M}\psi_{J'',K,M} \\ &+ c_{J',K} c_{J'',-K} \psi^*_{J',K,M}\psi_{J'',-K,M} + c_{J',-K} c_{J'',-K} \psi^*_{J',-K,M}\psi_{J'',-K,M} \Big] \,. \end{aligned} \tag{4.41}$$

The product of wavefunctions in the second term in this expansion is given by, excluding the $(-1)^{M-K}\sqrt{(2J'+1)(2J''+1)}/8\pi^2$ prefactor

$$D^{J'}_{M-K}D^{J''}_{-M-K} = \sum_k \langle J'M, J''-M|k0\rangle\langle J'-K, J''-K|k0\rangle P_k\left(\cos\theta_{\mu E}\right) \quad (4.42)$$

of which, the second Clebsch-Gordan coefficient is identically 0, as $-K-K \neq 0$ for $K > 0$. A similar situaton arises for the third term in the square brackets in Eq. 4.41. Hence, only the first and last terms survive.

Following the same procedure, Eq. 4.41 may be rewritten

$$P(\cos\theta_{\mu E}) = \frac{(-1)^{M-K}}{2}\sum_k\sum_{J'J''}\left[(2J'+1)(2J''+1)\right]^{\frac{1}{2}}\langle J'M, J''-M|k0\rangle \\ \Big[c_{J',K}c_{J'',K}\langle J'K, J''-K|k0\rangle + c_{J',-K}c_{J'',-K}\langle J'-K, J''K|k0\rangle\Big]P_k(\cos\theta_{\mu E}) \quad (4.43)$$

which upon manipulation of the Clebsch-Gordan coefficients becomes

$$P(\cos\theta_{\mu E}) = \sum_k\frac{2k+1}{2}\sum_{J'J''}\Big[c_{J',K}c_{J'',K} + (-1)^{J'+J''-k}c_{J',-K}c_{J'',-K}\Big] \\ \left(\frac{2J'+1}{2J''+1}\right)^{\frac{1}{2}}\langle J'M, k0|J''M\rangle\langle J'K, k0|J''K\rangle P_k(\cos\theta_{\mu E})\,. \quad (4.44)$$

By comparison with Eq. 4.30, it becomes possible to state

$$\mathcal{A}_0^{(k)} = \sum_{J'J''}\Big[c_{J',K}c_{J'',K} + (-1)^{J'+J''-k}c_{J',-K}c_{J'',-K}\Big] \\ \left(\frac{2J'+1}{2J''+1}\right)^{\frac{1}{2}}\langle J'M, k0|J''M\rangle\langle J'K, k0|J''K\rangle\,. \quad (4.45)$$

To solve for the coefficients $c_{J,K}$, one can first diagonalise the Hamiltonian matrix in the symmetry adapted basis set of $|J, K, M, \epsilon\rangle$ states. The relevant matrix elements are

$$\langle J,K,M,\epsilon|\hat{H}|J,K,M,\epsilon\rangle = E_{J,K,M,\epsilon} \tag{4.46}$$

$$\langle J,K,M,\epsilon|\hat{H}|J,K,M,-\epsilon\rangle = -\frac{MK}{J(J+1)}\mu E$$

$$\langle J+1,K,M,\epsilon|\hat{H}|J,K,M,\epsilon\rangle = -\frac{\sqrt{(J+1)^2-K^2}\sqrt{(J+1)^2-M^2}}{(J+1)\sqrt{(2J+1)(2J+3)}}\mu E$$

$$\langle J+1,K,M,\epsilon|\hat{H}|J,K,M,-\epsilon\rangle = 0\,. \tag{4.47}$$

This allows the evaluation of $c_{J,K,\epsilon}$ coefficients which may be converted into $c_{J,K}$ coefficients by

$$c_{J,K} = \frac{1}{\sqrt{2}}\left(c_{J,K,1} + c_{J,K,-1}\right)$$

$$c_{J,-K} = \frac{1}{\sqrt{2}}\left(c_{J,-K,1} - c_{J,-K,-1}\right)\,. \tag{4.48}$$

4.3.3 Asymmetric Top Molecules

For asymmetric top molecules, the field-free wavefunctions may be written as a linear combination of symmetric top states in K[125], *ie*

$$\psi^{(i)}_{JM} = \sum_K c^{(i)}_{J,K}\psi_{JKM}\,. \tag{4.49}$$

where i is a counting index to denote that different expansions (and hence states) are possible with the same values of J and M.

The coefficients $c^{(i)}_{J,K}$ may be calculated by diagonalization of the field-free Hamiltonian, with matrix elements given by[166]

$$\langle J,K,M|\hat{H}|J,K,M\rangle = \frac{B+C}{2}[J(J+1)-K^2] + AK^2$$

$$\langle J,K+2,M|\hat{H}|J,K,M\rangle = \frac{B-C}{2}\sqrt{J(J+1)-K(K+1)}$$
$$\sqrt{J(J+1)-(K+1)(K+2)}\,. \tag{4.50}$$

where A, B and C are the three rotational constants of the molecule in order of decreasing magnitude.

Upon introduction of an electric field, states of varying values of J, but equal M, may be superposed onto the field-free wavefunction. Hence, this wavefunction becomes

$$\Psi_E^{(i)} = \sum_J \sum_K c_{J,K,E}^{(i)} \psi_{JKM} \,. \tag{4.51}$$

Following the same procedures as above, for an a-type asymmetric top, one may obtain for the distribution of $\boldsymbol{\mu}$ about $\boldsymbol{E}$ for state i

$$P\left(\cos\theta_{\mu E}\right) = \sum_k \frac{2k+1}{2} \sum_{\substack{J'J'' \\ K'K''}} (-1)^{K'-K''} c_{J',K',E}^{(i)*} c_{J'',K'',E}^{(i)} \left(\frac{2J'+1}{2J''+1}\right)^{\frac{1}{2}} \langle J'M, k0|J''M\rangle \langle J'K', k0|J''K''\rangle P_k(\cos\theta_{\mu E}) \,. \tag{4.52}$$

and hence

$$\mathcal{A}_0^{(k)} = \sum_{\substack{J'J'' \\ K'K''}} (-1)^{K'-K''} c_{J',K',E}^{(i)*} c_{J'',K'',E}^{(i)} \left(\frac{2J'+1}{2J''+1}\right)^{\frac{1}{2}} \langle J'M, k0|J''M\rangle \langle J'K', k0|J''K''\rangle \,. \tag{4.53}$$

The values of the $c_{J,K,E}^{(i)}$ coefficients may be found by diagonalising the Hamiltonian matrix in the basis of $|J,K,M\rangle$ states. The Hamiltonian, $\hat{H} = \hat{H}_0 + \hat{H}_{\text{Stark}}$ is made up of a field free component, $\hat{H}_0$, and a perturbation due to the Stark effect, $\hat{H}_{\text{Stark}}$. The matrix elements of $\hat{H}_{\text{Stark}}$ are given in Appendix A.

Note that technically the angle given by the equations above is between the electric field, and the direction of a, the axis with the smallest moment of inertia, I_a. Hence, for b- and c-type symmetric tops, after calculating the eigenstates of the Hamiltonian in the field, the states must then be rotated such that the body-fixed axis lies along the dipole moment before $\mathcal{A}_0^{(k)}$ values may be calculated.

4.3.4 Orientation of Selected Symmetric Top Molecules

The orientations achievable for three candidate symmetric top molecules are shown in Figure 4.5, along with that achievable for NO. The orientations shown are for states

that would be the most likely candidate to be focussed through a hexapole. For NH_3, ND_3, CH_3F and NO, these states are $|J =, \bar{K} = 1, \epsilon = -1\rangle$, $|J =, \bar{K} = 1, \epsilon = -1\rangle$, $|J = 1, MK = -1\rangle$ and $|J = 1/2, \bar{\Omega} = 1/2, \epsilon = -1\rangle$, respectively.

Firstly, it must be noted that for CH_3F, the theory shown in this section suggests that at zero field, there is a significant degree of orientation. This is, of course, false. The theory assumes a symmetry axis has been defined by an electric field. Hence, if there is no field present, this assumption does not hold, and so there is no orientation. A field strong enough to overcome the very tiny hyperfine splitting is all that is required (below $200\,\mathrm{Vcm}^{-1}$ suffices for non-iodides[167]).

For the other three molecules, which are defined as linear combinations of the $\pm K$ or $\pm\Omega$ symmetric top states, there is little orientation at low fields. The orientation is created by producing a superposition of the $\epsilon = \pm 1$ states. At infinite field, assuming the involvement of no other J-states, the wavefunctions of these molecules tend toward a single symmetric top state with $MK = -1$ or $M\Omega = -1$. These states have a set degree of orientation at any field strength. As these are the same symmetric top states as shown for CH_3F, they tend toward the same limiting value of the orientation, $\langle \cos\theta_{\mu E} \rangle = -0.5$ (except for NO as this is a half-integer J-state, and thus tends to $-1/3$). As the electric field strength is increased, the degree of superposition of the two doublets (Λ or inversion) increases, and so the wavefunction becomes more characteristic of the asymptotic symmetric top state, leading to greater orientation.

For NH_3, as the tunnelling of the hydrogens in the umbrella inversion motion is more facile than for ND_3, the splitting between the two inversion doublets is significantly greater than for ND_3. This much larger inversion doubling, and to a much smaller degree the smaller dipole moment of NH_3 compared to ND_3 (1.471 D and 1.497 D[132]), therefore requires a stronger electric field to achieve the same degree of superposition. Hence, orientation is increased at a slower rate as the electric field strength increases. It is this effect that makes ND_3 an easier prospect to work with experimentally: it is more easily oriented, and for exactly the same reasons, it is more easily focussed and state selected through the double hexapole.

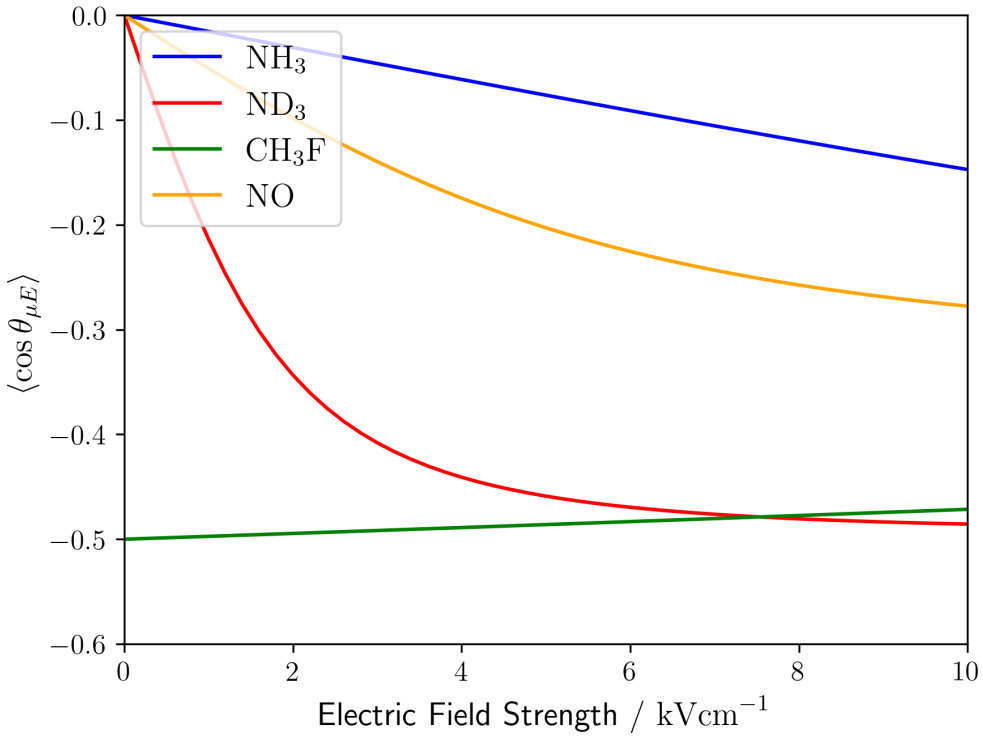

Figure 4.5: Expectation values of the first Legendre polynomial, $P_1(\cos\theta_{\mu E}) = \cos\theta_{\mu E}$, giving the degree of orientation achieved in dipolar electric fields of strengths in the range 0-10 kV cm^{-1}, for selected molecules. The states shown are those likely to be selected by a hexapole for each molecule. Hence for NH_3, ND_3, CH_3F and NO, the chosen states are $|J =, \bar{K} = 1, \epsilon = -1\rangle$, $|J =, \bar{K} = 1, \epsilon = -1\rangle$, $|J = 1, MK = -1\rangle$ and $|J = 1/2, \bar{\Omega} = 1/2, \epsilon = -1\rangle$, respectively.

In the case of CH_3F, it can be seen that the degree of orientation decreases as a function of electric field strength over the given range. This is due to increasing superposition of the $|J = 2, MK = -1\rangle$ state, which has a reduced tendency to be oriented in the field in comparison to the $|J = 1, MK = -1\rangle$ state. As the dipole moment is oriented antiparallel to the electric field, this reduction in orientation reduces the Stark energy of the system compared to if that state were not in a superposition. However, it is important to consider that even at 10 kV cm^{-1}, the coefficients, c_J, for these states are $c_1 = 0.999$ and $c_2 = 0.036$. Hence, there is still no significant mixing of J-states at these field strengths.

It should be noted that both ND_3 and particularly CH_3F require significantly lower electric fields to be significantly oriented compared to NO(X). This raises the prospect of being able to perform a scattering experiment in which NO scatters

with one of these symmetric top partners with an electric field strong enough to orient the symmetric top, but insufficient to non-negligibly orient NO. An electric field in the region of $1 - 2\,\mathrm{kV\,cm^{-1}}$ may be suitable for this purpose.

4.3.5 Orientation of an Asymmetric Top Molecule

The theory provided in Section 4.3.3 is now applied to an asymmetric top molecule. The molecule here is Formaldehyde, CH_2O, chosen due to its potentially interesting stereodynamic properties (see Section 4.6). Its rotational constants are given by: $A = 9.4053\,\mathrm{cm^{-1}}$, $B = 1.2953\,\mathrm{cm^{-1}}$ and $C = 1.1342\,\mathrm{cm^{-1}}$[168]. Formaldehyde is a near symmetric top, and so one might expect similar properties to a standard symmetric top.

In fact, it actually shares similar properties to a symmetric top with inversion doubling, such as NH_3/ND_3. The asymmetry causes coupling between states of the same J, but with $K \pm 2$. The direct consequence of this is the eigenvectors of the field-free hamiltonian for the $J = 1$ states form linear combinations of $|J, K, M\rangle$ states with $K = \pm 1$. The energies of these states are near-degenerate, separated by $0.161\,\mathrm{cm^{-1}}$. Hence, when an electric field is applied, these two states begin to superpose. Just with symmetric tops, they each become more like a single constituent $|J, K, M\rangle$ state.

The state which is low-field seeking, and therefore would be the most likely to be focussed by a hexapole, is the 1_{10} state. The notation here is $J_{K_{-1}K_1}$, where $K_{-1} = |K|$ in the limit of a prolate top, and $K_1 = |K|$ in the limit of an oblate top[125]. This state is very similar to the 1_1^- state in NH_3 and ND_3, and so is oriented in much the same way. This is shown in Figure 4.6, where the degree of orientation of CH_2O follows a similar path to ND_3 in Figure 4.5, but requiring slightly stronger electric fields to reach the same degree of orientation. The superposition of $J = 2$ states does cause a reduction in the degree of orientation, as can be seen by the difference between the converged basis set in blue, and the basis set only containing $J = 1$ states in red.

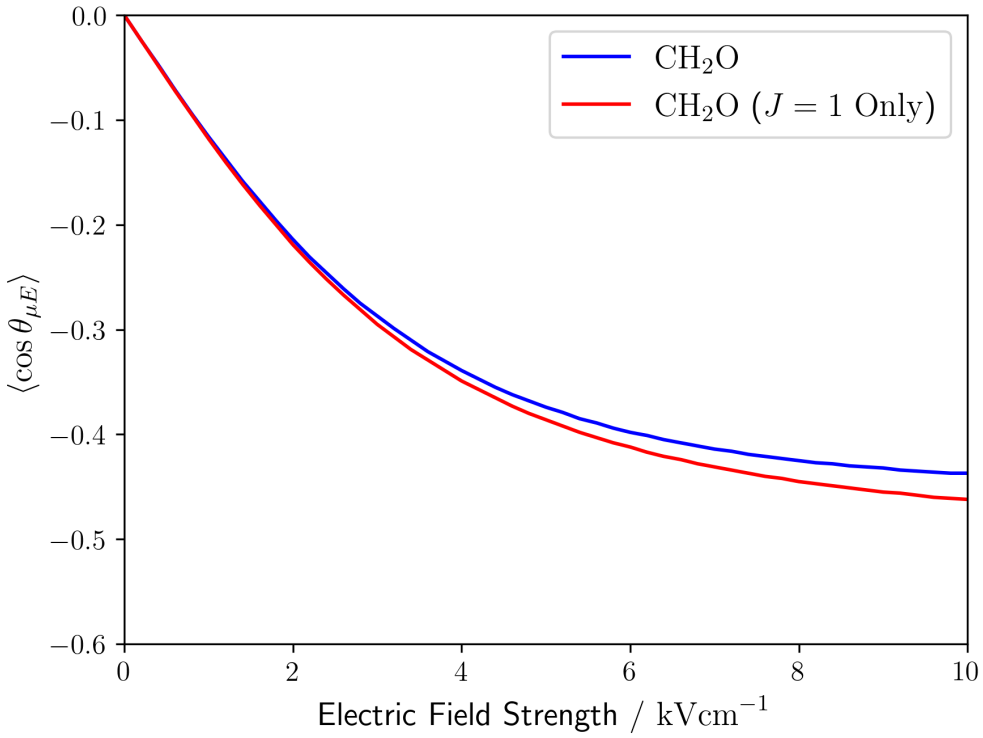

Figure 4.6: The calculated degree of orientation achieved in the 1_{10} state of a formaldehyde molecule in electric field strengths in the range $0 - 10\,\mathrm{kV\,cm^{-1}}$. In red is shown the result if a basis of only $J = 1$ states is used.

If a small, but less symmetric asymmetric top molecule were attempted to be oriented, it would likely be more challenging for two reasons. Firstly, the energy separation between the two states with $K = \pm 1$ is likely to be larger. This would, of course, reduce the ability of these two states to be superposed in the field, reducing the level or orientation at a given field strength. Secondly, a less symmetric asymmetric top could have its dipole moment not pointing along the principal axis of rotation a, about which the rotational constant A is calculated. If this is the case, the likelihood of superposition of states decreases dramatically due to the reduced value of the diagonal hamiltonian matrix elements of the $|J, K, M\rangle$ states (see Appendix A). The required rotation of the states such that the body fixed axis and the dipole moment align before calculating the degree of orientation is unlikely to increase the value significantly, if at all.

4.4 Double Hexapole Design

In choosing the hexapole design for state-selecting symmetric top molecules, it is important to ensure it is suitable for the requirements. The 2m long primary hexapole, designed for state-selecting NO molecules, would be too long to fit in the space available in the laboratory for a copy to be made for symmetric top state selection. Hence, a more compact design was required.

Symmetric top molecules tend to have electric dipole moments that are an order of magnitude larger than for NO. This can facilitate focussing though a shorter hexapole system due to the increased Stark effect at a given electric field strength. Reducing the inner radius of the hexapole, R_0, can also shorten the length required to focus by increasing the magnitude of the electric field. The degree to which this is possible depends on two factors. Firstly, reducing R_0 also necessitates the hexapole rods moving closer together, assuming a fixed ratio between R_0 and the radius of the rods, r. This increases the risk of arcing. Secondly, it is necessary that the radius is wide enough to be able to accept as many molecules as possible exiting the skimmer. If R_0 is too small, molecules may not enter the hexapole field region if their trajectories cause them to collide with the rods of the hexapole or miss the region entirely. Hence, evaluating what a floor for the value of R_0 requires knowledge of the packet of molecules released from the skimmer. A third factor that can allow a smaller length is increased potential applied to the hexapole rods, V_0. However, limitations are placed here due to safety concerns and the risk of arcing and so the maximum potential that can be applied is 10 kV.

Another consideration is the voltage separation between states. When travelling through a hexapole field, different states will be focussed with different strengths. Hence, a certain field strength that focuses a desired state should have a different focal point for undesired states, causing their population to be much lower along the centre-line of the hexapole. However, there are factors that complicate this. Firstly, because symmetric top molecules have relatively high dipole moments, the absolute difference in focussing voltages will be smaller. This reduces the margin for error in voltage selection, and hence requires an accurate simulation. Secondly,

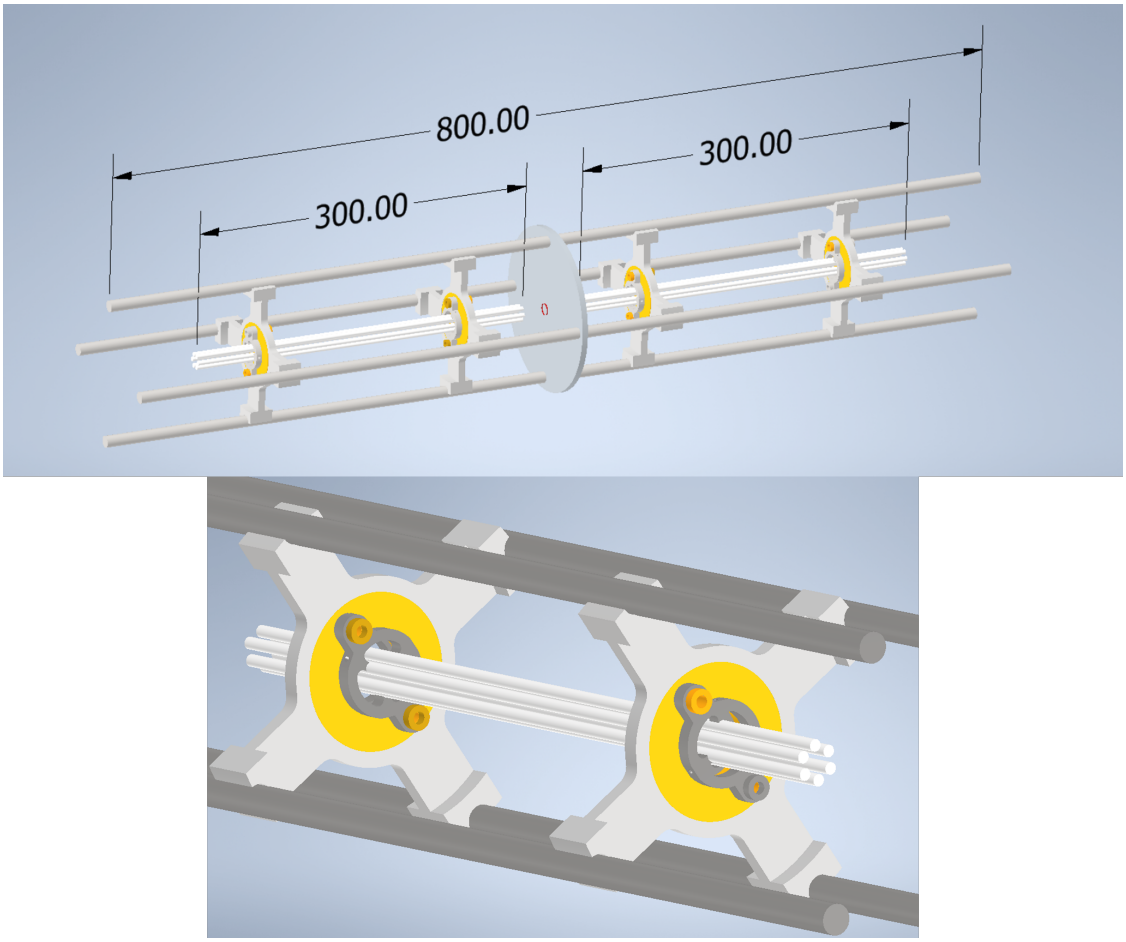

Figure 4.7: Upper Frame: an image of the CAD model of the double hexapole produced using Autodesk Inventor [169]. Each hexapole rod is 300 mm long, and sits with mounts towards either end of the rod. These mounts sit on rails of 800 mm in length, upon which they can be slid along to provide adjustment. The pinhole is held in a circular piece between the two hexapoles, with a removable faceplate which may be swapped in and out to give different sizes of pinhole. Lower Frame: a close up of the assembly for one of the hexapoles.

comparing symmetric top molecules to NO, there are a greater number of states that are likely to be populated thermally from the molecular beam due to different K states having similar energies; in NO, the spin-orbit exciting states are prohibitively high in energy to be populated. For a symmetric top molecule, a state such as $|2, 2, 2\rangle$ will have similar focussing abilities to $|1, 1, 1\rangle$.

This has two implications. Firstly, it is essential that the molecular beam is as rotationally cold as possible. This reinforces the need for correct positioning of the skimmer relative to the valve nozzle to capture the zone of silence. Secondly, it would

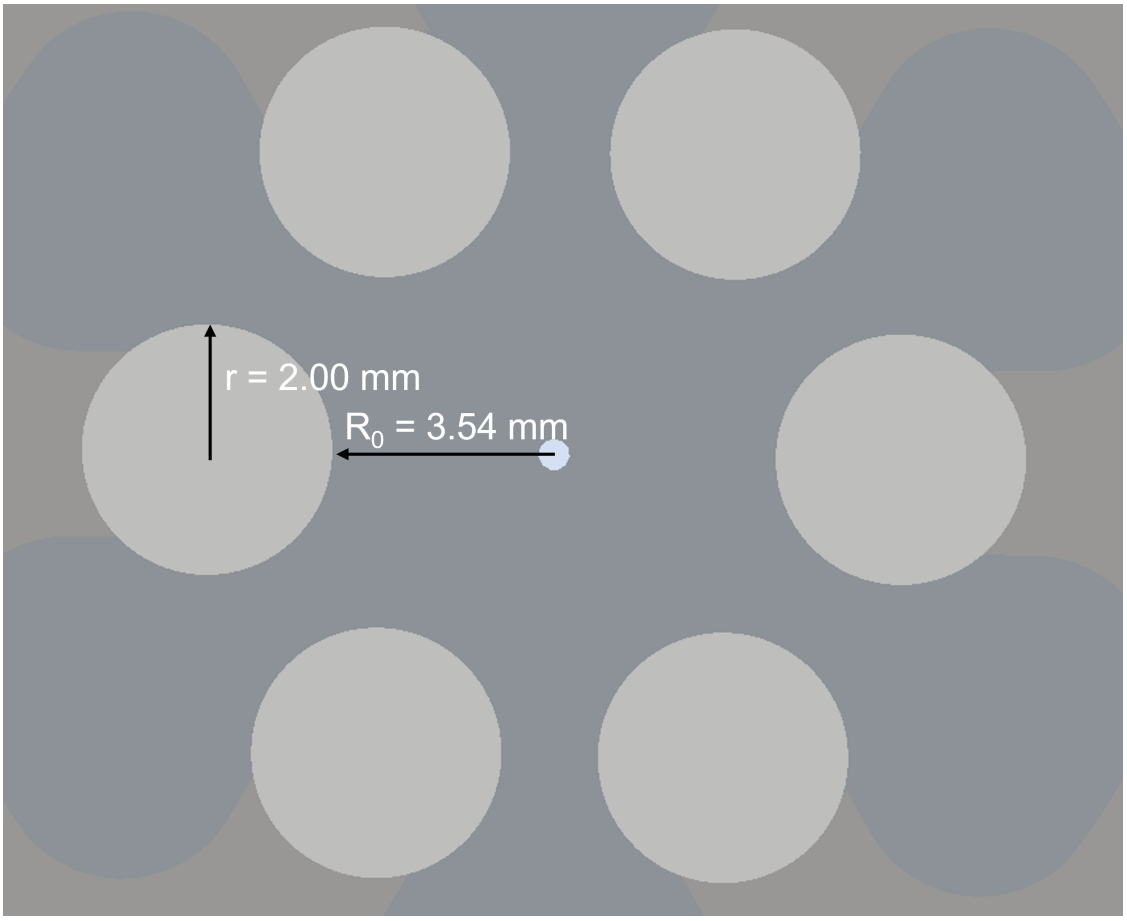

Figure 4.8: The measurements used in the double hexapole design for r, the radius of the hexapole rods, and R_0, the inner radius of the hexapole cavity.

be advantageous for molecules to undergo a full oscillation through the hexapole region, rather than a half oscillation. This is because the absolute difference in the focal points for each state will increase over a full oscillation. However, the concern might be that a molecule selected to be focussed with a full oscillation may have a similar focal point to one over a half oscillation. The solution to this dilemma is to split the hexapole into two, separated by a pinhole. Hence, those states which have undergone only a quarter oscillation at the pinhole will still be at the apex point of their trajectory, and hence will not be able to pass through. Those states which have undergone a half oscillation will, however pass through the pinhole. A CAD model of the double hexapole based on these design considerations is shown in Figure 4.7.

The ratio of r to R_0 is also consequential. An ideal hexapole, which the equations in Section 4.2 require, technically is only produced with hyperbolic shaped hexapole

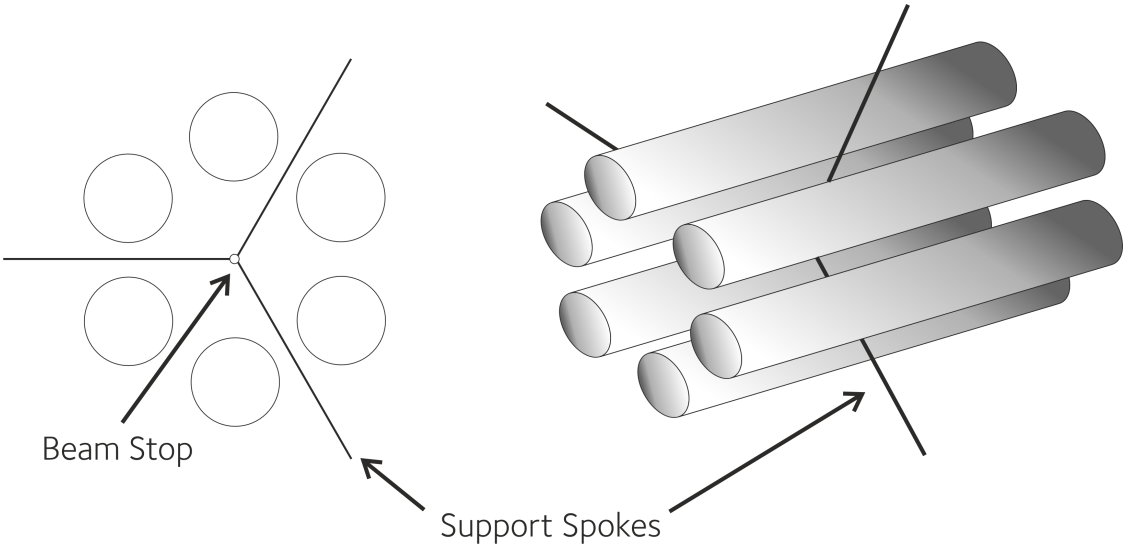

Figure 4.9: A schematic of the proposed beam stop. The left hand side displays how it might look in a cross section, while right hand side shows the support spokes entering the first hexapole halfway-down.

rods. However, mechanically these are hard to produce. It has been established that if cylindrical rods are used, the electric field of the hexapole best approximates an ideal hexapole when $r = 0.565R_0$[170, 171]. Hence, this ratio must be used in this design (see Figure 4.8).

The final consideration concerns the carrier gas. The target molecule is often seeded with a carrier gas to encourage the production of a colder beam, to prevent clustering, and to reduce any corrosive effects of the target. This carrier gas is usually a rare gas, such as Helium, Neon or Argon. These rare gases will not, at electric filed strengths considered, be deflected by the electric field. Hence, only those atoms which travel directly along the centre-line of the hexapole, through the pinhole, will arrive at the interaction region. However, if the system to be studied is NO(X) + Symmetric Top, and detection is through $(1 + 1')$ REMPI of NO(X), it cannot be determined whether the NO(X) collided with a symmetric top molecule or with a rare gas atom. Given that the proportion of carrier gas in a beam is typically around 85-99%, even if only a very small proportion of this gas reaches the interaction region, it could compete with the symmetric top molecules.

This could be remedied using a beam stop, such as that used in a similar setup by van de Meerakker and coworkers[42]. This involves placing a small, round thin

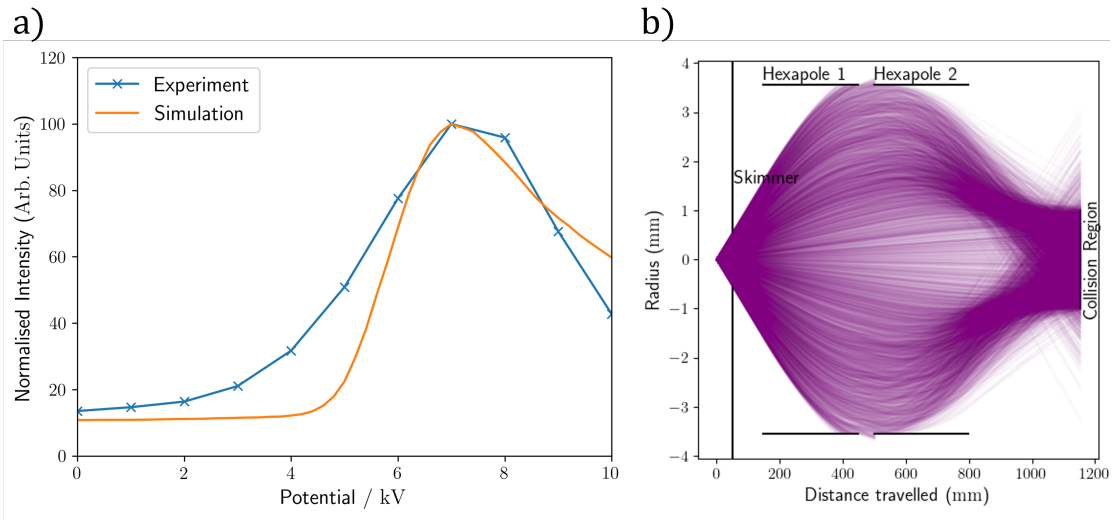

Figure 4.10: a)Experimental and simulated tuning curves, when a molecular beam of NO(X, $j = 0.5f$) travels through the double hexapole. The intensities are obtained by (1+1′) REMPI and then acceleration onto the MCP detector. A PMT is then used to capture signal levels, with the resulting peak being intergrated over. The simulation is obtained with a mean beam speed of 560 ms^{-1} with a standard deviation of 35 ms^{-1}, using a broad Gaussian distribution of angles centred at 0°. b) 10000 simulated trajectories at 7 kV.

piece of insulating material centrally, radially and lengthwise, in either the first hexapole or second hexapole region. This could be held in place using thin spokes attached to the chamber such that they are positioned between the rods of the hexapole. At this point in the symmetric top trajectory, it would have completed a quarter oscillation, and thus would be at its apex. Hence, it could pass around the edge of the beam stop, while those rare gas molecules travelling down the line-of-centre of the hexapole would terminate their trajectories. A schematic of a beam stop is shown in Figure 4.9.

The final design includes a set of rails upon which the mounts containing the hexapole rods may be slid along, allowing adjustment of the distances between the two hexapoles and to and from the pinhole. This provides a small degree of flexibility if desired.

4.4.1 Characterisation of the Double Hexapole

A tuning curve of the double hexapole was collected in much the same way as in Section 4.2.4, for which NO was used. As NO is much less easily focussed compared to, say, ND_3, this required the removal of the pinhole, as NO could not be focussed through it. The voltage of the two hexapoles was chosen to be identical for the purpose of this tuning curve. A simulation was also carried out to estimate the detected transmission of NO through the hexapole. The results of both the experimental and simulated tuning curves are shown in Figure 4.10.

The agreement between the experimental tuning curve and the simulated one is of reasonable quality. It is possible that due to the narrow size of the hexapoles, only a small deviation in measurement quality could have significant effects in the ability to simulate it due to deviation from ideality. Additionally, if the trajectories were to strike the edges of the hexapole rods, these could make their way to the detection region in subsequent cycles, adding to the signal. The region between the two hexapoles may also incur edge effects (due to the hexapole field not immediately going to 0 after the molecules leaves the hexapole region) which are not included in the simulation.

The tuning curve shows how the molecular beam of NO(X) may be manipulated to obtain high quantities of NO(X) in $j = 0.5f$. However, it is more important that no other states are also focussed into the interaction region. This may be tested by taking a REMPI spectrum of the interaction region, following the same process as for the tuning curve, but varying the wavelength of the probe laser rather than the voltage on the hexapoles. If this is done with the hexapoles on and off, it should be possible to obtain an idea of the state-selectivity of the hexapoles. The hexapoles may be defined as 'on' when they are set to the maximum transmisison of $j = 0.5f$, *ie* at $\pm 7\,\mathrm{kV}$. The REMPI spectra obtained under these circumstances are shown in Figure 4.11.

The upper frame of Figure 4.11, showing the REMPI spectrum when the double hexapole has no potential applied, shows the beam to be rotationally cold. A rotational temperature of 4.3 K was obtained from the spectrum by integrating the

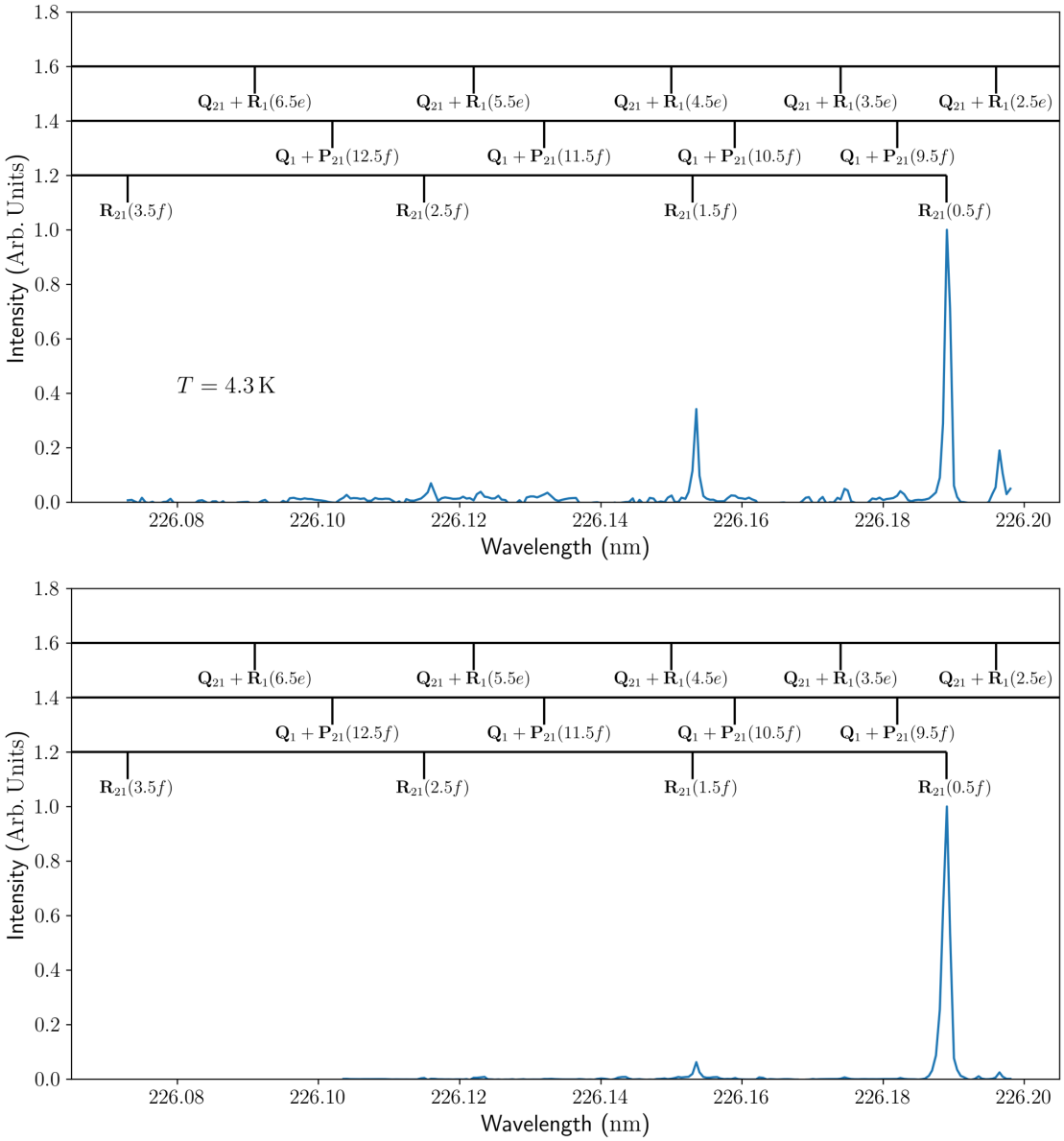

Figure 4.11: Upper Frame: The NO(X) REMPI spectrum obtained when no potential is applied to the hexapole rods. The positions of all relevant lines are shown above the spectrum, including their designations, and, in brackets, the initial state responsible for the line. The temperature displayed was obtained by integrating the peaks for the $\boldsymbol{R}_{21}$ branch lines originating from $j = 0.5f$, $1.5f$, and $2.5f$, and then fitting to a Boltzmann distribution. Lower Frame: The equivalent REMPI spectrum for when the hexapoles are on: all potentials are set to $\pm 7\,\mathrm{kV}$.

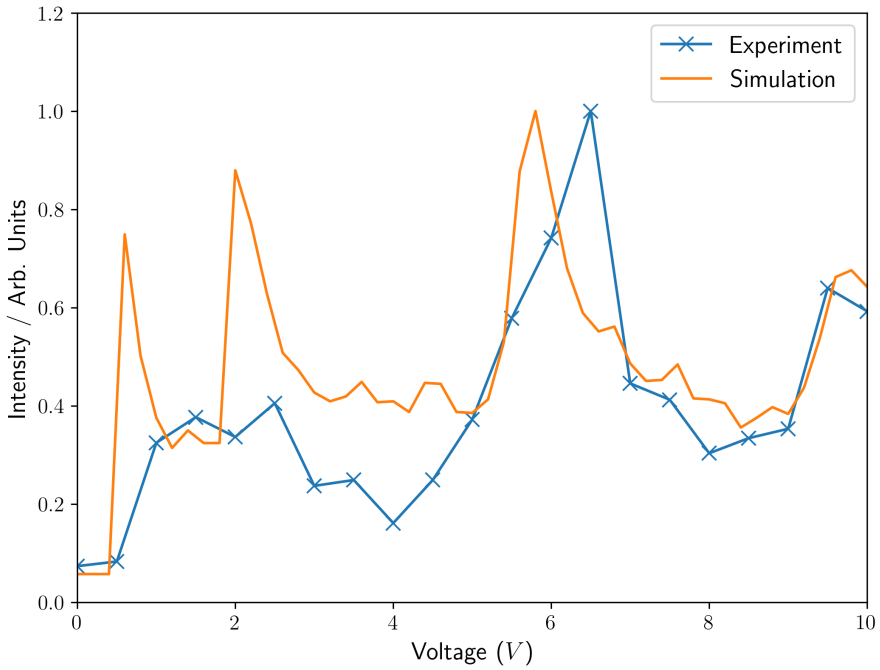

Figure 4.12: In blue is an experimental tuning curve for the 1_1^- state of ND_3, measuring REMPI signal as a function of voltage applied to the hexapoles. This has been taken with the pinhole removed and adjusting the voltages or each hexapole in concert. In orange is a simulated tuning curve for ND_3 in the same scenario.

peaks for the first three transitions in the $\boldsymbol{R}_{21}$ branch and fitting the populations to a Maxwell-Boltzmann distribution. The lower frame shows this spectrum upon increasing the potentials on the hexapole rods to $\pm 7\,\mathrm{kV}$. It becomes noticebale that the $\boldsymbol{R}_{21}$ line for $j = 0.5f$ is by some distance the strongest in this wavelength range, as it is the only line originating from $j = 0.5f$. According to this spectrum, the enhancement of $j = 0.5f$ over $j = 1.5f$ is around 14.5 times. Unsurprisingly, this is below the ≈ 35 times enhancement in the 2 m hexapole which is designed specifically for NO's low dipole moment. However, it is still an excellent enhancement. Hence, the state-selection is working well for NO(X) in this case.

A tuning curve was also taken for ND_3 passing through the hexapole. Again this was taken with the pinhole removed to maximise signal in this process. The signal was captured using the (2+1) REMPI scheme on the $r\boldsymbol{S}1(1)$ transition. The results of this are shown in Figure 4.12 alongside a simulation.

The agreement between the simulation and the experiment is qualitatively reasonable, but quantitatively quite poor at lower voltages. In the simulation, each

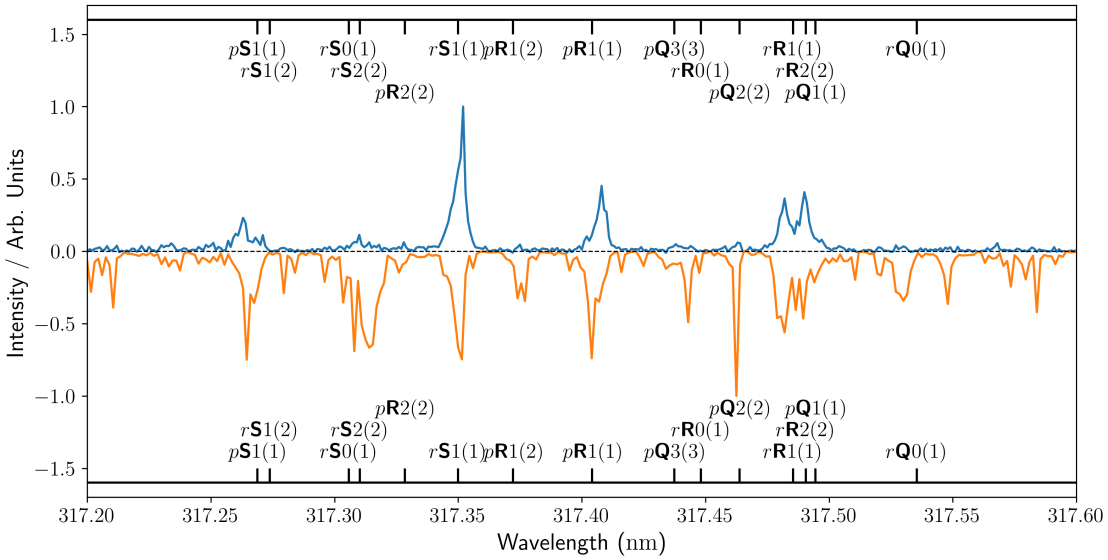

Figure 4.13: REMPI spectrum of the minus inversion doublet states of $ND_3(\tilde{X})$taken with the double hexapoles on at ±9.2 kV on the first hexapole and ±2.1 kV on the second hexapole (positive spectrum) and when they are off (negative spectrum). The positions of the most relevant lines are shown, obtained from PGOPHER[172].

peak corresponds to an extra half sine curve through the hexapoles in an harmonic motion approximation. The first peak at ≈ 600 V corresponds to a single half sine curve, such as that seen in Figure 4.10b. At just above 2000 V is the peak for a full sine curve. The process continues until the final peak shown here at ≈ 9700 V which corresponds to two full sine curves. In the experimental data, the first two peaks appear both smaller than expected but also less defined. The third peak is shifted in potential to around 6500 V, rather than at the expected ≈ 5800 V. The qualitative similarity between the simulation and the experiment suggests that the simulation may be accurate in its determination of trajectories (backed up by its accuracy in simulating the other curves). However, there appears to be an inaccuracy in the initial conditions, perhaps in terms of the initial positions and velocities of the molecules as they enter the hexapoles, or in the size or shape of the detection region in the model.

A REMPI spectrum has been taken of the ND_3 beam with the double hexapoles on, with ±9.2 kV on the first hexapole and ±2.1 kV on the second hexapole, and is shown in Figure 4.13. For the acquisition of this spectrum, the pinhole with

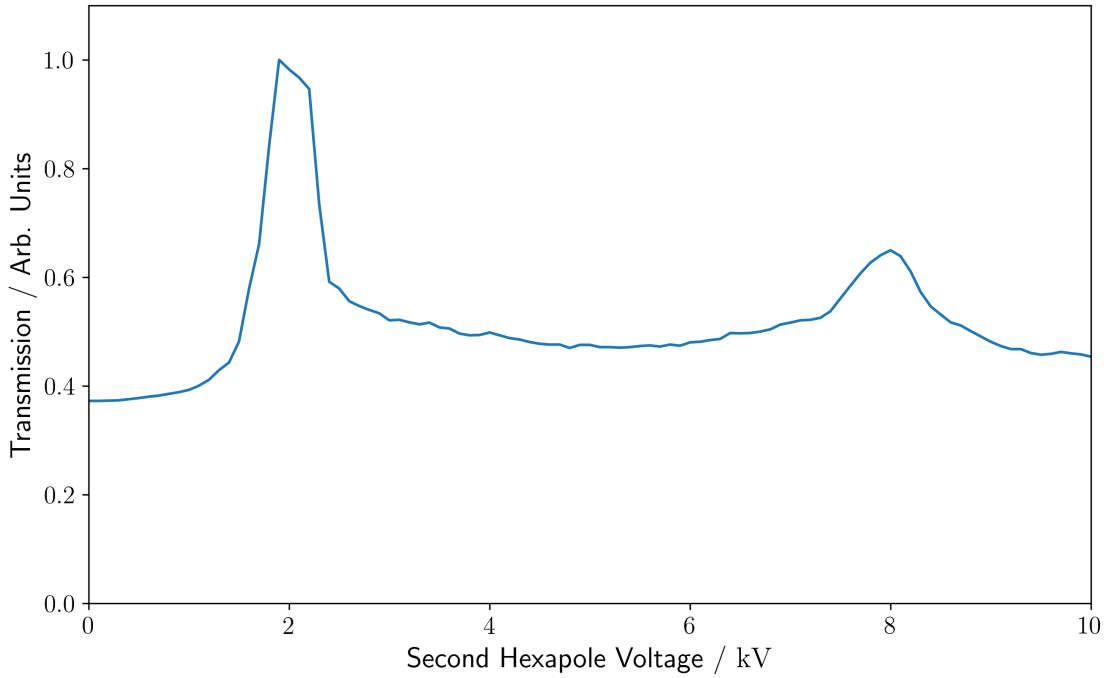

Figure 4.14: A simulated tuning curve for ND_3 with a 1.59 mm pinhole in place with the first hexapole set to ±9.2 kV.

a diameter of 1.59 mm was in place. The voltages were chosen empirically to maximise the signal of the 1_1^- state. A simulated tuning curve in which the first hexapole is set to ±9.2kV is shown in Figure 4.14, which shows the peak in signal at 2.1 kV. The spectrum when the hexapoles are off is inverted for comparison. Each spectrum is normalised separately. The positions of the expected lines, obtained from PGOPHER[172] are shown above and below the spectrum.

The first thing to notice is that there are many peaks in the REMPI spectrum with the hexapoles off, corresponding to many different states. There are significant peaks corresponding to states with $j = 2$, and some with $j = 3$. This suggests a very rotationally warm molecular beam, in the range of 20-40 K. This must be cooled before scattering experiments can take place to increase signal levels in the 1_1^- state. Hence, some adjustment of the valve nozzle is required. Exact calculation of the beam temperature is challenging as some peaks are not the expected height given the height of other peaks from the same state possibly due to the relatively coarse wavelength steps, e.g. $p\boldsymbol{Q}2(2)$ is much greater in intensity than would be expected.

The spectrum with the hexapoles on seems to suggest that the molecular beam is dominated by the 1_1^- state as intended. The peaks corresponding to other states are either very small or completely invisible, suggesting good state selection. There is some issue with the wavelength calibration within the experiment, as peaks are not appearing exactly where they are expected, possibly due to the readout from the laser being out, or due to a technological problem in the software used to record the spectrum. However, it seems clear that the 1_1^- state is dominating as hoped.

4.5 Orientation Considerations

In previous experiments, the ion optics have been left in an always on state during each cycle. One might imagine, therefore, that the velocity-mapping electric field generated could interfere with electric field used to orient the molecules.

In those erstwhile experiments, the orientation rods had potentials of $\pm 8\,\mathrm{kV}$ applied, producing an electric field of around $9.2\,\mathrm{kV\,cm^{-1}}$. If the repeller is set to $1.7\,\mathrm{kV}$ and the extractor to $1.2\,\mathrm{kV}$, which is approximately the standard voltages used on the experiment, the electric field caused by the ion optics only is $20.4\,\mathrm{Vcm^{-1}}$ when the orientation rods are present but grounded. Hence, as the orientation voltage is two orders of magnitude larger, the ion optics voltage has little to no effect on the orientation direction or overall electric field strength.

If the orientation rods are instead to be used to orient symmetric top molecules, rather than NO(X), the electric field required is significantly weaker. Depending on the molecule, this can range from any non-zero field up to field strengths as high as those for NO(X) (see Section 4.3.4). Hence, it seems possible that the ion optics voltages may alter the direction of the field at these voltages.

The electric field produced by the orientation rods when the ion optics were grounded was found using the SIMION package[173] at a variety of different magnitudes of potentials between $0\,\mathrm{kV}$ and $8\,\mathrm{kV}$. This led to a simple linear fitting to extract the result

$$|E| \approx 1.16 V_0 \,/\, \mathrm{kV} \tag{4.54}$$

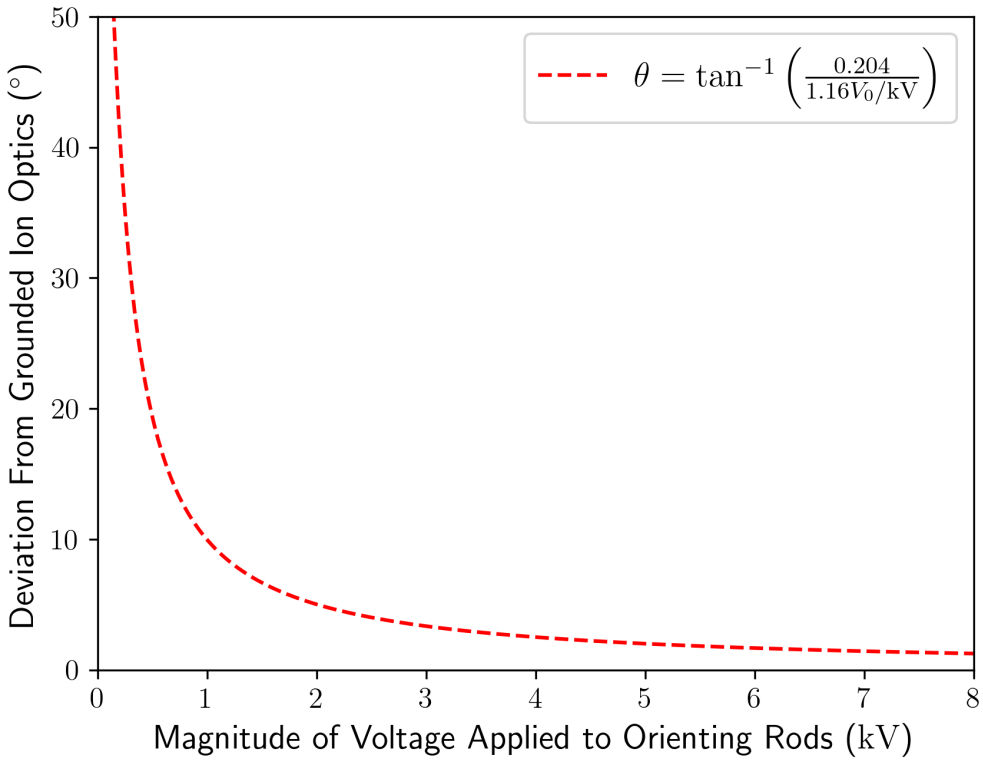

Figure 4.15: A plot showing the relationship between the deviation of the angle from the desired field direction when using voltages on the repeller and extractor of 1.7 kV and 1.2 kV respectively. This configuration would produce an electric field of 20.4 Vcm^{-1} if the orientation rods were grounded. An equation is provided for this line.

where E is the electric field strength, and V_0 is the magnitude of the potential applied.

This result, in turn, allows for the calculation of the angle of deviation from the intended direction of the orienting field for voltages in this range. This leads to the simple equation

$$\theta = \tan^{-1}\left(\frac{0.204}{1.16V_0\,/\,\mathrm{kV}}\right) \tag{4.55}$$

where θ is the deviation angle. This is plotted is Figure 4.15. Deviation becomes greater than 10° at for $V_0 \lesssim 1\,\mathrm{kV}$. However, for most voltages in this range the deviation is very small. Given the resolution of the experiment these deviations are unlikely to make a significant difference to the results.

Whenever there might be an issue, this could be resolved by pulsing the ion optics at the same time that the orientation rods switch to VMI voltages, therefore removing the electric field interfering at the time the molecule is oriented. However,

unless very low voltages are used, this seems unnecessary. It is also possible to simply include the deviation from desired direction in the analysis, but given the orientations are usually chosen to be exactly parallel or perpendicular to the relative velocity vector for ease of analysis, a constant small orientation out of the molecular beam plane would complicate matters for only a very small effect. In fact, as is shown in Chapter 6 and Appendix B, orientation out of the plane has no effect on the scattering if only one molecule is oriented. If the molecule begins in $j \geq 1$, there could also be an alignment effect induced by the field, which would impact the scattering. However, assuming a strong enough electric field is used, the effect of orientation in the xz plane will be significantly greater in the majority of scenarios. If both molecules are being oriented, this could have a greater effect, due to alignment terms from both molecules affecting the scattering, plus a term accounting for both molecules being oriented simultaneously. With careful planning with regards to field strengths or pulsing of the ion optics it should be possible to manage these concerns.

4.6 Conclusions and Future Work

Significant strides have been taken towards an experiment in which both collision partners have their bond axes oriented simultaneously prior to collision. Theory has been revised and extended for hexapole trajectory propagation and bond axis orientation of symmetric top molecules. A double hexapole system has been designed, built and implemented which will allow state selection of symmetric top molecules. The system has been tested with NO, which showed it fully capable of state selection. Concerns about whether the lower voltages required to orient certain symmetric top molecules may produce a need to pulse the ion optics voltages to prevent distortion of the orienting field have been shown to be unfounded for most potential electric field strengths.

There remains much work to do. The beam stop must be designed and implemented if experiments are to be carried out in which the collision partner, not the symmetric top, is to be detected. More work to try to understand the initial conditions of the beam could be useful to improve the quality of the trajectory

simulations in the hexapole, particularly for CH_3F, which cannot easily be detected in the experiment. The mathematical theory to characterise the stereodynamics in these sorts of experiments must also be determined.

Of course, the next stage is to carry out the planned experiments, perhaps investigating how the scattering process changes as the electric field is increased from one only strong enough to orient a symmetric top molecule, up to one capable of orienting both a symmetric top, and the NO collision partner. A potential future experiment could include the replacement of the symmetric top molecule with a near symmetric top, ideally one that may produce a reactive collision with NO, such as CH_2O. One might expect very large differences in reactivity when the NO collides at the C end or the O end. Long term it might seem desirable to state select water molecules using a hexapole, and then orient them. However, due to the large degree of asymmetry, this is likely very challenging.

It is the desire to progress towards more reactive systems that should drive decision making in future. Using a radical beam source, which could then be focussed by the hexapole system designed in this chapter, could provide insight into the stereodynamics of a system with a stable intermediate. This radical could, for example be a isotopologue of NO, or the OH radical.

The holy grail of these sorts of experiment would be to orient the bond axes of each molecule independently before the collision. However, it is not clear whether this is achievable at this stage. It would require pre-orientation of the beams before they meet, before then retaining that orientation as the molecules proceed to the collision region. It is the retaining of the orientation of the molecule which remains very challenging. It might also be conceivable to use magnetic field methods in conjunction with electric field methods to achieve this goal.

5

Data Analysis Methods for 3D Velocity Map Imaging

Contents

5.1 Introduction

Performing scattering experiments with 3D velocity map imaging, and with collision partners with potential for internal energy, poses new challenges with regards to data analysis. In this situation, the data taken will consist of a panoply of concentric spherical shells of ions, with each shell corresponding to an individual internal energy state of the collision partner. With full 3D resolution, it may be possible to to

resolve how the DCS and polarisation effects vary with different final rotational state in the collision partner, for a given final rotational state in the detected molecule.

In this chapter, two data analysis techniques to interpret 3D velocity map images will be presented. The first of these is novel, while the second has been presented before[174], but at that time did not work as intended - here it will be shown to be working.

5.2 Detection Implications of Collision Induced Alignment

As stated previously, after a scattering process, a product may have its angular momentum polarised such that it is distributed in such a way that may be described as oriented or aligned, or a combination of both. The degree to which this takes place is characterised as a function of the scattering angle by the $\boldsymbol{j'}$-PDDCSs, $\rho_q^{(k)}(\theta)$. This polarisation of the angular momentum affects the REMPI efficiency. This can be understood by examining the probability of a photon being absorbed by a molecule, which is classically given by[175]

$$P = |\hat{\boldsymbol{\epsilon}} \cdot \hat{\boldsymbol{\mu}}|^2 \propto \cos^2 \theta_{\mu\epsilon} \tag{5.1}$$

where $\boldsymbol{\epsilon}$ is the electric vector of the light, $\boldsymbol{\mu}$ is the transition dipole moment, and $\theta_{\mu\epsilon}$ is the angle between the two. The REMPI scheme used for NO(X) in this thesis utilises a perpendicular transition ($\Sigma - \Pi$), which requires $\boldsymbol{\mu}$ to be orthogonal to the bond axis vector. Classically, the rotational angular momentum, $\boldsymbol{j}$, must also be orthogonal to the bond axis vector. $\boldsymbol{\mu}$ lies perpendicular to $\boldsymbol{j}$ for P and R branch transitions, but parallel for Q branch transitions[24]. Hence, we can state that the distribution of $\boldsymbol{j}$ (or in this case $\boldsymbol{j'}$), influences the direction of $\boldsymbol{\mu}$, and thus influences the probability of detection.

It can be shown, by combining the angular momentum polarisation description given by the $\boldsymbol{j'}$-PDDCSs with the quantum mechanical description of $|\hat{\boldsymbol{\epsilon}} \cdot \hat{\boldsymbol{\mu}}|^2$, that

the polarisation dependent transition probability may be written[176]

$$P\left(\theta,\Gamma_{\mathrm{V/H}}\right)=CS\left[1+\sum_{kq}\rho_{q\pm}^{\{k\}}(\theta)F_{q\pm}^{\{k\}}\left(\Gamma_{\mathrm{V/H}}\right)\right] \tag{5.2}$$

where C is a constant, S is a line strength factor, $\Gamma_{\mathrm{V/H}}=(\phi,\Theta,\chi)$ are the Euler angles connecting the detector frame and the scattering frame, $F_{q\pm}^{\{k\}}\left(\Gamma_{\mathrm{V/H}}\right)$ are the contributions of each $\rho_{q\pm}^{\{k\}}$, which are given by, for $k=2$ and assuming the use of linearly polarised laser light[176]

$$\begin{aligned}
F_0^{\{2\}}\left(\Gamma_{\mathrm{V/H}}\right)&=\frac{1}{4}h^{(2)}(j_i,j_f)c_2(j_i)\left[3\sin^2\Theta\cos 2\chi-(3\cos^2\Theta-1)\right]\\
F_{1+}^{\{2\}}\left(\Gamma_{\mathrm{V/H}}\right)&=\frac{\sqrt{3}}{4}h^{(2)}(j_i,j_f)c_2(j_i)(2\sin\Theta\cos\phi\sin 2\chi\\
&\quad+2\sin\Theta\cos\Theta\sin\phi\cos 2\chi-\sin 2\Theta\cos\phi)\\
F_{2+}^{\{2\}}\left(\Gamma_{\mathrm{V/H}}\right)&=\frac{\sqrt{3}}{4}h^{(2)}(j_i,j_f)c_2(j_i)[(1+\cos^2\Theta)\cos 2\phi\cos 2\chi\\
&\quad-2\cos\Theta\sin 2\phi\sin 2\chi-\sin^2\Theta\cos 2\phi]
\end{aligned} \tag{5.3}$$

where j_i and j_f are the initial and final rotational states of the molecule for the excitation step of the REMPI process, $c_2(j_i)=[(2j_i+3)(2j_i-1)/j_i(j_i+1)]^{1/2}$ and $h^{(k)}(j_i,j_f)$ is a line strength factor given by[177]

$$h^{(k)}(j_i,j_f)=(-1)^{j_i-j_f}\begin{Bmatrix}j_i & j_i & k\\ 1 & 1 & j_f\end{Bmatrix}\Big/\begin{Bmatrix}j_i & j_i & k\\ 1 & 1 & j_i\end{Bmatrix} \tag{5.4}$$

where $\{:::\}$ are Wigner $6j$ symbols.

After the collision, there will be a time delay before detection. The rotational polarisation therefore may reduce due to interaction with the nuclear spin. In NO(X), the nuclear spin is $I=1$ from the ^{14}N. The depolarisation factor of rank k can be evaluated by [178, 179]

$$G^{(k)}(j_f)=\frac{1}{2I+1}\sum_F(2F+1)^2\begin{Bmatrix}F & F & k\\ j_f & j_f & I\end{Bmatrix}^2 \tag{5.5}$$

where F is a total angular momentum quantum number given by $F=|j_f-I|,|j_f-I|+1,...,j_f+I$. The depolarisation factor can then be convoluted with the line strength factor $h^{(k)}(j_i,j_f)$.

Therefore, the experimentally detected intensity at a specific angle is equal to the angular distribution of the scattering (proportional to the DCS) multiplied by the polarisation-dependent transition probability and so is given by

$$I\left(\theta, \Gamma_{\mathrm{V/H}}\right) = \tilde{C} S \frac{d\sigma}{d\omega}(\theta) \left[1 + \sum_{kq} \rho_{q\pm}^{\{k\}}(\theta) F_{q\pm}^{\{k\}}\left(\Gamma_{\mathrm{V/H}}\right)\right] \tag{5.6}$$

where $\tilde{C}$ is a constant taking into account the proportionality between the DCS and the scattering angular distribution.

For horizontally polarised light, the third Euler angle, χ, takes the value π, while for vertically polarised light, its value is $\pi/2$. Hence, if the same transition is utilised (and hence the $h^{(k)}(j_i, j_f)$ factor is the same), the values of the renormalised $\boldsymbol{j}'$-PDDCSs that pertain to alignment may be elucidated by varying the laser polarisation, and by varying the section of the Newton Sphere analysed; this will vary the angle χ, and by changing the angle between the $\boldsymbol{kk}'$ plane and the $\boldsymbol{kk}_{\mathbf{p}}$ plane, the angle ϕ, respectively.

5.3 Basis Function Fitting

The two data analysis methods that follow are both direct analysis methods, *ie* they require no fitting processes. However, previous data analysis on 2D VMI images from this experiment has relied upon fitting basis functions to the experimental ion image that were generated by convoluting Legendre polynomials with the instrument function obtained from the Monte Carlo simulation[36, 180]. However, moving to 3D, and potentially multiple scattering transitions in a single set of ion images due to the internal states of the scattering partner, this becomes more challenging. One would instead have to convolute the instrument function with products of spherical Bessel functions and spherical harmonics. To obtain a large enough basis set to capture likely behaviour would result in an exceptionally large number of images, leading to exceedingly slow analysis times.

Hence, the data analysis methods described in this Chapter require the division of the experimental ion image by the instrument function, so that direct analysis

of the image is possible. The difference in results between the two methods arises when finding the sum of the square of the differences in intensity in the fitting optimisation process between the test image and the experimental image. This will place more emphasis on regions with higher intensity, as these areas have a greater possibility of producing differences with larger magnitudes. Hence, the slow side of the image, with higher intensity, will be treated as more important in the fitting process. If direct extraction of the variables after division by an instrument function is carried out, there is no bias either way. As the slow side of the image has a greater intensity, one might expect it to produce more accurate outputs from a statistical point of view. Hence, if desired, direct extraction might be enhanced by weighting the mean of the fast and slow side outputs towards the slow side, and then fitting that to a set of Legendre polynomials. This would likely return a similar answer to a fitting process.

5.4 Slice Method

This method is an adaptation on that developed by Suits *et al.*[181]. In their method, they take a crushed velocity-mapped scattering image for both horizontal and vertical laser polarisations. They then take a distribution around the ring (after considering the flux-density correction) for each image and label these distributions as horizontal and vertical 'in-plane' (HIP and VIP). As these rings mainly probe the scattering in the molecular beams plane (in which $\boldsymbol{k}_{\mathbf{p}}$ also resides), these can be assigned $F_{q\pm}^{\{k\}}$ values with $\phi = 0$, but with different values of χ. They then take a slice directly through the ion image from front to back. From this, a distribution is obtainable for scattering perpendicular to the molecular beam plane, which they label 'out-of-plane' (HOOP and VOOP). These four distributions, VIP, VOOP, HIP and HOOP, shall now be considered as slices.

In their case, the angle $\Theta = 45°$, and so $F_{1+}^{\{2\}} = 0$ for all four slices, giving no sensitivity to the $\rho_{1+}^{\{2\}}$ moment. This also made the HIP slice completely identical to the HOOP slice. They then solved the simple set of simultaneous equations to find the values of $\rho_0^{\{2\}}$ and $\rho_{2+}^{\{2\}}$, as well as the DCS.

This method has been adapted for use in 3D imaging, where the 'out-of-plane' slices should be better resolved due to the introduction of time-of-flight information. 3D imaging also facilitates the analysis of x-axis oriented scattering, which introduces an azimuthal dependence to the scattering which disrupts the simple analysis described above.

5.4.1 Adaptations

Firstly, no assumption is made here that $\Theta = 90°$ (there is no reason that the propagation direction of the laser should be perpendicular to the relative velocity vector). The consequence of this is that there is some sensitivity to $\rho_{1+}^{\{2\}}$, and therefore HOOP and HIP will be different.

One of the effects of the fact that $\Theta \neq 90°$, is that the defintion of the four slices breaks down slightly. Inspecting Eq. 5.3, it becomes apparent that the two halves of the slice (the fast and slow side of the image for the 'in-plane' slice and the top and bottom sides of the image for 'out-of-plane' slice) will have different signs for the value of $F_{1+}^{\{2\}}$. Hence, the slices cannot be used as one, and must be separated into these sections. Thus, the four slices become eight. However, only four slices are required for the analysis, and so the analysis can be carried out on two sets of four, and then the results averaged.

Secondly, the azimuthal dependence to the scattering triggered by orienting the molecule in the $\pm x$ direction must be taken into account. All $\boldsymbol{r}$-PDDCSs with $q \neq 0$ cause a ϕ_E-dependent modification to the DCS. Here, a system with one oriented molecule will be considered, although this slice method should be extendable to systems with both molecules oriented.

This azimuthal dependence may be taken into account. Take, for example, orientation of NO(X) in $j = 1/2$. Generally, the DCS for a system with a bond axis polarised may be given by[22, 23, 26]

$$\left[\frac{d\sigma}{d\omega}\right]_{\theta_E}^{\phi_E} = \frac{\sigma_{\text{iso}}}{2\pi}\sum_k (2k+1)\mathcal{A}_0^{(k)}\sum_{q=0}^{k}\frac{2}{1+\delta_{q0}}R_q^{(k)}C_{kq}(\theta_E,0)\cos(q\phi_E)\,. \qquad (5.7)$$

which for a $j = 1/2$ molecule oriented in the $\pm x$ direction may be written[23, 26]

$$\left[\frac{d\sigma}{d\omega}\right]^{\phi_E}_{\theta_E=\pi/2} = \frac{\sigma_{\text{iso}}}{2\pi}\left[R_0^{(0)}(\theta) - 3\sqrt{2}\mathcal{A}_0^{(1)}R_1^{(1)}(\theta)\cos\left(\phi_E\right)\right] \tag{5.8}$$

where the $R_q^{(k)}$ moments are the bond axis dependent PDDCSs ($\boldsymbol{r}$-PDDCSs).

Therefore, experimentally, the magnitude of the effect of the $R_1^{(1)}$ moment is controlled by the azimuthal angle ϕ_E. ϕ and ϕ_E have a fixed relationship for any given electric field direction. Combining Eqs 5.6 and 5.8, one can obtain

$$\begin{aligned} I\left(\theta,\Gamma_{\text{V/H}}\right) &= \tilde{C}S\frac{d\sigma}{d\omega}(\theta,\phi_E)\left[1+\sum_{kq}\rho_{q\pm}^{\{k\}}(\theta)F_{q\pm}^{\{k\}}\left(\Gamma_{\text{V/H}}\right)\right] \\ &\propto \left[R_0^{(0)}(\theta) - 3\sqrt{2}\mathcal{A}_0^{(1)}R_1^{(1)}(\theta)\cos\left(\phi_E\right)\right] \\ &\quad \left[1+\rho_0^{\{2\}}(\theta)F_0^{\{2\}}+\rho_{1+}^{\{2\}}(\theta)F_{1+}^{\{2\}}+\rho_{2+}^{\{2\}}(\theta)F_{2+}^{\{2\}}\right]. \end{aligned} \tag{5.9}$$

To solve these equations, as has been done with 2D images, one can take the sum and difference of the $\pm z$ or $\pm x$ orientations. The intensity of the sum image, will then be proportional to $R_0^{(0)}$ and the difference image will be proportional to $R_0^{(1)}$ and $R_1^{(1)}$ respectively (convoluted with the detection probability effects).

In the case of $\pm x$, the image intensity will also be proportional to $\cos\phi_E$. This results in a plane (defined as containing $\boldsymbol{k}$ and the time-of-flight axis) with zero intensity. Hence, the VOOP and HOOP slices will have zero intensity, preventing their use in determining the $\boldsymbol{j}'$-PDDCSs. To resolve this, a different slice may be taken, suitably different in angle from the 'in-plane' slices to have significant differences in detection efficiency, but not so close to the 'out-of-plane' slices that the intensity is too close to zero. A suitable slice is one with $\phi_E = \pi/3, 4\pi/3$, or alternatively, $\phi_E = 2\pi/3, 5\pi/3$. Then these slices can be divided through by $\cos\phi_E$ to remove this dependency, and facilitate simple solution.

5.4.2 Limitations

The limitations of this method are threefold. Firstly, it requires near-certainty of the position of the detection volume, determined by the overlap of the laser beams. As the first step of this analysis is to divide through by an instrument function generated by the Monte Carlo simulation of the experiment, this instrument

function must be accurate for the analysis to succeed. However, the instrument function can change significantly with the laser positions. Hence, the larger the difference in position of the actual detection volume and the detection volume used for calculation of the instrument function, the less accurate the values for DCS and $\boldsymbol{j'}$-PDDCSs. In theory, this should be resolvable to some degree by comparing the DCSs obtained from both the fast and slow sides of the VIP and HIP slices, and varying the position of the detection volume in the simulation of the instrument function until these match, similar to as has been shown in ref. [182]. This should help to locate the ionisation position in the directions perpendicular to $\boldsymbol{k}$, but gives no information about the position along $\boldsymbol{k}$.

Secondly, this method only uses a subsection of the 3D image collected, wasting some of the data, which could be used to get more reliable values for the desired quantities. This can be resolved by interpolating the 3D image onto a polar coordinate grid, and performing the calculation on a set of slices that rotates around the sphere. For example, assuming $\boldsymbol{k_p}$ lies in the direction described in Chapter 3, the 'out-of-plane' slice from the top hemisphere (the side closest in space to the detector at the moment of extraction) has $\phi = \pi/2$, while the 'in-plane' slice on the slow side of the image will have $\phi = 0$. You could then rotate the value of ϕ by the grid spacing used from interpolation, and calculate the values. This process could be repeated until returning to the first slice and then the mean values calculated. This is facilitated by using the general equations to solve these simultaneous equations provided in Appendix C. If a difference image is used with a ϕ_E dependence, the values could be weighted in the mean with the product of the values of $\cos\phi_E$ of the two slices used for both vertical and horizontal laser polarisation.

Finally, if the ϕ_E dependence of the oriented DCS has a ϕ dependence that cannot easily be resolved with linear combinations of the two opposing orientations as described above, as may be likely with higher initial j-states, it may be difficult to disentangle the $\boldsymbol{r}$-PDDCSs from the $\boldsymbol{j'}$-PDDCSs. A good example of this issue would be with OH(X), which has a $j = 3/2$ ground state, and therefore have $R_q^{(3)}$ moments in the stereodynamic expansion of the DCS. All of these moments except $R_0^{(3)}$ will

have a ϕ_E dependence, which will not all change sign on flipping the polarisation (and if they did one wouldn't be able to disentangle them from other moments whose contributions change sign similarly, e.g. $R_1^{(3)}$ and $R_1^{(1)}$). This could also be resolved by taking many images at arbitrary orientation angles, and involving them in the linear combination, but that would require the ability to achieve this while keeping other factors stable, such as molecular beam density and laser power, to ensure there is no difference in normalisation between the images taken for these orientations.

5.4.3 Application to Simulated Data

This method was tested with simulated data. This data was generated using the Monte Carlo simulation described in section 3.6.2. These simulations were carried out using scattering angular distributions equivalent to those obtained by orienting NO(X, $j = 1/2f$) in the $\pm x$ directions (see Figure 5.1). Hence, sample functions for $R_0^{(0)}$ and $R_1^{(1)}$, were fed in to create the scattering angular distribution. The simulations also included some sample functions for the $\rho_0^{\{2\}}$, $\rho_{1+}^{\{2\}}$ and $\rho_{2+}^{\{2\}}$ moments, with these having their expected effects on detection efficiency. The sum of the two images generated for the $\pm x$ allows determination of $R_0^{(0)}$, and the difference allows determination of $R_1^{(1)}$. These are known as the sum image and the difference image.

Figure 5.2 shows the extracted values using the slice method for each of the moments to which the sum image is sensitive. As $\Theta = 95° \approx 90°$, the method has essentially no sensitivity to $\rho_{1+}^{\{2\}}$, and so its extracted value is highly inaccurate, and thus not shown. In this analysis, each variable is extracted twice: once using the slow side of the image for VIP and HIP slices with the top side of the image for VOOP and HOOP, and then a second time using the fast side of the image for VIP and HIP with the bottom side of the image for VOOP and HOOP. These are then averaged to produce the values shown.

Figure 5.3 shows the generic $R_1^{(1)}$ extracted from the difference image, using slices with $\phi = 3\pi/4, 7\pi/4$ in all possible combinations with the 'in-plane' slices from the fast and slow side of the image, and then averaged. Values for $\rho_0^{\{2\}}$ and $\rho_{2+}^{\{2\}}$ were calculated, but are less accurate than those from the sum image,

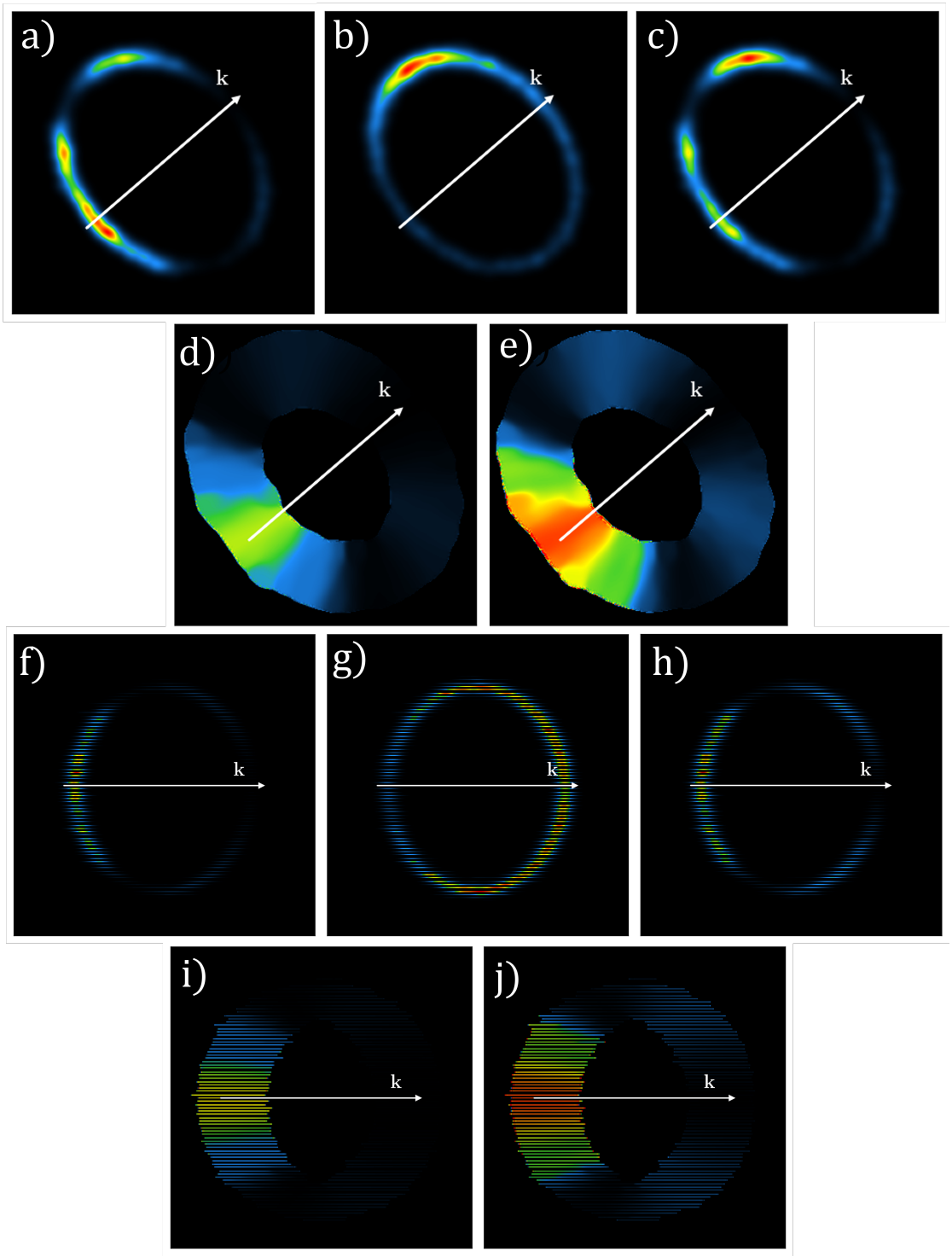

Figure 5.1: A set of simulated sum images for the slices used in the slice method. a) and c) are the vertical and horizontal laser polarisation in-plane slices, respectively. b) is the instrument function for the in-plane slice. d) and e) are a) and c) divided by b) respectively. f) and h) are the vertical and horizontal laser polarisation out-of-plane slices, respectively. g) is the instrument function for the out-of-plane slice. i) and j) are f) and h) divided by g) respectively. Note there is a distortion applied to these images, causing a deviation from circularity as would be likely if the orientation rods were present.

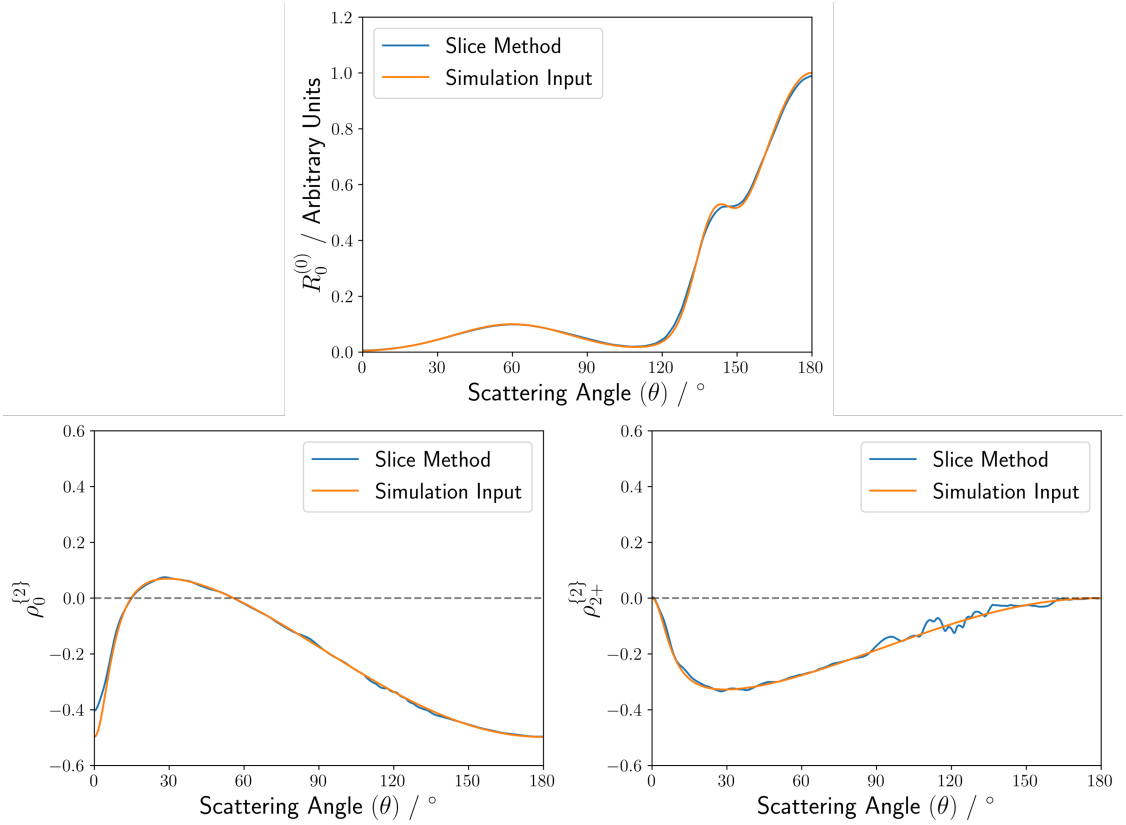

Figure 5.2: Extracted $R_0^{(0)}$ (top), $\rho_0^{\{2\}}$ (bottom left) and $\rho_{2+}^{\{2\}}$ (bottom right) using the slice method on simulated data of the sum 3D image of $\pm x$ orientation of NO(X, $j = 1/2f$). In this case these results were extracted from the mean of the results from using the slow side of the image for the 'in-plane' slices with the top side of the image for the 'out-of-plane' slices and using the fast side of the image for the 'in-plane' slices with the bottom side of the image for the 'out-of-plane' slices. There was insufficient sensitivity to extract $\rho_{1+}^{\{2\}}$ accurately at $\Theta = 95°$, and so the result for this moment is not shown.

due to the smaller range of ϕ values sampled, and due to the generally lower intensity of the difference image.

It is clear that the inputs and outputs of this process match excellently. This is to be expected given the same simulation code was used to produce both the instrument function and the simulated scattering images. Experimental data is highly unlikely to be as accurate, with a lot hinging on the quality of the instrument function. The extracted $R_1^{(1)}$ moment does fail to capture a sharp trough in the forward scattering region. This would not be expected to be resolved experimentally, but the fact it is not resolved here could be seen as concerning. It is perhaps possible that a better method of extracting $R_1^{(1)}$ from the difference image is to only use the 'in-plane'

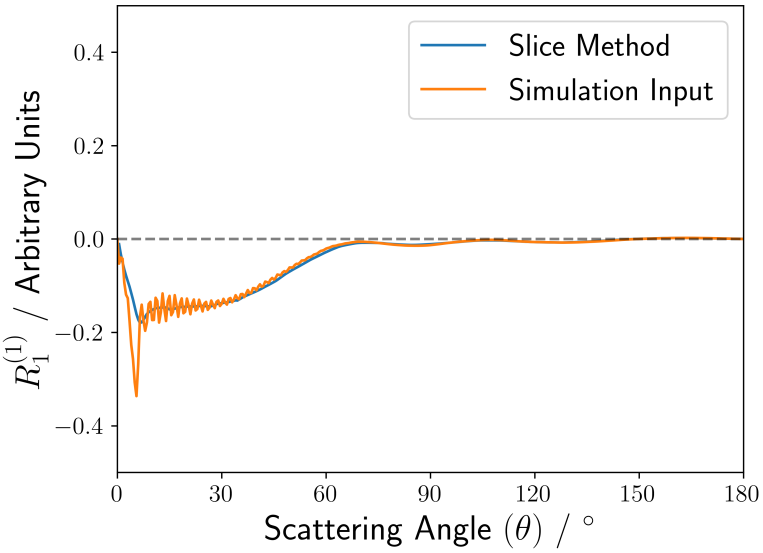

Figure 5.3: Extracted $R_1^{(1)}$ using the slice method on simulated data of the difference 3D image of $\pm x$ orientation of NO(X, $j = 1/2f$). In this case these these results were extracted from the mean of the results from using all possible combinations of the 'in-plane' fast and slow slices, and the $3\pi/4$ and $7\pi/4$ slices. While values were determined for $\rho_0^{\{2\}}$ and $\rho_{2+}^{\{2\}}$, due the not having as wide a range of ϕ values as for the sum image and the much lower intensity of the sum image, they are much less accurate than those obtained from the sum image, and are not displayed.

slices, which have maximum intensity, and use the $\boldsymbol{j}'$-PDDCSs extracted from the sum image. However, these results do provide evidence that this method could work.

5.5 Reflection Method

If the system studied does have $\Theta \approx 90°$, then $F_{1+}^{\{2\}} \approx 0$ and so can be neglected. This opens up a possibility. According to Eq. 5.3, the only ϕ-dependent term in the polarisation dependent detection probability is the one containing $F_{2+}^{\{2\}}$ which, for vertical laser polarisations has a simple $\cos 2\phi$ dependence. Given this, it is possible to conceive of an elegant way to simultaneously analyse the whole 3D image, rather than extract the desired results from a small subset. This method was described in ref. [174].

For horizontal polarisation, the value of $F_{2+}^{\{2\}}$ will be 0 independent of the value of ϕ. Hence, there is no ϕ distribution to the image obtained with horizontal polarisation (other than any ϕ_E dependence of the DCS). For vertical polarisation,

two different 3D images can be constructed from the original. If the Newton Sphere is split along the plane defined by $\phi = 3\pi/4$ and $\phi = 7\pi/4$, and then each hemisphere is reflected in the same plane, it produces two different images. If we label the ϕ angle in one of these slices ϕ' and the other ϕ'', then $(\phi' + \phi'') \bmod 2\pi = 3\pi/2$. Hence

$$\begin{aligned}\cos 2\phi' &= \cos(3\pi - 2\phi'') \\ &= \cos 3\pi \cos(-2\phi'') + \sin 3\pi \sin(-2\phi'') \\ &= -\cos(-2\phi'') \\ &= -\cos 2\phi'' \,. \end{aligned} \tag{5.10}$$

The corollary of this is that it is possible to rewrite the ϕ distribution of $F_{2+}^{\{2\}}$ of one of these images as the negative of the ϕ distribution of the other. Labelling these two distributions $I_{\mathrm{V}'}$ and $I_{\mathrm{V}''}$, and the horizontal polarisation image I_{H}, this can be mathematically formulated as

$$\begin{aligned} I_{\mathrm{H}} &= \tilde{C}S\frac{d\sigma}{d\omega}(\theta)\left(1 + h^{(2)}(j_i, j_f)c_2(j_i)\rho_0^{\{2\}}\right) \\ I_{\mathrm{V}'} &= \tilde{C}S\frac{d\sigma}{d\omega}(\theta)\Bigg(1 - \frac{1}{2}h^{(2)}(j_i, j_f)c_2(j_i)\rho_0^{\{2\}} \\ &\qquad - \frac{\sqrt{3}}{2}h^{(2)}(j_i, j_f)c_2(j_i)\rho_{2+}^{\{2\}}\cos 2\phi'\Bigg) \\ I_{\mathrm{V}''} &= \tilde{C}S\frac{d\sigma}{d\omega}(\theta)\Bigg(1 - \frac{1}{2}h^{(2)}(j_i, j_f)c_2(j_i)\rho_0^{\{2\}} \\ &\qquad + \frac{\sqrt{3}}{2}h^{(2)}(j_i, j_f)c_2(j_i)\rho_{2+}^{\{2\}}\cos 2\phi'\Bigg)\,. \end{aligned} \tag{5.11}$$

This in turn allows the DCS and $\boldsymbol{j}'$-PDDCSs to be found using the equations

$$\begin{aligned} \tilde{C}S\frac{d\sigma}{d\omega}(\theta) &= \frac{1}{3}\left(I_{\mathrm{H}} + I_{\mathrm{V}'} + I_{\mathrm{V}''}\right) \\ \rho_0^{\{2\}} &= \frac{3I_{\mathrm{H}} - \left(I_{\mathrm{H}} + I_{\mathrm{V}'} + I_{\mathrm{V}''}\right)}{h^{(2)}(j_i, j_f)c_2(j_i)\left(I_{\mathrm{H}} + I_{\mathrm{V}'} + I_{\mathrm{V}''}\right)} \\ \rho_{2+}^{\{2\}} &= \frac{\sqrt{3}(I_{\mathrm{V}'} - I_{\mathrm{V}''})}{h^{(2)}(j_i, j_f)c_2(j_i)\cos 2\phi'\left(I_{\mathrm{H}} + I_{\mathrm{V}'} + I_{\mathrm{V}''}\right)}\,. \end{aligned} \tag{5.12}$$

The constant $\tilde{C}$ cannot easily be evaluated, and thus are left undetermined. Hence, there is no need to evaluate S either.

5.5.1 Limitations

The first and third limitation that were discussed in Section 5.4.2 also apply here, and could potentially be resolved in a similar manner.

The third limitation for this method lies in its restriction that $\Theta = 90°$. There is no reason why this must be true, and, in fact, is unlikely to be true in collisions between heaver and lighter molecules, for example NO(X) + H_2. The H_2 is likely to have a much faster velocity in a molecular beam than NO. Hence, if using the restricted geometry that is often present in these sorts of experiments (*ie* molecular beam arms and laser propagation directions cannot be easily moved), the the angle between $\boldsymbol{k}$ and $\boldsymbol{k_p}$ will deviate from $\Theta = 90°$. Another factor that must be considered is that if $\Theta \neq 90°$ but is relatively close to it. In which case, neglecting the effects of $\rho_{1+}^{\{2\}}$ may distort the values of the other extracted values. This limitation does not exist in the slice method.

5.5.2 Application to Simulated Data

Ref. [174] shows some values extracted from simulated scattering data, for a variety of quantities, and shows that these distributions can be expanded using products of spherical Bessel functions and spherical harmonics. However, the values extracted in that thesis were not accurate with respect to the input of the simulation due to an inaccuracy in the definition of ϕ in the analysis. This has been resolved, and a comparison between those simulation inputs and the extracted values is shown here.

It is apparent when comparing the results from Figure 5.4 that the reflection method is less accurate than the slice method for the same simulated data, although the agreement is still, on the whole, good. There is an anomaly in the extracted $\rho_{2+}^{\{2\}}$ from around $\theta = 110°$ to $\theta = 140°$. This anomaly also exists in the slice method when only the slow side is used with the top of the Newton Sphere, but disappears when averaged with the fast and bottom sides. In this case, it may be possible that this anomaly can be resolved if the Newton Sphere reflection occurs along the plane defined by $\phi = \pi/4$ and $\phi = 5\pi/4$, which has the same properties as the other reflection in that $\cos 2\phi' = -\cos 2\phi''$. Once the distributions for the

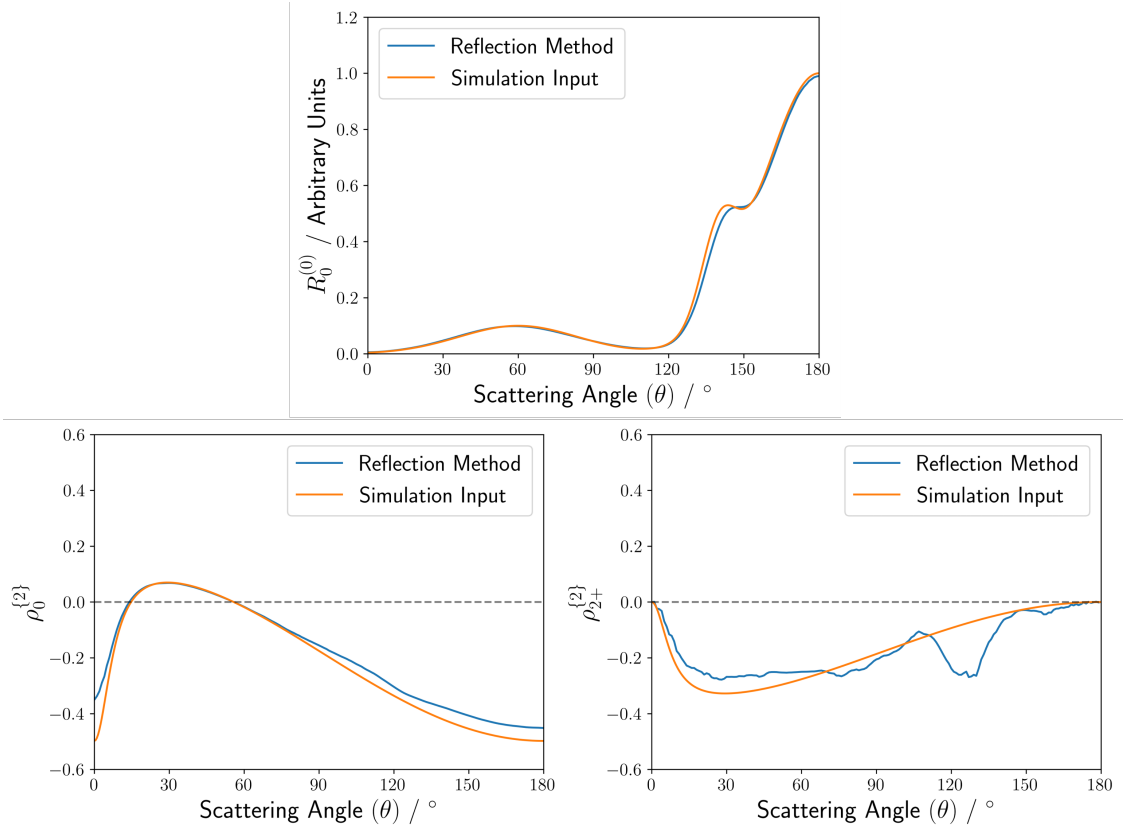

Figure 5.4: Extracted $R_0^{(0)}$ (top), $\rho_0^{\{2\}}$ (bottom left) and $\rho_{2+}^{\{2\}}$ (bottom right) using the reflection method on simulated data of the sum 3D image of $\pm x$ orientation of NO(X, $j = 1/2f$).

variables are then created, they can be averaged with those from the other reflection to obtain a result which may remove the anomaly.

5.6 Conclusions and Future Work

Two data analysis methods for extracting stereodynamical parameters from 3D ion images have been presented. While the reflection method inherently uses all of the data, it assumes that the propagation axis of the excitation laser is at 90° to the initial relative velocity vector, something which cannot be guaranteed. On the other hand, although the slice method can be accomplished without using all of the data, as it can be extended to include all of the data by simply taking many sets of slices through the Newton Sphere and calculating a mean, it would appear to be the superior method.

To be certain of this, the priority would be to apply these methods to a set of experimental data. Comparison to QM scattering calculations could then provide validation. This theory given here also assumes a one photon excitation process involved in REMPI. For NO(X), this is a very good assumption as, experimentally, a $(1 + 1')$ scheme is employed. However, if the molecule to be detected were, for example, ND_3, for which the standard REMPI scheme is $(2 + 1)$, the equations for how detection efficiency changes with product angular momentum distribution will change, as excitation becomes a two photon process. It is of course possible to use a one photon excitation process for REMPI of ND_3, as has recently been shown using a wavelength of $\approx 157\,\mathrm{nm}$[183]. However, this would require the ability to generate VUV photons, something not possible with the current experimental setup.

6

Scattering of a $^2\Pi$ Molecule in an Arbitrary Electric Field

Contents

Declaration of Authorship

This work presented in this chapter is based on the publication

> M. McCrea*, M. Strutton*, J. Featherstone, C. G. Heid, M. Brouard, P. G. Jambrina and F. J. Aoiz, "A general formalism to describe the stereodynamics of bond axis orientation in the scattering of a linear molecule with an atom", J. Chem. Phys. **162**, 154306 (2025). *These authors contributed equally to this work

This publication was co-authored by the author of this thesis and another

Doctor of Philosophy Candidate, Matthew Strutton. The mathematical work in this thesis, and the vast majority of the analysis was performed by this author, while calculations and additional analysis were performed Matthew Strutton. The paper was then compiled by the author of this thesis.

6.1 Introduction

The formalism to describe and characterise the stereodynamics of a $^2\Pi$ molecule in $j = 1/2$ oriented by an electric field in specific directions has been described before [22, 23, 26]. However, no complete description has ever been produced which can describe oriented scattering for a $^2\Pi$ molecule in other rotational states. While the ability to describe the oriented scattering of excited rotational states has its own merits, there are also $^2\Pi$ molecules with a $j = 3/2$ ground state, such as OH(X).

Hence, in this chapter, the general stereodynmical mathematical framework will be laid out. Following this, some examples of its power will be displayed, using, in particular, the example of the OH(X) + Ar system. The principles involved in the derivation of the description in this chapter will then act as the foundation for the more complex derivation of the 4-vector correlation in Chapter 7.

There have been previous studies which have provided formulae for the stereodynamics for these sorts of systems[184–186]. However, these studies only focus on orientation of the bond axis parallel and antiparallel to the bond axis vector, whereas the framework here allows orientation in any chosen direction.

Note that throughout this chapter, the absolute value of a quantity x shall be represented by $\bar{x}$.

6.2 Mathematical Formulation

If all quantum numbers of initial and final states are well defined, the state-to-state differential cross section, written using the shorthand $\mathrm{d}\sigma$, is defined as

$$\mathrm{d}\sigma(jm\,\bar{\Omega}\epsilon \to j'm'\,\bar{\Omega}'\epsilon') = \left| f_{j'm'\bar{\Omega}'\epsilon',\, jm\bar{\Omega}\epsilon}(\theta) \right|^2, \tag{6.1}$$

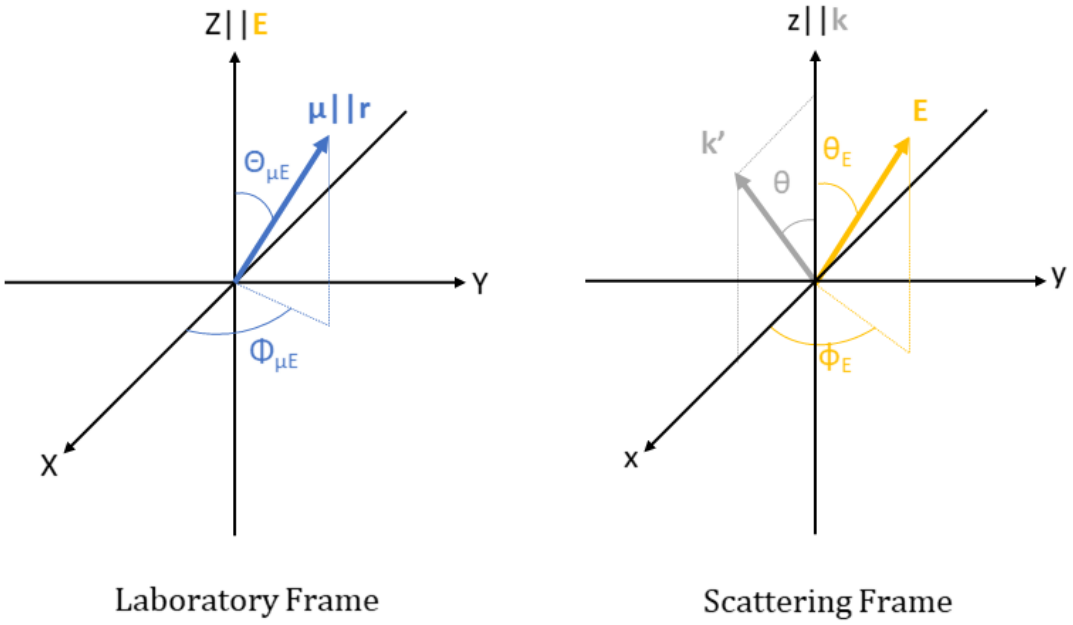

Figure 6.1: Left panel: sketch of the laboratory (LAB) frame in which the orienting electric field, $\boldsymbol{E}$, is along the Z-axis. The direction of the electric dipole moment (and of the molecular axis) is defined by the $\Theta_{\mu E}$ and $\Phi_{\mu E}$ angles. Right panel: scattering frame with the initial relative velocity, $\boldsymbol{k}$, along the z-axis and the xz-hemiplane defined by $\boldsymbol{k}$ and recoil relative velocity, $\boldsymbol{k}'$. In this frame, the orienting field is defined by the angles θ_E and ϕ_E. In the particular case of the $+z$ and $-z$ orientations, the electric field is parallel ($\Theta_{\mu E} = 0°$) and antiparallel ($\Theta_{\mu E} = 180°$) to $\boldsymbol{k}$, respectively. If $\boldsymbol{E}$ is along the $+x$ ($-x$) axis, the direction of $\boldsymbol{E}$ is given by $\theta_E = 90°$ and $\phi_E = 0°$ ($\theta_E = 90°$ and $\phi_E = 180°$).

where $f_{j'm'\bar{\Omega}'\epsilon',jm\bar{\Omega}\epsilon}(\theta)$ is the scattering amplitude, the expression for which may be found in references [46, 184] in the helicity representation. Here, m and m' are the projections of $\boldsymbol{j}$ and $\boldsymbol{j}'$ onto the initial relative velocity vector $\boldsymbol{k}$ and the final relative velocity vector $\boldsymbol{k}'$.

Hereafter, for brevity's sake, the scattering amplitudes for a given j, j', $\bar{\Omega}$, and $\bar{\Omega}'$ shall be written[23]

$$f_{j'm'\bar{\Omega}'\epsilon',\,jm\bar{\Omega}\epsilon}(\theta) \equiv F_{m'\epsilon'\,m\epsilon}\,. \tag{6.2}$$

To appreciate the next step, it is necessary to consider the two relevant reference frames displayed in Figure 6.1. First of all, there is the laboratory (LAB) frame, in which the Z-axis is defined as collinear to the electric field vector, $\boldsymbol{E}$. The distribution of the dipole moment brought about by the electric field is cylindrically symmetric, so the angle $\Phi_{\mu E}$ is superfluous. In this frame, the projection of $\boldsymbol{j}$

is denoted by m_E. The scattering frame is defined with $\boldsymbol{k}$ along the z-axis, and $\boldsymbol{k}'$ in the $+xz$ plane, as in Section 1.3. Hence, the direction of the electric field is given by θ_E, the polar angle and ϕ_E, the azimuthal angle. In this frame, the projection of $\boldsymbol{j}$ is given by m.

Rotating the states $|jm\bar{\Omega}\epsilon\rangle$ from the scattering frame into the LAB frame results in states given by

$$|jm_E\bar{\Omega}\epsilon\rangle = \sum_m D^j_{m\,m_E}(\phi_E, \theta_E, 0)|jm\bar{\Omega}\epsilon\rangle\,, \tag{6.3}$$

where $D^j_{m\,m_E}(\phi_E, \theta_E, 0)$ (henceforth denoted by $D^j_{m\,m_E}$) is a Wigner rotation matrix element. Analogously, the scattering amplitude may also be rotated from the scattering frame into the LAB frame.

$$F_{m'\epsilon'\,m_E\epsilon} = \sum_m D^j_{m\,m_E}\, F_{m'\epsilon'\,m\epsilon}\,. \tag{6.4}$$

In the presence of an electric field, the coherent superposition of the e and f states, formed can be expressed as a function of the states in Eq. (6.3)

$$|jm_E\bar{\Omega}\,\hat{E}\rangle = \frac{1}{\sqrt{2}}\sum_m D^j_{m\,m_E}\Big[\alpha|jm\bar{\Omega}e\rangle + \beta|jm\bar{\Omega}f\rangle\Big]\,. \tag{6.5}$$

Once again, the scattering amplitude from the state $|jm_E\bar{\Omega}\,\boldsymbol{E}\rangle$ to a given final state $|j'm'\bar{\Omega}'\epsilon'\rangle$ may analogously be written

$$F_{m'\epsilon'\,m_E\hat{E}} = \frac{1}{\sqrt{2}}\sum_m D^j_{m\,m_E}\Big[\alpha F_{m'\epsilon'\,me} + \beta F_{m'\epsilon'\,mf}\Big]\,. \tag{6.6}$$

The next step consists of constructing the DCS for the $|jm_E\bar{\Omega}\,\boldsymbol{E}\rangle \to |j'm'\bar{\Omega}'\epsilon'\rangle$ transition:

$$\mathrm{d}\sigma(jm_E\,\bar{\Omega}\hat{E} \to j'm'\,\bar{\Omega}'\epsilon') = \left|F_{m'\epsilon'\,m_E\hat{E}}\right|^2\,. \tag{6.7}$$

Summing over all final m' states to give a DCS for scattering into a single rotational level returns

$$\mathrm{d}\sigma(jm_E\,\bar{\Omega}\hat{E} \to j'\,\bar{\Omega}'\epsilon') = \sum_{m'} \left| F_{m'\epsilon'\,m_E\hat{E}} \right|^2 = \frac{1}{2}\sum_{m'} \left| \sum_{m} D^{j}_{m\,m_E} \left(\alpha F_{m'\epsilon'\,me} + \beta F_{m'\epsilon'\,mf}\right) \right|^2 . \tag{6.8}$$

From here onwards, the sum of over m' of the complex product of scattering amplitudes will expressed as

$$Q_{m_1\epsilon_1 m_2\epsilon_2} \equiv \sum_{m'} F_{m'\epsilon' m_1\epsilon_1} F^{*}_{m'\epsilon' m_2\epsilon_2} \,. \tag{6.9}$$

6.2.1 Matrix of the scattering amplitude products

For given j, $\bar{\Omega}$, j', $\bar{\Omega}'$, the products of scattering amplitudes, $Q_{m_1\epsilon_1\,m_2\epsilon_2}$ in Eq. (6.9) can be considered as the elements of the matrices $\boldsymbol{Q}^{\epsilon_1\,\epsilon_2}$, for which the labels m_1 and m_2 represent the indices. Taking into account the symmetry of the scattering amplitudes, given by

$$F_{-m'\epsilon'-m\epsilon} = \epsilon\epsilon'(-1)^{m-m'} F_{m'\epsilon' m\epsilon} \tag{6.10}$$

one can determine that the elements of the matrix exhibit the following properties:

- Symmetry:

$$Q_{m_1\epsilon_1\,m_2\epsilon_2} = \epsilon_1\epsilon_2(-1)^{m_1+m_2-1} Q_{-m_1\epsilon_1\,-m_2\epsilon_2} \tag{6.11}$$

- Complex conjugate:

$$Q^{*}_{m_1\epsilon_1\,m_2\epsilon_2} = Q_{m_2\epsilon_2\,m_1\epsilon_1} \tag{6.12}$$

  Therefore the $\boldsymbol{Q}^{\epsilon\,\epsilon}$ matrix is Hermitian (self-adjoint), while $\boldsymbol{Q}^{e\,f}$ and $\boldsymbol{Q}^{f\,e}$ are mutually adjoint.

- If $m_1 = m_2 = m$

$$Q_{m\epsilon_1\,m\epsilon_2} = \epsilon_1\epsilon_2\, Q_{-m\epsilon_1\,-m\epsilon_2} \tag{6.13}$$

- If, additionally, $\epsilon_1 = \epsilon_2 = \epsilon$

$$Q_{m\epsilon\, m\epsilon} = Q_{-m\epsilon\, -m\epsilon} = Q^*_{m\epsilon\, m\epsilon} = \sum_{m'} |F_{m'\epsilon'\, m\epsilon}|^2 = \sum_{m'} |F_{m'\epsilon'\, -m\epsilon}|^2 \tag{6.14}$$

  and hence the elements are real.

- If $m_1 = m = -m_2$:

$$Q_{m\epsilon_1\, -m\epsilon_2} = -\epsilon_1\epsilon_2\, Q_{-m\epsilon_1\, m\epsilon_2} = Q^*_{-m\epsilon_2\, m\epsilon_1} \tag{6.15}$$

  As a consequence:

$$Q_{m\epsilon_1\, -m\epsilon_2} + Q_{m\epsilon_2\, -m\epsilon_1} = Q_{-m\epsilon_1\, m\epsilon_2} + Q_{-m\epsilon_2\, m\epsilon_1} \tag{6.16}$$

- If, additionally to $m_2 = -m_1$, $\epsilon_1 = \epsilon_2$,

$$Q_{m\epsilon\, -m\epsilon} = -\, Q_{-m\epsilon\, m\epsilon} = -Q^*_{m\epsilon\, -m\epsilon} \tag{6.17}$$

  that is, the matrix element is pure imaginary.

- If $m_1 \neq m_2$ and they are contiguous ($|m_1 - m_2| = 1$),

$$Q_{m_1\epsilon_1\, -m_2\epsilon_2} = \epsilon_1\epsilon_2\, Q_{-m_1\epsilon_1\, m_2\epsilon_2} = \epsilon_1\epsilon_2 Q^*_{m_2\epsilon_2\, -m_1\epsilon_1} \tag{6.18}$$

  If, in addition, $\epsilon_1 \neq \epsilon_2$,

$$Q_{m_1\epsilon_1\, m_2\epsilon_2} + Q_{m_1\epsilon_2\, m_2\epsilon_1} = Q_{-m_1\epsilon_1\, -m_2\epsilon_2} + Q_{-m_1\epsilon_2\, -m_2\epsilon_1} \tag{6.19}$$

6.2.2 Derivation of the *r*-PDDCSs

Eq. (6.8) can be expanded:

$$\begin{aligned}
&\mathrm{d}\sigma(j\, m_E\, \bar{\Omega}\hat{E} \rightarrow j'\, \bar{\Omega}'\epsilon') = \\
&\frac{1}{2}\Big[\alpha^2 \sum_{m_1,m_2} D^{j}_{m_1\, m_E} D^{j*}_{m_2\, m_E} Q_{m_1 e, m_2 e} \\
&+\alpha\beta \sum_{m_1,m_2} D^{j}_{m_1\, m_E} D^{j*}_{m_2\, m_E} (Q_{m_1 f, m_2 e} + Q_{m_1 e, m_2 f}) \\
&+\beta^2 \sum_{m_1,m_2} D^{j}_{m_1\, m_E} D^{j*}_{m_2\, m_E} Q_{m_1 f, m_2 f}\Big]. \qquad (6.20)
\end{aligned}$$

Note that in Eq. (6.20) m_E can have positive, $+\bar{m}_E$, or negative, $-\bar{m}_E$, values. When $m_E > 0$, $\alpha\beta = -|\alpha\beta|$ and when $m_E < 0$, $\alpha\beta = +|\alpha\beta|$ due to the change in sign of κ (see Equation 4.13).

Using the relation[125]

$$\begin{aligned}
&D^{j}_{m_1 m_E}(\phi,\theta,0)\, D^{j*}_{m_2 m_E}(\phi,\theta,0) = \\
&\sum_{k,q} \left(\frac{2k+1}{2j+1}\right) \langle jm_1, k\ -q|jm_2\rangle\, \langle jm_E, k0|jm_E\rangle C_{k-q}(\theta,\phi) \qquad (6.21)
\end{aligned}$$

Eq, (6.20) may be rewritten as

$$\begin{aligned}
&\mathrm{d}\sigma(jm_E\, \bar{\Omega}\hat{E} \rightarrow j'\, \bar{\Omega}'\epsilon') = \\
&\qquad \frac{1}{2}\Big[\alpha^2\, T^{m_E}_{ee} + \alpha\beta\, T^{m_E}_{ef} + \beta^2\, T^{m_E}_{ff}\Big] \qquad (6.22)
\end{aligned}$$

where

$$\begin{aligned}
T^{(m_E)}_{\epsilon\epsilon} &= \sum_{k,q} \left(\frac{2k+1}{2j+1}\right)\, \langle jm_E, k0|jm_E\rangle \sum_{m_1,m_2} C_{k-q}(\theta_E,\phi_E)\langle jm_1, k-q|jm_2\rangle Q_{m_1\epsilon\, m_2\epsilon} \\
&= \sum_{k} \left(\frac{2k+1}{2j+1}\right)\, \langle jm_E, k0|jm_E\rangle\, \sum_{q} C_{kq}(\theta_E,\phi_E) \sum_{m} \langle jm, kq|j(m+q)\rangle Q_{m\epsilon\,(m+q)\epsilon} \qquad (6.23)
\end{aligned}$$

and

$$\begin{aligned}
T^{(m_E)}_{\epsilon_1\epsilon_2} = &\sum_{k} \left(\frac{2k+1}{2j+1}\right)\, \langle jm_E, k0|jm_E\rangle\, \sum_{q} C_{kq}(\theta_E,\phi_E) \\
&\sum_{m} \langle jm, kq|j(m+q)\rangle (Q_{m\epsilon_1\,(m+q)\epsilon_2} + Q_{m\epsilon_2 (m+q)\epsilon_1}) \qquad (6.24)
\end{aligned}$$

where the relationship $m_2 = m_1 - q$, enforced by the Clebsch-Gordan coefficient, is used, the variable m_1 is replaced by m, and the sum over q is inverted.

In an electric field, there are equal quantities of states with $m_E = \pm\bar{m}_E$, and thus to obtain the DCS, one must average over these two values of m_E to give

$$\begin{aligned}\mathrm{d}\sigma(j\,\bar{m}_E\,\bar{\Omega}\hat{E} \to j'\,\bar{\Omega}'\epsilon') = \frac{1}{2}\Big[&\mathrm{d}\sigma(j\,m_E\,\bar{\Omega}\hat{E} \to j'\,\bar{\Omega}'\epsilon') + \\ &\mathrm{d}\sigma(j\ -m_E\,\bar{\Omega}\hat{E} \to j'\,\bar{\Omega}'\epsilon')\Big]. \end{aligned} \tag{6.25}$$

Hence, one can write the averaged DCS as

$$\begin{aligned}\mathrm{d}\sigma(j\bar{m}_E\bar{\Omega}\hat{E} \to j'\bar{\Omega}'\epsilon')\Big|_{\theta_E}^{\phi_E} &= \frac{1}{4}\Big[\alpha^2\,(T_{ee}^{(\bar{m}_E)} + T_{ee}^{(-\bar{m}_E)}) \\ &\quad - |\alpha\beta|\,(T_{ef}^{(\bar{m}_E)} - T_{ef}^{(-\bar{m}_E)}) + \beta^2(T_{ff}^{\bar{m}_E} + T_{ff}^{(-\bar{m}_E)})\Big] \\ &= \frac{1}{4}\Big[\alpha^2\,T^{(ee)} - |\alpha\beta|\,T^{(ef)} + \beta^2\,T^{(ff)}\Big] \end{aligned} \tag{6.26}$$

where

$$\begin{aligned}T^{(\epsilon\epsilon)} =& T_{\epsilon\epsilon}^{(\bar{m}_E)} + T_{\epsilon\epsilon}^{(-\bar{m}_E)} = 2\sum_k \left(\frac{2k+1}{2j+1}\right)\,\langle j\bar{m}_E, k0|j\bar{m}_E\rangle \\ &\delta_{k,\mathrm{even}} \sum_q C_{kq}(\theta_E,\phi_E) \sum_m \langle jm, kq|j(m+q)\rangle Q_{m\epsilon\,(m+q)\epsilon} \end{aligned} \tag{6.27}$$

and

$$\begin{aligned}T^{(ef)} =& T_{ef}^{(\bar{m}_E)} - T_{ef}^{(-\bar{m}_E)} = 2\sum_k \left(\frac{2k+1}{2j+1}\right)\,\langle j\bar{m}_E, k0|j\bar{m}_E\rangle \\ &\delta_{k,\mathrm{odd}} \sum_q C_{kq}(\theta_E,\phi_E) \sum_m \langle jm, kq|j(m+q)\rangle (Q_{mf\,(m+q)e} + Q_{me\,(m+q)f})\,. \end{aligned} \tag{6.28}$$

The Kronecker deltas arise from the properties of the $\langle jm_E, k0|jm_E\rangle$ Clebsch-Gordan coefficient for $m_E = \pm\bar{m}_E$.

For any value of j, Eq. (6.25) can be written as

$$\left[\mathrm{d}\sigma(j\,\bar{m}_E\bar{\Omega}\,\hat{E}\to j'\,\bar{\Omega}'\epsilon')\right]_{\theta_E}^{\phi_E}=\sum_k(2k+1)\sum_{q=-k}^{k}\tilde{R}_q^{(k)}(\theta)a_q^{(k)} \tag{6.29}$$

where $a_q^{(k)}=\mathcal{A}_0^{(k)}C_{kq}\,(\theta_E,\phi_E)$ are the extrinsic polarisation parameters in the scattering frame, and $\tilde{R}_q^{(k)}(\theta)$ are the unnormalised $\boldsymbol{r}$-PDDCSs.

To rearrange Eq. (6.26) into a form similar to Eq. (6.29), the extrinsic polarisation moments must be included in the expansion. Hence, inserting these moments from Eq. (3.39), one obtains, for even values of k

$$\begin{aligned}
&(j\bar{m}_E\bar{\Omega}\hat{E}\to j'\bar{\Omega}'\epsilon')\Big|_{\theta_E,\,\text{even }k}^{\phi_E}=\frac{1}{4}\alpha^2T^{(ee)}+\frac{1}{4}\beta^2T^{(ff)}\\
&=\frac{1}{2}\sum_{k=\text{even}}\left(\frac{2k+1}{2j+1}\right)\frac{\mathcal{A}_0^{(\text{even}k)}}{\left\langle j\bar{\Omega},k0|j\bar{\Omega}\right\rangle}\sum_q C_{kq}(\theta_E,\phi_E)\\
&\qquad\sum_m\langle jm,kq|j(m+q)\rangle\left(\alpha^2Q_{me(m+q)e}+\beta^2Q_{mf(m+q)f}\right)\\
&=\frac{1}{2(2j+1)}\sum_{k=\text{even}}(2k+1)\frac{\mathcal{A}_0^{(\text{even}k)}}{\left\langle j\bar{\Omega},k0|j\bar{\Omega}\right\rangle}\sum_q C_{kq}(\theta_E,\phi_E)\\
&\qquad\sum_m\langle jm,kq|j(m+q)\rangle\sum_{\epsilon=e,f}\gamma_\epsilon^2\;Q_{m\epsilon(m+q)\epsilon}
\end{aligned}\tag{6.30}$$

and, for odd values of k,

$$\begin{aligned}
&\mathrm{d}\sigma(j\bar{m}_E\bar{\Omega}\hat{E}\to j'\bar{\Omega}'\epsilon')\Big|_{\theta_E,\text{odd }k}^{\phi_E}=-\frac{1}{4}|\alpha\beta|T^{(ef)}\\
&=\frac{1}{2}\sum_{k=\text{odd}}\left(\frac{2k+1}{2j+1}\right)\frac{\mathcal{A}_0^{(k)}}{\left\langle j\bar{\Omega},k0|j\bar{\Omega}\right\rangle}\sum_q C_{kq}(\theta_E,\phi_E)\\
&\qquad\sum_m\langle jm,kq|j(m+q)\rangle\left(Q_{mf(m+q)e}+Q_{me(m+q)f}\right)\\
&=\frac{1}{2(2j+1)}\sum_{k=\text{odd}}(2k+1)\frac{\mathcal{A}_0^{(k)}}{\left\langle j\bar{\Omega},k0|j\bar{\Omega}\right\rangle}\sum_q C_{kq}(\theta_E,\phi_E)\times\\
&\qquad\sum_m\langle jm,kq|j(m+q)\rangle\sum_{\substack{\epsilon_1=e,f\\ \epsilon_1\neq\epsilon_2}}Q_{m\epsilon_1(m+q)\epsilon_2}\,.
\end{aligned}\tag{6.31}$$

By comparison with Eq. (6.29) one obtains expressions for the $\boldsymbol{r}$-PDDCSs

$$\tilde{R}_q^{(\text{even } k)}(\theta) = \frac{1}{2(2j+1)} \frac{1}{\langle j\bar{\Omega}, k0 | j\bar{\Omega}\rangle} \sum_m \langle jm, kq | j(m+q)\rangle \sum_{\epsilon=e,f} \gamma_\epsilon^2 \, Q_{m\epsilon(m+q)\epsilon} \tag{6.32}$$

and

$$\tilde{R}_q^{(\text{odd } k)}(\theta) = \frac{1}{2(2j+1)} \frac{1}{\langle j\bar{\Omega}, k0 | j\bar{\Omega}\rangle} \sum_m \langle jm, kq | j(m+q)\rangle \sum_{\substack{\epsilon_1=e,f \\ \epsilon_1 \neq \epsilon_2}} Q_{m\epsilon_1(m+q)\epsilon_2} \tag{6.33}$$

where $\gamma_\epsilon = \alpha$ or β when $\epsilon = e$ or f, respectively.

In Eq. (6.29), all extrinsic polarisation effects (those imparted by the preparation of the system) are encapsulated in the $\mathcal{A}_0^{(k)}$ moment, while intrinsic polarisation effects (those that depend on the collision dynamics regardless of the specific preparation of the reactants) are included in $\tilde{R}_q^{(k)}(\theta)$.

Note that the $\tilde{R}_0^{(0)}(\theta)$ moment for a given j state can be written as

$$\tilde{R}_0^{(0)}(\theta) = \frac{\alpha^2}{2} \, \mathrm{d}\sigma(j, \bar{\Omega}, e \to j', \bar{\Omega}', \epsilon') + \frac{\beta^2}{2} \, \mathrm{d}\sigma(j, \bar{\Omega}, f \to j', \bar{\Omega}', \epsilon') \, . \tag{6.34}$$

Therefore, the isotropic DCS in the presence of the orienting field is the average of the $e \to \epsilon'$ and $f \to \epsilon'$ DCSs weighted by the α^2 and β^2 coefficients. This is in contrast to the isotropic DCS in the absence of the field for the f selected state that is given by Eq. (6.34) with $\alpha = 0$ and $\beta = \sqrt{2}$. One can also define the normalised $\boldsymbol{r}$-PDDCSs, $R_q^{(k)}(\theta)$, such that

$$\tilde{R}_q^{(k)}(\theta) = \frac{\sigma_{\text{iso}}}{2\pi} R_q^{(k)}(\theta) \, , \tag{6.35}$$

where σ_{iso}, for given j, Ω, j', and Ω', can be written as

$$\sigma_{\text{iso}} = 2\pi \int_{-1}^{1} \tilde{R}_0^{(0)} \mathrm{d}\cos\theta = \frac{\alpha^2}{2} \, \sigma_{e\to\epsilon'} + \frac{\beta^2}{2} \, \sigma_{f\to\epsilon'} \tag{6.36}$$

and is the isotropic integral cross section in the field. By making use of the fact that for achiral systems the $\boldsymbol{r}$-PDDCSs are real, which implies that $R_q^{(k)}(\theta) = (-1)^q R_{-q}^{(k)}(\theta)$, one can rewrite Eq. (6.29) to obtain

$$\mathrm{d}\sigma(j\,\bar{m}_E\,\bar{\Omega}\,\hat{E} \to j'\,\bar{\Omega}'\epsilon')\Big]_{\theta_E}^{\phi_E} = \frac{\sigma_{\mathrm{iso}}}{2\pi}\sum_{k}^{2j}(2k+1)\mathcal{A}_0^{(k)} \sum_{q=0}^{k}\frac{2}{1+\delta_{q0}}R_q^{(k)}(\theta)C_{kq}(\theta_E,0)\cos(q\phi_E)\,. \tag{6.37}$$

A particular case is when $\theta_E = 90°$ and $\phi_E = 90°$ or 270°, that is, when the field is oriented along the y axis (perpendicular to the scattering plane). In this case, all orientation terms in Eq. (6.37), with k odd, vanish and only the alignment terms, including $k = 0$, remain.

The intrinsic $\boldsymbol{r}$-Polarisation Parameters, which define the effect of orientation on the integral cross section, are defined as

$$r_q^{(k)} = \int_{-1}^{1} R_q^{(k)}(\theta)\mathrm{d}\cos\theta\,. \tag{6.38}$$

Integrating Eq. (6.29) over the scattering angle for a given orientation of the orienting field with respect the scattering frame, yields an integral cross section that can be expressed as

$$\sigma\Big]_{\theta_E}^{\phi_E} = \frac{\sigma_{\mathrm{iso}}}{2\pi}\sum_{k,q}(2k+1)\,r_q^{(k)}\mathcal{A}_0^{(k)}\,C_{kq}(\theta_E,\phi_E)\,. \tag{6.39}$$

Further integration over the azimuthal angle between the scattering plane and the plane defined by $\boldsymbol{k}$ and $\boldsymbol{E}$ leads to

$$\sigma\Big]_{\theta_E} = \sigma_{\mathrm{iso}}\sum_{k}(2k+1)\,r_0^{(k)}\mathcal{A}_0^{(k)}\,C_{k0}(\theta_E,0) \tag{6.40}$$

In the particular case of $\boldsymbol{E}$ oriented along the relative velocity vector, where $\theta_E = 0$ or π ($\pm z$ orientation), there is azimuthal symmetry and integration over ϕ_E is equivalent to multiplying by $2\,\pi$:

$$\sigma\Big]_{\theta_E=0} = \sigma_{\text{iso}} \sum_k (2k+1)\, r_0^{(k)} \mathcal{A}_0^{(k)}$$
$$\sigma\Big]_{\theta_E=180^\circ} = \sigma_{\text{iso}} \sum_k (2k+1)\, (-1)^k r_0^{(k)} \mathcal{A}_0^{(k)} \tag{6.41}$$

6.2.3 Integral and Differential Steric Asymmetries

The integral steric asymmetry (ISA) measures the preference of the scattering event for one orientation over its opposite. Specifically, for end-on ($\pm z$, $\theta_E = 0^\circ$ or 180°) and side-on ($\pm x$, $\theta_E = 90^\circ$, $\phi_E = 0^\circ$ or 180° and $\pm y, \theta_E = 90^\circ, \phi_E = 90^\circ$ or $\phi_E = 270^\circ$) orientation the respective definitions are

$$S_z = \frac{\sigma_{-z} - \sigma_{+z}}{\sigma_{-z} + \sigma_{+z}} = \frac{\sigma_{\theta_E=180^\circ} - \sigma_{\theta_E=0^\circ}}{\sigma_{\theta_E=180^\circ} + \sigma_{\theta_E=0^\circ}} \tag{6.42}$$
$$S_x = \frac{\sigma_{+x} - \sigma_{-x}}{\sigma_{+x} + \sigma_{-x}} = \frac{\sigma_{\theta_E=90^\circ}^{\phi_E=0^\circ} - \sigma_{\theta_E=90^\circ}^{\phi_E=180^\circ}}{\sigma_{\theta_E=90^\circ}^{\phi_E=0^\circ} + \sigma_{\theta_E=90^\circ}^{\phi_E=180^\circ}} \tag{6.43}$$
$$S_y = \frac{\sigma_{+y} - \sigma_{-y}}{\sigma_{+y} + \sigma_{-y}} = \frac{\sigma_{\theta_E=90^\circ}^{\phi_E=90^\circ} - \sigma_{\theta_E=90^\circ}^{\phi_E=270^\circ}}{\sigma_{\theta_E=90^\circ}^{\phi_E=90^\circ} + \sigma_{\theta_E=90^\circ}^{\phi_E=270^\circ}}\,. \tag{6.44}$$

The differential steric asymmetry (DSA) resolves this preference over the scattering angle, θ. It is given analogously for all three orientations

$$\mathrm{d}\sigma_{\text{diff}}^{z}(\theta) = \frac{\mathrm{d}\sigma_{-z}(\theta) - \mathrm{d}\sigma_{+z}(\theta)}{\mathrm{d}\sigma_{-z}(\theta) + \mathrm{d}\sigma_{+z}(\theta)} \tag{6.45}$$
$$\mathrm{d}\sigma_{\text{diff}}^{x}(\theta) = \frac{\mathrm{d}\sigma_{+x}(\theta) - \mathrm{d}\sigma_{-x}(\theta)}{\mathrm{d}\sigma_{+x}(\theta) + \mathrm{d}\sigma_{-x}(\theta)} \tag{6.46}$$
$$\mathrm{d}\sigma_{\text{diff}}^{y}(\theta) = \frac{\mathrm{d}\sigma_{+y}(\theta) - \mathrm{d}\sigma_{-y}(\theta)}{\mathrm{d}\sigma_{+y}(\theta) + \mathrm{d}\sigma_{-y}(\theta)}\,. \tag{6.47}$$

It should be noted that for $j \leq 1$, σ_{+y} and σ_{-y} are equal, as are $\mathrm{d}\sigma_{+y}(\theta)$ and $\mathrm{d}\sigma_{-y}(\theta)$. Hence, $S_y = 0$ and $\mathrm{d}\sigma_{\text{diff}}^{y}(\theta) = 0$.

6.3 Application

6.3.1 Computational Procedures

In this section, quantum mechanial (QM) calculations were performed using the HIBRIDON 4 suite of codes[187–189]. Those calculations pertaining to the NO(X)

+ Ar system used the PESs of Alexander[190]. These calculations were performed with $E_{\text{coll}} = 530\,\text{cm}^{-1}$ and $651\,\text{cm}^{-1}$ for the spin-orbit conserving and spin-orbit changing collisions respectively to match the experimental energies. Approximate QM data for NO(X) + N_2 were obtained using the PESs of Wen *et al.*[191], which is averaged over N_2 orientations. These were performed at $E_{\text{coll}} = 845\,\text{cm}^{-1}$. OH(X) + Ar calculations were performed using the PESs of Kłos *et al.*[192] with a collision energy of $746\,\text{cm}^{-1}$, with a maximum value of $J_{\text{TOT}} = 200.5$ and $R_{\text{end}} = 150\,\text{a}_0$.

QCT calculations were also performed using the sum PES (see Section 2.1) for each system. These sum PESs are the same as those used in the QM calculations, and the QCT calculations are performed at the same collision energies as for the QM calculations.

6.3.2 Integral Steric Asymmetries

The simplest use of this framework is through the integral steric asymmetry (ISA) for collisions involving NO($X^2\Pi$, $j = 1/2$, $\bar{\Omega} = 1/2$). In Figure 6.2, experimental ISAs for the scattering of NO($X^2\Pi$, $j = 1/2$, $\bar{\Omega} = 1/2$) with Ar, N_2 and O_2, obtained using the procedures outlined in reference [22], are shown for a variety of values of Δj for both spin-orbit conserving collisions, $\bar{\Omega}' = 1/2$ and spin-orbit changing, $\bar{\Omega}' = 3/2$, collisions using orienting electric fields strengths of $9.2\,\text{kV}\,\text{cm}^{-1}$ (see Figure 6.3). The integral steric asymmetry is defined such that a positive value corresponds to a preference for collisions at the N-end of the molecule, $\theta_E = 180°$.

Theoretical results in the form of quantum mechanical calculations and QCT are included in the figure for comparison, where such calculations are available. Note that there are no QCT calculations for the spin-orbit changing manifold, as the QCT calculations treat NO(X) as a closed shell molecule.

As can be seen in Figure 6.2, at low and middle $\Delta j = j' - j$, all three systems exhibit distinct oscillations in $S(z)$, with a tendency for more positive values for odd Δj and more negative values for even Δj transitions. In the region above about $\Delta j = 12$, the oscillations die out and the steric asymmetry increases in the positive direction. While the QM calculations reproduce well the position and magnitude

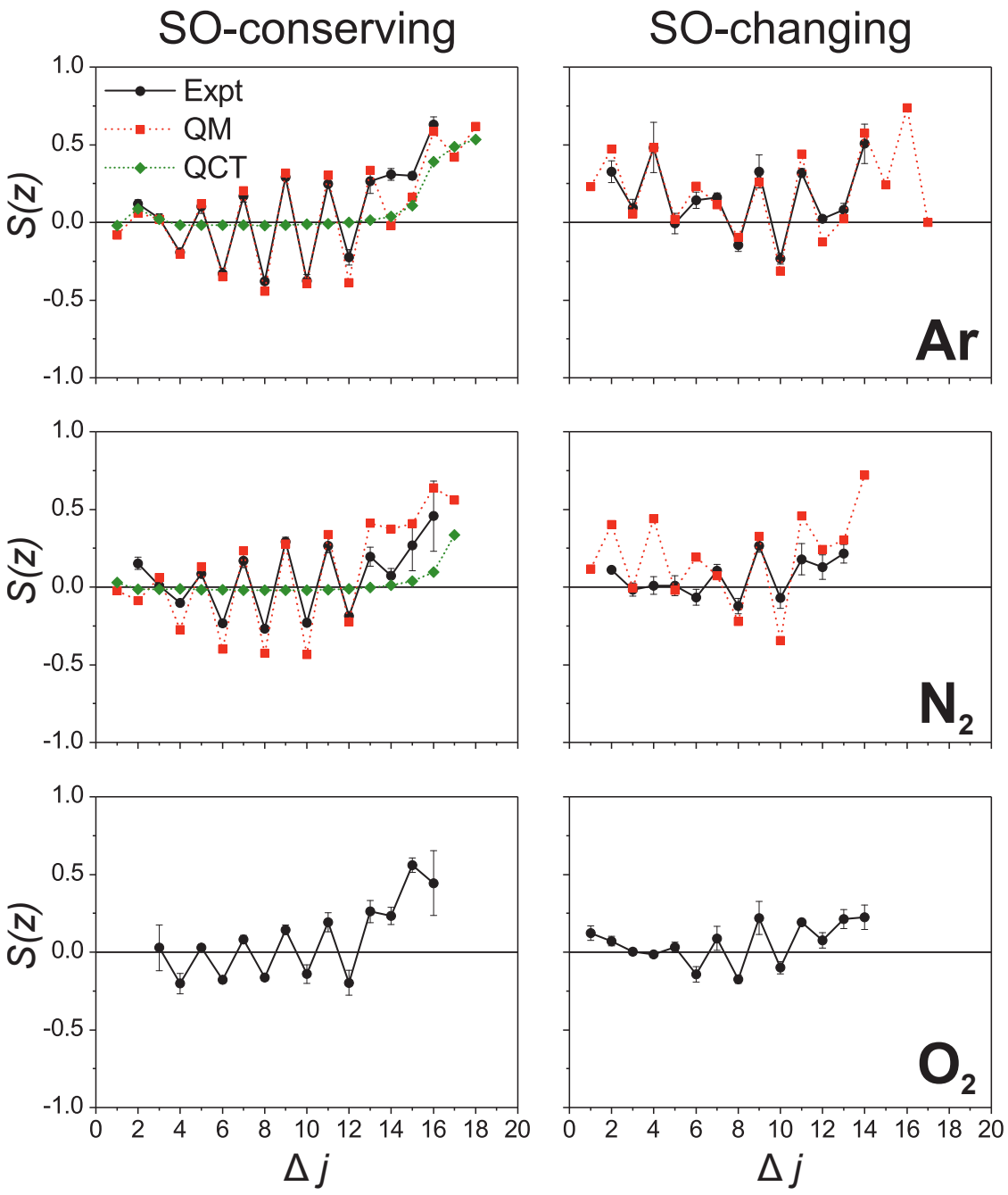

Figure 6.2: Integral z-axis steric asymmetries, $S(z)$, as a function of Δj for collisions of NO($X^2\Pi; |j = 1/2, \bar{\Omega} = 1/2, \boldsymbol{E}\rangle$ with Ar (top), N_2 (middle), and O_2 (bottom), for spin-orbit conserving (left) and spin-orbit changing (right) transitions to the final e states. [193] Positive values of $S(z)$ correspond to preferential scattering off the N-end of NO. The experimental data is represented in black, the QM data in red, and the QCT data in green. The experiments were performed at the following collision energies: NO + Ar (spin-orbit conserving transitions) 530 cm^{-1}; NO + Ar (spin-orbit changing transitions) 651 cm^{-1}; NO + N_2 845 cm^{-1}; NO + O_2 550 cm^{-1}[193].

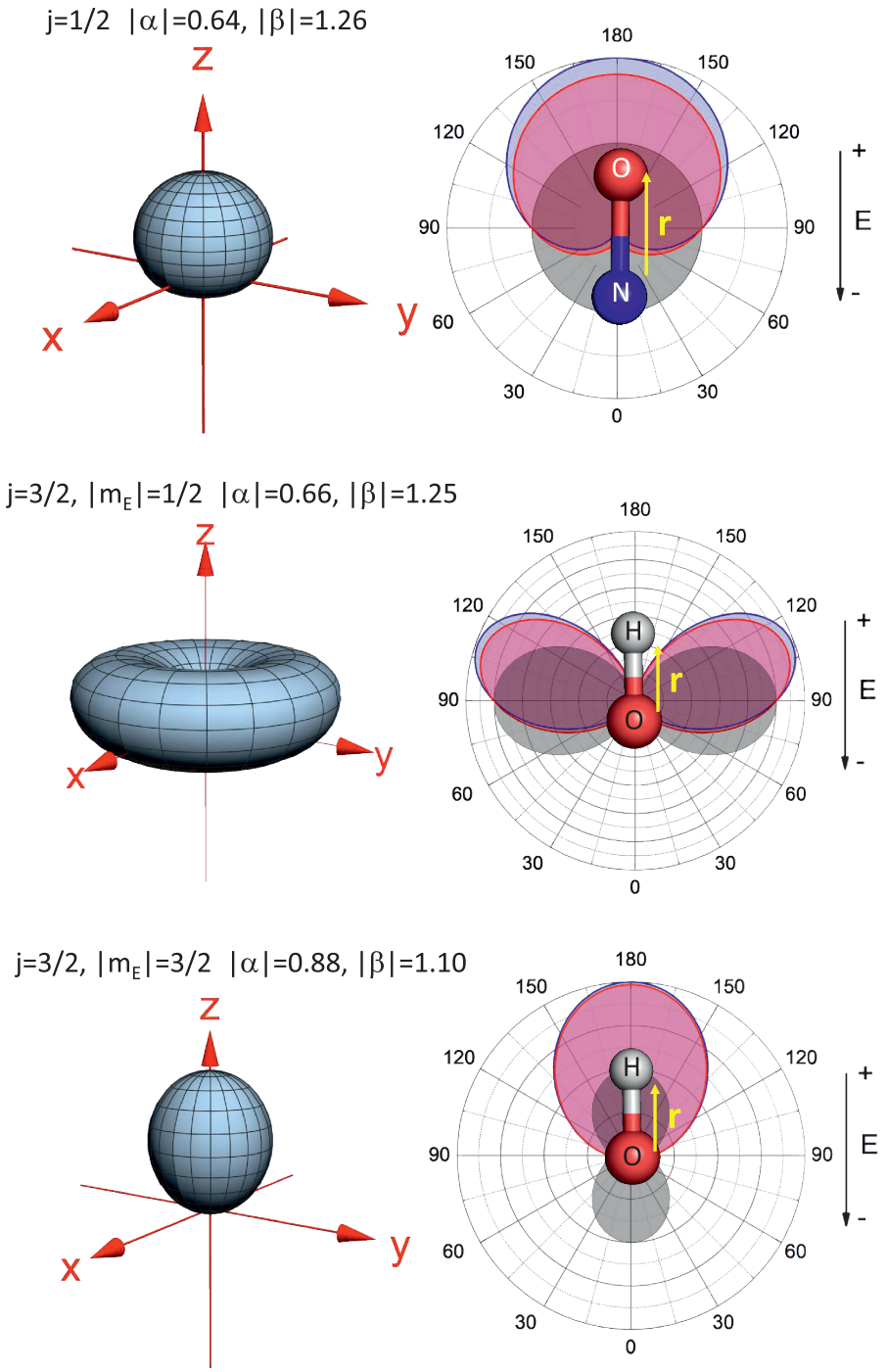

Figure 6.3: Left panels: $\boldsymbol{r}$-portraits (3D contour surfaces of the probability density function of the bond axis) for NO (upper row) and OH (middle and bottom rows) in an electric field. The extent of polarisation is calculated with the values of $|\alpha|$ and $|\beta|$ shown in the figures with the respective values of the extrinsic $\boldsymbol{r}$-polarisation parameters given by Eq. (3.39). The electric field strengths are 9.2 kV cm^{-1} for NO and 7.5 kV cm^{-1} for OH. The right panels show the corresponding stereographic projections of the angular axis distributions of NO and OH (pink shading), or at infinite field (blue shading). The hypothetical field-free bond axis distributions with selected values of $\bar{m}_E$ are indicated by the shaded area.

of the oscillations observed experimentally at all Δj, the QCT calculations for collisions of NO with Ar and N_2 predict almost no z-axis steric preference at low and middle Δj, but agree with the experiment and the QM calculations in the high Δj region. These findings indicate the quantum nature of the inelastic scattering of NO in the region below $\Delta j \simeq 12$, and allow rationalisation of the region above $\Delta j \simeq 12$ in terms of classical arguments[194, 195]. In a QCT theoretical study on NO(X) + He, it has also been shown that at the N-end of the potential, the collision partner is able to penetrate further into the repulsive region, and thus transitions involving higher rotational energy transfer (larger Δj) are more likely to occur at the N-end than at the O-end of the NO molecule[196].

The oscillations in the low and middle Δj range can be quantitatively reproduced employing a quasi-quantum treatment (QQT)[197], which is based on a hard-shell NO potential. The model reveals that the alternating preference for N-end and O-end collisions are due to constructive and destructive interferences between trajectories at the two ends of the molecule[193]. Furthermore, due to the lack of attractive forces in the QQT model, the results imply that it is to a large extent the repulsive parts of the potential that are responsible for the observed oscillations.

Comparison between the data for the spin-orbit conserving and the spin-orbit changing data, in the left and right panels of Figure 6.2 respectively, shows an overall increased preference for N-end collisions in the spin-orbit changing manifold; although the same oscillations as for the spin-orbit conserving manifold persist, the integral z-axis steric asymmetry is shifted towards positive values. The reason for this shift can be understood by considering the underlying PESs for the spin-orbit conserving and changing transitions. As described in Section 2.1, the NO plus rare gas system involves two PESs, one of A' and one of A'' symmetry. In the Hund's case (a) description, which applies reasonably to NO for the lowest and middle j-values, spin-orbit conserving transitions can be approximated to occur on the sum of the two potentials, while spin-orbit changing transitions can be approximated to occur on the difference potential[46, 198]. The difference potential has a pronounced

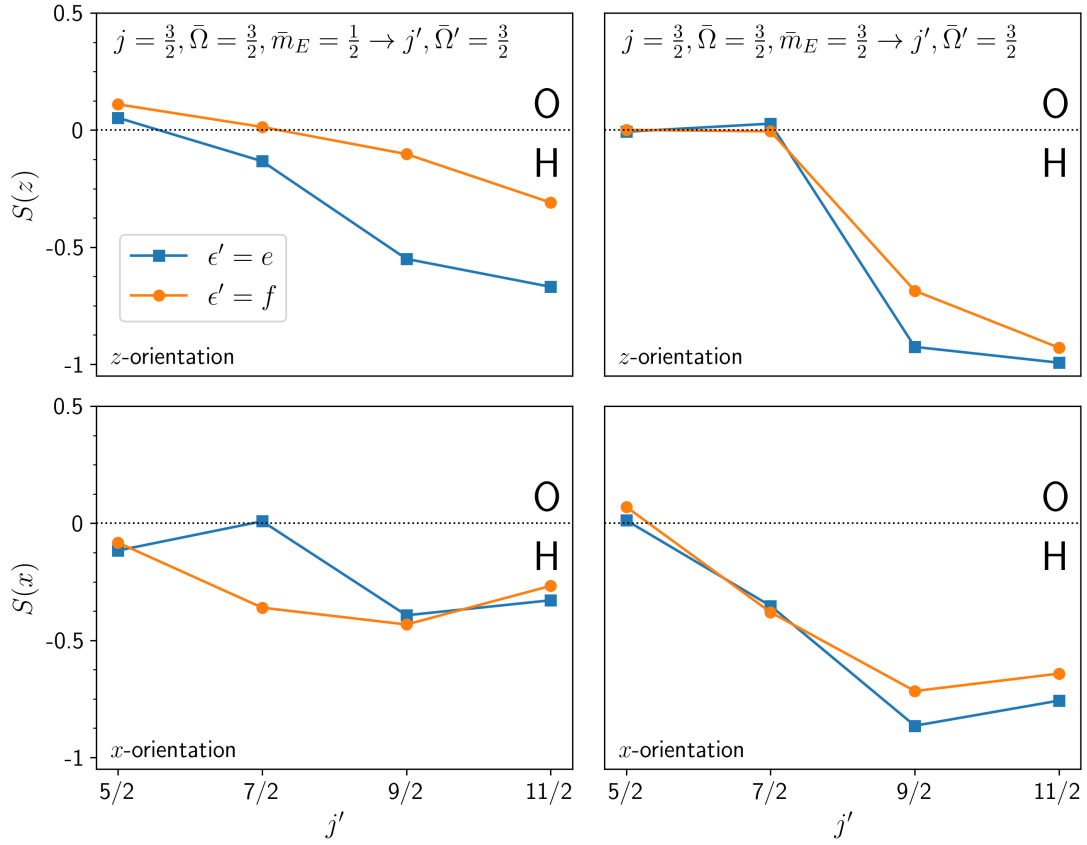

Figure 6.4: Integral z-axis (top row) and x-axis (bottom row) steric asymmetries ($S(z/x)$) for inelastic scattering of OH(X) with Ar from the initial $|\bar{\Omega} = \frac{3}{2}, j = \frac{3}{2}\rangle$ state, at a collision energy of 746 cm^{-1}. The panels show QM calculations for spin-orbit conserving scattering from the initial $\bar{m}_E = 1/2$ (left) and 3/2 (right) states. In both cases transitions are shown for both final Λ-doublets with the f and e states shown with circles and squares, respectively. Negative $S(z)$ values correspond to preferential scattering off the H-end of OH, and negative $S(x)$ values correspond to *repulsive* scattering off the H-end of the OH molecule.

repulsive wall at the O-end, but is purely attractive at the N-end, so that, overall, collisions at the N-end are favoured for spin-orbit changing transitions[193].

The dynamics of collisions of NO with N_2 and O_2 are, of course, more complicated than those of NO with a rare gas atom. The molecular collision partners can now also be rotationally excited and so the internal and translational energies of the detected NO may be correlated with different quantum states of the partner product. However, the main features in the integral steric asymmetry data appear to be similar for NO + Ar and NO + N_2/O_2, indicating that the measured (and calculated) quantities are signatures of the scattered NO species which are only subtly modified

by the nature of the collision partner. Perhaps the biggest difference can be seen between the NO(X) + Ar and the NO(X) + O_2 data: the magnitudes of $S(z)$ are clearly smaller and exhibit less of a curved profile with increasing Δj for O_2 than for Ar. It can be speculated that these differences arise from a more isotropic and possibly more attractive potential for NO + O_2, but may also reflect the more complex electronic structure of the NO-O_2 system compared to collisions of NO with the closed shell collision partners[193] (O_2 has a $^3\Sigma_g^-$ ground state, rather than $^1\Sigma_g^+$). An accurate theoretical description would clearly be desirable to gain further insight into the finer details of the scattering dynamics of the NO + diatom system. This should be achievable for the closed shell diatom partners, provided an accurate PES is calculated. For open shell partners, this is not currently possible.

6.3.3 OH($X^2\Pi$) + Ar Integral and Differential Effects

A series of comprehensive experiments with the aim of investigating the integral steric effects in collisions of OH($X^2\Pi_{3/2}$) with Ar were carried out by ter Meulen and coworkers at a collision energy of $E_{\rm coll} = 746\,{\rm cm}^{-1}$ using laser induced fluorescence (LIF) as a state specific detection method[199–201]. In their experiments, the OH $|j = 3/2, \bar{\Omega} = 3/2, f\rangle$ initial state was selected using two different hexapole arrangements: one consisted of a single hexapole and another used a tandem of consecutive hexapoles. The two possible $\bar{m}_E$ states resulting from that selection, $\bar{m}_E = 1/2$ and $3/2$, are split in energy by the Stark effect upon application of a static electric field that orients the OH bond-axis.

The QM integral steric asymmetries, for the inelastic scattering of OH(X) with Ar, as a function of j', are shown in Figure 6.4, for scattering from the two initial $|j = 3/2, \bar{\Omega} = 3/2, \bar{m}_E, \boldsymbol{E}\rangle$ states, where $\bar{m}_E = 1/2$ and $3/2$ in the left and right panels, respectively. The two upper panels depict the orientation along the z-axis (coincident with $\boldsymbol{k}$, the initial relative velocity) and the lower panels correspond to orientation along the x-axis (recall that $\boldsymbol{k} - \boldsymbol{k}'$ defines the xz-plane). Before entering into the discussion of these results, it is pertinent to examine the extent of agreement with the existing experimental data. The comparison between the

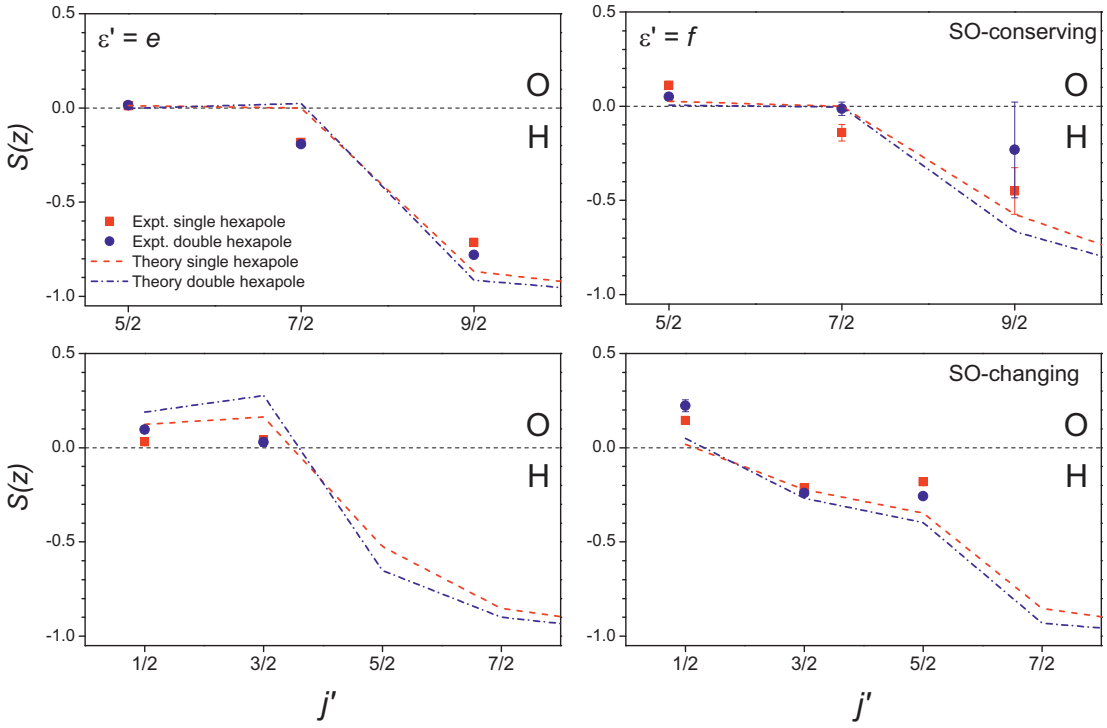

Figure 6.5: Comparison of the QM calculations and the experimental integral steric asymmetry, $S(z)$, of ter Meulen *et al.*[200] for the final e (left) and f (right) Λ-doublets for OH(X) + Ar at a collision energy of of 746 cm^{-1}. The upper panels show data for spin-orbit conserving transitions, whilst the lower panels show data for the spin-orbit changing transitions. Experimental data for the initial $|\bar{\Omega} = \frac{3}{2}, j = \frac{3}{2}\rangle$ state is shown by points, whilst theory is shown by dashed lines. Red and blue lines correspond to passage of the OH(X) molecules through either a single or double hexapole, respectively, before the collision. Note that negative $S(z)$ implies a preference for scattering off the H-end of the OH molecule.

experimental results of van Beek *et al.*[200] for the z-axis polarisation and those from QM calculations using the formalism detailed in Section 6.2 is shown in the top and bottom panels of Figure 6.5 for spin-conserving, $\bar{\Omega} = 3/2 \rightarrow \bar{\Omega}' = 3/2$, and spin-orbit changing collisions, $\bar{\Omega} = 3/2 \rightarrow \bar{\Omega}' = 1/2$, respectively. In this figure, the left and right panels correspond to collisions leading to e and f final Λ-doublet states, respectively. In addition, within each panel, the two sets of experimental data obtained with single and double hexapole selection are also shown, along with their respective theoretical simulations. The theoretical results for the OH($j = 3/2$, $\bar{\Omega} = 3/2$) initial state have been calculated by weighting the contribution of the $\bar{m}_E = 1/2$ and $3/2$ states shown in Figure 6.4 according to the experimental conditions: 1:2.6 for the single hexapole, and 1:15.8 for the

double hexapole [199, 200]. In the two cases, the values of the mixing parameters are different for the two $\bar{m}_E$ states. For $\bar{m}_E = 1/2$, $|\alpha| = 0.66$ and $|\beta| = 1.25$, whilst for $\bar{m}_E = 3/2$, $|\alpha| = 0.88$ and $|\beta| = 1.10$ at an electric field strength of $E = 7.5\,\mathrm{kV\,cm^{-1}}$. Note that in the original article by van Beek *et al.*[200], the α and β coefficients are exchanged with respect to those used here, and in addition their parameters are normalised to $\alpha^2 + \beta^2 = 1$, whereas the sum of the squares used in this work is 2. With these parameters, average orientations of $\langle\cos\Theta_{\mu E}\rangle_{1/2} = 0.162$ and $\langle\cos\Theta_{\mu E}\rangle_{3/2} = 0.574$ are achieved. As can be seen in Figure 6.3, not only the average orientation but also the resulting distributions of internuclear axes are remarkably different. The average orientation (including both $\bar{m}_E$ states) with the double hexapole ($\langle\cos\Theta_{\mu E}\rangle = 0.549$) is higher than with the single hexapole ($\langle\cos\Theta_{\mu E}\rangle = 0.458$) due to the larger proportion of molecules in the more highly oriented $\bar{m}_E = 3/2$ state. For comparison, at the limit of an infinite field with the pure $\bar{m}_E = 3/2$ state, the maximal orientation achievable is $\langle\cos\Theta_{\mu E}\rangle^{\infty}_{3/2} = 0.6$. The resulting distribution of internuclear axes is shown at infinite field and under experimental conditions in Figure 6.3; they are almost identical.

For spin-orbit conserving collisions, the agreement between the experimental results and the QM calculations is fairly good for both final Λ-doublet states and, as expected, the QM data presented here are practically identical to the QM results shown in ref. [200] using the same PES. In principle, it is expected that the absolute magnitude of ISAs should be larger for the double hexapole than for the single hexapole experiments due to the increase in orientation achieved in this experimental setup[200]. This is experimentally observed for the spin-orbit conserving, final e state, however, the trend appears to be reversed for larger transitions to the final f state. This is attributed to the small integral cross sections of these states along with the residual population of these states which pass through the hexapole[200]. van Beek *et al.* have also studied the steric effect in the spin-orbit changing collisions of OH($j = 3/2$, $\bar{\Omega} = 3/2$) $\rightarrow$ OH($\bar{\Omega}' = 1/2$)[200, 201], whose comparison with present QM results is shown in the bottom panels for final f and e states. The

agreement with the present theoretical calculations is also fairly good, comparable to that obtained for $\bar{\Omega}$ conserving collisions.

Returning to Figure 6.4, the next thing to consider is the z-axis polarised steric asymmetry for OH + Ar for spin-orbit conserving transitions. For both values of $\bar{m}_E$ the value of $S(z)$ decreases with increasing rotational energy transfer, although its value is considerably less negative for $j' > 7/2$ with $\bar{m}_E = 1/2$, due to the lower degree of orientation as a consequence of the distribution of axes not being strictly along the z-axis (see Figure 6.3). The results indicate a very slight preference for O-end collisions (positive $S(z)$) for low rotational energy transfer collisions, $j' \leq 7/2$, but a definitively stronger preference for H-end collisions (negative $S(z)$) at higher j' values. This may be explained via largely classical mechanisms. The potential at the H-end of the molecule extends much further from the COM than the O-end of the molecule. Hence, collisions occurring when Ar approaches the H-end are able to produce more torque, resulting in greater rotational excitation. Meanwhile, trajectories approaching the O-end of the molecule almost hit the COM of the molecule and therefore cannot lead to rotational energy transfer into high rotational states. The steric effect depends on the final Λ-doublet of the transition (unlike the collisions of NO with Ar [22, 195]); $S(z)$ takes more negative values for transitions into the final e state than for transitions into the final f state. This is observed more strongly for $\bar{m}_E = 1/2$ than for $\bar{m}_E = 3/2$, and also increases as a function of Δj. There is currently no simple explanation for this behaviour[202]. The trend is also observed in the experimental data of ter Meulen and coworkers[200].

The magnitude of $S(z/x)$ is similar in the case of the orientation along the z- and x-axes, and both also follow a roughly similar, monotonic trend with respect to Δj. The x-axis steric effect (see the lower panels of Figure 6.4) also depends on the final Λ-doublet state of the transition, again somewhat more strongly for the $\bar{m}_E = 1/2$ state than for the $\bar{m}_E = 3/2$ state, with a larger difference observed for larger rotational energy transfer. The theoretical predictions indicate that $S(x)$ becomes negative (preference for H-end collisions) at lower j' values but at the highest j' it levels off. The trend observed for the x-axis steric effect may be understood in a

similar way to that of the z-axis, based upon differences in the PES of the OH + Ar collision. Collisions corresponding to $+x/-x$ scattering are equivalent to repulsive 'near-side' collisions at the O/H-ends of the molecule; as such the preference for H-end collisions at high j' may be understood in terms of the larger extension of the potential as in the z-axis case. Similarly, for low rotational energy transfer, where the attractive parts of the potential are important in determining the scattering dynamics, the small negative value of $S(x)$ may be understood in terms of the preference for attractive 'far-side' scattering off the H-end of the molecule where the attractive part of the potential extends further.

The QM DCSs for the inelastic scattering of $\mathrm{OH}(\mathrm{X}^2\Pi_{1/2})$ + Ar for the $|j = 3/2, \bar{m}_E = 3/2, \bar{\Omega} = 1/2, E = \infty\rangle \rightarrow |\bar{\Omega}', \epsilon' = 3/2, e\rangle$ transitions are shown in Figure 6.6, for $j' = 5/2 - 11/2$ at $746\,\mathrm{cm}^{-1}$ collision energy.

In each case, the DCSs for (preferable) parallel and anti-parallel orientation of $\boldsymbol{r}$ along the x- and z-axes are shown, alongside that for orientation along the y-axis, which is equivalent in the $+y$ and $-y$ directions, as only alignment terms, not orientation terms, contribute. In each figure, the DCS in an isotropic electric field, the average of the DCS for initial e and f states, is also shown.

The general trends observed in the differential steric effect are essentially independent of the x- or z- choice of orientation axis. In both cases, collisions imparting substantial rotational energy transfer occur with the H-end of the molecule, leading to sideways scattering for intermediate j', and to backwards scattering for the highest j'. Furthermore, fast diffraction oscillations alongside glory scattering at extreme forward scattering angles ($0° \leq \theta \leq 20°$) are also observed for both z and x polarisations. The z-axis oriented DCSs in Figure 6.6, as in the case of the integral steric effect, show an increasing preference for H-end orientation as a function of increasing rotational state to the point that, for $j' = 11/2$, $\mathrm{d}\sigma_{\mathrm{O}} - \mathrm{d}\sigma_{\mathrm{H}} \approx -\mathrm{d}\sigma_{\mathrm{H}}$. This feature was observed in terms of the integral steric asymmetry, and can be explained by resorting to the classical mechanisms discussed with respect to $S(z)$. Since the COM of the molecule almost lies on the O atom and the potential dies off very quickly around this atom, head-on collisions with the O-end of the OH molecule

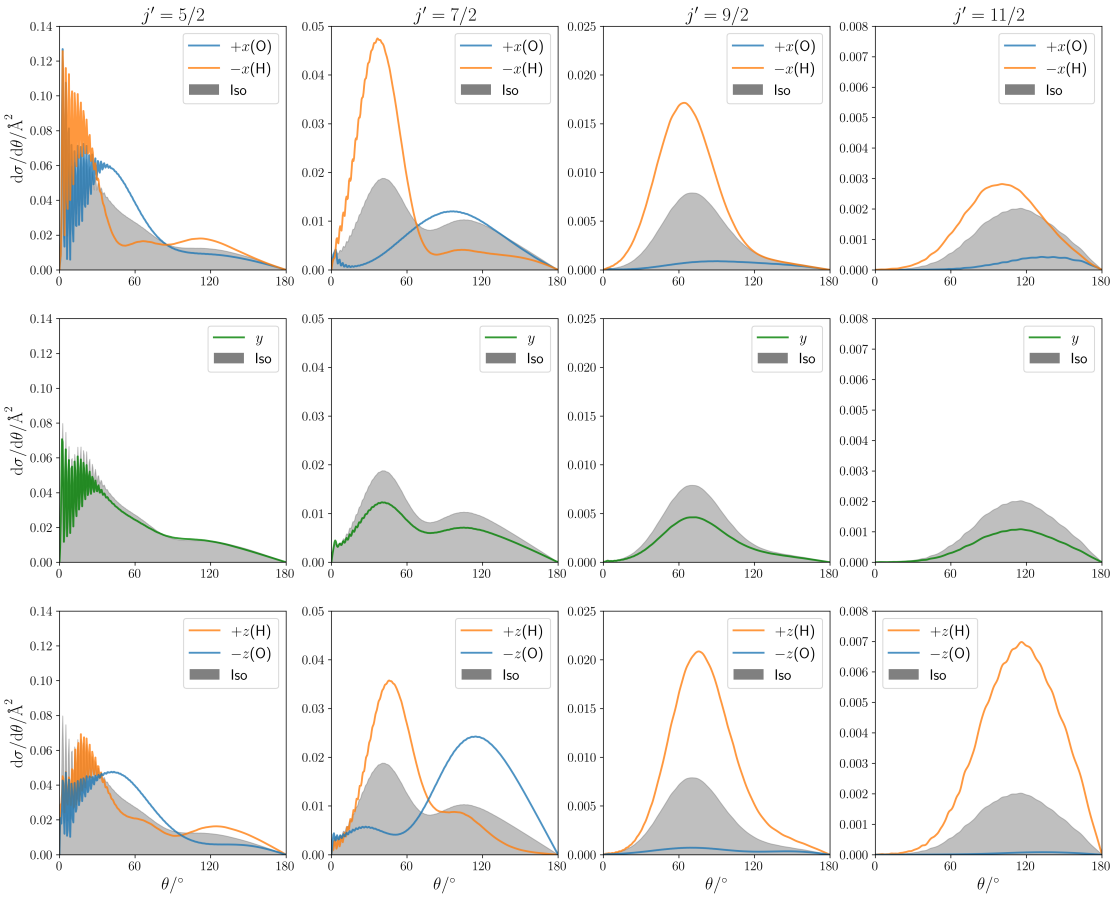

Figure 6.6: Differential cross sections for the energetically accessible j', e final states of the OH(X) + Ar system at a collision energy of 746 cm^{-1}, in the high-field limit ($\alpha = \beta = 1$), starting from the $|\bar{\Omega} = 3/2, j = 3/2, \bar{m}_E = 3/2\rangle$ initial state. The top row in each panel is for orientation along the x-axis: $+x$(O) and $-x$(H) are shown in blue and orange, respectively. The middle row shows orientation along the y-axis, in which the $+y$ and $-y$ orientations are equivalent. The bottom row shows orientation along the z-axis: $+z$(H) and $-z$(O) data are shown in blue and orange, respectively. The isotropic DCS, proportional to $R_0^{(0)}(\theta)$, in each case is indicated by the grey shaded area.

are largely ineffective in achieving rotational energy transfer, whilst collisions with the H-end of the molecule give rise to torques that cause the rotation of the molecule much more readily. It is worth noting that, as has previously been observed in the bond-oriented collisions of NO(X)[22, 195], the same features are observed in the DCSs for both the z-axis orientations, however the intensity of these peaks varies for the two orientations. Unlike the case of NO(X), the position of the peaks in the DCS are shifted relative to one another for intermediate and high Δj.

While the x-axis oriented DCSs exhibit similar features to those of the z-axis

polarisation, since the same $R_0^{(0)}(\theta)$ term in Eq. (6.37) is at work, some differences are observed related to differences in the $R_0^{(1)}(\theta)$ and $R_1^{(1)}(\theta)$ moments that account for the differential steric asymmetry effect when the OH bond is oriented along either the z- or x-axis, respectively. As in the integral steric effect, a preponderance of scattering with H-side orientation (with the electric field along $-x$) with respect to the O-side orientation (electric field along $+x$) is observed with increasing j', corresponding to an increasing preference for repulsive 'near-side' collisions at the H-side of the molecule, where the extent of the repulsive potential is larger. The shift in peak position for the $\pm x$ orientations may be rationalised in a similar way to that discussed in terms of the z-axis, in which more 'head-on' trajectories are required to achieve rotational energy transfer at the O-side of the molecule into the same state, leading to more backwards scattering. Note that the difference between scattering from these two 'side-on' orientations is not as large in comparison to scattering in the two 'end-on' orientations, as observed for the integral steric effect in Figure 6.4. This implies the preference for scattering off of the H- or O-ends of the OH molecule are less strong when the atom approaches the side of the molecule. For the $j' = 5/2$ transition, a strong preference for O-side (with the field aligned along $+x$) scattering is observed in the forward scattered region, along with oscillations that are sharper than those found for the z orientation. The diffraction patterns correspond to attractive 'far-side' collisions at the H-end of the molecule caused by the larger extent of the attractive part of the potential at the H-end of the molecule compared to the O-end. This is not surprising since, for side-on collisions, Fraunhofer diffraction is expected to be more prominent due to the larger area of the NO molecule in the xy plane[76].

6.4 Conclusions and Outlook

A general formalism has been presented to describe the stereodynamics of a $^2\Pi$ molecule oriented in an electric field and colliding with a rare gas or an unoriented molecule. Its utility and versatility has then been displayed through a set of specific examples, helping to provide insights into how the anisotropy of the PES produces

different outcomes upon the sampling of different regions. This is a powerful tool to assist in the unravelling of steric effects in reaction dynamics.

The equations presented are applicable to other molecules with closely-spaced energy levels of opposite parity, such as symmetric top and near-symmetric top molecules. However, in many cases, states above the ground state will also be oriented at electric field strengths used to orient the initial state. Hence, the product states would be oriented too, something which is not touched upon here. Therefore the theory presented here would need to be developed further.

A limitation of this framework derives from its assumption that the only consequence of the Stark effect in the electric is to produce a superposition of the Λ-doublet states. However, in reality there will be other effects, such as some mixing in of other j states and the energy shift in the energy levels. These, effects would change the values of the scattering amplitudes and allow greater values of k in the expansion of the DCS. However, at the electric filed strengths dealt with here ($\leq 10\,\mathrm{kV\,cm^{-1}}$), and the collision energies considered ($\geq 100\,\mathrm{cm^{-1}}$), these effects are negligible. In fact, if the dipole moment of the molecule is small enough, as for NO, these effects are negligible down to collision energies on the order of $1\,\mathrm{cm^{-1}}$[203].

Moving forward to more complex systems, i.e. those with two polarised molecules, this formalism can be expanded further. In that case, it could be that both molecules have their initial angular momenta polarised, or their initial bond axis distributions polarised, or a combination of the two. An extension to such systems would represent a step-change towards systems with more relevance to real world applications. A first example of this is shown in Chapter 7.

7

Stereodynamics of Two Oriented Molecules

Contents

7.1 Introduction

To fully harness stereodynamic control in a collision between two molecules, both collision partners must be independently oriented or aligned before the scattering process. While there is literature investigating how scattering outcomes may be influenced by polarisation of one molecule in molecule-molecule scattering[204–211], mostly at low energies, there is scant research into how polarising both molecules simultaneously affects the collision.

In recent years, there has been an increased focus on the potential of simultaneous polarisation. Experiments have been conducted on the scattering of two aligned D_2 molecules [43, 44]. Theoretical studies of the same system have since also been completed[212, 213]. However, this system has an extra degree of symmetry compared to two distinguishable molecules (aligning one molecule one way will have the same effect as aligning the other molecule the same way), and the experimental studies discussed also have the restriction of both molecules having to be aligned in the same direction. Hence, there is still a path to tread towards full stereodynamic control.

In this chapter, a potential experiment will be posited that could allow the experimental study of two independently oriented, distinguishable molecules. A mathematical description of the stereodynamic effects of this scattering will be derived before it used in two theoretical studies, similar to the proposed experiment, to explain and display its power. One study will focus on effects in low energy collisions in the resonance regime, while the other investigates what effects might be seen at higher collision energies.

7.2 Proposed Experiment

An experiment to study a system in which both molecules are polarised can be devised by combining elements of two experiments which have already been performed. The first of these experiments is the crossed molecular beam apparatus around which Chapters 4 and 6 are based, and which was described in Section

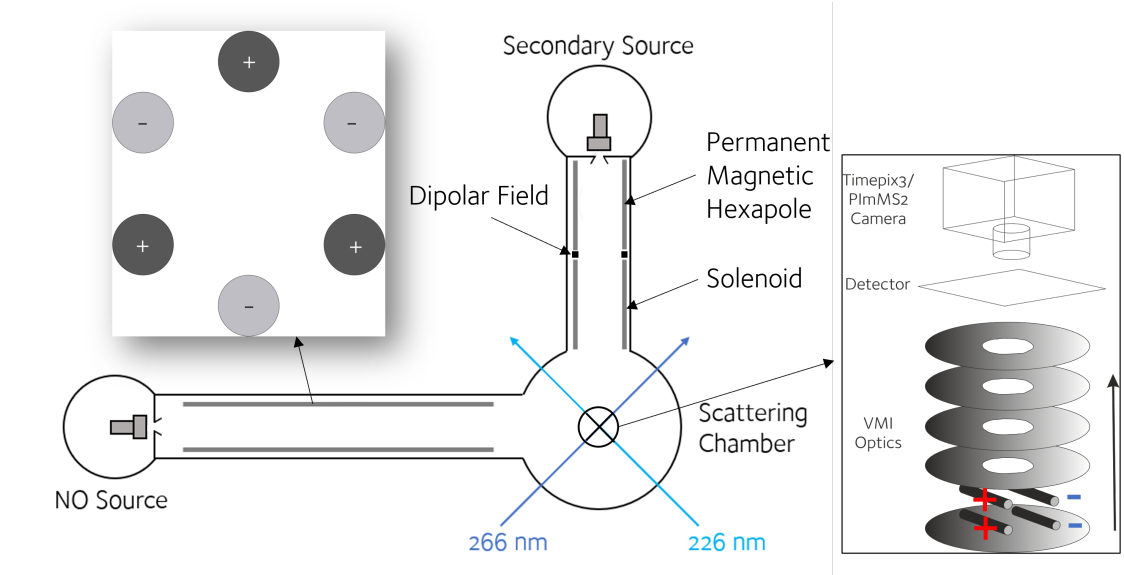

Figure 7.1: A schematic of the proposed experiment combining elements of the crossed molecular beam machine in Oxford, with a molecular beam arm of the sort developed by Alexandrowicz and coworkers [214–217].

3.3. This apparatus provides most of the infrastructure required, including the ability to orient one molecule using an electric field, and a detection system through REMPI-VMI.

The second relevant experiment is the surface scattering experiments of Alexandrowicz and coworkers[214–217], in which magnetic field manipulation is used to produce orientation of the angular momentum of H_2 or D_2. This method uses a permanent magnetic hexapole to state select specific m states for a given j, by interacting with the magnetic moment of the molecule due to rotation when $j \neq 0$. A dipolar field is then placed after the end of the hexapole to define the quantisation axis, in much the same way the rods act in the bond axis orientation experiment using electric fields. Hence, at this stage the molecule remains in pure m states (with some bias in their populations). The molecules then move adiabatically into a solenoid which produces a magnetic field antiparallel to the molecular beam propagation direction, such that initially the molecules are in superpositions of states along the new quantisation axis in the direction of the magnetic field. The density matrix of these molecules then evolves in a predictable way, depending on the strength of the magnetic field, which can be calculated using the Hamiltonian of Ramsey[218].

One can then model the m state populations using the quantisation axis of the dipolar field, propagating the molecular beam to the interaction region. By choosing a specific strength magnetic field produced by the solenoid, a chosen bias of m states can be propagated to the interaction region, giving orientation of the angular momentum of the molecule on collision.

The most obvious system this setup could be used to study would be NO(X, $j = 1/2$) + H_2 in $j = 1$, but other molecules could have their bond axis oriented, and the H_2 could be replaced by D_2 or another closed shell diatomic.

7.3 Classical Description

Classically, a scattering angular distribution in a system in which two vectors are polarised, as well as $\boldsymbol{k}$ and $\boldsymbol{k}'$, may be given

$$P(\theta, \theta_\mathrm{A}, \phi_\mathrm{A}, \theta_\mathrm{B}, \phi_\mathrm{B}) = \sum_{\substack{k_\mathrm{A}, q_\mathrm{A} \\ k_\mathrm{B}, q_\mathrm{B}}} \frac{(2k_\mathrm{A}+1)(2k_\mathrm{B}+1)}{16\pi^2} [X^{(k_\mathrm{A},k_\mathrm{B})}_{q_\mathrm{A}\cdot q_\mathrm{B}}(\theta)]^* \\ C_{k_\mathrm{A}q_\mathrm{A}}(\theta_\mathrm{A}, \phi_\mathrm{A}) C_{k_\mathrm{B}q_\mathrm{B}}(\theta_\mathrm{B}, \phi_\mathrm{B}) \tag{7.1}$$

where $X^{(k_\mathrm{A},k_\mathrm{B})}_{q_\mathrm{A}\cdot q_\mathrm{B}}(\theta)$ is a generic 4-vector normalised PDDCS, and θ_x and ϕ_x are the angles that describe the polarisation of each initial vector in the scattering frame. Classically, the moments of a multipolar expansion are the expectation values of the multipole, in this case a product of spherical harmonics. This can be represented by

$$\begin{aligned} X^{(k_\mathrm{A},k_\mathrm{B})}_{q_\mathrm{A}\cdot q_\mathrm{B}}(\theta) &= \int_0^{2\pi}\int_0^{2\pi}\int_{-1}^{1}\int_{-1}^{1} P(\theta, \theta_\mathrm{A}, \phi_\mathrm{A}, \theta_\mathrm{B}, \phi_\mathrm{B}) \\ &\qquad C_{k_\mathrm{A}q_\mathrm{A}}(\theta_\mathrm{A}, \phi_\mathrm{A}) C_{k_\mathrm{B}q_\mathrm{B}}(\theta_\mathrm{B}, \phi_\mathrm{B}) \mathrm{d}(\cos\theta_\mathrm{A}) \mathrm{d}(\cos\theta_\mathrm{B}) \mathrm{d}\phi_\mathrm{A} \mathrm{d}\phi_\mathrm{B} \\ &= \langle C_{k_\mathrm{A}q_\mathrm{A}}(\theta_\mathrm{A}, \phi_\mathrm{A}) C_{k_\mathrm{B}q_\mathrm{B}}(\theta_\mathrm{B}, \phi_\mathrm{B}) \rangle \,. \end{aligned} \tag{7.2}$$

The vectors $\boldsymbol{A}$ and $\boldsymbol{B}$ are both polarised by some external forces. These forces are labelled $\boldsymbol{Y}$ and $\boldsymbol{Z}$ respectively. The polarisations of $\boldsymbol{A}$ and $\boldsymbol{B}$ can be evaluated using the equation

$$P(\theta_x, \phi_x) = \sum_{k_x} \frac{(2k_x + 1)}{4\pi} \sum_{q_x} a_{q_x}^{(k_x)} C^*_{k_x q_x}(\theta_x, \phi_x) \tag{7.3}$$

where

$$a_{q_x}^{(k_x)} = \int_0^{2\pi} \int_{-1}^{1} P(\theta_x, \phi_x) C_{k_x q_x}(\theta_x, \phi_x) \mathrm{d}\cos\theta_x \mathrm{d}\phi_x \,. \tag{7.4}$$

These may be convoluted with Eq. 7.1 to give a scattering angular distribution, which is dependent of the degree of polarisation of the vectors $\boldsymbol{A}$ and $\boldsymbol{B}$. This is done using the equation

$$\begin{aligned} P(\theta) = &\int_0^{2\pi} \int_0^{2\pi} \int_{-1}^{1} \int_{-1}^{1} 16\pi^2 P(\theta, \theta_\mathrm{A}, \phi_\mathrm{A}, \theta_\mathrm{B}, \phi_\mathrm{B}) \\ &P(\theta_\mathrm{A}, \phi_\mathrm{A}) P(\theta_\mathrm{B}, \phi_\mathrm{B}) \mathrm{d}(\cos\theta_\mathrm{A}) \mathrm{d}(\cos\theta_\mathrm{B}) \mathrm{d}\phi_\mathrm{A} \mathrm{d}\phi_\mathrm{B} \\ = &\sum_{\substack{k_A, q_A \\ k_B, q_B}} \sum_{\substack{k'_A, q'_A \\ k'_B, q'_B}} \frac{(2k_A + 1)(2k_B + 1)(2k'_A + 1)(2k'_B + 1)}{16\pi^2} [X^{(k_\mathrm{A}, k_\mathrm{B})}_{q_\mathrm{A}. q_\mathrm{B}}(\theta)]^* a^{(k'_A)}_{q'_A} a^{(k'_B)}_{q'_B} I \end{aligned} \tag{7.5}$$

where

$$\begin{aligned} I = &\int_0^{2\pi} \int_{-1}^{1} C_{k_A, q_A}(\theta_\mathrm{A}, \phi_\mathrm{A}) C^*_{k'_A, q'_A}(\theta_\mathrm{A}, \phi_\mathrm{A}) \mathrm{d}(\cos\theta_\mathrm{A}) \mathrm{d}\phi_\mathrm{A} \\ &\int_0^{2\pi} \int_{-1}^{1} C_{k_B, q_B}(\theta_\mathrm{B}, \phi_\mathrm{B}) C^*_{k'_B, q'_B}(\theta_\mathrm{B}, \phi_\mathrm{B}) \mathrm{d}(\cos\theta_\mathrm{B}) \mathrm{d}\phi_\mathrm{B} \\ = &\frac{16\pi^2}{(2k_A + 1)(2k_B + 1)} \delta_{k_A k'_A} \delta_{q_A q'_A} \delta_{k_B k'_B} \delta_{q_B q'_B} \,. \end{aligned} \tag{7.6}$$

This then finally becomes

$$P(\theta) = \sum_{k_A, k_B} (2k_A + 1)(2k_B + 1) \sum_{q_A, q_B} [X^{(k_\mathrm{A}, k_\mathrm{B})}_{q_\mathrm{A}. q_\mathrm{B}}(\theta)]^* a^{(k_A)}_{q_A} a^{(k_B)}_{q_B} \,. \tag{7.7}$$

To obtain the differential cross section, one multiplies by the integral cross section when forces $\boldsymbol{Y}$ and $\boldsymbol{Z}$ are isotropic in nature, σ_iso, and divide by 2π, yielding

$$\frac{\mathrm{d}\sigma}{\mathrm{d}\omega}(\theta) = \frac{\sigma_\mathrm{iso}}{2\pi} \sum_{k_A, k_B} (2k_A + 1)(2k_B + 1) \sum_{q_A, q_B} [X^{(k_\mathrm{A}, k_\mathrm{B})}_{q_\mathrm{A}. q_\mathrm{B}}(\theta)]^* a^{(k_A)}_{q_A} a^{(k_B)}_{q_B} \,. \tag{7.8}$$

7.4 Quantum Mechanical Description

7.4.1 Density Matrix Theory

In a situation in which the angular momentum of a molecule is oriented, it becomes key when analysing the quantum mechanics to understand the concept of the density matrix.

There are two types of states in quantum mechanics: a pure state and a mixed state. A pure state is any state which can described as a coherent superposition of states in a given basis set. These pure states can therefore be represented as a wavefunction produced from a linear combination of the basis state wavefunctions[178]

$$\psi_n = \sum_m a_m^{(n)} \phi_m \tag{7.9}$$

where ϕ_m is the wavefunction of basis state m and $a_m^{(n)}$ is the expansion coefficient of pure state n in term of basis state m.

A mixed state, on the other hand, is a combination of these pure states added together with statistical weights. Hence, incoherent superposition occurs in these states. This makes representation by a wavefunction impossible. Instead, these states must be described using a density matrix. The density operator, $\hat{\rho}$, is defined

$$\hat{\rho} = \sum_n W_n |\psi_n\rangle\langle\psi_n| \tag{7.10}$$

where n represents all the pure states contributing to the state being described and W_n is the statistical weight of state n. Converting Eq. (7.9) to vector space and inserting into Eq. (7.10), one instead obtains for the density operator

$$\hat{\rho} = \sum_n W_n a_m^{(n)} a_{m'}^{(n)*} |\phi_m\rangle\langle\phi_{m'}| \tag{7.11}$$

where the dummy variables m and m' have been used for each iteration of the pure state ψ_n. Elements of the density matrix may then be expressed as

$$\langle\phi_m|\hat{\rho}|\phi_{m'}\rangle = \sum_n W_n a_m^{(n)} a_{m'}^{(n)*} . \tag{7.12}$$

This formulation allows one to make certain inferences about the form of the density matrix for different sorts of states. In the case of a pure state, the index n would represent only one state with a statistical weight $W_n = 1$. Hence, diagonal elements would be the complex square of the expansion coefficients, while the off-diagonal elements refer to the complex products of expansion coefficients of different basis states. These off-diagonal elements, therefore, give an indication of the level of coherence in the superposition of the basis states. At the extreme other end, a mixed state which is a completely incoherent superposition of the basis states will be a diagonal matrix. As both pure and mixed states may be represented using a density matrix, but only pure states may be expressed as wavefunctions, the density matrix is the more general form of representing a state.

In density matrix theory, the expectation value of an operator $\hat{A}$ is given by

$$\langle \hat{A} \rangle = \frac{\mathrm{tr}(\hat{\rho}\hat{A})}{\mathrm{tr}(\hat{\rho})} \tag{7.13}$$

allowing the extraction of measurables from the state.

7.4.2 Oriented Cross Sections

The differential cross section when one molecule, A, has its bond axis oriented in an electric field, $\boldsymbol{E}$ whilst simultaneously another molecule, B, has its angular momentum oriented using a magnetic field, $\boldsymbol{\mathcal{B}}$ (which in the experiment posited in Section 7.2 would point in the direction of the dipolar magnetic field), starting from a given magnetic quantum number of molecule A[28] is given by

$$\mathrm{d}\sigma(m_{\mathrm{A},E}) = \sum_{\substack{m'_{\mathrm{A}} m'_B \\ m_{\mathrm{B},\mathcal{B},1} \\ m_{\mathrm{B},\mathcal{B},2}}} F_{m'_{\mathrm{A}},m'_B,m_{\mathrm{A},E},m_{\mathrm{B},\mathcal{B},1},E}(\theta) F^*_{m'_{\mathrm{A}},m'_B,m_{\mathrm{A},E},m_{\mathrm{B},\mathcal{B},2},E}(\theta) \langle j_B m_{\mathrm{B},\mathcal{B},1} | \hat{\rho} | j_B m_{\mathrm{B},\mathcal{B},2} \rangle \tag{7.14}$$

where m'_{A} and m'_B are the final magnetic quantum numbers for molecules A and B respectively, $m_{\mathrm{A},E}$ is the initial magnetic quantum number of molecule A using the electric field vector $\boldsymbol{E}$ as the quantisation axis, while $m_{\mathrm{B},\mathcal{B},1\,\mathrm{or}\,2}$ are the possible

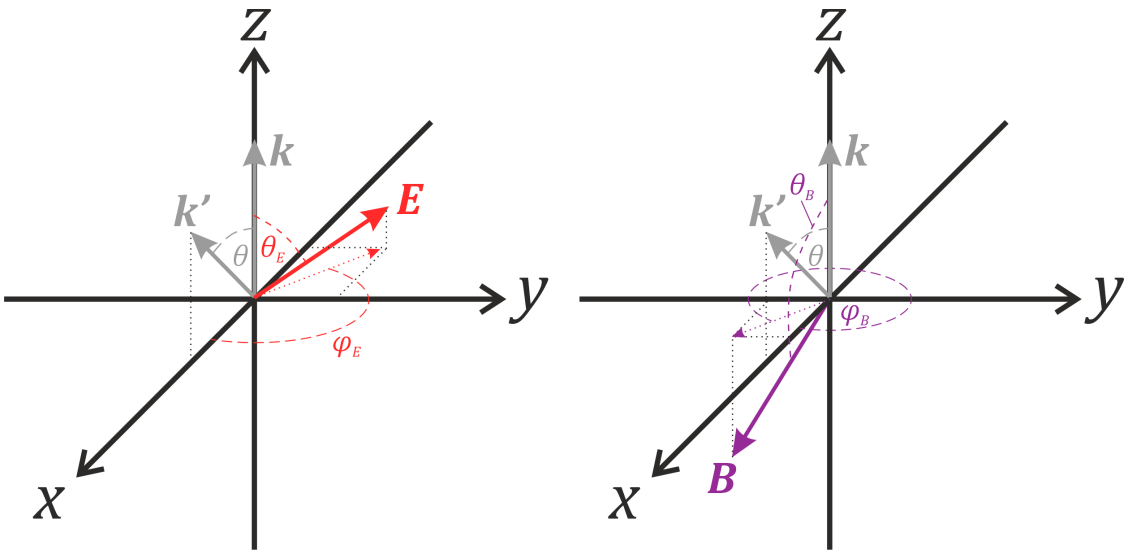

Figure 7.2: The definition of the scattering frame used in this chapter. The angles θ_E and ϕ_E are the polar and azimuthal angles of the electric field vector $\boldsymbol{E}$, and $\theta_\mathcal{B}$ and $\phi_\mathcal{B}$ are the polar and azimuthal angles of the magnetic field vector, $\boldsymbol{\mathcal{B}}$. These angles then each link to a frame in which these vectors point along the z-axis, allowing a definition in which these vectors are the quantisation axes for molecules A and B respectively.

values of $m_{\mathrm{B},\mathcal{B}}$, the magnetic projection of molecule B on the quantization axis used for orientation. The quantity inside the angled brackets is a density matrix element. $F_{m'_\mathrm{A},m'_B,m_{\mathrm{A},E},m_{\mathrm{B},\mathcal{B},E}}(\theta)$ is given by the equation

$$F_{m'_\mathrm{A},m'_B,m_{\mathrm{A},E},m_{\mathrm{B},\mathcal{B},E}}(\theta) = \frac{1}{\sqrt{2}} \sum_{m_\mathrm{A} m_\mathrm{B}} D^{j_A}_{m_\mathrm{A} m_{\mathrm{A},E}}(\phi_E, \theta_E, 0) D^{j_B}_{m_\mathrm{B} m_{\mathrm{B},\mathcal{B}}}(\phi_\mathcal{B}, \theta_\mathcal{B}, 0) \\ [\alpha f_{m'_\mathrm{A},m'_B,m_A,m_{B,e}}(\theta) + \beta f_{m'_\mathrm{A},m'_B,m_A,m_{B,f}}(\theta)] \qquad (7.15)$$

where $D^j_{m'm}(\alpha,\beta,\gamma)$ are Wigner rotation matrix elements (henceforth written $D^j_{m'm}$) for which θ_E and ϕ_E are the polar and azimuthal angles describing the direction of the electric field in the scattering frame, and $\theta_\mathcal{B}$ and $\phi_\mathcal{B}$ are the equivalent angles for the magnetic field (see Figure 7.2). $f_{m'_\mathrm{A},m'_B,m_A,m_{B,\epsilon}}(\theta)$ are the field free scattering amplitudes for each Λ-doublet state given in Eq. (2.22), and α and β are the expansion coefficients for the e and f state respectively normalised such that $\alpha^2 + \beta^2 = 2$.

Inserting Eq. 7.15 into Eq. 7.14 gives

$$\begin{aligned}\mathrm{d}\sigma(m_{\mathrm{A},E}) = \frac{1}{2} \sum_{\substack{m'_{\mathrm{A}} m'_B \\ m_{A,1} m_{A,2} \\ m_{B,1} m_{B,2} \\ m_{\mathrm{B},\mathcal{B},1} \\ m_{\mathrm{B},\mathcal{B},2}}} \Big[& \alpha^2 D^{j_A}_{m_{A,1} m_{\mathrm{A},E}} D^{j_B}_{m_{B,1} m_{\mathrm{B},\mathcal{B},1}} D^{j_A *}_{m_{A,2} m_{\mathrm{A},E}} D^{j_B *}_{m_{B,2} m_{\mathrm{B},\mathcal{B},2}} F_{1e} F^*_{2e} \\ & + \alpha\beta\, D^{j_A}_{m_{A,1} m_{\mathrm{A},E}} D^{j_B}_{m_{B,1} m_{\mathrm{B},\mathcal{B},1}} D^{j_A *}_{m_{A,2} m_{\mathrm{A},E}} D^{j_B *}_{m_{B,2} m_{\mathrm{B},\mathcal{B},2}} \left(F_{1f} F^*_{2e} + F_{1e} F^*_{2f} \right) \\ & + \beta^2 D^{j_A}_{m_{A,1} m_{\mathrm{A},E}} D^{j_B}_{m_{B,1} m_{\mathrm{B},\mathcal{B},1}} D^{j_A *}_{m_{A,2} m_{\mathrm{A},E}} D^{j_B *}_{m_{B,2} m_{\mathrm{B},\mathcal{B},2}} F_{1f} F^*_{2f} \Big] \\ & \langle j_B m_{\mathrm{B},\mathcal{B},1} | \hat{\rho} | j_B m_{\mathrm{B},\mathcal{B},2} \rangle \,. \end{aligned} \tag{7.16}$$

where the shorthand $F_{a\epsilon} = f_{m'_{\mathrm{A}}, m'_B, m_{A,a}, m_{B,a}, \epsilon}(\theta)$ is used.

The relationship [125]

$$D^j_{m'_1 m_1} D^{j*}_{m'_2 m_2} = (-1)^{m'_2 - m_2} \sum_{kq} (-1)^q \langle j m'_1, j - m'_2 | kq \rangle \langle j m_1, j - m_2 | k0 \rangle C_{k-q}(\theta, \phi) \tag{7.17}$$

may be altered using the properties of Clebsch-Gordan coefficients to give

$$\begin{aligned} D^j_{m'_1 m_1} D^{j*}_{m'_2 m_2} = \sum_{kq} (-1)^{2j+q-m'_1-m_1+m'_2-m_2} & \frac{2k+1}{2j+1} \\ & \langle j m'_1, k-q | j m'_2 \rangle \langle j m_1, k0 | j m_2 \rangle C_{k-q}(\theta, \phi) \,. \end{aligned} \tag{7.18}$$

Using a further property of Clebsch-Gordan coefficients, we can ascertain that $q = m'_1 - m'_2$ and $m_1 = m_2$ for non-zero terms. Hence

$$D^j_{m'_1 m_1} D^{j*}_{m'_2 m_2} = (-1)^{2(j-m_1)} \sum_{kq} \frac{2k+1}{2j+1} \langle j m'_1, k-q | j m'_2 \rangle \langle j m_1, k0 | j m_2 \rangle C_{k-q}(\theta, \phi) \,. \tag{7.19}$$

and as $(j - m_1)$ is an integer

$$D^j_{m'_1 m_1} D^{j*}_{m'_2 m_2} = \sum_{kq} \frac{2k+1}{2j+1} \langle j m'_1, k-q | j m'_2 \rangle \langle j m_1, k0 | j m_2 \rangle C_{k-q}(\theta, \phi) \,. \tag{7.20}$$

.

Now we can rewrite Eq. 7.16 as

$$\begin{aligned}
\mathrm{d}\sigma(m_{\mathrm{A},E}) = \frac{1}{2} \sum_{\substack{m'_{\mathrm{A}} m'_B \\ m_{A,1} m_{A,2} \\ m_{B,1} m_{B,2} \\ m_{\mathrm{B},\mathcal{B},1} \\ m_{\mathrm{B},\mathcal{B},2}}} \sum_{\substack{k_{\mathrm{A}}, q_{\mathrm{A}} \\ k_{\mathrm{B}}, q_{\mathrm{B}}}} \frac{(2k_{\mathrm{A}}+1)(2k_{\mathrm{B}}+1)}{(2j_A+1)(2j_B+1)} \\
\langle j_A m_{A,1}, k_{\mathrm{A}} - q_{\mathrm{A}} | j_A m_{A,2} \rangle \langle j_B m_{B,1}, k_{\mathrm{B}} - q_{\mathrm{B}} | j_B m_{B,2} \rangle \\
\langle j_A m_{\mathrm{A},E}, k_{\mathrm{A}} 0 | j_A m_{\mathrm{A},E} \rangle \langle j_B m_{\mathrm{B},\mathcal{B},1}, k_{\mathrm{B}} 0 | j_B m_{\mathrm{B},\mathcal{B},2} \rangle C_{k_{\mathrm{A}} - q_{\mathrm{A}}}(\theta_E, \phi_E) \\
C_{k_{\mathrm{B}} - q_{\mathrm{B}}}(\theta_{\mathcal{B}}, \phi_{\mathcal{B}}) \left[\alpha^2 F_{1e} F^*_{2e} + \alpha\beta \left(F_{1f} F^*_{2e} + F_{1e} F^*_{2f} \right) + \beta^2 F_{1f} F^*_{2f} \right] \\
\langle j_B m_{\mathrm{B},\mathcal{B},1} | \hat{\rho} | j_B m_{\mathrm{B},\mathcal{B},2} \rangle
\end{aligned} \tag{7.21}$$

After state selection with a hexapole, the initial magnetic quantum number selected is $\pm|m_{\mathrm{A},E}|$. Hence the differential cross section is determined as an average of these states

$$\mathrm{d}\sigma(|m_{\mathrm{A},E}|) = \frac{1}{2} \left[\mathrm{d}\sigma(m_{\mathrm{A},E}) + \mathrm{d}\sigma(-m_{\mathrm{A},E}) \right] \tag{7.22}$$

where $\alpha\beta > 0$ when $m_{\mathrm{A},E} < 0$ and $\alpha\beta < 0$ when $m_{\mathrm{A},E} > 0$. We can then split up the terms of the DCS into the two incoherent terms and the coherent term

$$\mathrm{d}\sigma(|m_{\mathrm{A},E}|) = T_{ee} + T_{ef} + T_{ff} \tag{7.23}$$

The coherent term concerning the e Λ-doublet, T_{ee}, is given by

$$\begin{aligned}
T_{ee} = \frac{1}{4} \sum_{\substack{m'_{\mathrm{A}} m'_B \\ m_{A,1} m_{A,2} \\ m_{B,1} m_{B,2} \\ m_{\mathrm{B},\mathcal{B},1} \\ m_{\mathrm{B},\mathcal{B},2}}} \sum_{\substack{k_{\mathrm{A}}, q_{\mathrm{A}} \\ k_{\mathrm{B}}, q_{\mathrm{B}}}} \frac{(2k_{\mathrm{A}}+1)(2k_{\mathrm{B}}+1)}{(2j_A+1)(2j_B+1)} \\
\langle j_A m_{A,1}, k_{\mathrm{A}} - q_{\mathrm{A}} | j_A m_{A,2} \rangle \langle j_B m_{B,1}, k_{\mathrm{B}} - q_{\mathrm{B}} | j_B m_{B,2} \rangle \\
\langle j_B m_{\mathrm{B},\mathcal{B},1}, k_{\mathrm{B}} 0 | j_B m_{\mathrm{B},\mathcal{B},2} \rangle C_{k_{\mathrm{A}} - q_{\mathrm{A}}}(\theta_E, \phi_E) \, C_{k_{\mathrm{B}} - q_{\mathrm{B}}}(\theta_{\mathcal{B}}, \phi_{\mathcal{B}}) \, \alpha^2 F_{1e} F^*_{2e} \\
\left(\langle j_A \bar{m}_{A,E}, k_{\mathrm{A}} 0 | j_A \bar{m}_{A,E} \rangle + \langle j_A - \bar{m}_{A,E}, k_{\mathrm{A}} 0 | j_A - \bar{m}_{A,E} \rangle \right) \\
\langle j_B m_{\mathrm{B},\mathcal{B},1} | \hat{\rho} | j_B m_{\mathrm{B},\mathcal{B},2} \rangle
\end{aligned} \tag{7.24}$$

which becomes

$$T_{ee} = \frac{1}{4} \sum_{\substack{m'_{\rm A} m'_B \\ m_{A,1} m_{A,2} \\ m_{B,1} m_{B,2} \\ m_{{\rm B},\mathcal{B},1} \\ m_{{\rm B},\mathcal{B},2}}} \sum_{\substack{k_{\rm A}, q_{\rm A} \\ k_{\rm B}, q_{\rm B}}} \frac{(2k_{\rm A}+1)(2k_{\rm B}+1)}{(2j_A+1)(2j_B+1)}$$
$$\langle j_A m_{A,1}, k_{\rm A} - q_{\rm A} | j_A m_{A,2} \rangle \langle j_B m_{B,1}, k_{\rm B} - q_{\rm B} | j_B m_{B,2} \rangle$$
$$\langle j_B m_{{\rm B},\mathcal{B},1}, k_{\rm B} 0 | j_B m_{{\rm B},\mathcal{B},2} \rangle C_{k_{\rm A}-q_{\rm A}}(\theta_E, \phi_E)\, C_{k_{\rm B}-q_{\rm B}}(\theta_{\mathcal{B}}, \phi_{\mathcal{B}})\, \alpha^2 F_{1e} F^*_{2e}$$
$$\left(\langle j_A \bar{m}_{A,E}, k_{\rm A} 0 | j_A \bar{m}_{A,E} \rangle + (-1)^{k_{\rm A}} \langle j_A \bar{m}_{A,E}, k_{\rm A} 0 | j_A \bar{m}_{A,E} \rangle \right)$$
$$\langle j_B m_{{\rm B},\mathcal{B},1} | \hat{\rho} | j_B m_{{\rm B},\mathcal{B},2} \rangle \tag{7.25}$$

and hence

$$T_{ee} = \frac{1}{2} \sum_{\substack{m'_{\rm A} m'_B \\ m_{A,1} m_{A,2} \\ m_{B,1} m_{B,2} \\ m_{{\rm B},\mathcal{B},1} \\ m_{{\rm B},\mathcal{B},2}}} \sum_{\substack{k_{\rm A}, q_{\rm A} \\ k_{\rm B}, q_{\rm B}}} \delta_{k_{\rm A}\,\text{even}} \frac{(2k_{\rm A}+1)(2k_{\rm B}+1)}{(2j_A+1)(2j_B+1)}$$
$$\langle j_A m_{A,1}, k_{\rm A} - q_{\rm A} | j_A m_{A,2} \rangle \langle j_B m_{B,1}, k_{\rm B} - q_{\rm B} | j_B m_{B,2} \rangle$$
$$\langle j_B m_{{\rm B},\mathcal{B},1}, k_{\rm B} 0 | j_B m_{{\rm B},\mathcal{B},2} \rangle C_{k_{\rm A}-q_{\rm A}}(\theta_E, \phi_E)\, C_{k_{\rm B}-q_{\rm B}}(\theta_{\mathcal{B}}, \phi_{\mathcal{B}})\, \alpha^2 F_{1e} F^*_{2e}$$
$$\langle j_B m_{{\rm B},\mathcal{B},1} | \hat{\rho} | j_B m_{{\rm B},\mathcal{B},2} \rangle \,. \tag{7.26}$$

Similarly for T_{ff}

$$T_{ff} = \frac{1}{2} \sum_{\substack{m'_{\rm A} m'_B \\ m_{A,1} m_{A,2} \\ m_{B,1} m_{B,2} \\ m_{{\rm B},\mathcal{B},1} \\ m_{{\rm B},\mathcal{B},2}}} \sum_{\substack{k_{\rm A}, q_{\rm A} \\ k_{\rm B}, q_{\rm B}}} \delta_{k_{\rm A}\,\text{even}} \frac{(2k_{\rm A}+1)(2k_{\rm B}+1)}{(2j_A+1)(2j_B+1)}$$
$$\langle j_A m_{A,1}, k_{\rm A} - q_{\rm A} | j_A m_{A,2} \rangle \langle j_B m_{B,1}, k_{\rm B} - q_{\rm B} | j_B m_{B,2} \rangle$$
$$\langle j_B m_{{\rm B},\mathcal{B},1}, k_{\rm B} 0 | j_B m_{{\rm B},\mathcal{B},2} \rangle C_{k_{\rm A}-q_{\rm A}}(\theta_E, \phi_E)\, C_{k_{\rm B}-q_{\rm B}}(\theta_{\mathcal{B}}, \phi_{\mathcal{B}})\, \beta^2 F_{1f} F^*_{2f}$$
$$\langle j_A \bar{m}_{A,E}, k_{\rm A} 0 | j_A \bar{m}_{A,E} \rangle$$
$$\langle j_B m_{{\rm B},\mathcal{B},1} | \hat{\rho} | j_B m_{{\rm B},\mathcal{B},2} \rangle \,. \tag{7.27}$$

Finally, for T_{ef}, win initially obtain

$$\begin{aligned} T_{ef} = \frac{1}{4} \sum_{\substack{m'_{\rm A} m'_B \\ m_{A,1} m_{A,2} \\ m_{B,1} m_{B,2} \\ m_{{\rm B},\mathcal{B},1} \\ m_{{\rm B},\mathcal{B},2}}} \sum_{\substack{k_{\rm A}, q_{\rm A} \\ k_{\rm B}, q_{\rm B}}} \frac{(2k_{\rm A}+1)(2k_{\rm B}+1)}{(2j_A+1)(2j_B+1)} \\ \langle j_A m_{A,1}, k_{\rm A} - q_{\rm A} | j_A m_{A,2} \rangle \langle j_B m_{B,1}, k_{\rm B} - q_{\rm B} | j_B m_{B,2} \rangle \\ \langle j_B m_{{\rm B},\mathcal{B},1}, k_{\rm B} 0 | j_B m_{{\rm B},\mathcal{B},2} \rangle C_{k_{\rm A}-q_{\rm A}}(\theta_E, \phi_E) \, C_{k_{\rm B}-q_{\rm B}}(\theta_{\mathcal{B}}, \phi_{\mathcal{B}}) \\ |\alpha\beta| \left(F_{1f} F^*_{2e} + F_{1e} F^*_{2f} \right) \\ \left(- \langle j_A \bar{m}_{A,E}, k_{\rm A} 0 | j_A \bar{m}_{A,E} \rangle + (-1)^{k_{\rm A}} \langle j_A \bar{m}_{A,E}, k_{\rm A} 0 | j_A \bar{m}_{A,E} \rangle \right) \\ \langle j_B m_{{\rm B},\mathcal{B},1} | \hat{\rho} | j_B m_{{\rm B},\mathcal{B},2} \rangle \end{aligned} \tag{7.28}$$

which then becomes

$$\begin{aligned} T_{ef} = -\frac{1}{2} \sum_{\substack{m'_{\rm A} m'_B \\ m_{A,1} m_{A,2} \\ m_{B,1} m_{B,2} \\ m_{{\rm B},\mathcal{B},1} \\ m_{{\rm B},\mathcal{B},2}}} \sum_{\substack{k_{\rm A}, q_{\rm A} \\ k_{\rm B}, q_{\rm B}}} \delta_{k_{\rm A}\,\text{odd}} \frac{(2k_{\rm A}+1)(2k_{\rm B}+1)}{(2j_A+1)(2j_B+1)} \\ \langle j_A m_{A,1}, k_{\rm A} - q_{\rm A} | j_A m_{A,2} \rangle \langle j_B m_{B,1}, k_{\rm B} - q_{\rm B} | j_B m_{B,2} \rangle \\ \langle j_B m_{{\rm B},\mathcal{B},1}, k_{\rm B} 0 | j_B m_{{\rm B},\mathcal{B},2} \rangle C_{k_{\rm A}-q_{\rm A}}(\theta_E, \phi_E) \, C_{k_{\rm B}-q_{\rm B}}(\theta_{\mathcal{B}}, \phi_{\mathcal{B}}) \\ |\alpha\beta| \left(F_{1f} F^*_{2e} + F_{1e} F^*_{2f} \right) \\ \langle j_A \bar{m}_{A,E}, k_{\rm A} 0 | j_A \bar{m}_{A,E} \rangle \langle j_B m_{{\rm B},\mathcal{B},1} | \hat{\rho} | j_B m_{{\rm B},\mathcal{B},2} \rangle \, . \end{aligned} \tag{7.29}$$

The differential cross section may, in these cases, be written in the form

$$\mathrm{d}\sigma(|m_{{\rm A},E}|) = \sum_{\substack{k_{\rm A} q_{\rm A} \\ k_{\rm B} q_{\rm B}}} (2k_{\rm A}+1)(2k_{\rm B}+1) [O^{(k_{\rm A},k_{\rm B})}_{q_{\rm A},q_{\rm B}}(\theta)]^* a^{(k_{\rm A})}_{q_{\rm A}} a^{(k_{\rm B})}_{q_{\rm B}} \, . \tag{7.30}$$

where $O^{(k_{\rm A},k_{\rm B})}_{q_{\rm A},q_{\rm B}}(\theta)$ are the intrinsic r_A, j_B-PDDCSs, and $a^{(k)}_q$ are the extrinsic polarisation moments for each molecule in the scattering frame. Hence, to pull out the PDDCSs, we must insert the extrinsic moments. The LAB frame moments are given by

$$\mathcal{A}^{(k_{\rm A})}_0 = \begin{cases} -|\alpha\beta| \langle j \bar{m}_{A,E}, k_{\rm A} 0 | j_A \bar{m}_{A,E} \rangle \cdot \langle j_A \bar{\Omega}_A, k_{\rm A} 0 | j_A \bar{\Omega}_A \rangle & k_{\rm A} \text{ odd} \\ \langle j_A \bar{m}_{A,E}, k_{\rm A} 0 | j_A \bar{m}_{A,E} \rangle \cdot \langle j_A \bar{\Omega}_A, k_{\rm A} 0 | j_A \bar{\Omega}_A \rangle & k_{\rm A} \text{ even} \end{cases} \tag{7.31}$$

and [28, 179]

$$A_0^{(k_\mathrm{B})} = \sum_{m_{\mathrm{B},\mathcal{B},1}} \sum_{m_{\mathrm{B},\mathcal{B},2}} \langle j_B m_{\mathrm{B},\mathcal{B},1}|\hat{\rho}|j_B m_{\mathrm{B},\mathcal{B},2}\rangle \langle j_B m_{\mathrm{B},\mathcal{B},1}, k_\mathrm{B}0|j_B m_{\mathrm{B},\mathcal{B},2}\rangle \tag{7.32}$$

which are linked to the scattering frame moments by

$$a_{q_\mathrm{A}}^{(k_\mathrm{A})} = \mathcal{A}_0^{(k_\mathrm{A})} C_{k_\mathrm{A} q_\mathrm{A}}(\theta_E, \phi_E) \tag{7.33}$$

and

$$a_{q_\mathrm{B}}^{(k_\mathrm{B})} = A_0^{(k_\mathrm{B})} C_{k_\mathrm{B} q_\mathrm{B}}(\theta_\mathcal{B}, \phi_\mathcal{B})\,. \tag{7.34}$$

Returning to Eqs. 7.26, 7.27 and 7.29, one can chose to invert the summations over q_A and q_B and use the relationship between m_1 and m_2 with q for both A and B. If we do T_{ee} becomes

$$\begin{aligned} T_{ee} = \frac{1}{2} \sum_{\substack{m'_\mathrm{A} m'_B \\ m_\mathrm{A} m_\mathrm{B} \\ m_{\mathrm{B},\mathcal{B},1} \\ m_{\mathrm{B},\mathcal{B},2}}} \sum_{\substack{k_\mathrm{A}, q_\mathrm{A} \\ k_\mathrm{B}, q_\mathrm{B}}} & \delta_{k_\mathrm{A}\,\mathrm{even}} \frac{(2k_\mathrm{A}+1)(2k_\mathrm{B}+1)}{(2j_A+1)(2j_B+1)} \\ & \langle j_A m_A, k_\mathrm{A} q_\mathrm{A}|j_A(m_\mathrm{A}+q_\mathrm{A})\rangle \langle j_B m_\mathrm{B}, k_\mathrm{B} q_\mathrm{B}|j_B(m_\mathrm{B}+q_\mathrm{B})\rangle \\ & \langle j_B m_{\mathrm{B},\mathcal{B},1}, k_\mathrm{B}0|j_B m_{\mathrm{B},\mathcal{B},2}\rangle C_{k_\mathrm{A} q_\mathrm{A}}(\theta_E, \phi_E)\, C_{k_\mathrm{B} q_\mathrm{B}}(\theta_\mathcal{B}, \phi_\mathcal{B})\, \alpha^2 F_{1e} F_{2e}^* \\ & \langle j_A \bar{m}_{A,E}, k_\mathrm{A}0|j_A \bar{m}_{A,E}\rangle \\ & \langle j_B m_{\mathrm{B},\mathcal{B},1}|\hat{\rho}|j_B m_{\mathrm{B},\mathcal{B},2}\rangle\,. \end{aligned} \tag{7.35}$$

T_{ff} similarly becomes

$$\begin{aligned} T_{ff} = \frac{1}{2} \sum_{\substack{m'_\mathrm{A} m'_B \\ m_\mathrm{A} m_\mathrm{B} \\ m_{\mathrm{B},\mathcal{B},1} \\ m_{\mathrm{B},\mathcal{B},2}}} \sum_{\substack{k_\mathrm{A}, q_\mathrm{A} \\ k_\mathrm{B}, q_\mathrm{B}}} & \delta_{k_\mathrm{A}\,\mathrm{even}} \frac{(2k_\mathrm{A}+1)(2k_\mathrm{B}+1)}{(2j_A+1)(2j_B+1)} \\ & \langle j_A m_A, k_\mathrm{A} q_\mathrm{A}|j_A(m_\mathrm{A}+q_\mathrm{A})\rangle \langle j_B m_\mathrm{B}, k_\mathrm{B} q_\mathrm{B}|j_B(m_\mathrm{B}+q_\mathrm{B})\rangle \\ & \langle j_B m_{\mathrm{B},\mathcal{B},1}, k_\mathrm{B}0|j_B m_{\mathrm{B},\mathcal{B},2}\rangle C_{k_\mathrm{A} q_\mathrm{A}}(\theta_E, \phi_E)\, C_{k_\mathrm{B} q_\mathrm{B}}(\theta_\mathcal{B}, \phi_\mathcal{B})\, \beta^2 F_{1f} F_{2f}^* \\ & \langle j_A \bar{m}_{A,E}, k_\mathrm{A}0|j_A \bar{m}_{A,E}\rangle \langle j_B m_{\mathrm{B},\mathcal{B},1}|\hat{\rho}|j_B m_{\mathrm{B},\mathcal{B},2}\rangle \end{aligned} \tag{7.36}$$

while T_{ef} becomes

$$T_{ef} = -\frac{1}{2}\sum_{\substack{m'_{\rm A}m'_B\\ m_{\rm A}m_{\rm B}\\ m_{{\rm B},\mathcal{B},1}\\ m_{{\rm B},\mathcal{B},2}}}\sum_{\substack{k_{\rm A},q_{\rm A}\\ k_{\rm B},q_{\rm B}}}\delta_{k_{\rm A}\,\rm odd}\frac{(2k_{\rm A}+1)(2k_{\rm B}+1)}{(2j_A+1)(2j_B+1)}$$
$$\langle j_A m_A, k_{\rm A}q_{\rm A}|j_A(m_{\rm A}+q_{\rm A})\rangle\langle j_B m_{\rm B}, k_{\rm B}q_{\rm B}|j_B(m_{\rm B}+q_{\rm B})\rangle$$
$$\langle j_B m_{{\rm B},\mathcal{B},1}, k_{\rm B}0|j_B m_{{\rm B},\mathcal{B},2}\rangle C_{k_{\rm A}q_{\rm A}}(\theta_E,\phi_E)\,C_{k_{\rm B}q_{\rm B}}(\theta_{\mathcal{B}},\phi_{\mathcal{B}})$$
$$|\alpha\beta|\left(F_{1f}F^*_{2e}+F_{1e}F^*_{2f}\right)$$
$$\langle j_A\bar{m}_{A,E}, k_{\rm A}0|j_A\bar{m}_{A,E}\rangle\langle j_B m_{{\rm B},\mathcal{B},1}|\hat{\rho}|j_B m_{{\rm B},\mathcal{B},2}\rangle\,. \tag{7.37}$$

The DCS for even values of $k_{\rm A}$ is given by

$$\mathrm{d}\sigma(|m_{{\rm A},E}|)|_{\rm even\,k_A} = T_{ee}+T_{ff}\,. \tag{7.38}$$

Substituting in Eqs. 7.35 and 7.36, and then Eqs. 7.31, 7.32 and 7.34, one obtains

$$\mathrm{d}\sigma(|m_{{\rm A},E}|)|_{\rm even\,k_A} = \frac{1}{2}\sum_{\substack{m'_{\rm A}m'_B\\ m_{\rm A}m_{\rm B}}}\sum_{\substack{k_{\rm A},q_{\rm A}\\ k_{\rm B},q_{\rm B}}}\frac{(2k_{\rm A}+1)(2k_{\rm B}+1)}{(2j_A+1)(2j_B+1)}\frac{1}{\langle j_A\bar{\Omega}_A, k_{\rm A}0|j_A\bar{\Omega}_A\rangle}$$
$$\langle j_A m_A, k_{\rm A}q_{\rm A}|j_A(m_{\rm A}+q_{\rm A})\rangle\langle j_B m_{\rm B}, k_{\rm B}q_{\rm B}|j_B(m_{\rm B}+q_{\rm B})\rangle$$
$$\left(\alpha^2F_{1e}F^*_{2e}+\beta^2F_{1f}F^*_{2f}\right)a^{(k_{\rm A})}_{q_{\rm A}}a^{(k_{\rm B})}_{q_{\rm B}} \tag{7.39}$$

The shorthand

$$Q_{\epsilon_1\epsilon_2} = \sum_{m'_{\rm A}m'_{\rm B}}F_{1\epsilon_1}F^*_{2\epsilon_2} \tag{7.40}$$

is used allowing Eq. 7.39 to be rewritten

$$\mathrm{d}\sigma(|m_{{\rm A},E}|)|_{\rm even\,k_A} = \sum_{\substack{k_{\rm A},q_{\rm A}\\ k_{\rm B},q_{\rm B}}}(2k_{\rm A}+1)(2k_{\rm B}+1)$$
$$\left[\sum_{m_{\rm A}m_{\rm B}}\frac{1}{2}\frac{1}{(2j_A+1)(2j_B+1)}\frac{1}{\langle j_A\bar{\Omega}_A, k_{\rm A}0|j_A\bar{\Omega}_A\rangle}\right.$$
$$\langle j_A m_A, k_{\rm A}q_{\rm A}|j_A(m_{\rm A}+q_{\rm A})\rangle\langle j_B m_{\rm B}, k_{\rm B}q_{\rm B}|j_B(m_{\rm B}+q_{\rm B})\rangle$$
$$\left.\left(\alpha^2Q_{ee}+\beta^2Q_{ff}\right)\right]a^{(k_{\rm A})}_{q_{\rm A}}a^{(k_{\rm B})}_{q_{\rm B}}\,. \tag{7.41}$$

By comparison with Eq. 7.30, one can define $O^{(k_{\rm A},k_{\rm B})}_{q_{\rm A},q_{\rm B}}(\theta)$ as

$$[O^{(k_\mathrm{A},k_\mathrm{B})}_{q_\mathrm{A},q_\mathrm{B}}(\theta)|_{\mathrm{even}\,k_\mathrm{A}}]^* = \frac{1}{2}\frac{1}{(2j_A+1)(2j_B+1)}\frac{1}{\langle j_A\bar{\Omega}_A, k_\mathrm{A}0|j_A\bar{\Omega}_A\rangle} \sum_{\substack{m_\mathrm{A}m_\mathrm{B}\\ \epsilon=e\,\mathrm{or}\,f}} \langle j_A m_A, k_\mathrm{A}q_\mathrm{A}|j_A(m_\mathrm{A}+q_\mathrm{A})\rangle \langle j_B m_\mathrm{B}, k_\mathrm{B}q_\mathrm{B}|j_B(m_\mathrm{B}+q_\mathrm{B})\rangle \gamma_\epsilon^2 Q_{\epsilon\epsilon} \tag{7.42}$$

where $\gamma_\epsilon = \alpha$ or β for the e and f states respectively.

For odd values of k_A, the DCS becomes

$$\mathrm{d}\sigma(|m_{\mathrm{A},E}|)|_{\mathrm{odd}\,k_\mathrm{A}} = T_{ef}\,. \tag{7.43}$$

Following the same procedure as above, this leads to

$$\mathrm{d}\sigma(|m_{\mathrm{A},E}|)|_{\mathrm{odd}\,k_\mathrm{A}} = \sum_{\substack{k_\mathrm{A},q_\mathrm{A}\\ k_\mathrm{B},q_\mathrm{B}}} (2k_\mathrm{A}+1)(2k_\mathrm{B}+1) \left[\sum_{m_\mathrm{A}m_\mathrm{B}} \frac{1}{2}\frac{1}{(2j_A+1)(2j_B+1)}\frac{1}{\langle j_A\bar{\Omega}_A, k_\mathrm{A}0|j_A\bar{\Omega}_A\rangle} \langle j_A m_A, k_\mathrm{A}q_\mathrm{A}|j_A(m_\mathrm{A}+q_\mathrm{A})\rangle\langle j_B m_\mathrm{B}, k_\mathrm{B}q_\mathrm{B}|j_B(m_\mathrm{B}+q_\mathrm{B})\rangle (Q_{fe}+Q_{ef})\right] a^{(k_\mathrm{A})}_{q_\mathrm{A}} a^{(k_\mathrm{B})}_{q_\mathrm{B}}\,. \tag{7.44}$$

and hence

$$[O^{(k_\mathrm{A},k_\mathrm{B})}_{q_\mathrm{A},q_\mathrm{B}}(\theta)|_{\mathrm{odd}\,k_\mathrm{A}}]^* = \frac{1}{2}\frac{1}{(2j_A+1)(2j_B+1)}\frac{1}{\langle j_A\bar{\Omega}_A, k_\mathrm{A}0|j_A\bar{\Omega}_A\rangle} \sum_{\substack{m_\mathrm{A}m_\mathrm{B}\\ \epsilon_1\neq\epsilon_2\\ \epsilon_1=e\,\mathrm{or}\,f}} \langle j_A m_A, k_\mathrm{A}q_\mathrm{A}|j_A(m_\mathrm{A}+q_\mathrm{A})\rangle \langle j_B m_\mathrm{B}, k_\mathrm{B}q_\mathrm{B}|j_B(m_\mathrm{B}+q_\mathrm{B})\rangle Q_{\epsilon_1\epsilon_2}\,. \tag{7.45}$$

Equation 7.30 may be integrated over the scattering angle, θ, to obtain stereodynamical information on the integral cross section. This gives

$$\sigma^{\phi_E,\phi_\mathcal{B}}_{\theta_E,\theta_\mathcal{B}}(|m_{\mathrm{A},E}|) = \sum_{\substack{k_\mathrm{A}q_\mathrm{A}\\ k_\mathrm{B}q_\mathrm{B}}} (2k_\mathrm{A}+1)(2k_\mathrm{B}+1)[o^{(k_\mathrm{A},k_\mathrm{B})}_{q_\mathrm{A},q_\mathrm{B}}]^* a^{(k_\mathrm{A})}_{q_\mathrm{A}} a^{(k_\mathrm{B})}_{q_\mathrm{B}} \tag{7.46}$$

where

$$o^{(k_\mathrm{A},k_\mathrm{B})}_{q_\mathrm{A},q_\mathrm{B}} = 2\pi\int_{-1}^{1} O^{(k_\mathrm{A},k_\mathrm{B})}_{q_\mathrm{A},q_\mathrm{B}}(\theta)\mathrm{d}\cos\theta\,. \tag{7.47}$$

Note that the ICS defined in Equation 7.46 is technically not a true ICS, as it is dependent on azimuthal angles, which are integrated over during an integration over a solid angle, which is how an ICS is defined. When integrating over the azimuthal angles, one obtains

$$\sigma_{\theta_E,\theta_\mathcal{B}}(|m_{\mathrm{A},E}|) = \sum_{k_\mathrm{A}k_\mathrm{B}} (2k_\mathrm{A}+1)(2k_\mathrm{B}+1) o_{0,0}^{(k_\mathrm{A},k_\mathrm{B})} a_0^{(k_\mathrm{A})} a_0^{(k_\mathrm{B})} \tag{7.48}$$

where the complex conjugate on the polarisation parameters $o_{0,0}^{(k_\mathrm{A},k_\mathrm{B})}$ have been removed due to them being necessarily real due to their relationship to products of spherical harmonics outlined in Section 7.3. However, whenever the ICS is described in the rest of this chapter, it will be referring to Eq, 7.46.

A normalised version of Eq. 7.46 may be defined as

$$\sigma_{\theta_E,\theta_\mathcal{B}}^{\phi_E,\phi_\mathcal{B}}(|m_{\mathrm{A},E}|) = \sigma_\mathrm{iso} \sum_{\substack{k_\mathrm{A}q_\mathrm{A} \\ k_\mathrm{B}q_\mathrm{B}}} (2k_\mathrm{A}+1)(2k_\mathrm{B}+1) \left(\frac{[o_{q_\mathrm{A},q_\mathrm{B}}^{(k_\mathrm{A},k_\mathrm{B})}]^*}{o_{0,0}^{(0,0)}} \right) a_{q_\mathrm{A}}^{(k_\mathrm{A})} a_{q_\mathrm{B}}^{(k_\mathrm{B})} \tag{7.49}$$

where $[o_{q_\mathrm{A},q_\mathrm{B}}^{(k_\mathrm{A},k_\mathrm{B})}]^*/o_{0,0}^{(0,0)}$ are the normalised polarisation parameters, and it should be noted that $o_{0,0}^{(0,0)} \equiv \sigma_\mathrm{iso}$.

7.5 Hertel-Stoll Normalisation

While the complex moments above contain all the stereodynamical information for the system described, they are not intuitive to interpret physically. However, these expansion moments can be converted into real versions with simple physical meanings. This process is known as Hertel-Stoll normalisation[219], and has been shown before for a single oriented molecule, but never before for two oriented molecules. Hence, this process has been extended to that case.

7.5.1 Definitions

For the full derivation of the 4-vector Hertel-Stoll moments, and its validation by comparison to the complex case, see Appendix B. A generic intrinsic 4-vector Hertel-Stoll normalised correlation expansion moment $X_{q_\mathrm{A}\pm,q_\mathrm{B}\pm}^{\{k_\mathrm{A},k_\mathrm{B}\}}(\theta)$ may be defined

$$X^{\{k_{\rm A},k_{\rm B}\}}_{q_{\rm A}\pm,q_{\rm B}\pm} = \pm\frac{1}{2}\Big[(-1)^{q_A+q_B}X^{(k_{\rm A},k_{\rm B})}_{q_{\rm A},q_{\rm B}} + X^{(k_{\rm A},k_{\rm B})}_{-q_{\rm A},-q_{\rm B}} \pm (-1)^{q_{\rm B}}\left((-1)^{q_A+q_B}X^{(k_{\rm A},k_{\rm B})}_{q_{\rm A},-q_{\rm B}} + X^{(k_{\rm A},k_{\rm B})}_{-q_{\rm A},q_{\rm B}}\right)\Big] q_{\rm A}>0,\, q_{\rm B}>0 \quad (7.50)$$

$$X^{\{k_{\rm A},k_{\rm B}\}}_{q_{\rm A}\pm,q_{\rm B}\mp} = \frac{1}{2i}\Big[(-1)^{q_A+q_B}X^{(k_{\rm A},k_{\rm B})}_{q_{\rm A},q_{\rm B}} - X^{(k_{\rm A},k_{\rm B})}_{-q_{\rm A},-q_{\rm B}} \mp (-1)^{q_{\rm B}}\left((-1)^{q_A+q_B}X^{(k_{\rm A},k_{\rm B})}_{q_{\rm A},-q_{\rm B}} - X^{(k_{\rm A},k_{\rm B})}_{-q_{\rm A},q_{\rm B}}\right)\Big] q_{\rm A}>0,\, q_{\rm B}>0 \quad (7.51)$$

and

$$X^{\{k_{\rm A},k_{\rm B}\}}_{0,q_{\rm B}+} = \frac{1}{\sqrt{2}}\left[(-1)^{q_B}X^{(k_{\rm A},k_{\rm B})}_{0,q_{\rm B}} + X^{(k_{\rm A},k_{\rm B})}_{0,-q_{\rm B}}\right] \quad q_{\rm A}=0 \quad \text{and} \quad q_{\rm B}>0 \quad (7.52)$$

$$X^{\{k_{\rm A},k_{\rm B}\}}_{0,q_{\rm B}-} = \frac{1}{i\sqrt{2}}\left[(-1)^{q_B}X^{(k_{\rm A},k_{\rm B})}_{0,q_{\rm B}} - X^{(k_{\rm A},k_{\rm B})}_{0,-q_{\rm B}}\right] \quad q_{\rm A}=0 \quad \text{and} \quad q_{\rm B}>0 \quad (7.53)$$

$$X^{\{k_{\rm A},k_{\rm B}\}}_{q_{\rm A}+,0} = \frac{1}{\sqrt{2}}\left[(-1)^{q_A}X^{(k_{\rm A},k_{\rm B})}_{q_{\rm A},0} + X^{(k_{\rm A},k_{\rm B})}_{-q_{\rm A},0}\right] \quad q_{\rm A}>0 \quad \text{and} \quad q_{\rm B}=0 \quad (7.54)$$

$$X^{\{k_{\rm A},k_{\rm B}\}}_{q_{\rm A}-,0} = \frac{1}{i\sqrt{2}}\left[(-1)^{q_A}X^{(k_{\rm A},k_{\rm B})}_{q_{\rm A},0} - X^{(k_{\rm A},k_{\rm B})}_{-q_{\rm A},0}\right] \quad q_{\rm A}>0 \quad \text{and} \quad q_{\rm B}=0 \quad (7.55)$$

$$X^{\{k_{\rm A},k_{\rm B}\}}_{0,0} = X^{(k_{\rm A},k_{\rm B})}_{0,0}, \quad q_{\rm A}=0 \quad \text{and} \quad q_{\rm B}=0\,. \quad (7.56)$$

where the angle dependence of $X^{\{k_{\rm A},k_{\rm B}\}}_{q_{\rm A}\pm,q_{\rm B}\pm}(\theta)$ has been suppressed. An Hertel-Stoll normalised extrinsic moment may be defined analogously

$$a^{\{k_{\rm A},k_{\rm B}\}}_{q_{\rm A}\pm,q_{\rm B}\pm} = \pm\frac{1}{2}\Big[(-1)^{q_A+q_B}a^{(k_{\rm A})}_{q_{\rm A}}a^{(k_{\rm B})}_{q_{\rm B}} + a^{(k_{\rm A})}_{-q_{\rm A}}a^{(k_{\rm B})}_{-q_{\rm B}} \pm (-1)^{q_{\rm B}}\left((-1)^{q_A+q_B}a^{(k_{\rm A})}_{q_{\rm A}}a^{(k_{\rm B})}_{-q_{\rm B}} + a^{(k_{\rm A})}_{-q_{\rm A}}a^{(k_{\rm B})}_{q_{\rm B}}\right)\Big] q_{\rm A}>0,\, q_{\rm B}>0 \quad (7.57)$$

$$a^{\{k_{\rm A},k_{\rm B}\}}_{q_{\rm A}\pm,q_{\rm B}\mp} = \frac{1}{2i}\Big[(-1)^{q_A+q_B}a^{(k_{\rm A})}_{q_{\rm A}}a^{(k_{\rm B})}_{q_{\rm B}} - a^{(k_{\rm A})}_{-q_{\rm A}}a^{(k_{\rm B})}_{-q_{\rm B}} \mp (-1)^{q_{\rm B}}\left((-1)^{q_A+q_B}a^{(k_{\rm A})}_{q_{\rm A}}a^{(k_{\rm B})}_{-q_{\rm B}} - a^{(k_{\rm A})}_{-q_{\rm A}}a^{(k_{\rm B})}_{q_{\rm B}}\right)\Big] q_{\rm A}>0,\, q_{\rm B}>0 \quad (7.58)$$

and

$$a^{\{k_{\rm A},k_{\rm B}\}}_{0,q_{\rm B}+} = \frac{1}{\sqrt{2}}\left[(-1)^{q_B}a^{(k_{\rm A})}_{0}a^{(k_{\rm B})}_{q_{\rm B}} + a^{(k_{\rm A})}_{0}a^{(k_{\rm B})}_{-q_{\rm B}}\right] \quad q_{\rm A}=0 \quad \text{and} \quad q_{\rm B}>0 \quad (7.59)$$

$$a^{\{k_{\rm A},k_{\rm B}\}}_{0,q_{\rm B}-} = \frac{1}{i\sqrt{2}}\left[(-1)^{q_B}a^{(k_{\rm A})}_{0}a^{(k_{\rm B})}_{q_{\rm B}} - a^{(k_{\rm A})}_{0}a^{(k_{\rm B})}_{-q_{\rm B}}\right] \quad q_{\rm A}=0 \quad \text{and} \quad q_{\rm B}>0 \quad (7.60)$$

$$a^{\{k_{\rm A},k_{\rm B}\}}_{q_{\rm A}+,0} = \frac{1}{\sqrt{2}}\left[(-1)^{q_A}a^{(k_{\rm A})}_{q_{\rm A}}a^{(k_{\rm B})}_{0} + a^{(k_{\rm A})}_{-q_{\rm A}}a^{(k_{\rm B})}_{0}\right] \quad q_{\rm A}>0 \quad \text{and} \quad q_{\rm B}=0 \quad (7.61)$$

$$a^{\{k_{\rm A},k_{\rm B}\}}_{q_{\rm A}-,0} = \frac{1}{i\sqrt{2}}\left[(-1)^{q_A}a^{(k_{\rm A})}_{q_{\rm A}}a^{(k_{\rm B})}_{0} - a^{(k_{\rm A})}_{-q_{\rm A}}a^{(k_{\rm B})}_{0}\right] \quad q_{\rm A}>0 \quad \text{and} \quad q_{\rm B}=0\,. \quad (7.62)$$

Superscript	Subscript	Positive	Negative
0	0	Isotropic	N/A
1	1-	Orientation along $\hat{\boldsymbol{y}}$	Orientation along -$\hat{\boldsymbol{y}}$
1	0	Orientation along $\hat{\boldsymbol{z}}$	Orientation along -$\hat{\boldsymbol{z}}$
1	1+	Orientation along $\hat{\boldsymbol{x}}$	Orientation along -$\hat{\boldsymbol{x}}$
2	2-	Alignment along $\hat{\boldsymbol{x}}$+$\hat{\boldsymbol{y}}$	Alignment along $\hat{\boldsymbol{x}}$-$\hat{\boldsymbol{y}}$
2	1-	Alignment along $\hat{\boldsymbol{y}}$+$\hat{\boldsymbol{z}}$	Alignment along $\hat{\boldsymbol{y}}$-$\hat{\boldsymbol{z}}$
2	0	Alignment along $\hat{\boldsymbol{z}}$	Alignment perpendicular to $\hat{\boldsymbol{z}}$
2	1+	Alignment along $\hat{\boldsymbol{x}}$+$\hat{\boldsymbol{z}}$	Alignment along $\hat{\boldsymbol{x}}$-$\hat{\boldsymbol{z}}$
2	2+	Alignment along $\hat{\boldsymbol{x}}$	alignment along $\hat{\boldsymbol{y}}$

Table 7.1: Directional meanings of the superscripts and subscripts of the moments[25].

7.5.2 Physical Meaning of The Moments

The directional meanings of these Hertel-Stoll moments are completely analogous to those for single molecule alignment. However, there are now pairs of subscripts and superscripts for each moment, with one pair describing the geometry of one molecule, and the other describing the geometry of the other molecule. Using Table 7.1, we can therefore ascertain that the $O_{0,1-}^{\{1,2\}}$ moment, for example, represents changes to the differential cross section brought about by orienting the bond axis of molecule A along $\hat{\boldsymbol{z}}$ while aligning the angular momentum of molecule B along $\hat{\boldsymbol{y}}$+$\hat{\boldsymbol{z}}$.

If the geometry of the molecule is chosen to have a particular alignment or orientation for each molecule, then

- If the geometry chosen leads to pairs of superscripts and subscripts that both fall into the same column (positive or negative) of Table 7.1, then this orientation will increase the DCS when the moment is positive and deccrease the DCS when the moment is negative

- If the geometry chosen leads to pairs of superscripts and subscripts such that one falls into the positive column of Table 7.1 and one into the negative column, then this orientation will increase the DCS when the moment is negative, and decrease the DCS when the moment is positive.

7.5.3 Reflection Symmetry Properties of The Moments

A DCS must be invariant to a reflection in the scattering plane [220]. This can be understood in terms of the PES. When the PES is reflected, the effect of the potential gradients on one side of the plane become reflected onto the other side. Hence, when the collision partner approaches on one side the scattering plane, the forces it experiences are exactly the same but opposite as when the system is not reflected and the partner approaches from the opposite side. Hence their contribution to a quantity describing the distribution between two vectors in the scattering plane, the DCS, must be equal.

However, this is not the whole story. Of course, for some molecules, reflection in a plane changes the molecule into a different molecule. These molecules are chiral and upon reflection produce their enantiomer. If at least one of the reactants or products are chiral, so must the transition state. Hence, if the transition state is chiral then upon reflection, either the reactants, products or both are no longer the same molecules, and so the reaction looked at is now a different process. Hence the scattering process is not invariant with respect to reflection in the scattering plane for chiral transition states[29, 220].

The question now is: what qualifies as a chiral transition state? Having four different atoms placed in different locations in space is not a sufficient condition here. Instead, they must form a rigid structure which cannot be rotated independently to produce the reflected structure. For example, in scattering between NO and HD, in which all four atoms are different, no chiral transition state is formed: the HD molecule and the NO molecule, which are not connected by bonds, can be rotated to to produce a reflected configuration. Hence, any non-reactive scattering in which neither collision partner is chiral will have reflection symmetry in the scattering plane.

The NO(X) + H_2 system does not produce a chiral, bound transition state. Hence, the DCS must be invariant with respect to a reflection in the xz, or scattering, plane, which is defined by the initial and final relative velocity vectors.

All other vectors in the vector correlation shall, for the purposes of this thesis, either represent the direction of the bond axis of one molecule, $\boldsymbol{r}_{\mathrm{X}}$, or the direction of the angular momentum of a molecule, $\boldsymbol{j}_{\mathrm{X}}$. The former of these is a true vector, while the latter is a pseudovector. Hence, upon reflection in the xz plane, the angles defining the direction of these vectors transform thus

$$\begin{aligned}
\theta_{\mathrm{r}} &\to \theta_{\mathrm{r}} \\
\phi_{\mathrm{r}} &\to -\phi_{\mathrm{r}} \\
\theta_{\mathrm{j}} &\to \pi - \theta_{\mathrm{j}} \\
\phi_{\mathrm{j}} &\to \pi - \phi_{\mathrm{j}} \,.
\end{aligned}$$

For a four vector correlation, the probability distribution of the scattering angle can be given by Eq. (B.30). Using the reflection symmetry, it can be said

$$P(\theta|\theta_{\mathrm{A}}, \phi_{\mathrm{A}}, \theta_{\mathrm{B}}, \phi_{\mathrm{B}}) = \hat{\mathcal{S}} P(\theta|\theta_{\mathrm{A}}, \phi_{\mathrm{A}}, \theta_{\mathrm{B}}, \phi_{\mathrm{B}}) \tag{7.63}$$

where $\hat{\mathcal{S}}$ is the operator representing reflection in the xz plane.

Hence, all products in Eq. 7.63 must be equal after reflection, and thus $C^{\{k_A,k_B\}}_{q_A\pm,q_B\pm}$, of which the $X^{\{k_A,k_B\}}_{q_A\pm,q_B\pm}$ moments are the expectation values, must be invariant with respect to reflection. This is because the moments themselves are invariant to reflection. Therefore, for any of the products in Eq. 7.63 to be non-zero, the relationship

$$C^{\{k_A,k_B\}}_{q_A\pm,q_B\pm} = \hat{\mathcal{S}} C^{\{k_A,k_B\}}_{q_A\pm,q_B\pm} \tag{7.64}$$

must be satisfied.

$\boldsymbol{r}_{\mathrm{A}} - \boldsymbol{j}_{\mathrm{B}} - \boldsymbol{k} - \boldsymbol{k}'$ correlation

For this correlation, the bond axis of molecule A and the angular momentum of molecule B is oriented. Hence, there are a set of angles θ_{r}, ϕ_{r}, θ_{j} and ϕ_{j}, which shall be written here to correlate to their corresponding molecule to give θ_{A}, ϕ_{A}, θ_{B} and ϕ_{B} respectively.

Hence

$$\begin{aligned}\hat{\mathcal{S}}C^{\{k_A,k_B\}}_{q_A+,q_B+} &= \hat{\mathcal{S}}\left[C^{(k_A)}_{-q_A}(\theta_{\mathrm{A}},0)\,C^{(k_B)}_{-q_B}(\theta_{\mathrm{B}},0)\cos(q_A\phi_{\mathrm{A}})\cos(q_B\phi_{\mathrm{B}})\right]\\ &= C^{(k_A)}_{-q_A}(\theta_{\mathrm{A}},0)\,C^{(k_B)}_{-q_B}(\pi-\theta_{\mathrm{B}},0)\cos(-q_A\phi_{\mathrm{A}})\cos(q_B(\pi-\phi_{\mathrm{B}}))\\ &= C^{(k_A)}_{-q_A}(\theta_{\mathrm{A}},0)\,(-1)^{k_B+q_B}C^{(k_B)}_{-q_B}(\theta_{\mathrm{B}},0)\cos(q_A\phi_{\mathrm{A}})\,(-1)^{q_B}\cos(q_B\phi_{\mathrm{B}})\\ &= (-1)^{k_B}C^{\{k_A,k_B\}}_{q_A+,q_B+} \qquad (7.65)\end{aligned}$$

and analogously

$$\hat{\mathcal{S}}C^{\{k_A,k_B\}}_{q_A-,q_B-} = (-1)^{k_B}C^{\{k_A,k_B\}}_{q_A-,q_B-} \qquad (7.66)$$

$$\hat{\mathcal{S}}C^{\{k_A,k_B\}}_{q_A+,q_B-} = (-1)^{k_B-1}C^{\{k_A,k_B\}}_{q_A+,q_B-} \qquad (7.67)$$

$$\hat{\mathcal{S}}C^{\{k_A,k_B\}}_{q_A-,q_B+} = (-1)^{k_B-1}C^{\{k_A,k_B\}}_{q_A-,q_B+} \qquad (7.68)$$

$$\hat{\mathcal{S}}C^{\{k_A,k_B\}}_{0,q_B+} = (-1)^{k_B}C^{\{k_A,k_B\}}_{0,q_B+} \qquad (7.69)$$

$$\hat{\mathcal{S}}C^{\{k_A,k_B\}}_{0,q_B-} = (-1)^{k_B-1}C^{\{k_A,k_B\}}_{0,q_B-} \qquad (7.70)$$

$$\hat{\mathcal{S}}C^{\{k_A,k_B\}}_{q_A+,0} = (-1)^{k_B}C^{\{k_A,k_B\}}_{q_A+,0} \qquad (7.71)$$

$$\hat{\mathcal{S}}C^{\{k_A,k_B\}}_{q_A-,0} = (-1)^{k_B-1}C^{\{k_A,k_B\}}_{q_A-,0} \qquad (7.72)$$

$$\hat{\mathcal{S}}C^{\{k_A,k_B\}}_{0,0} = (-1)^{k_B}C^{\{k_A,k_B\}}_{0,0}\,. \qquad (7.73)$$

where the identities

$$C^{(k)}_{-q}(\pi-\theta,0) = (-1)^{k+q}C^{(k)}_{-q}(\theta,0) \qquad (7.74)$$

$$\sin(q(\pi-\phi)) = (-1)^{q-1}\sin(q\phi) \qquad (7.75)$$

$$\cos(q(\pi-\phi)) = (-1)^{q}\cos(q\phi)\ , \qquad (7.76)$$

which hold for $k, q \in \mathbb{Z}$, have been used.

The consequences of this symmetry requirement is that some Hertel-Stoll normalised moments are necessarily zero. The moments that remain non-zero are listed in table 7.2.

k_B	Sign after q_A	Sign after q_B
even	$\pm$	$\pm$
odd	$\pm$	$\mp$

Table 7.2: Rules for non-zero Hertel-Stoll normalised moments for the $\boldsymbol{r}_\mathrm{A} - \boldsymbol{j}_\mathrm{B} - \boldsymbol{k} - \boldsymbol{k}'$ correlation of the sort $O^{\{k_A,k_B\}}_{q_A\pm,q_B\pm/\mp}$. Note that if q_A or q_B are 0, they should be treated as having a positive sign.

7.5.4 Pictorial Explanation of the Reflection Symmetry Properties

For a moment to be non-zero, as the DCS is invaraint with respect to reflection in the scattering plane, the polarisation it describes must have a consistent effect, and not an opposing effect upon this reflection. As the moments are the expectation values of products of Hertel-Stoll normalised modified spherical harmonics, if this product changes sign upon reflection, the polarisation effect will be cancelled out, and so cannot contribute to the DCS.

To explore this it helps to think about the vectors and their corresponding spherical harmonics pictorially. First of all, it is useful to look at why orienting the bond axis of one molecule along the y-axis, while leaving the other molecule unoriented does not have an effect, but orienting the molecules along the z- or x-axes does.

In Figure 7.3, the vectors describing a $+z$ orientation are shown, in comparison to the vectors describing a $+y$ orientation. For both of these scenarios, we shall assume no polarisation of a second vector, which will be described by the subscript B. For orientation along $+z$, as seen in panel a), the corresponding Hertel-Stoll normalised spherical harmonic product is $C_0^{\{1\}}(\theta_r,\phi_r)C_0^{\{0\}}(\theta_\mathrm{B},\phi_\mathrm{B}) = C_0^{\{1\}}(\theta_r,\phi_r)$, and is displayed in panel c). This is symmetric with respect to reflection in the scattering plane (the $\pm y$ hemispheres are equivalent), and so this polarisation will influence the DCS. In panel b) however, orientation along $+y$ corresponds to $C_{1-}^{\{1\}}(\theta_r,\phi_r)C_0^{\{0\}}(\theta_\mathrm{B},\phi_\mathrm{B}) = C_{1-}^{\{1\}}(\theta_r,\phi_r)$, which is antisymmetric with respect to reflection (panel d)) in the scattering plane, and so this polarisation has no effect on the DCS.

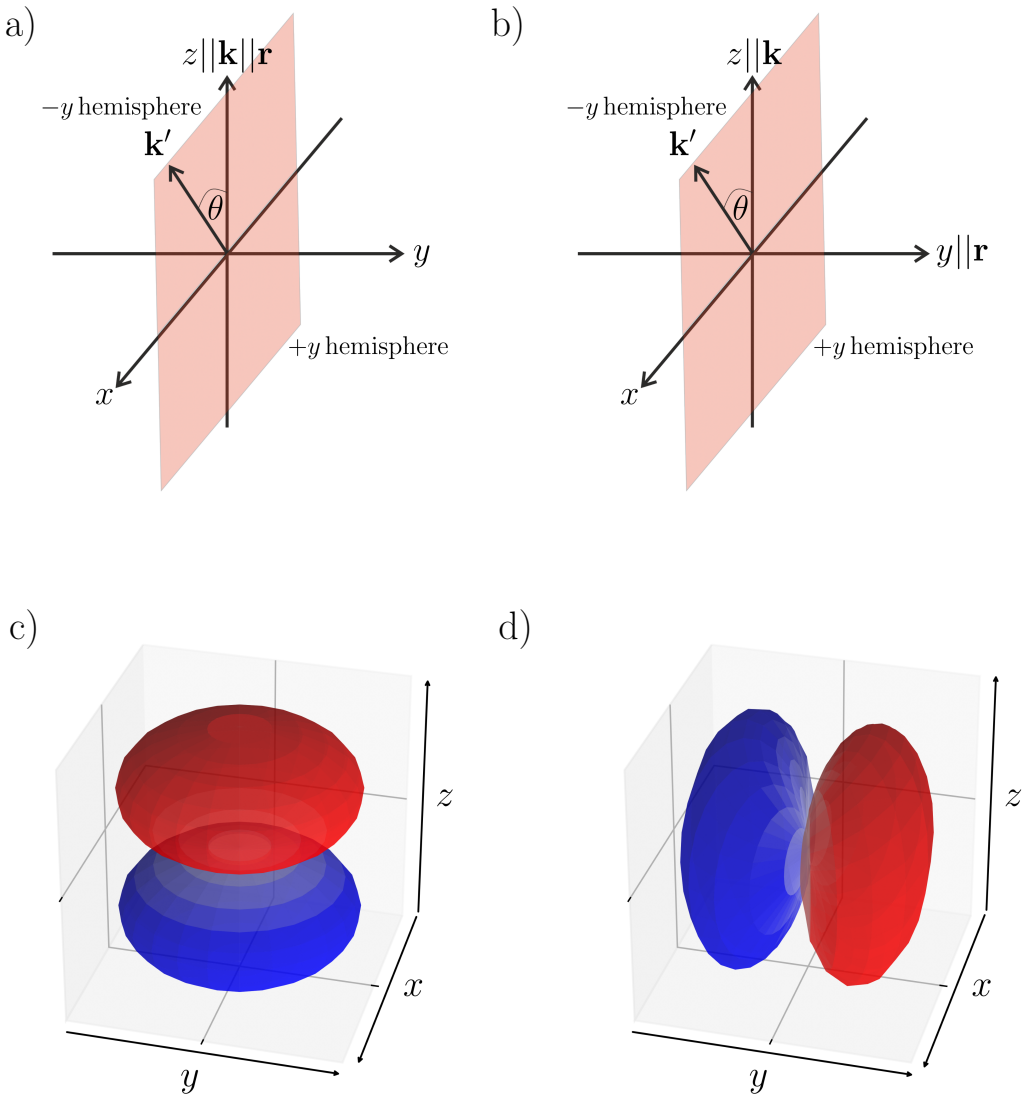

Figure 7.3: The vectors corresponding to bond axis orientation of a molecule in a scattering process along the a) $+z$ and b) $+y$ directions in the scattering frame. The scattering, xz, plane is shown in peach. Panels c) and d) are pictorial representations of $C_0^{\{1\}}(\theta, \phi)$ and $C_{1-}^{\{1\}}(\theta, \phi)$.

If one looks at a scenario in which both molecules are oriented simultaneously, a similar picture holds. This is illustrated in Figure 7.4. Panel a) shows the vectors corresponding to orientation of the bond axis of molecule A, $\boldsymbol{r}_{\mathrm{A}}$ in the $+y$ direction and the angular momentum of molecule B, $\boldsymbol{j}_{\mathrm{B}}$, in the $+x$ direction. Upon reflection in the scattering plane, we obtain panel b), where $\boldsymbol{j}_{\mathrm{B}}$ changes direction due to its properties as a pseudovector. The relevant spherical harmonic product is, therefore, $C_{1-}^{\{1\}}(\theta_{\mathrm{A}}, \phi_{\mathrm{A}}) C_{1+}^{\{1\}}(\theta_{\mathrm{B}}, \phi_{\mathrm{B}})$. These two spherical harmonics are drawn in panels c)

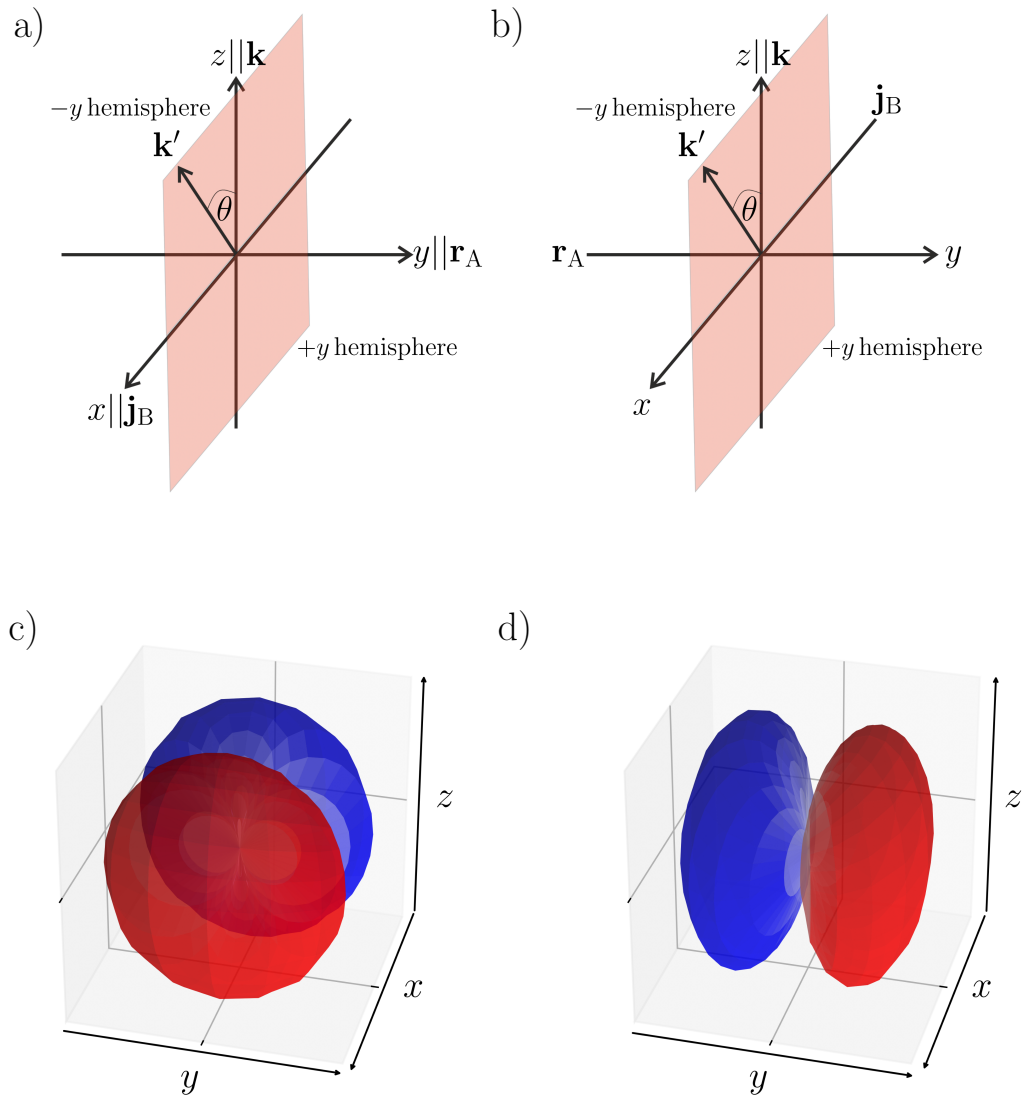

Figure 7.4: a) The vectors corresponding to concurrent bond axis orientation of molecule A in a scattering process along $+y$, and angular momentum orientation of molecule B along $+x$. Reflection in the scattering frame results in panel b), with $\boldsymbol{r}_\mathrm{A}$ pointing along $-y$, and $\boldsymbol{j}_\mathrm{B}$ pointing along $-x$ (as it is a pseudovector). c) and d) show $C_{1+}^{\{1\}}(\theta,\phi)$ and $C_{1-}^{\{1\}}(\theta,\phi)$ respectively.

Moment	Relationship at Extrema	Relationship With
$O_{0,0}^{\{k_\mathrm{A},k_\mathrm{B}\}}$	None	-
$O_{0,q_\mathrm{B}\pm}^{\{k_\mathrm{A},k_\mathrm{B}\}}$ or $O_{q_\mathrm{A}\pm,0}^{\{k_\mathrm{A},k_\mathrm{B}\}}$	0	-
$O_{q_\mathrm{A}\pm,q_\mathrm{B}\pm}^{\{k_\mathrm{A},k_\mathrm{B}\}}$ $k_\mathrm{A},k_\mathrm{B}\neq 0, q_\mathrm{A}+q_\mathrm{B}=$ even	Equal to	$O_{q_\mathrm{A}\mp,q_\mathrm{B}\mp}^{\{k_\mathrm{A},k_\mathrm{B}\}}$ $k_\mathrm{A},k_\mathrm{B}\neq 0, q_\mathrm{A}+q_\mathrm{B}=$ even
$O_{q_\mathrm{A}\pm,q_\mathrm{B}\mp}^{\{k_\mathrm{A},k_\mathrm{B}\}}$ $k_\mathrm{A},k_\mathrm{B}\neq 0, q_\mathrm{A}+q_\mathrm{B}=$ even	Negative of	$O_{q_\mathrm{A}\mp,q_\mathrm{B}\pm}^{\{k_\mathrm{A},k_\mathrm{B}\}}$ $k_\mathrm{A},k_\mathrm{B}\neq 0, q_\mathrm{A}+q_\mathrm{B}=$ even
$O_{q_\mathrm{A}\pm,q_\mathrm{B}\pm}^{\{k_\mathrm{A},k_\mathrm{B}\}}$ $k_\mathrm{A},k_\mathrm{B}\neq 0, q_\mathrm{A}+q_\mathrm{B}=$ odd	0	-

Table 7.3: The properties of all moments relevant to this thesis at the extrema of $\theta = 0°$ and $\theta = 180°$.

and d). Both will change sign upon the reflection in the scattering frame (in the case of $C_{1+}^{\{1\}}(\theta_\mathrm{B},\phi_\mathrm{B})$ due to the pseudovector nature of $\boldsymbol{j}_\mathrm{B}$). Hence, the product will not change sign and will be invariant with respect to reflection, and thus the moment this corresponds to, $O_{1-,1+}^{\{1,1\}}(\theta)$, will be non-zero.

7.5.5 Properties of the Moments at the Extrema

Due to their symmetry properties, the values of some of the moments have specific values or relationships with the values of other moments at $\theta = 0°$ and $\theta = 180°$. As is the case when only one molecule is oriented, when only one of k_A and k_B are non-zero, those moments with q_A or q_B non-zero are identically 0 at the two extrema. This also remains true when k_A and k_B are non-zero and one of q_A and q_B are non-zero. Those moments where q_A and q_B are 0 are unrestricted in value at the extrema for all possible values of k_A and k_B (unless identically zero at all angles due to symmetry constraints).

If both k_A and k_B are non-zero and both q_A and q_B are non-zero, there are multiple possible relationships. If $q_\mathrm{A}+q_\mathrm{B}$ is even (but neither are zero), and if the signs after q_A and q_B are the same, then there is no restriction on the value at the extrema, except that it must be the same as the moment with the opposite signs after q_A and q_B. If the signs after q_A and q_B are different, then there is again no restriction in value at the extrema, except that the value must be the negative of the

value when the signs are inverted. Finally, if $q_A + q_B$ is odd (but neither are zero), the moments must go to zero at the extrema. This is summarised in Table 7.3.

While this has been ascertained from the moments achievable in this system, more work is required to ensure these rules remain the case in general.

7.6 Theoretical Study I: Low Collision Energy

This section will now focus on the applying this theory to a potential system of interest. This system will be, as in the proposed experiment in Section 7.2, NO(X, $j_{NO} = 1/2$) + H_2(X, $j_{H_2} = 1$). However, rather than for collision energies one might expect in that experiment (on the order of hundreds of cm), the results shown here are for collision energies below $20\,cm^{-1}$. This is because higher collision energies require significantly more computationally challenging calculations, and because there are effects that can be seen in the cold collision regime, such as resonances, which cannot be seen at higher collision energies. At these lower energies the H_2 will undergo an elastic process due to the large spacing of H_2 energy levels and the nuclear spin statistics of H_2 which removes every other rotational level for each nuclear spin modification. The transition studied for NO involves excitation from $j_{NO} = 1/2$ in the field to $j'_{NO} = 3/2e$.

Quantum scattering calculations were performed by solving the close-coupled equations using the program HIBRIDON 5.1[85]. They are performed on the potential energy surfaces of Kłos *et al.*[221] using a J_{TOT} of 20.5, and an R_{End} of $100\,a_0$.

The value of $\mathcal{A}_0^{(1)}$ for the orientation of NO due to the electric filed was taken to be the infinite field solution, in which the e and f Λ-doublets are completely superposed, and so $\mathcal{A}_0^{(1)} = -1/3$. A sample density matrix was provided[222] which characterises the ensemble of molecules produced by the magnetic hexapole m-state selection process in Section 7.2. From this density matrix, an estimate of $A_0^{(1)}$ for H_2 was calculated to be $A_0^{(1)} \approx 0.4$ and $A_0^{(2)}$ was calculated to be $A_0^{(2)} \approx 0$. Hence, these values are used in this Section, suggesting there is strong orientation of $\boldsymbol{j}_{H_2}$ but no alignment before the collision.

The aim of this study to illustrate the utility and power of this mathematical framework and what can be achieved with this high level of stereodynamic control. Where any insights into the mechanisms involved are found, they are also discussed.

This is not the first study of the scattering of the NO(X) + H_2 (or D_2) system. The first study of this kind used basic ion imaging to calculate differential cross sections with D_2[223]. After the calculation of the surfaces used in this paper, an increase in the studies of this system followed. These include experiments analysing diffraction oscillations in collisions with D_2 in $j_{D_2} = 0$[224] and the measurements of differential cross sections with H_2 in $j_{H_2} = 0$[225]. Studies have also looked at low energy collisions, helping to establish the high accuracy of the Kłos PES[226, 227]. The calculations and experiments in ref. [227] also include the system in which ortho-H_2 is used, with initial $j_{H_2} = 1$ H_2 ground state, analysing integral cross sections and resonances in the quasi-elastic $j_{NO} = 1/2f \rightarrow j'_{NO} = 1/2e$ transition at total energies below $8\,cm^{-1}$. There has also been a study performed analysing the stereodynamics of the NO + H_2 system, in which the ISAs were calculated[204]. Hence, no study has analysed this system in which both molecules are oriented in some way. This is the first such example.

7.6.1 Comparison With Previous Calculations

Firstly, ICSs were calculated for the $j_{NO} = 1/2f \rightarrow j'_{NO} = 3/2e$ transition for H_2 in $j_{H_2} = 0$. The purpose of these calculations was to ensure a good match with those in ref. [226]. The results of these calculations are shown in Figure 7.5.

The data shown in blue are the calculations done for this thesis. These calculations are performed on a coarser energy grid than those of Vogels *et al.*, and that data was retrieved directly from the figure, resulting in small discrepancies from the true values. Generally the agreement between the two calculations is good. The greatest deviations come with the discrepancy of the location of the peak a little above $12\,cm^{-1}$. Great care was taken to ensure the calculations in this work have converged, and thus any discrepancy must come from differences in the constants to represent the system. No increases to the number of partial

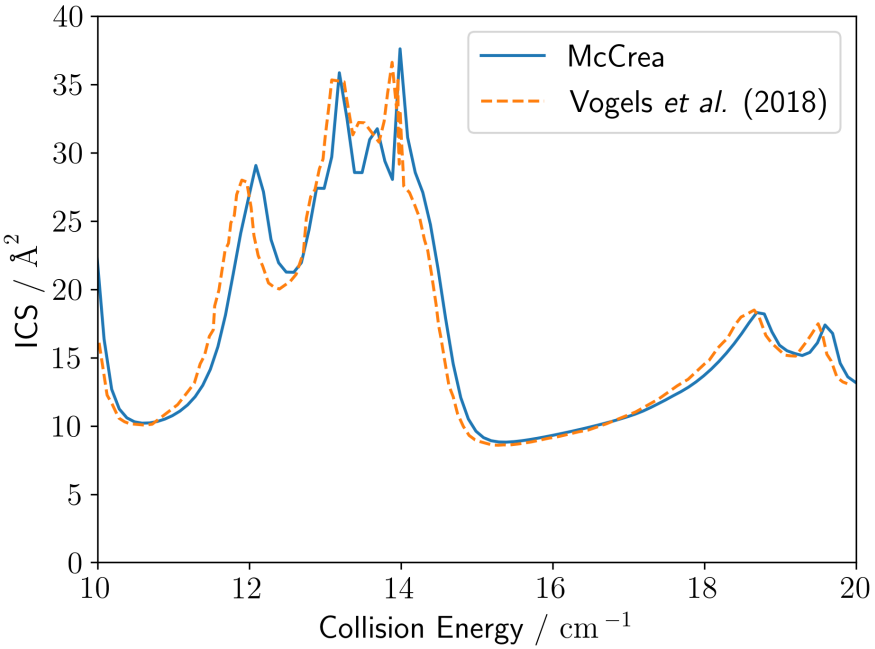

Figure 7.5: Results of calculations from HIBRIDON for the ICSs for the $j_{NO} = 1/2f \rightarrow j'_{NO} = 3/2e$ transition with H_2 elastic in $j = 0$. The blue line shows the ICSs calculated for this work, while the orange line shows those calculated by Vogels *et al.*[226] (those calculation were not performed in HIBRIDON, but were benchmarked against it). Note that the data from Vogels *et al.* is taken directly from the figure, and thus very small discrepancies from the true value are inevitable, seen in small deviations from a smooth curve.

waves or the value of R_{end}, nor decreases in the grid spacing produce different results. Hence, confidence may be had in assuming the accuracy of calculations presented here onwards for H_2 in $j_{H_2} = 1$.

7.6.2 Stereodynamic Changes Over a Resonance

Resonances are characterised by rapid changes in cross section as a function of collision energy, often due to a single partial wave. In Figure 7.6 panel a), the excitation function is shown for energies between $10\,cm^{-1}$ and $20\,cm^{-1}$ for NO + H_2 in an isotropic electric field. An excitation function shows the ICS as a function of collision energy. In this plot, total energy is plotted on the x-axis rather than collision energy. However, here, total energy and collision energy are only separated by the Λ-doublet splitting in NO for $j = 1/2$ of $E_\Lambda = 0.01172\,cm^{-1}$. In panel b), the same plot is broken down into individual partial waves. From this it becomes clear

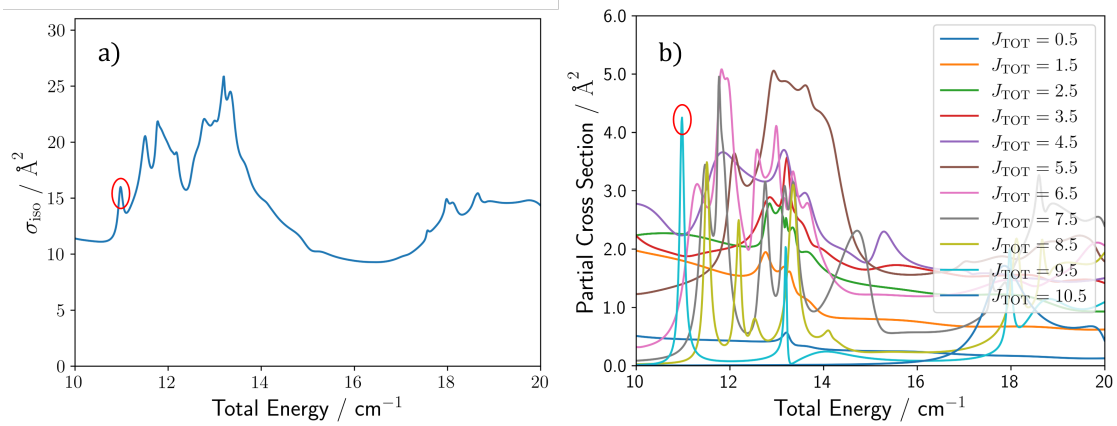

Figure 7.6: a) Calculated excitation function for $|j = 1/2, \bar{\Omega} = 1/2, \bar{m}_E = 1/2, E\rangle \rightarrow |j = 3/2, \bar{\Omega} = 1/2, e\rangle$ for collision energies between $10\,\mathrm{cm}^{-1}$ and $20\,\mathrm{cm}^{-1}$. b) Partial cross sections for $J_{\mathrm{TOT}} = 0.5$ to $J_{\mathrm{TOT}} = 10.5$ for the same range of collision energies. The red circles highlight the resonance dominated by $J_{\mathrm{TOT}} = 9.5$ at $10.98\,\mathrm{cm}^{-1}$.

that the sharp peak at $E_{\mathrm{TOT}} = 10.98\,\mathrm{cm}^{-1}$ in the excitation function, highlighted by the red oval, is caused by a similar sharp peak in the partial cross section for $J_{\mathrm{TOT}} = 9.5$. Due to the significant overlapping of features in other high σ_{iso} regions, this peak is the easiest to ascribe to a single partial wave, although it is also true that a high base is provided by contributions from other partial waves that are much more consistent over the energy range.

This section will investigate whether there are significant stereodynamic changes across the resonance. Hence, analysis shall be presented probing stereodynamic preference on either side and at the resonance, at E_{TOT} values of $10.88\,\mathrm{cm}^{-1}$, $10.98\,\mathrm{cm}^{-1}$, and $11.08\,\mathrm{cm}^{-1}$.

Maximised and Minimised Cross Sections

Figure 7.7 shows how the ICS may be affected by orienting both molecules before the collision. The percentage change in the ICS from σ_{iso} for situations where both molecules are oriented before the collision in arbitrary directions to maximise and minimise the ICS are shown. In this region the changes are all roughly around $\pm 15\%$. While it is clear that, at the resonance, the increase in the cross section by maximisation is somewhat smaller than at the two energies either

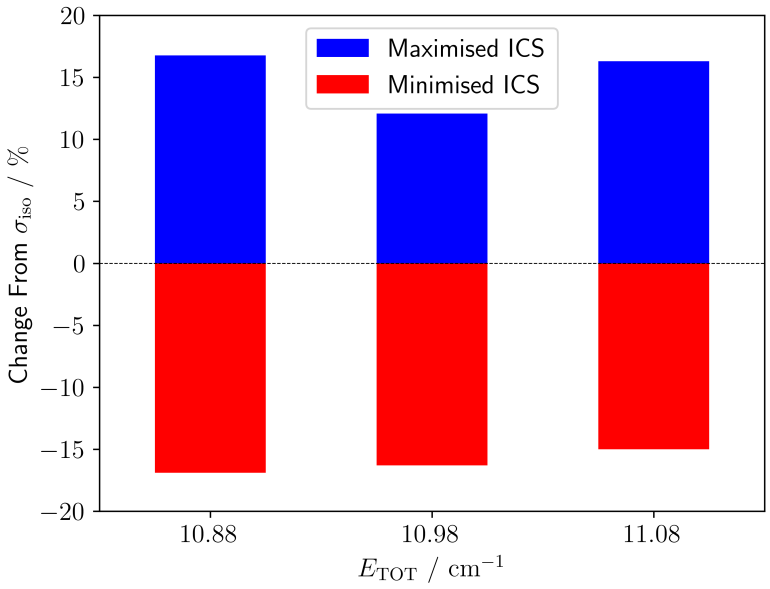

Figure 7.7: The percentage change from the value of σ_{iso} when the ICS is maximised (blue) and minimised (red) by orienting the electric and magnetic fields in specific directions for energies at and around the resonance at $10.98\,\mathrm{cm}^{-1}$.

side of it, overall there appears to be no drastic change in sensitivity towards orientation over the resonance.

Where there are clearer effects is in the direction of orientation for the maximised and minimised ICSs. These are explored in Figure 7.8. In this figure, the directions of the orientation of the NO bond axis, $\boldsymbol{r}_{NO}$ and the H_2 angular momentum, $\boldsymbol{j}_{H_2}$, to produce the maximised and minimised ICSs are shown in the scattering frame (with $\boldsymbol{k}$ along $+z$ and $\boldsymbol{k}'$ in the $+xz$ plane).

Before looking at how the preferences change over a resonance, it is worth noting the directions of orientation in both the minimised and maximised scenario at $E_{TOT} = 10.88\,\mathrm{cm}^{-1}$. In a situation in which only the bond axis of one molecule is oriented, the only non-zero orientation moments are $R_0^{\{1\}}$, $R_{1+}^{\{1\}}$, where the molecule is oriented along the z-axis and the x-axis. Hence, orientation along y is never favoured nor disfavoured. If only the angular momentum of one molecule is oriented, the only non-zero orientation moment is $S_{1-}^{\{1\}}$, corresponding to orientation along the y-axis. Hence, orientation along the z-axis and the x-axis is never favoured nor disfavoured. However, in this scenario where both molecules are oriented, despite the moments corresponding to single molecule orientation (ie. $k_A = 1, k_B = 0$ or

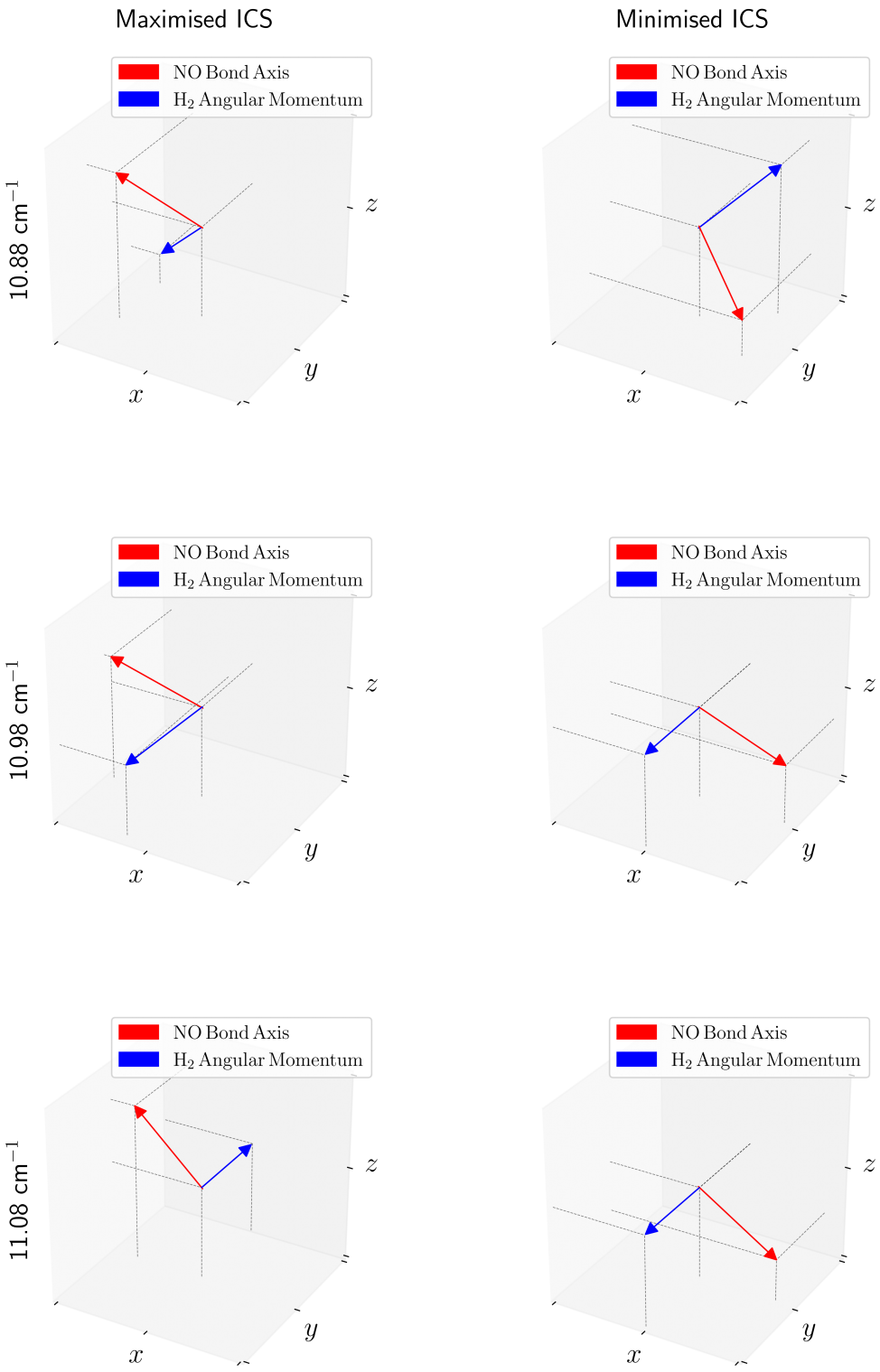

Figure 7.8: Directions of orientation of the NO bond axis (red), $\boldsymbol{r}_{\mathrm{NO}}$, and the H_2 angular momentum (blue), $\boldsymbol{j}_{H_2}$, to maximise (left) and minimise (right) the ICS in the scattering frame (with $\boldsymbol{k}$ along $+z$ and $\boldsymbol{k}'$ in the $+xz$ plane). The $+z$ direction is bottom to top, $+y$ is bottom left to top right, and $+x$ is top left to bottom right. From top to bottom, the rows correspond to $E_{\mathrm{TOT}} = 10.88\,\mathrm{cm}^{-1}$, $10.98\,\mathrm{cm}^{-1}$ and $11.08\,\mathrm{cm}^{-1}$.

$k_A = 0, k_B = 1$) following the same properties as above, there is some degree of x- and z-polarisation of $\boldsymbol{j}_{\mathrm{H_2}}$ and y-polarisation of $\boldsymbol{r}_{\mathrm{NO}}$. This can be completely ascribed as an effect of the mixed moments, where $k_A \neq 0$ and $k_B \neq 0$.

In this particular case, there are two prominent mixed moments. The first of these is $o^{\{1,1\}}_{1-,1+}$, which when normalised is given by $o^{\{1,1\}}_{1-,1+}/o^{\{0,0\}}_{0,0} = 0.0446$. While this may seem small, when multiplied by the prefactor $(2k_A + 1)(2k_B + 1) = 9$, its value is significant. This moment corresponds to orientation along the y-axis for $\boldsymbol{r}_{\mathrm{NO}}$ while simultaneously orienting $\boldsymbol{j}_{\mathrm{H_2}}$ along the x-axis. As its value is positive, this corresponds to a preference when either $\boldsymbol{r}_{\mathrm{NO}}$ is oriented along $+y$ and $\boldsymbol{j}_{\mathrm{H_2}}$ is oriented along $+x$ or, alternatively, to when $\boldsymbol{r}_{\mathrm{NO}}$ is oriented along $-y$ and $\boldsymbol{j}_{\mathrm{H_2}}$ is oriented along $-x$. The other prominent mixed moment is $o^{\{1,1\}}_{1-,0}/o^{\{0,0\}}_{0,0} = 0.0452$. This corresponds to orienting $\boldsymbol{r}_{\mathrm{NO}}$ in the $+y$ direction while also orienting $\boldsymbol{j}_{\mathrm{H_2}}$ in the $+z$ direction or, alternatively, to when $\boldsymbol{r}_{\mathrm{NO}}$ is oriented along $-y$ and $\boldsymbol{j}_{\mathrm{H_2}}$ is oriented along $-z$.

Only one of these pairs of preferences is shown from the Maximised ICS in the top row of Figure 7.8. However, providing that orientation of $\boldsymbol{j}_{\mathrm{H_2}}$ is fixed along y and that orientation of $\boldsymbol{r}_{\mathrm{NO}}$ is fixed along along x and z, one can invert the y coordinate of the $\boldsymbol{r}_{\mathrm{NO}}$ vector and the x and z coordinates of $\boldsymbol{j}_{\mathrm{H_2}}$ and still retain the same cross section. This is because, for moments that cause preference for orientation in directions that cannot be preferred for individual molecule orientation, there are no other moments that act either in harmony or in conflict with them. For example, if the $o^{\{1,1\}}_{1+,1-}$ moment were to have an effect, so necessarily must the non-zero $o^{\{1,0\}}_{1+,0}$ and $o^{\{0,1\}}_{0,1-}$ moments. Therefore, one cannot simply investigate the behaviour described in the $o^{\{1,1\}}_{1+,1-}$ moment on its own, but must do so in concert with other moments describing a given set of orientations. In the case of $o^{\{1,1\}}_{1-,1+}$, the are no equivalent moments that are also involved as $o^{\{1,0\}}_{1-,0}$ and $o^{\{0,1\}}_{0,1+}$ are identically 0.

Focussing now on the changes in stereodynamic preference over the resonance, one can see significant differences in, particularly, the direction of $\boldsymbol{j}_{\mathrm{H_2}}$. Moving from $E_{\mathrm{TOT}} = 10.88\,\mathrm{cm}^{-1}$ to $10.98\,\mathrm{cm}^{-1}$ to $11.08\,\mathrm{cm}^{-1}$, in the maximised ICSs, $\boldsymbol{j}_{\mathrm{H_2}}$ moves from being mainly in the $-x$, $-z$ direction (or alternatively the $+x$,

$+z$ direction, see above), to being strongly in the $-y$ direction to then being perfectly along the $+y$ direction.

This is described by how some of the moments change over this period. First of all, the $o_{0,1-}^{\{0,1\}}$ moment becomes more important over this range of increasing energies, changing in renormalised value from $-0.0013 \rightarrow 0.0176 \rightarrow 0.0351$. This increase in magnitude and change of sign causes an increasing preference for orientation along $-y$ for $\boldsymbol{j}_{\mathrm{H_2}}$, an effect which is completely realised at $11.08\,\mathrm{cm}^{-1}$. However, this does not explain the behaviour at the resonance. Instead this is best understood by looking at the moment $o_{1+,1-}^{\{1,1\}}$, as well as the $o_{1+,0}^{\{1,0\}}$ moment. The former has the normalised values $-0.0077 \rightarrow 0.0398 \rightarrow 0.0010$ while the latter has the normalised values $-0.1113 \rightarrow -0.0851 \rightarrow -0.0891$. Hence, the mixed moment is essentially negligible, except at the resonance. This mixed moment with a negative value causes a preference for $-x$ $(+x)$ orientation of $\boldsymbol{r}_{\mathrm{NO}}$ with $+y$ $(-y)$ orientation of $\boldsymbol{j}_{\mathrm{H_2}}$. Due to $o_{1+,0}^{\{1,0\}}$'s effect to favour $-x$ orientation of $\boldsymbol{r}_{\mathrm{NO}}$, which is greater than the effect $o_{0,1-}^{\{0,1\}}$ describes encouraging $+y$ orientation of $\boldsymbol{j}_{\mathrm{H_2}}$, the mixed moment causes a favouring of orientation of $\boldsymbol{r}_{\mathrm{NO}}$ in the $-x$ direction with $\boldsymbol{j}_{\mathrm{H_2}}$ orientation in the $-y$ direction. At $E_{\mathrm{TOT}} = 11.08\,\mathrm{cm}^{-1}$, this mixed moment is essentially zero, and thus the single molecule orientation moments take over, favouring orientation of $\boldsymbol{j}_{\mathrm{H_2}}$ along $+y$ and $\boldsymbol{r}_{\mathrm{NO}}$ along $-x$ and $+z$. The tendency of some moments to spike in magnitude at a resonance is discussed later.

7.6.3 Selected Orientations

In this section, the ICSs at a specific set of orientations are calculated and analysed. These orientations correspond to $\pm x, \pm y, \pm z$ orientations of both $\boldsymbol{r}_{\mathrm{NO}}$ and $\boldsymbol{j}_{\mathrm{H_2}}$. Note that throughout the rest of the chapter, the term 'orientation set' will be used to refer to a scenario in which each molecule is oriented in a specific way, independently from each other. For example, an orientation set could be $\boldsymbol{r}_{\mathrm{NO}}$ oriented in the $+z$ direction while $\boldsymbol{j}_{\mathrm{H_2}}$ is oriented in the $+y$ direction.

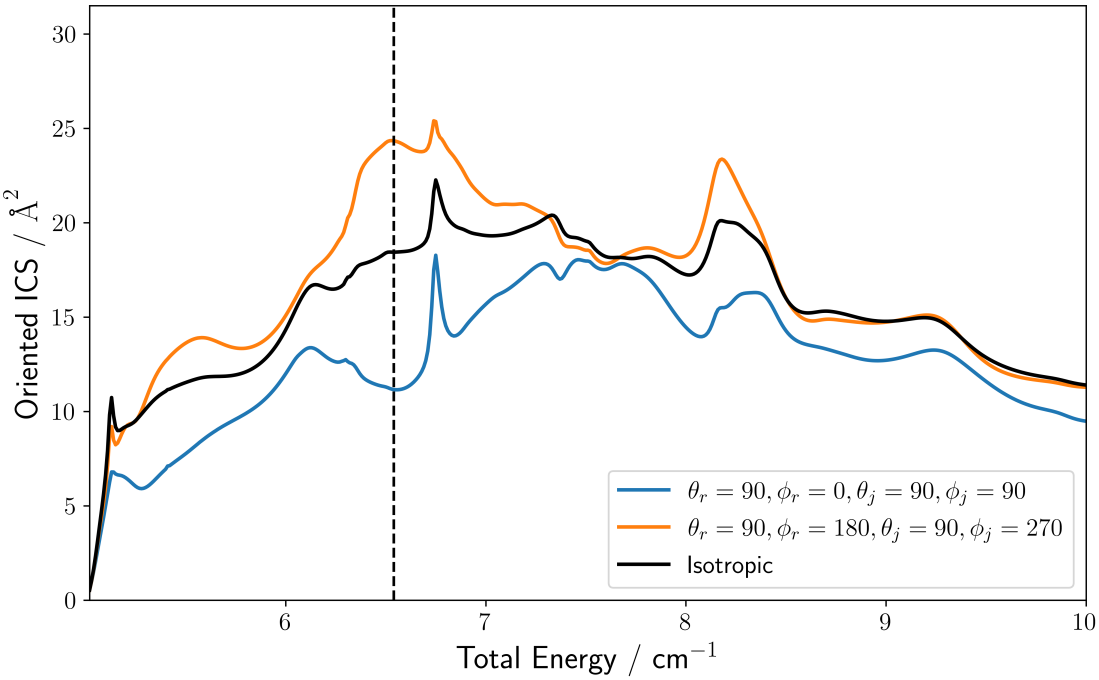

Figure 7.9: Oriented ICSs for energies ranging from $E_{\mathrm{TOT}} = 5.02\,\mathrm{cm}^{-1}$ to $10.00\,\mathrm{cm}^{-1}$. The orientations shown are $\boldsymbol{r}_{\mathrm{NO}}$ oriented in the $-x$ ($+x$) direction with $\boldsymbol{j}_{\mathrm{H_2}}$ oriented in $-y$ ($+y$) coloured in orange (blue). All angles are given in degrees. The vertical line is positioned at $E_{\mathrm{TOT}} = 6.54\,\mathrm{cm}^{-1}$. This is the energy discussed in the text.

Large Changes in the ICS

In Figure 7.9, two of these orientation sets are shown with energies in the range $E_{\mathrm{TOT}} = 5.02\,\mathrm{cm}^{-1}$ to $10.00\,\mathrm{cm}^{-1}$. The orange line corresponds to $-x$ orientation of $\boldsymbol{r}_{\mathrm{NO}}$ and $-y$ orientation of $\boldsymbol{j}_{\mathrm{H_2}}$. The blue line corresponds to the opposite of that, with $+x$ orientation of $\boldsymbol{r}_{\mathrm{NO}}$ and $+y$ orientation of $\boldsymbol{j}_{\mathrm{H_2}}$. The black line is the isotropic ICS.

The dashed vertical black line is positioned at $E_{\mathrm{TOT}} = 6.54\,\mathrm{cm}^{-1}$. At this energy there is a very large difference in the observed ICS. The orange orientation set has an ICS 2.18 times that of the blue orientation set. This effect is a combination of single molecule orientation effects, described by non-mixed moments, and of mutual orientation effects, described by mixed moments. Firstly, the moments corresponding to $\pm x$ orientation of $\boldsymbol{r}_{\mathrm{NO}}$ and $\pm y$ orientation of $\boldsymbol{j}_{\mathrm{H_2}}$, $o^{\{1,0\}}_{1+,0}$ and $o^{\{0,1\}}_{0,1-}$, have the normalised values -0.1255 and -0.1932 respectively at this energy. This hence gives a clear preference for $-x$ orientation of $\boldsymbol{r}_{\mathrm{NO}}$ and $-y$ orientation of

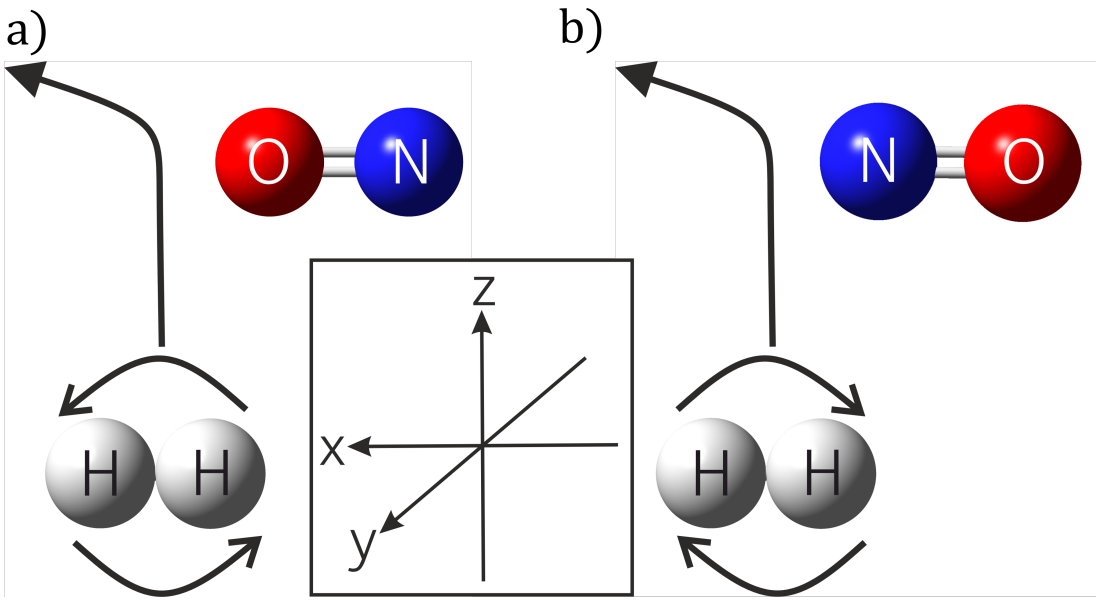

Figure 7.10: Cartoon depictions of the orientations shown in Figure 7.9. Panel a) Shows $+x$ orientation of $\boldsymbol{r}_{\mathrm{NO}}$ and $+y$ orientation of $\boldsymbol{j}_{\mathrm{H_2}}$, shown in blue in Figure 7.9. Panel b) shows $-x$ orientation of $\boldsymbol{r}_{\mathrm{NO}}$ and $-y$ orientation of $\boldsymbol{j}_{\mathrm{H_2}}$, shown in orange in Figure 7.9. Inset is a diagram of this axes used in these cartoons. The final angle of the arrow describing the scattering is arbitrary (except that in must be restricted to $+x$) in both panels, as only integral effects are discussed in the text, not differential effects.

$\boldsymbol{j}_{\mathrm{H_2}}$. There is also a not insignificant mutual orientation effect, as described by $o_{1+,1-}^{\{1,1\}}$, which has a normalised value of -0.0312. This negative value favours orientation sets with $+x$ ($-x$) orientation of $\boldsymbol{r}_{\mathrm{NO}}$ and $-y$ ($+y$) orientation of $\boldsymbol{j}_{\mathrm{H_2}}$. Hence, as the moment favours orientation sets in which one of the molecules has its polarisation inverted from the geometries portrayed in Figures 7.9 and 7.10, it actually disfavours both of those geometries, causing both to decrease by $0.69\,\text{Å}^2$. Therefore, although in this case the mutual orientation is not the driving force behind this large change in ICS, it is the fact that both molecules are oriented simultaneously and independently that facilitates it.

Mixed Moment Effects on Inverted Orientations

The dashed vertical line in Figure 7.11 is placed at $E_{\mathrm{TOT}} = 8.67\,\mathrm{cm}^{-1}$. At this point, the orange line passes through the black line, while the blue line is somewhat higher.

If a single molecule is oriented in a system, whatever effect occurs when it is oriented in one direction must be the opposite of what occurs in the opposite

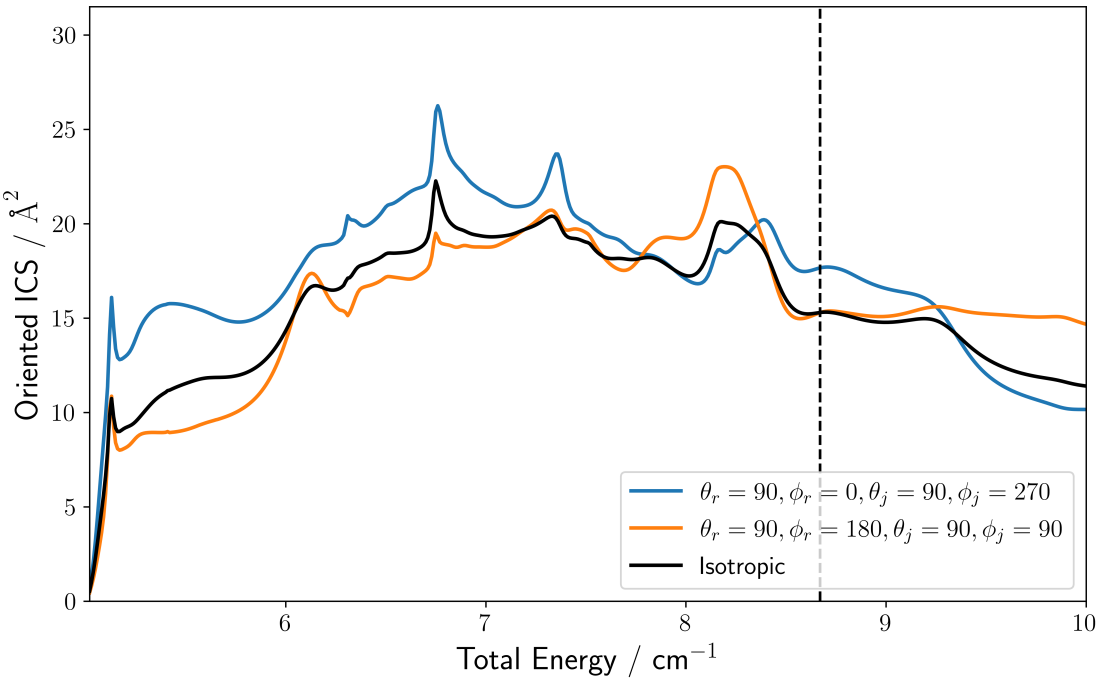

Figure 7.11: Oriented ICSs for energies ranging from $E_{\mathrm{TOT}} = 5.02\,\mathrm{cm}^{-1}$ to $10.00\,\mathrm{cm}^{-1}$. The orientations shown are $\boldsymbol{r}_{\mathrm{NO}}$ oriented in the $-x$ ($+x$) direction with $\boldsymbol{j}_{\mathrm{H_2}}$ oriented in $+y$ ($-y$) coloured in orange (blue). All angles are given in degrees. The vertical line is positioned at $E_{\mathrm{TOT}} = 8.67\,\mathrm{cm}^{-1}$. This is the energy discussed in the text.

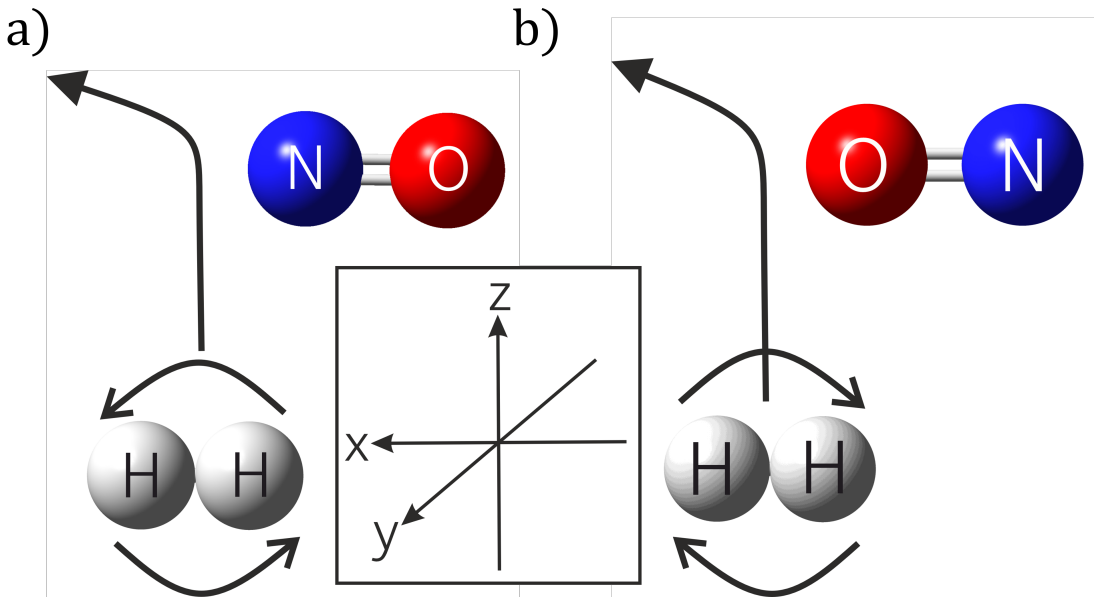

Figure 7.12: Cartoon depictions of the orientations shown in Figure 7.11. Panel a) Shows $-x$ orientation of $\boldsymbol{r}_{\mathrm{NO}}$ and $+y$ orientation of $\boldsymbol{j}_{\mathrm{H_2}}$, shown in orange in Figure 7.11. Panel b) shows $+x$ orientation of $\boldsymbol{r}_{\mathrm{NO}}$ and $-y$ orientation of $\boldsymbol{j}_{\mathrm{H_2}}$, shown in blue in Figure 7.11. Inset is a diagram of this axes used in these cartoons. The final angle of the arrow describing the scattering is arbitrary (except that in must be restricted to $+x$) in both panels, as only integral effects are discussed in the text, not differential effects.

direction. For example, if the ICS for NO oriented in the $+z$ direction with an Ar atom is 20% larger than the isotropic ICS, the ICS for $-z$ orientation must be 20% smaller. When both molecules are oriented, this no longer holds. Although the contributions to the ICS from non-mixed moments will follow the same pattern when both molecules have their orientations inverted, the contributions from the mixed moments will not change sign. This is illustrated well at $E_{\mathrm{TOT}} = 8.67\,\mathrm{cm}^{-1}$. The same three moments are at work as above. The normalised values of the $o_{1+,0}^{\{1,0\}}$, $o_{0,1-}^{\{0,1\}}$ and $o_{1+,1-}^{\{1,1\}}$ moments at this energy are 0.0151, -0.0527 and -0.0642 respectively. Hence, if $\boldsymbol{r}_{\mathrm{NO}}$ is oriented in the $-x$ direction and $\boldsymbol{j}_{\mathrm{H_2}}$ is oriented in the $+y$ direction, the non-mixed moments suggest an decrease in the ICS, while the mixed moment suggests a increase. The contributions to the oriented ICS in this case of these three moments is $-0.2308\,\mathrm{Å}^2$, $-0.9550\,\mathrm{Å}^2$ and $1.1780\,\mathrm{Å}^2$, giving a total contribution from the polarisation of $-0.0078\,\mathrm{Å}^2$, which is essentially negligible. However, when the polarisation of both molecules is inverted, now all of the contributions are positive, and of the same magnitude, giving a total contribution of $2.3638\,\mathrm{Å}^2$, which is definitely not negligible. This mutual orientation effect has the potential to be very powerful, particularly if it can be used in harmony with single molecule orientation effects to suppress or enhance a transition.

Suppression or Enhancement of a Resonance

Panel a) of Figure 7.13 shows the excitation function for different sets of orientations in the region between the energies $E_{\mathrm{TOT}} = 10.00\,\mathrm{cm}^{-1}$ and $20.00\,\mathrm{cm}^{-1}$. The orientation sets shown are for $-z$ orientation of $\boldsymbol{r}_{\mathrm{NO}}$ with $-y$ orientation of $\boldsymbol{j}_{\mathrm{H_2}}$, which is shown in blue, and $-x$ orientation of $\boldsymbol{r}_{\mathrm{NO}}$ with $+y$ orientation of $\boldsymbol{j}_{\mathrm{H_2}}$, shown in orange.

At $E_{\mathrm{TOT}} = 17.97\,\mathrm{cm}^{-1}$, a very small resonance may be seen in the isotropic ICS shown in black. This resonance is marked by a dashed black line. A dashed black line marks the same energy in Panel b), where the partial cross sections contributing to the isotropic ICS at these energies are shown. It is clear this

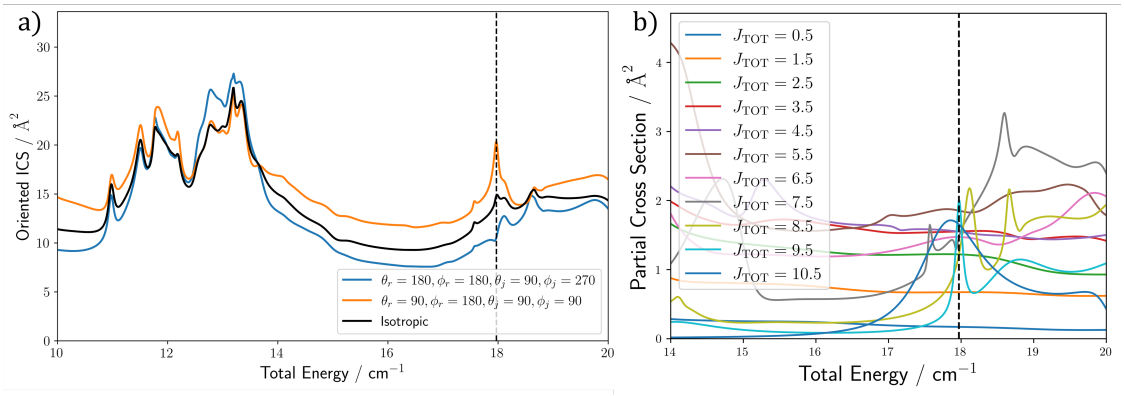

Figure 7.13: a) ICSs in the energy range $E_{\mathrm{TOT}} = 10.00\,\mathrm{cm}^{-1}$ to $20.00\,\mathrm{cm}^{-1}$. The black curve is the isotropic ICS. The ICS for $-z$ orientation of $\boldsymbol{r}_{\mathrm{NO}}$ with $-y$ orientation of $\boldsymbol{j}_{\mathrm{H_2}}$ is shown in blue. The ICS for $-x$ orientation of $\boldsymbol{r}_{\mathrm{NO}}$ with $+y$ orientation of $\boldsymbol{j}_{\mathrm{H_2}}$ is shown in orange. All angles are given in degrees. b) Partial cross sections in the same energy range for the isotropic ICS for partial waves from $J_{\mathrm{TOT}} = 0.5$ to 10.5. In both a) and b), a dashed line is drawn at $E_{\mathrm{TOT}} = 17.97\,\mathrm{cm}^{-1}$ to show the position of the resonance discussed in the text.

resonance is caused by the sharp peak in the $J_{\mathrm{TOT}} = 9.5$, although there are sharp increases in other partial waves nearby.

The two orientation sets have been chosen in Panel a) such that they maximise and minimise this resonance with respect to their surroundings (ie to not necessarily maximise the baseline ICS, but the size of the peak relative to this baseline). The orientation set represented by the blue curve causes a complete suppression of the resonance, while the set represented by the orange curve drastically enhances it.

The large enhancement or suppression of the resonance is made possible by harmonising the effects of the mixed moments with the non-mixed moments. Taking the $-x$ and $+y$ orientations of $\boldsymbol{r}_{\mathrm{NO}}$ and $\boldsymbol{j}_{\mathrm{H_2}}$ respectively, shown in orange in Figure 7.13, this becomes clear. The three relevant moments are $o_{0,1-}^{\{0,1\}}$, $o_{1+,0}^{\{1,0\}}$ and $o_{1+,1-}^{\{1,1\}}$ with normalised values of 0.1547, −0.0808 and −0.0889. Hence, in this configuration, they provide contributions of 2.7540 Å^2, 1.1989 Å^2 and 1.5813 Å^2 leading to a total contribution of 5.5343 Å^2. On the other hand, to remove the resonance, all three contributions must be negative. This cannot be achieved by inverting the orientation of the two molecules, as the mixed moment's contribution would not change sign. However by reorienting $\boldsymbol{r}_{\mathrm{NO}}$ in the $-z$ direction and $\boldsymbol{j}_{\mathrm{H_2}}$ in the $-y$ direction, shown in blue in Figure 7.13, this becomes possible. $o_{0,1-}^{\{0,1\}}$ remains pertinent here, while

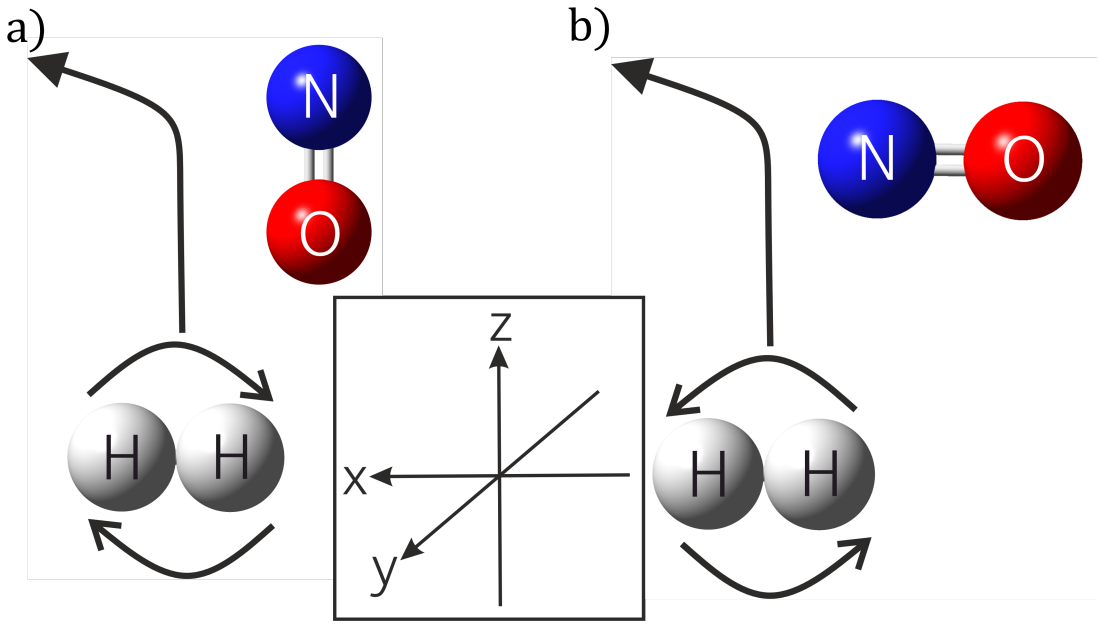

Figure 7.14: Cartoon depictions of the orientations shown in Figure 7.13. Panel a) Shows $-z$ orientation of $\boldsymbol{r}_{\mathrm{NO}}$ and $-y$ orientation of $\boldsymbol{j}_{\mathrm{H_2}}$, shown in blue in Figure 7.13. Panel b) shows $-x$ orientation of $\boldsymbol{r}_{\mathrm{NO}}$ and $+y$ orientation of $\boldsymbol{j}_{\mathrm{H_2}}$, shown in orange in Figure 7.13. Inset is a diagram of this axes used in these cartoons. The final angle of the arrow describing the scattering is arbitrary (except that in must be restricted to $+x$) in both panels, as only integral effects are discussed in the text, not differential effects.

the other two relevant moments are $o_{0,0}^{\{1,0\}}$ and $o_{0,1-}^{\{1,1\}}$ which have the normalised values 0.0499 and -0.0446. Hence, in this orientation, the contributions of the three moments are all negative: $-2.7540\,\text{Å}^2$, $-0.7394\,\text{Å}^2$ and $-0.7937\,\text{Å}^2$. This leads to a total contribution of $-4.2871\,\text{Å}^2$, and complete suppression of the resonance.

Interestingly, as in Section 7.6.2, rapid changes in the magnitudes of the mixed moments can be seen at the resonance. For example, across the range $E_{\mathrm{TOT}} = 17.87\,\mathrm{cm}^{-1} \rightarrow 17.97\,\mathrm{cm}^{-1} \rightarrow 18.07\,\mathrm{cm}^{-1}$, $o_{1+,1-}^{\{1,1\}}$'s normalised value becomes $-0.0358 \rightarrow -0.0889 \rightarrow -0.0454$, while $o_{0,1-}^{\{1,1\}}$'s normalised value becomes $-0.0024 \rightarrow -0.0446 \rightarrow 0.0027$. A similar pattern also appears for the $o_{0,1-}^{\{0,1\}}$ moment, whose value becomes $0.0926 \rightarrow 0.1547 \rightarrow 0.0413$. The sharp increases in the magnitude of the mixed moments at the resonance suggests that the resonance itself actually depends significantly on the mutual orientation of the molecules, although there is also evidence from non-mixed moments that it also depends on individual orientations, as has been shown before in other systems[209].

7.7 Theoretical Study II: Higher Collision Energy

In this study, the same system was analysed, but at a higher collision energy of $100\,\mathrm{cm}^{-1}$. This energy was chosen as a compromise between a desire to increase the energy to see more effects that may be described classically, and computational constraints. Ideally, a collision energy similar to that achievable in the proposed experiment would be studied, but this produces an exceptionally large basis set which becomes unmanageable with the compute available. One of the reasons a higher collision energy would be preferable is that one might expect larger contributions from the moments including orientation of the angular momentum of H_2 transitions that are rotationally inelastic in H_2. This is because if energy is being transferred from rotation in H_2, it would be expected that the direction of rotation of the molecule would strongly influence the efficiency of energy transfer. However, the next highest energy level for orthohydrogen is at $j_{H_2} = 3$, which lies almost $300\,\mathrm{cm}^{-1}$ above $j_{H_2} = 1$. Hence, all transitions shown in this study will be rotationally elastic in H_2.

However, the increased energy does allow for energy transfer into the rotation of NO. At $100\,\mathrm{cm}^{-1}$, the open channel with the greatest degree of rotational excitation has $j'_{NO} = 6.5$, and hence $\Delta j = 6$. At high Δj, one might expect the collisions to be more impulsive, and therefore, more likely to follow a more classical explanation for its behaviour. Hence, this study will focus on the changes in stereodynamic preferences with Δj, and investigate the differential steric effects at $j'_{NO} = 6.5$.

The quantum scattering calculations are performed using a maximum value of $J_{TOT} = 77.5$, and with $R_{End} = 80\,a_0$.

7.7.1 Integral Steric Asymmetry

The integral steric asymmetry (ISA) is a valuable way of visualising how the integral non-mixed moments vary as a function of Δj. For the purposes of this exercise, as the focus is on the non-mixed moments when investigating the ISA of NO, it is assumed that H_2 is unpolarised.

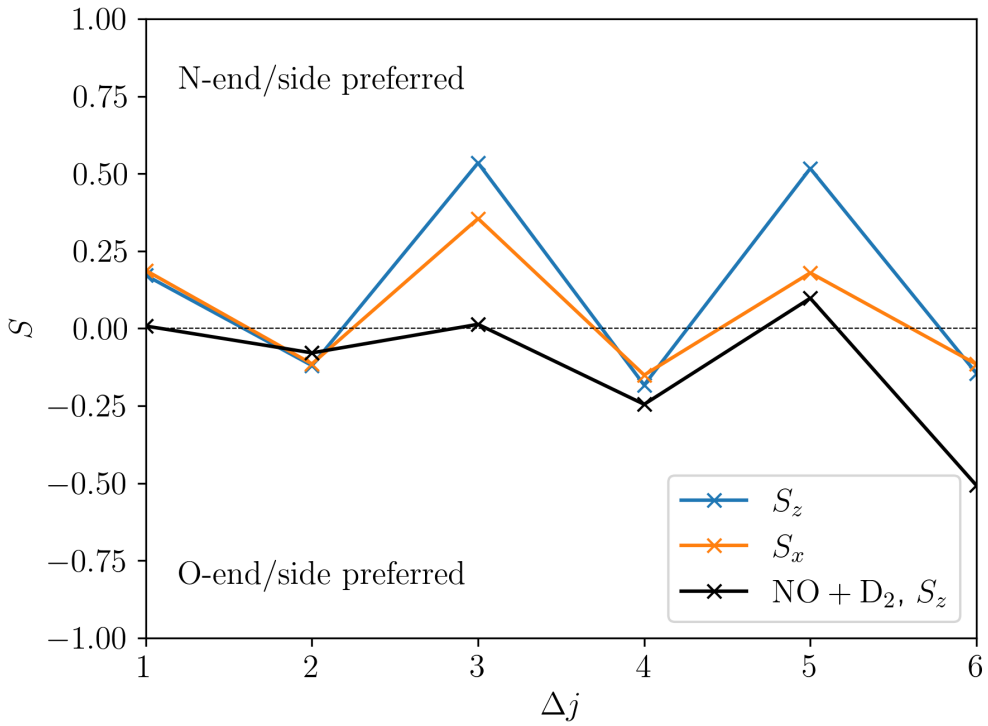

Figure 7.15: Integral Steric Asymmetries of NO + H_2 at $E_{coll} = 100\,cm^{-1}$ for orientation of the NO molecule in the $\pm z$ and $\pm x$ directions in blue and orange, respectively. Those with positive values of S correspond to collisions off the N-end or N-side for S_z and S_x respectively. The values of the experimental ISA for NO + D_2 at $551\,cm^{-1}$ is shown in black, with the data taken from reference [204]. Note that the values for this experimental data have been multiplied by -1, to make them consistent with the calculations shown for reasons described in reference [193]. In all three cases, the results are for a final e Λ-doublet state.

In Figure 7.15, the ISAs for orientation of NO along z and x are shown for NO + H_2, along with an experimental set of data for S_z in NO + D_2, collected by Stolte and coworkers[204] at a much higher energy of $551\,cm^{-1}$. This data is multiplied by -1 to make it consistent with the definitions provided in this chapter, as also described in reference [193]. These ISAs are all for a final e Λ-doublet in NO.

Firstly, it is reassuring that the oscillations in the ISAs as a function of Δj are reproduced with the same phase as is the experimental data, and with the same phase as those seen in Chapter 6. Secondly, it is also reassuring that S_x shares the same phase of oscillation, suggesting that when an N-end collision is preferred, as is an N-side collision. This is consistent with previous work on NO orientation [26, 228]. As both S_z and S_x are still oscillating significantly with Δj, it would be

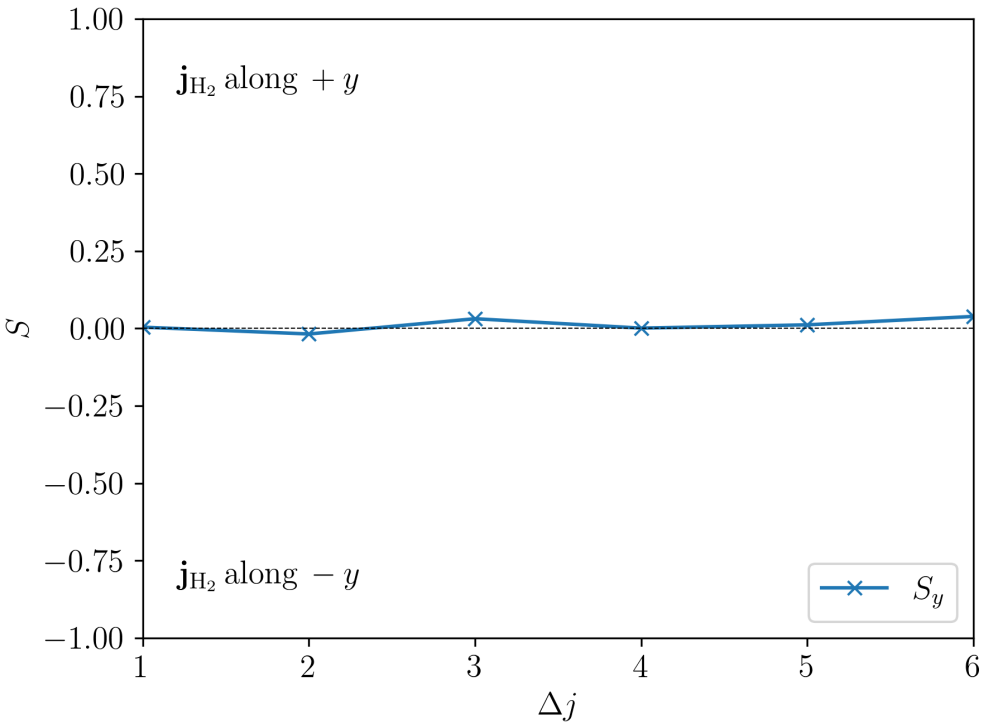

Figure 7.16: Integral Steric Asymmetry of NO + H_2 at $E_{coll} = 100\,cm^{-1}$ for orientation of the H_2 molecule's angular momentum along $\pm y$. A positive value corresponds to $\boldsymbol{j}_{H_2}$ preferentially oriented along $+y$, and vice versa.

unwise to attempt to use classical arguments to describe any behaviour here.

Figure 7.16 shows the ISA for orientation of $\boldsymbol{j}_{H_2}$ along $\pm y$. The first thing that should be noted, is that the values are all ≈ 0. There is no large oscillation in the value of S_y with Δj, as there is for S_z and S_x for NO orientation. There is some oscillation, but its amplitude is very small. Unfortunately, there are currently no studies looking at how H_2 angular momentum polarisation affects inelastic collisions at energies higher than a few wavenumbers, so the reasons for the behaviour of this ISA have not previously been discerned. Classically, one can make an argument that as the collision is elastic in H_2, and thus no rotational energy transfer takes place, the direction of rotation should make little difference. However, this cannot explain the lack of quantum mechanical interference effects.

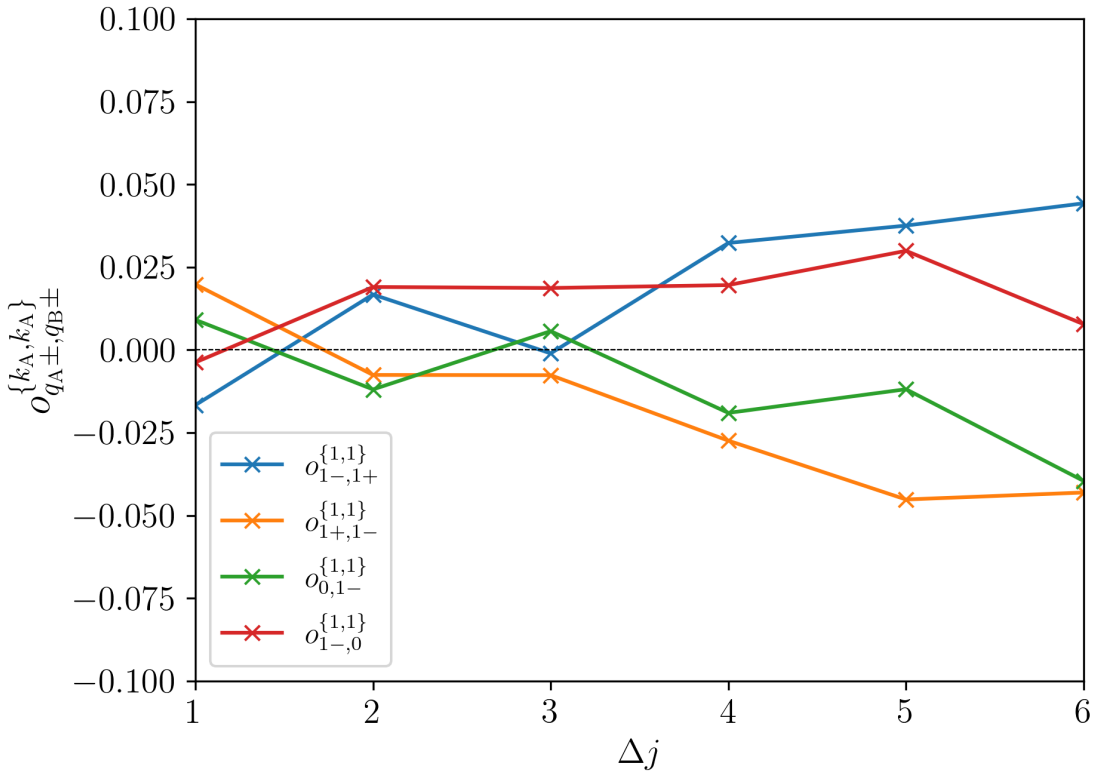

Figure 7.17: The values of the non-zero mixed moments as a function of Δj. The moments are: $o^{\{1,1\}}_{1+,1-}$ in orange, $o^{\{1,1\}}_{1-,1+}$ in blue, $o^{\{1,1\}}_{0,1-}$ in green and $o^{\{1,1\}}_{1-,0}$ in red.

7.7.2 Integral Values of the Mixed Moments

The mixed moments are also small at this energy, again likely due to the elastic nature of the collisions in H_2. However, the trends that are present can largely be explained classically. These moments are shown as a function of Δj in Figure 7.17. The oscillatory feature remarked upon in the context of the ISAs of the NO molecule are also present in these mixed moments, although to a much reduced degree. Two of these moments tend toward a positive value at high Δj, while two others tend toward a negative value at high Δj.

Note that favoured orientation sets of all of these mixed moments are shown in Figure 7.18 for clarity.

$o^{\{1,1\}}_{1+,1-}$, shown in orange, has a trend that may be explained classically. The COM of the NO molecule lies closer to the O-end than to the N-end. Hence, a greater torque is possible with a collision at the N-end. Supplementary to this, if

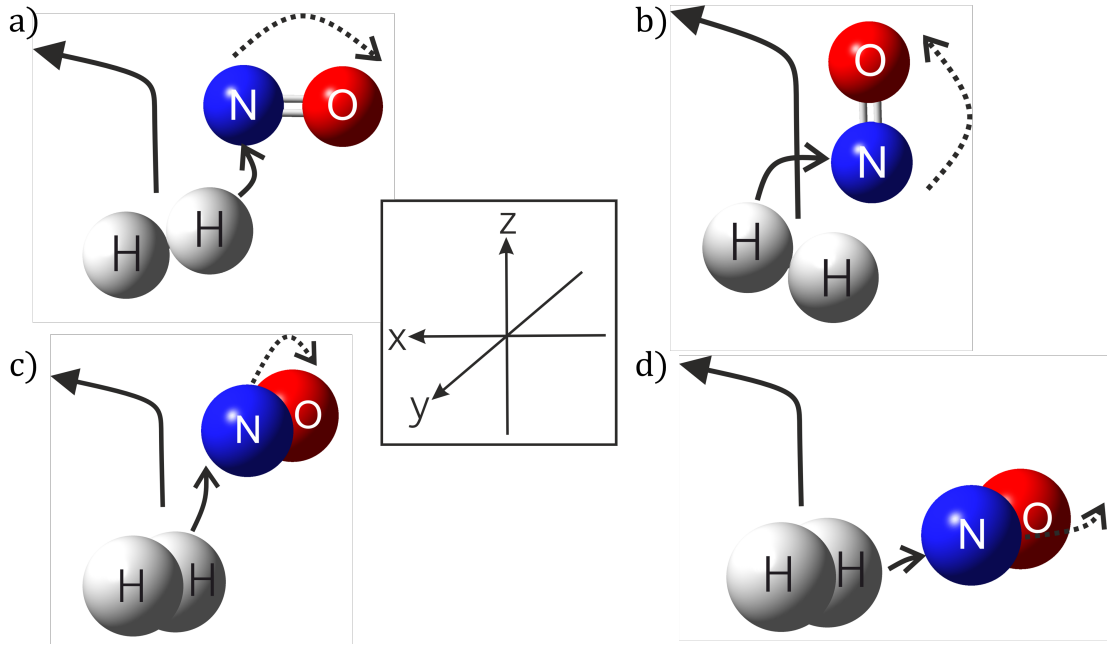

Figure 7.18: Cartoons depicting the orientation sets favoured by each non-zero mixed moment: a) $o^{\{1,1\}}_{1+,1-}$, b) $o^{\{1,1\}}_{0,1-}$, c) $o^{\{1,1\}}_{1-,1+}$ and d) $o^{\{1,1\}}_{1-,0}$. The axes defining the frame of reference is also shown. The vertical arrow that turns left represents the relative velocity of the system. The final direction of this arrow within the $+zx$ plane is arbitrary as these are integral moments.

the H_2 is rotating in such a way that imparts an extra degree of torque on collision, then this will further enhance the probability of a high Δj transition in NO. One of the orientation sets enhanced by the negative value of this moment is where $\boldsymbol{r}_{\mathrm{NO}}$ is oriented along $-x$ and $\boldsymbol{j}_{\mathrm{H_2}}$ is oriented along $+y$.

To ascertain how this orientation set would behave classically, it is crucial to know an estimate for the impact parameters that produce this transition. That information can be obtained by analysing the partial cross sections as a function of the total angular momentum quantum number J, as seen in Figure 7.19. There is no single value of l, the orbital angular momentum for a given J, and hence assigning exact impact parameters is impossible. However, for the mean value of J in the distribution, $J = 6.10$, impact parameters in the region of 1.8-2.3 Å can be assumed. NO has a bond length of ≈ 1.15 Å. Hence, given the masses of the two molecules, the N end of the bond lies ≈ 0.61 Å from the COM. In H_2 the bond length is ≈ 0.74 Å, with each H atom lying ≈ 0.37 Å away from the COM. Hence, an

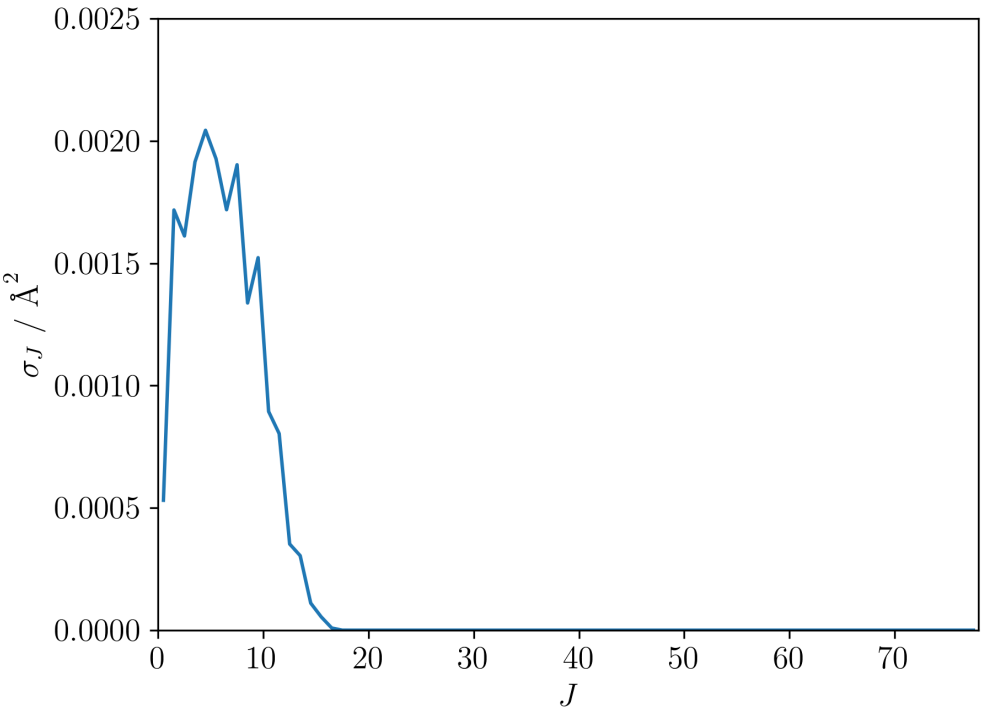

Figure 7.19: Partial cross sections, σ_J as a function of total angular momentum, J for the transition giving a final state of $j' = 6e$ in NO. The mean value of J in this transition is $J \approx 6.10$. $E_{\text{coll}} = 100\,\text{cm}^{-1}$.

impact parameter of around 2 Å places the entire H_2 molecule outside the NO bond.

Rotation orienting $\boldsymbol{j}_{H_2}$ along $+y$ produces an action in which the H_2 near the N-side of the molecule is moving upwards into the NO molecule with extra velocity in comparison to the COM frame velocity of H_2. This extra velocity increases the torque applied to the NO molecule, helping to produce higher levels of rotational excitation.

In the case of $o_{0,1-}^{\{1,1\}}$, in which one of the two favoured orientation sets for negative values involves $\boldsymbol{r}_{\text{NO}}$ oriented along $+z$ and $\boldsymbol{j}_{H_2}$ oriented along $-y$, a very similar rationalisation can be made. In this case, the H_2 will collide with the N-end of the molecule, with the force applied to the NO molecule causing initial motion of the N atom in the $-x$ direction. Orienting $\boldsymbol{j}_{H_2}$ along $-y$ allows the H_2 to hit the N end of the molecule with its rotation in such a way that it increases the torque applied to the N-end of the molecule in the same fashion as the general motion of the H_2 molecule. Hence, higher Δj transitions should become more likely with this orientation.

In cases where the NO molecule is oriented in the $\pm y$ direction, the classical

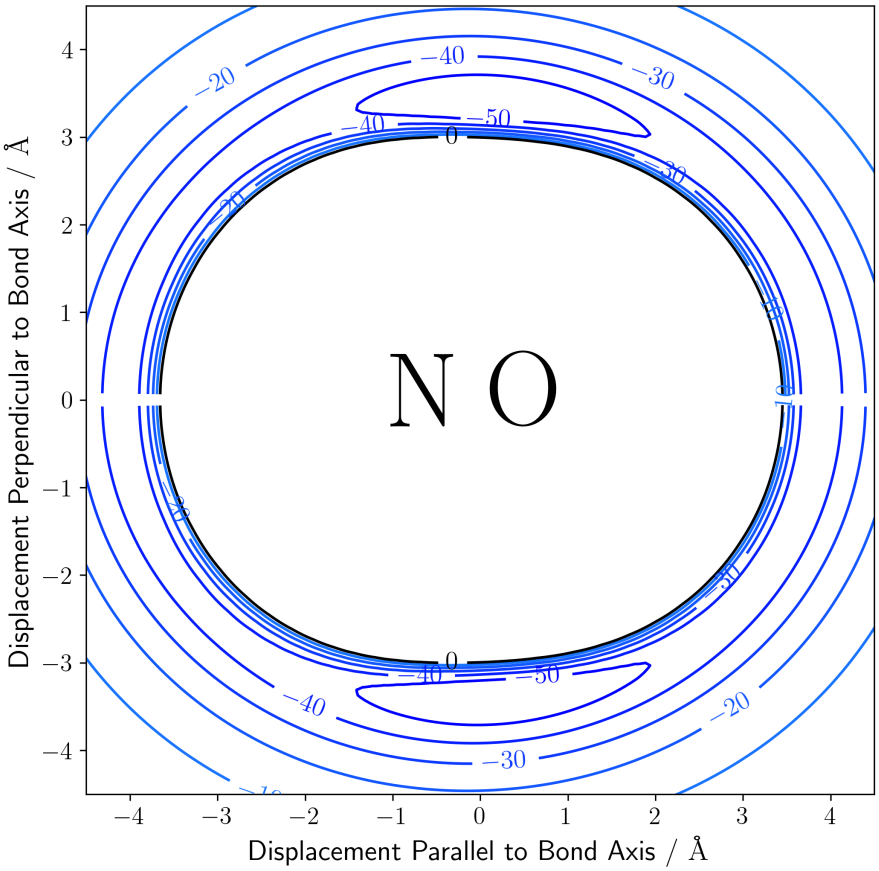

Figure 7.20: The sum of the diagonal terms of the potential energy matrix given by Kłos *et al.*[221] integrated over H_2 angles. The origin is the COM of the NO molecule. Energies are given in Hartrees.

explanation for the behaviour of the mixed moments is less clear. If $\boldsymbol{r}_{\mathrm{NO}}$ is oriented in the $-y$ direction, then the positive value of $o^{\{1,1\}}_{1-,1+}$ favours orientation of $\boldsymbol{j}_{\mathrm{H_2}}$ in the $-x$ direction. If the H_2 molecule were to travel such that the centre of mass of both molecules were to lie in the xz plane, then the H_2 molecule would be totally subsumed with the bond length of NO. One might then expect the rotation of H_2 that caused the H atom on the N-side of the molecule to move in the $+z$ direction as the two molecules collide would be best placed to cause greater rotational excitation. However, this would be a $+x$ orientation of $\boldsymbol{j}_{\mathrm{H_2}}$, the opposite of what is preferred according to Figure 7.17.

There is, however another explanation for this behaviour. It is highly unlikely in the scenario described above that the torque applied to the NO molecule is significant enough to cause an excitation to $j' = 6e$. Hence, the most plausible

geometry has the COM of the NO molecule offset from the xz plane, bringing the N-side of the molecule closer to the COM of the H_2 molecule. In that scenario, the same explanation as for $o^{\{1,1\}}_{1+,1-}$ may be applied, in which the inner hydrogen atom (relative to the NO molecule) rotates upwards to produce extra torque on the N-side. This would give a preference for $-x$ orientation of $\boldsymbol{j}_{H_2}$, helping to provide an explanation for the behaviour of the $o^{\{1,1\}}_{1-,1+}$ moment.

Evidence for this explanation may be found in Figure 7.20. Due to NO(X)'s $^2\Pi$ electronic state, there are two near-degenerate PESs which both contribute to the scattering process. The potential energy can then be given as a matrix in the basis of linear combinations of these electronic states [47, 229]. As discussed in Section 2.1, spin-orbit conserving collisions for a $^2\Pi$ molecule are governed by the diagonal elements of the potential energy matrix. Figure 7.20 shows these diagonal terms of the potential energy matrix, integrated over all H_2 angles. One would expect, in the orientation set required for $o^{\{1,1\}}_{1-,1+}$, for the H_2 molecule to approach the NO molecule side-on and then scatter such that it came no closer to either the N-side or O-side (see Figure 7.18). For the potential in Figure 7.20, it is clear that in the region at the top and bottom of the figure (the potential experienced in a side-on collision), the location in which the potential is parallel to the horizontal is slightly on the N-side of the molecule. Thus it would be collisions here resulting in the scattering described by $o^{\{1,1\}}_{1-,1+}$. If this is the case, with a collision on the N-side of the molecule, the same argument made above about the behaviour of this moment holds.

The classical argument for the behaviour of the $o^{\{1,1\}}_{1-,0}$ moment is very similar to $o^{\{1,1\}}_{1+,1-}$. One must consider the COM of the NO molecule offset from the scattering plane in the $-y$ orientation, and then, if $\boldsymbol{j}_{H_2}$ is oriented in the $-z$ direction, the H_2 molecule will be rotating in such a way that an extra 'kick' may be imparted on the N-side of the molecule, increasing the torque, and hence increasing the likelihood of higher rotational excitation in the NO molecule.

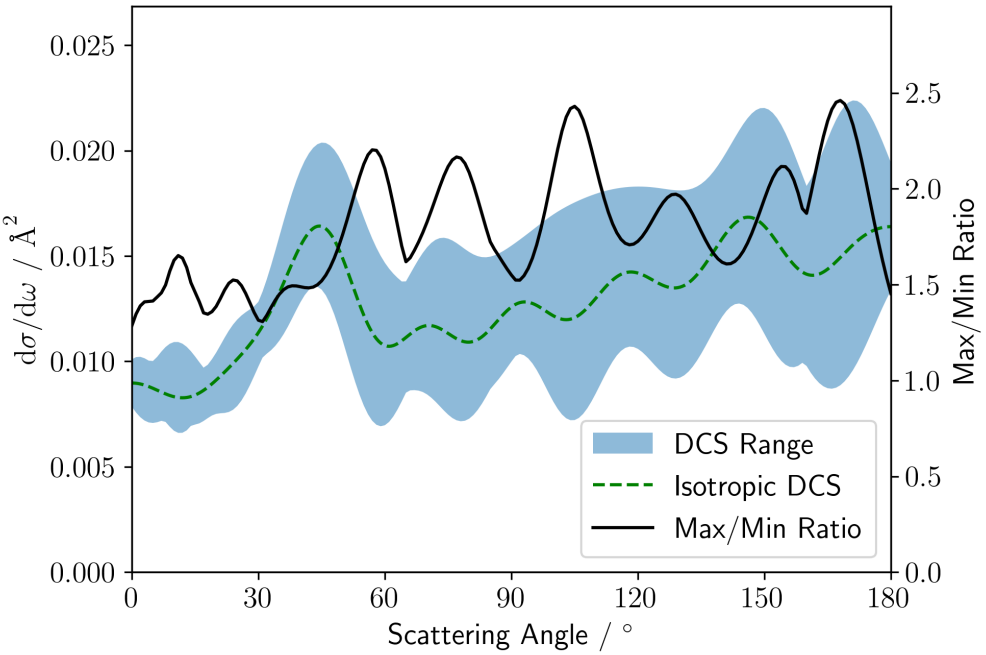

Figure 7.21: The range of possible values of the DCS for the transition from $j_{\mathrm{NO}} = 0.5$ at infinite field to $j'_{\mathrm{NO}} = 6.5e$ achievable by altering the directions of $\boldsymbol{r}_{\mathrm{NO}}$ and $\boldsymbol{j}_{\mathrm{H_2}}$. The isotropic DCS is shown as a dashed green line. Additionally, the ratio of the maximised DCS to the minimised DCS is shown in black.

7.7.3 Maximised and Minimised DCSs

In this section, the stereodynamical effects on the DCS for the transition to $j'_{\mathrm{NO}} = 6.5e$ will be analysed. A starting point for this analysis is Figure 7.21, in which the range of possible values for the DCS is shown for all possible directions of $\boldsymbol{r}_{\mathrm{NO}}$ and $\boldsymbol{j}_{\mathrm{H_2}}$. The upper limit of this range is the maximised DCS, while the lower limit is the minimised DCS. The dashed green line is the isotropic DCS. Also shown is black is the ratio between in the maximised and minimised DCSs.

Looking at this ratio, multiple locations can be identified where the difference between the minimised and maximised DCSs is particularly large. One such region is at around $\theta = 168°$. This scattering angle shows the largest ratio between the maximised and minimised DCSs. To understand this difference, the effects of the non-mixed moments, and also to a lesser extent the mixed moments, are required.

In the case of the maximised DCS, the optimised geometry involves $\boldsymbol{j}_{\mathrm{H_2}}$ oriented along the $-y$ direction, and $\boldsymbol{r}_{\mathrm{NO}}$ oriented somewhere in between $+x$ and $-z$. The

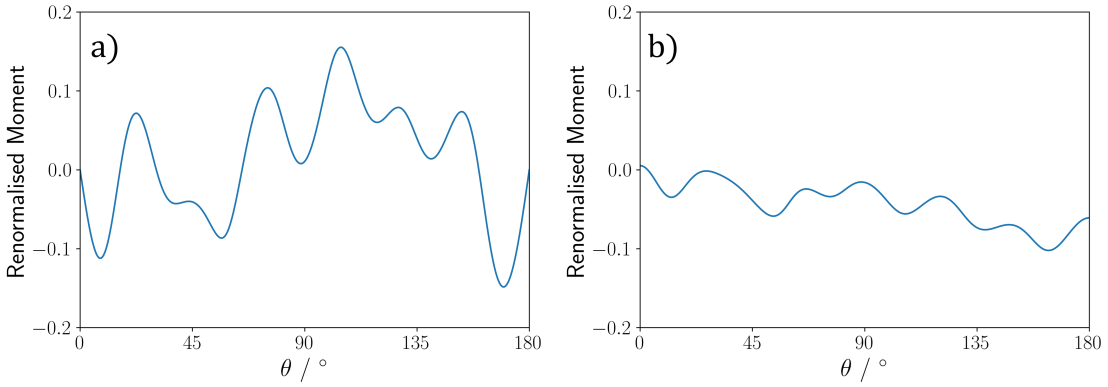

Figure 7.22: a) $O^{\{0,1\}}_{0,1-}(\theta)/O^{\{0,0\}}_{0,0}(\theta)$ and b) $O^{\{1,1\}}_{1+,1-}(\theta)/O^{\{0,0\}}_{0,0}(\theta)$ as a function of θ for the $j = 0.5$ at infinite field to $j = 6.5e$ transition.

key moments here are the three non-zero non-mixed moments, $O^{\{1,0\}}_{0,0}(\theta = 168°)$, $O^{\{1,0\}}_{1+,0}(\theta = 168°)$ and $O^{\{0,1\}}_{0,1-}(\theta = 168°)$, and the mixed moment $O^{\{1,1\}}_{1+,1-}(\theta = 168°)$. These have renormalised values (the unnormalised value divided by $O^{\{0,0\}}_{0,0}(\theta = 168°)$) of -0.2103, 0.1084, -0.1431 and -0.0949 respectively. In the maximised configuration, this results in contributions from the isotropic DCS of $+13.5\%$, $+8.3\%$, $+17.2\%$ and $+8.7\%$ respectively. Hence, this is one of the occasions where a mixed moment's value works in conjunction with the non-mixed moments to further increase the DCS.

In fact, it is the presence of the mixed moments that ensures a degree of $+x$ orientation in $\boldsymbol{r}_{\mathrm{NO}}$. Due to the significantly larger magnitude of the $O^{\{1,0\}}_{0,0}(\theta = 168°)$ moment over the $O^{\{1,0\}}_{1+,0}(\theta = 168°)$ moment, if there were no combined effects of orientation, one would expect full orientation of $\boldsymbol{r}_{\mathrm{NO}}$ along $-x$. However, the mixed moment corresponding to this orientation is small, but has an effect to depress the DCS slightly. On the other hand, when incorporating significant $+x$ orientation, the mixed moment $O^{\{1,1\}}_{1+,1-}(\theta = 168°)$ has a significant enhancing effect.

Analysing how the value of $O^{\{1,1\}}_{1+,1-}(\theta)$ changes with scattering angle (see Figure 7.22b), it becomes apparent that this moment trends toward becoming more important as the scattering becomes more concentrated in the backward direction. This can be attributed to the same mechanism as in Figure 7.18a. In the backward direction, one expects more impulsive scattering with smaller impact parameters. Thus the inner H atom would be able to hit a part of the PES with greater potential energy gradients as it swings up, resulting in a greater torque being applied to the

NO, producing high rotational excitation. This explains why this mixed moment only starts to contribute significantly in the backward scattering regime.

It is worth noting that the non-mixed $O_{0,1-}^{\{0,1\}}(\theta)$ in Figure 7.22, corresponding to orientation of $\boldsymbol{j}_{\mathrm{H_2}}$ along $\pm y$, varies significantly moving from backward to forward scattering. The integral version of this moment is ≈ 0, but slightly positive, as may be seen in Figure 7.16. Here, the more granular differential moment tells a different story. Rather than simply being small, it is significant, but oscillates between positive and negative values. At $\theta = 168°$, the value of this moment reaches a negative nadir, while at a different peak in the maximised DCS to minimised DCS ratio, at $\theta = 105°$, the value of $O_{0,1-}^{\{0,1\}}(\theta)$ reaches a positive peak. These effects cannot be simply explained by classical mechanics, and so is likely a quantum mechanical effect.

7.7.4 Simulated Ion Images For Selected Orientations

The focus of of much of this chapter has been to explore the theoretical framework that underlies analysis of the stereodynamics of this system. However, the purpose of the development of this framework is to be able to characterise the results of a future experiment. Hence, in Figure 7.23, some simulated central slice velocity-mapped ion images are produced for specific experimental geometries. The ion images shown are produced using the Monte Carlo simulation described in Chapter 3, but have flux-density and laser polarisation effects removed for generality. In each case a DCS, corresponding to the given set of orientations for scattering into $j'_{\mathrm{NO}} = 6.5e$, is inputted, with the slice shown being the centre of 45 slices. No distortions due to the presence of the rods in the ion optics are shown either.

Note that at $E_{\mathrm{coll}} = 100\,\mathrm{cm}^{-1}$, scattering into this final state would produce only a very small range of final COM frame velocities. Hence, given the experimental setup and its current limitations, the radius of the ion image would be very small, and thus a detailed angular distribution analysis would become challenging. However, given experimental collision energies would likely be in excess of $E_{\mathrm{coll}} = 500\,\mathrm{cm}^{-1}$, where the issue stated above would not appear, it is not unreasonable to look at this transition as an example of what might be expected.

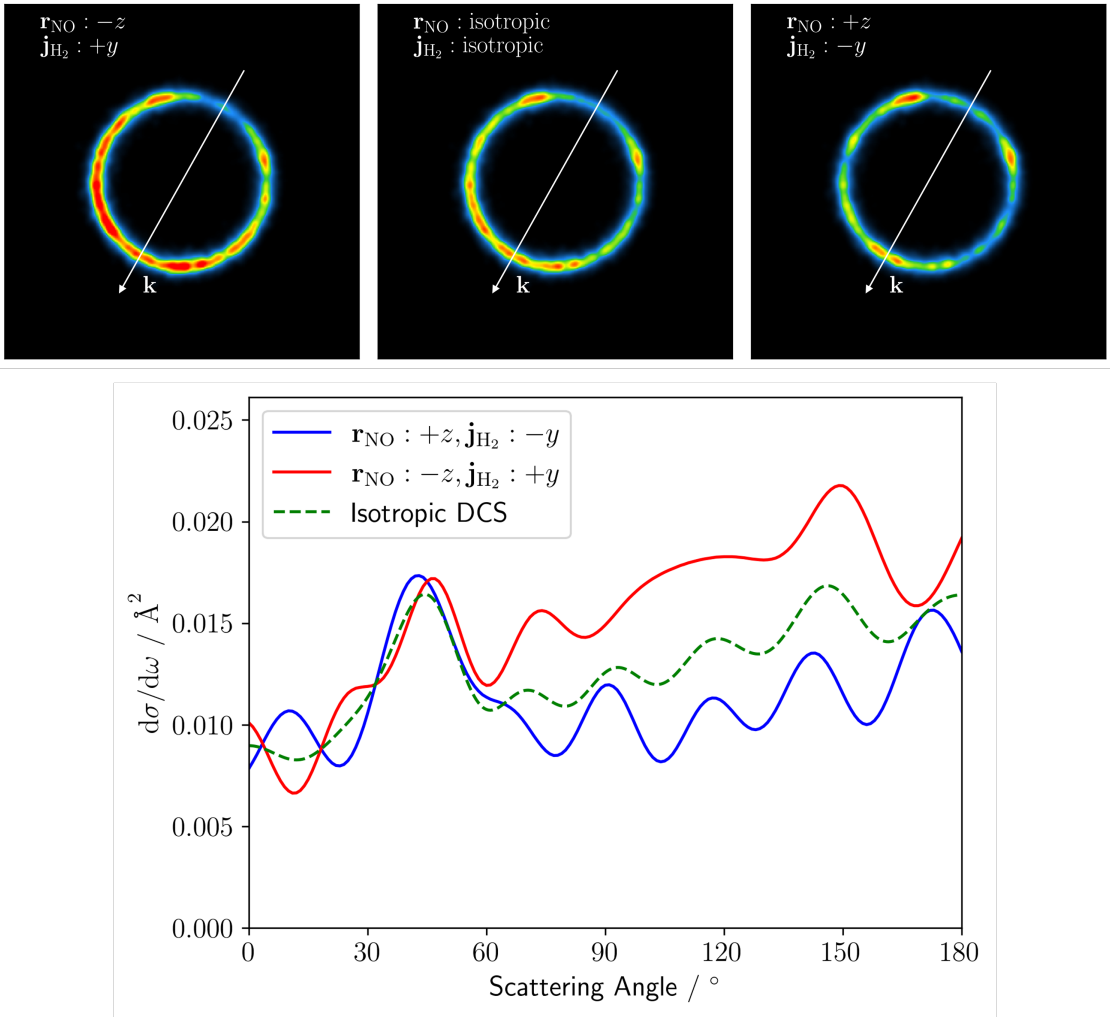

Figure 7.23: Upper Frames: A set of simulated central slice ion images, with flux-density and laser polarisation effects removed, for what could be observed experimentally for two opposite orientation sets ($\boldsymbol{r}_{NO} : -z, \boldsymbol{j}_{H_2} : +y$ and $\boldsymbol{r}_{NO} : +z, \boldsymbol{j}_{H_2} : -y$) and for the case in which there is no polarisation. Note that the relative velocity vector is defined $\boldsymbol{k} = \boldsymbol{v}_{H_2} - \boldsymbol{v}_{NO}$. Experimentally, it is the NO that is detected. Hence, the forward scattering region in the signal is in the opposite direction to $\boldsymbol{k}$. Lower Frame: The DCSs for each of the upper frames.

The central image uses the isotropic differential cross section, $O_{0,0}^{\{0,0\}}(\theta)$ (note this is isotropic in terms of polarisation, not scattering angle). The left hand side shows how the ion image changes upon the change in DCS when $\boldsymbol{r}_{NO}$ is oriented in the $-z$ direction, and $\boldsymbol{j}_{H_2}$ is oriented in the $+y$ direction. From the plots of the DCS below, it is easily ascertained that this set of orientations results in a significant increase in the DCS sideways to backward scattering regions. This is easily identifiable from the increase in the red hues towards the lower left corner of the image in comparison to

the isotropic DCS image. The right hand side image has its molecular orientations inverted with respect to the left hand image. From the plot of the DCSs, it is clear this has reduced intensity in the sideways to backward scattering direction with respect to the isotropic DCS, which is also easily visible in these regions of the image.

7.8 Conclusions and Future Work

This chapter has shown a significant extension of the work in Chapter 6, extending the mathematical framework of bond axis orientation of $^2\Pi$ molecules in an arbitrarily oriented electric field, to a situation in which, simultaneously and independently, a closed shell diatomic collision partner has its angular momentum oriented by magnetic fields. An experiment has been proposed, using the magnetic manipulation techniques of Alexandrowicz and coworkers to produce an oriented H_2 beam and applying them to the crossed molecular beam machine described in this thesis.

The mathematical basis for this experiment and the theoretical studies within this thesis has been outlined, stretching from the initial derivation of the complex PDDCSs, which describe how each possible polarisation of the two molecules affects differential and integral cross sections, to then applying Hertel-Stoll normalisation to these expansion moments to give them physical directional meanings.

Two theoretical studies have been performed. Firstly, an investigation of how the NO(X) + H_2 system might be influenced by the polarisation of $\boldsymbol{r}_{\mathrm{NO}}$ and $\boldsymbol{j}_{\mathrm{H_2}}$ at low collision energies, within the resonance regime. The power of this framework is to facilitate geometric mechanistic understanding of these processes. Some orientations were shown to be significantly enhancing transitions, while others suppressed transitions. Stereodynamic properties of the resonances were analysed, finding significant changes in steric preference across the energy range of a resonance. Some so-called 'mixed moments' were shown to spike in value specifically at resonances, hinting at specific geometric combinations being vital to support the resonance. This can lead to specific resonances being switched 'on' and 'off' with specific mutual orientations.

The second study focussed on some higher energy collisions at $E_{\text{coll}} = 100\,\text{cm}^{-1}$. While this energy remains below likely experimental collision energies, this higher energy did facilitate the exploration of some mixed moments via classical mechanics. A greater focus on differential effects in this study allowed analysis of how the value of some moments change with scattering angle, and hence impact parameter.

The proposed experiment in Section 7.2 does have the limitation that the quantisation axis along which the angular momentum of the H_2 would be oriented must be perpendicular to the propagation axis of the beam. Hence, not all of the orientations discussed in the theoretical discussion would be achievable with the experiment as it has been outlined. More work must be done to ascertain how to obtain orientation along the propagation axis of the beam.

This mathematical framework has the potential, as with Chapter 6, to also be applied to some symmetric top systems with inversion splitting, such as NH_3/ND_3, or to near-symmetric tops such as formaldehyde. Some extra work would be required for these systems due to the much greater possibility of superposition of inversion or K-doublets in the product states, which must be taken into account.

Similar work could also be completed in which the bond axes of two molecules are simultaneously oriented by a single electric field. The obvious example of which is the NO(X) + $ND_3(\tilde{X})$ system discussed in the context of the double hexapole in Chapter 4.

This work marks another step towards ultimate control of chemical reactions, providing a platform from which geometric control of both molecules can be investigated to provide a powerful tool to promote or suppress a chemical outcome at the user's discretion.

8
Conclusions

The work in this thesis is limited to inelastic scattering studies; however, this foundational work is essential to provide a platform for forging an ambitious new path toward significantly greater control of chemical reactions.

Firstly, preparatory work for an experiment in which both collision partners have their symmetry axes oriented in an electric field has been completed. This has principally been through the design and implementation of a double hexapole system to state select symmetric top molecules. This system has been tested and is working as intended. For an experiment in which the symmetric top molecule is not detected, it is likely to be necessary to add a beam stop into the beamline, a design for which was also presented.

Next, data analysis methods for 3D scattering data allowing inference of the product angular momentum distribution alongside the differential cross sections were presented. Having been applied to simulated data, these analysis methods both work as intended, although the so-called 'Slice Method' is the more versatile method and can be made more robust by analysing a wide array of slices through the ion cloud and solving for each one before averaging the results.

Following this, a general mathematical formulation that allows the characterisation of experimental stereodynamic effects in oriented scattering in electric fields involving a $^2\Pi$ molecule was shown. This extended work from previous publications

which looked at specific cases to one applicable to any initial j state. It may also be used to calculate these stereodynamic observables from the scattering amplitude, a quantity which may be derived from close-coupled equations. Hence, direct comparisons of theory and experiment become become possible. This was displayed through stereodynamic calculations of integral steric asymmetries and oriented differential cross sections. These calculations include those for NO(X) in $j = 1/2$, but are also shown for OH(X), with a $j = 3/2$ ground state. This has facilitated a comparison between experimental and theoretical stereodynamic data for bond axis orientation of OH in the ground state for the first time.

Finally, this framework was then extended to a system in which both molecules have a form of orientation: in this case, a $^2\Pi$ molecule with its bond axis oriented and another molecule with its angular momentum oriented by magnetic field manipulation. This was done with a potential experiment in mind in which the double hexapole is replaced by the magnetic hexapole system of Alexandrowicz and coworkers. Hence, an experiment in which NO(X) with its bond axis oriented could collide with H_2 with its angular momentum oriented is feasible and planned. This study showed the power of being able to control the polarisation in both molecules with regards to cross sections, both integral and differential. By combining the effects of orienting each molecule individually, and also the modification to these effects of having both molecules oriented simultaneously, great control of cross section is achievable. Evidence was also found that particular scattering resonances seem to be connecting to particular orientations of both molecules.

This work has been driving toward analysing collisions in which both molecules are oriented. Experimentally, the next step must be to carry out experiments on the NO(X) + $ND_3(\tilde{X})$ system and on the NO(X) + CH_3I system in which both molecules are simultaneously oriented before collision. These would be the first experiments analsying the complex stereodynamics of two oriented molecules. This could be extended to a system in which the symmetric top molecule is replaced with a radical, such as O or OH (which would also be oriented in the field). These would produce reactive collisions, an important next step toward systems

that are more relevant to real-world issues, which is the direction that modern scattering experiments are headed. Another potential future experiment involves using the double hexapole to focus and state select formaldehyde, potentially allowing analysis of how orientation of the formaldehyde molecule affects likelihood of radical addition into the carbonyl bond. Finally, the experiment involving H_2 with its angular momentum oriented should be carried out, realising the prospect of independent control of polarisation of both reactants.

On a theoretical front, mathematical frameworks must be devised to allow the characterisation of experiments in which both molecules have their symmetry axes oriented. This may be complicated due to the possibility that a symmetric top scattering partner could find itself reoriented by the electric field after the collision in a way the NO(X) does not. Development of MQCT methods to facilitate the calculation of accurate scattering amplitudes for inelastic collisions would then allow high quality theoretical calculation of the stereodynamics of complex systems, as full quantum mechanical calculations become too computationally expensive.

Further testing of the data analysis methods is required, particularly on real experimental data. These methods could also be adapted for transitions involving more than one photon.

By combining these mathematical frameworks, by testing theoretically calculated PESs, and by feeding a huge amount of experimental data into computers much more advanced than those of today, it should be possible to predict all of chemistry. If humanity can gain this power, control is at its fingertips.

Appendices

A

Matrix Elements of the Stark Effect Perturbation to the Hamiltonian for Asymmetric Tops

The contribution to the Hamiltonian of an asymmetric top due to an electric field, $\boldsymbol{E}$ is given by $\hat{H}_{\text{Stark}}$, as in Section 4.3.3. This may be further broken down into contributions from the dipole moment, $\boldsymbol{\mu}$, along each of the rotational axes used to calculate the three rotational constant. The axis labelled a corresponds to rotational constant A. The same principle applies to both b and c. Hence, $\hat{H}_{\text{Stark}} = \hat{H}_{\text{Stark,a}} + \hat{H}_{\text{Stark,b}} + \hat{H}_{\text{Stark,c}}$.

The matrix elements for the contribution along axis a are given by[166, 230]

$$\begin{aligned}\langle J,K,M|\hat{H}_{\text{Stark,a}}|J,K,M\rangle &= -\frac{MK}{J(J+1)}\mu_{\text{a}}E \\ \langle J+1,K,M|\hat{H}_{\text{Stark,a}}|J,K,M\rangle &= -\frac{\sqrt{(J+1)^2-K^2}\sqrt{(J+1)^2-M^2}}{(J+1)\sqrt{(2J+1)(2J+3)}}\mu_{\text{a}}E\,. \end{aligned} \quad \text{(A.1)}$$

The matrix elements for the contribution along axis b are given by

$$\begin{aligned}
\langle J, K+1, M|\hat{H}_{\mathrm{Stark,b}}|J, K, M\rangle &= \frac{M\sqrt{(J-K)(J+K+1)}}{2J(J+1)}\mu_{\mathrm{b}}E \\
\langle J+1, K\pm 1, M|\hat{H}_{\mathrm{Stark,b}}|J, K, M\rangle &= \\
&\pm \frac{\sqrt{(J\pm K+1)(J\pm K+2)}\sqrt{(J+1)^2-M^2}}{2J(J+1)\sqrt{(2J+1)(2J+3)}}\mu_{\mathrm{b}}E\,.
\end{aligned} \tag{A.2}$$

The matrix elements for the contribution along axis c are given by

$$\begin{aligned}
\langle J, K+1, M|\hat{H}_{\mathrm{Stark,c}}|J, K, M\rangle &= i\frac{M\sqrt{(J-K)(J+K+1)}}{2J(J+1)}\mu_{\mathrm{c}}E \\
\langle J+1, K\pm 1, M|\hat{H}_{\mathrm{Stark,c}}|J, K, M\rangle &= \\
&- i\frac{\sqrt{(J\pm K+1)(J\pm K+2)}\sqrt{(J+1)^2-M^2}}{2J(J+1)\sqrt{(2J+1)(2J+3)}}\mu_{\mathrm{c}}E\,.
\end{aligned} \tag{A.3}$$

All other matrix elements are 0, except those that can be inferred from the above using the Hamiltonian's hermitian properties. By combining these matrix elements with the field-free elements in Eq. 4.50, one can obtain a full Hamiltonian, which can then be diagonalised for its eigenvectors.

B

Hertel-Stoll Normalisation For 4-Vector Correlations

In this appendix, the derivation for the Hertel-Stoll normalised 4-vector correlation expansion moments will be provided.

B.1 Definitions

Returning to Eq. 7.1, and the definition of the 4-vector correlation moments in Eq. 7.2, the symmetry properties of the moments must be analysed. Using the relationship $C_{kq}(\theta,\phi) = (-1)^q C^*_{k-q}(\theta,\phi)$, Eq. 7.2 becomes

$$X^{(k_\mathrm{A},k_\mathrm{B})}_{q_\mathrm{A}.q_\mathrm{B}}(\theta) = (-1)^{q_\mathrm{A}+q_\mathrm{B}}\langle C^*_{k_\mathrm{A}-q_\mathrm{A}}(\theta_\mathrm{A},\phi_\mathrm{A})C^*_{k_\mathrm{B}-q_\mathrm{B}}(\theta_\mathrm{B},\phi_\mathrm{B})\rangle \tag{B.1}$$

and hence

$$[X^{(k_\mathrm{A},k_\mathrm{B})}_{q_\mathrm{A}.q_\mathrm{B}}(\theta)]^* = (-1)^{q_\mathrm{A}+q_\mathrm{B}}\langle C_{k_\mathrm{A}-q_\mathrm{A}}(\theta_\mathrm{A},\phi_\mathrm{A})C_{k_\mathrm{B}-q_\mathrm{B}}(\theta_\mathrm{B},\phi_\mathrm{B})\rangle \tag{B.2}$$

and finally

$$[X^{(k_\mathrm{A},k_\mathrm{B})}_{q_\mathrm{A}.q_\mathrm{B}}(\theta)]^* = (-1)^{q_\mathrm{A}+q_\mathrm{B}} X^{(k_\mathrm{A},k_\mathrm{B})}_{-q_\mathrm{A}.-q_\mathrm{B}}(\theta)\,. \tag{B.3}$$

Equivalently,

$$[C^{(k_{\rm A},k_{\rm B})}_{q_{\rm A}.q_{\rm B}}(\theta_{\rm A},\phi_{\rm A},\theta_{\rm B},\phi_{\rm B})]^* = (-1)^{q_{\rm A}+q_{\rm B}} C^{(k_{\rm A},k_{\rm B})}_{-q_{\rm A}.-q_{\rm B}}(\theta_{\rm A},\phi_{\rm A},\theta_{\rm B},\phi_{\rm B}) \tag{B.4}$$

$$= (-1)^{q_{\rm A}+q_{\rm B}} C_{k_{\rm A},q_{\rm A}}(\theta_{\rm A},\phi_{\rm A}) C_{k_{\rm B},q_{\rm B}}(\theta_{\rm B},\phi_{\rm B})\,. \tag{B.5}$$

This relationship provides enough information to devise linear combinations to obtain real and imaginary terms from the spherical harmonic products, before dividing imaginary terms by i, to obtain only real terms. Note that for brevity, the spherical harmonics will, from now on, be given as $C^{(k_{\rm A},k_{\rm B})}_{q_{\rm A}.q_{\rm B}}(\theta_{\rm A},\phi_{\rm A},\theta_{\rm B},\phi_{\rm B}) = C^{(k_{\rm A},k_{\rm B})}_{q_{\rm A}.q_{\rm B}}$.

$$C^{\{k_{\rm A},k_{\rm B}\}}_{(q_{\rm A},q_{\rm B})+} = \frac{1}{\sqrt{2}}\left[(-1)^{q_A+q_B} C_{k_{\rm A}q_{\rm A}} C_{k_{\rm B}q_{\rm B}} + C_{k_{\rm A}-q_{\rm A}} C_{k_{\rm B}-q_{\rm B}}\right] \quad q_{\rm A} \geq 0 \quad \text{and} \quad q_{\rm B} \neq 0 \tag{B.6}$$

$$C^{\{k_{\rm A},k_{\rm B}\}}_{(q_{\rm A},q_{\rm B})-} = \frac{1}{i\sqrt{2}}\left[(-1)^{q_A+q_B} C_{k_{\rm A}q_{\rm A}} C_{k_{\rm B}q_{\rm B}} - C_{k_{\rm A}-q_{\rm A}} C_{k_{\rm B}-q_{\rm B}}\right] \quad q_{\rm A} \geq 0 \quad \text{and} \quad q_{\rm B} \neq 0 \tag{B.7}$$

$$C^{\{k_{\rm A},k_{\rm B}\}}_{(q_{\rm A},0)+} = \frac{1}{\sqrt{2}}\left[(-1)^{q_A} C_{k_{\rm A}q_{\rm A}} C_{k_{\rm B}0} + C_{k_{\rm A}-q_{\rm A}} C_{k_{\rm B}0}\right] \quad q_{\rm A} \neq 0 \quad \text{and} \quad q_{\rm B} = 0 \tag{B.8}$$

$$C^{\{k_{\rm A},k_{\rm B}\}}_{(q_{\rm A},0)-} = \frac{1}{i\sqrt{2}}\left[(-1)^{q_A} C_{k_{\rm A}q_{\rm A}} C_{k_{\rm B}0} - C_{k_{\rm A}-q_{\rm A}} C_{k_{\rm B}0}\right] \quad q_{\rm A} \neq 0 \quad \text{and} \quad q_{\rm B} = 0 \tag{B.9}$$

$$C^{\{k_{\rm A},k_{\rm B}\}}_{(0,0)} = C_{k_{\rm A}0} C_{k_{\rm B}0} \qquad q_{\rm A} = q_{\rm B} = 0 \tag{B.10}$$

Next, one must then convert these real combinations of the modified spherical harmonics into a form which can be easily understood. The first step is to use the relation $C_{kq}(\theta,\phi) = C_{kq}(\theta,0)e^{iq\phi}$ to find

$$C^{\{k_{\rm A},k_{\rm B}\}}_{(q_{\rm A},q_{\rm B})+} = \sqrt{2} C_{k_{\rm A}-q_{\rm A}}(\theta_A,0) C_{k_{\rm B}-q_{\rm B}}(\theta_B,0)\cos\left(q_{\rm A}\phi_A + q_{\rm B}\phi_B\right) \quad q_{\rm A} > 0,\, q_{\rm B} > 0 \tag{B.11}$$

$$C^{\{k_{\rm A},k_{\rm B}\}}_{(q_{\rm A},-q_{\rm B})+} = (-1)^{q_{\rm B}}\sqrt{2} C_{k_{\rm A}-q_{\rm A}}(\theta_A,0) C_{k_{\rm B}-q_{\rm B}}(\theta_B,0)\cos\left(q_{\rm A}\phi_A - q_{\rm B}\phi_B\right) \quad q_{\rm A} > 0,\, q_{\rm B} > 0 \tag{B.12}$$

and

$$C^{\{k_{\rm A},k_{\rm B}\}}_{(q_{\rm A},q_{\rm B})-} = \sqrt{2} C_{k_{\rm A}-q_{\rm A}}(\theta_A,0) C_{k_{\rm B}-q_{\rm B}}(\theta_B,0)\sin\left(q_{\rm A}\phi_A + q_{\rm B}\phi_B\right) \quad q_{\rm A} > 0,\, q_{\rm B} > 0 \tag{B.13}$$

$$C^{\{k_{\rm A},k_{\rm B}\}}_{(q_{\rm A},-q_{\rm B})-} = (-1)^{q_{\rm B}}\sqrt{2} C_{k_{\rm A}-q_{\rm A}}(\theta_A,0) C_{k_{\rm B}-q_{\rm B}}(\theta_B,0)\sin\left(q_{\rm A}\phi_A - q_{\rm B}\phi_B\right) \quad q_{\rm A} > 0,\, q_{\rm B} > 0 \tag{B.14}$$

Hence, one can choose to define the Hertel-Stoll normalised spherical harmonic products

$$C^{\{k_{\rm A},k_{\rm B}\}}_{q_{\rm A}+,q_{\rm B}+} = \frac{1}{\sqrt{2}}\left[C^{\{k_{\rm A},k_{\rm B}\}}_{(q_{\rm A},q_{\rm B})+} + (-1)^{q_{\rm B}} C^{\{k_{\rm A},k_{\rm B}\}}_{(q_{\rm A},-q_{\rm B})+}\right] q_{\rm A} > 0,\, q_{\rm B} > 0 \tag{B.15}$$

$$C^{\{k_{\rm A},k_{\rm B}\}}_{q_{\rm A}-,q_{\rm B}-} = -\frac{1}{\sqrt{2}}\left[C^{\{k_{\rm A},k_{\rm B}\}}_{(q_{\rm A},q_{\rm B})+} - (-1)^{q_{\rm B}} C^{\{k_{\rm A},k_{\rm B}\}}_{(q_{\rm A},-q_{\rm B})+}\right] q_{\rm A} > 0,\, q_{\rm B} > 0 \tag{B.16}$$

$$C^{\{k_{\rm A},k_{\rm B}\}}_{q_{\rm A}+,q_{\rm B}-} = \frac{1}{\sqrt{2}}\left[C^{\{k_{\rm A},k_{\rm B}\}}_{(q_{\rm A},q_{\rm B})-} - (-1)^{q_{\rm B}} C^{\{k_{\rm A},k_{\rm B}\}}_{(q_{\rm A},-q_{\rm B})-}\right] q_{\rm A} > 0,\, q_{\rm B} > 0 \tag{B.17}$$

$$C^{\{k_{\rm A},k_{\rm B}\}}_{q_{\rm A}-,q_{\rm B}+} = \frac{1}{\sqrt{2}}\left[C^{\{k_{\rm A},k_{\rm B}\}}_{(q_{\rm A},q_{\rm B})-} + (-1)^{q_{\rm B}} C^{\{k_{\rm A},k_{\rm B}\}}_{(q_{\rm A},-q_{\rm B})-}\right] q_{\rm A} > 0,\, q_{\rm B} > 0 \tag{B.18}$$

which gives

$$C^{\{k_{\rm A},k_{\rm B}\}}_{q_{\rm A}+,q_{\rm B}+} = C_{k_{\rm A}-q_{\rm A}}(\theta_A,0) C_{k_{\rm B}-q_{\rm B}}(\theta_B,0)\cos(q_{\rm A}\phi_A)\cos(q_{\rm B}\phi_B) \tag{B.19}$$

$$C^{\{k_{\rm A},k_{\rm B}\}}_{q_{\rm A}-,q_{\rm B}-} = C_{k_{\rm A}-q_{\rm A}}(\theta_A,0) C_{k_{\rm B}-q_{\rm B}}(\theta_B,0)\sin(q_{\rm A}\phi_A)\sin(q_{\rm B}\phi_B) \tag{B.20}$$

$$C^{\{k_{\rm A},k_{\rm B}\}}_{q_{\rm A}+,q_{\rm B}-} = C_{k_{\rm A}-q_{\rm A}}(\theta_A,0) C_{k_{\rm B}-q_{\rm B}}(\theta_B,0)\cos(q_{\rm A}\phi_A)\sin(q_{\rm B}\phi_B) \tag{B.21}$$

$$C^{\{k_{\rm A},k_{\rm B}\}}_{q_{\rm A}-,q_{\rm B}+} = C_{k_{\rm A}-q_{\rm A}}(\theta_A,0) C_{k_{\rm B}-q_{\rm B}}(\theta_B,0)\sin(q_{\rm A}\phi_A)\cos(q_{\rm B}\phi_B) \tag{B.22}$$

in which the effects of all four angles are separable.

Hence, the Hertel-Stoll normalised spherical harmonic products are given by

$$\begin{aligned} C^{\{k_{\rm A},k_{\rm B}\}}_{q_{\rm A}\pm,q_{\rm B}\pm} =& \pm\frac{1}{2}\Big[(-1)^{q_A+q_B} C^{(k_{\rm A},k_{\rm B})}_{q_{\rm A},q_{\rm B}} + C^{(k_{\rm A},k_{\rm B})}_{-q_{\rm A},-q_{\rm B}} \\ & \pm (-1)^{q_{\rm B}}\left((-1)^{q_A+q_B} C^{(k_{\rm A},k_{\rm B})}_{q_{\rm A},-q_{\rm B}} + C^{(k_{\rm A},k_{\rm B})}_{-q_{\rm A},q_{\rm B}}\right)\Big] q_{\rm A} > 0,\, q_{\rm B} > 0 \end{aligned} \tag{B.23}$$

$$\begin{aligned} C^{\{k_{\rm A},k_{\rm B}\}}_{q_{\rm A}\pm,q_{\rm B}\mp} =& \frac{1}{2i}\Big[(-1)^{q_A+q_B} C^{(k_{\rm A},k_{\rm B})}_{q_{\rm A},q_{\rm B}} - C^{(k_{\rm A},k_{\rm B})}_{-q_{\rm A},-q_{\rm B}} \\ & \mp (-1)^{q_{\rm B}}\left((-1)^{q_A+q_B} C^{(k_{\rm A},k_{\rm B})}_{q_{\rm A},-q_{\rm B}} - C^{(k_{\rm A},k_{\rm B})}_{-q_{\rm A},q_{\rm B}}\right)\Big] q_{\rm A} > 0,\, q_{\rm B} > 0 \end{aligned} \tag{B.24}$$

and

$$C^{\{k_{\rm A},k_{\rm B}\}}_{0,q_{\rm B}+} = \frac{1}{\sqrt{2}}\left[(-1)^{q_B} C^{(k_{\rm A},k_{\rm B})}_{0,q_{\rm B}} + C^{(k_{\rm A},k_{\rm B})}_{0,-q_{\rm B}}\right] \quad q_{\rm A} = 0 \quad \text{and} \quad q_{\rm B} > 0 \tag{B.25}$$

$$C^{\{k_{\rm A},k_{\rm B}\}}_{0,q_{\rm B}-} = \frac{1}{i\sqrt{2}}\left[(-1)^{q_B} C^{(k_{\rm A},k_{\rm B})}_{0,q_{\rm B}} - C^{(k_{\rm A},k_{\rm B})}_{0,-q_{\rm B}}\right] \quad q_{\rm A} = 0 \quad \text{and} \quad q_{\rm B} > 0 \tag{B.26}$$

$$C^{\{k_{\rm A},k_{\rm B}\}}_{q_{\rm A}+,0} = \frac{1}{\sqrt{2}}\left[(-1)^{q_A} C^{(k_{\rm A},k_{\rm B})}_{q_{\rm A},0} + C^{(k_{\rm A},k_{\rm B})}_{-q_{\rm A},0}\right] \quad q_{\rm A} > 0 \quad \text{and} \quad q_{\rm B} = 0 \tag{B.27}$$

$$C^{\{k_{\rm A},k_{\rm B}\}}_{q_{\rm A}-,0} = \frac{1}{i\sqrt{2}}\left[(-1)^{q_A} C^{(k_{\rm A},k_{\rm B})}_{q_{\rm A},0} - C^{(k_{\rm A},k_{\rm B})}_{-q_{\rm A},0}\right] \quad q_{\rm A} > 0 \quad \text{and} \quad q_{\rm B} = 0 \tag{B.28}$$

$$C^{\{k_{\rm A},k_{\rm B}\}}_{0,0} = C^{(k_{\rm A},k_{\rm B})}_{0,0}, \quad q_{\rm A} = 0 \quad \text{and} \quad q_{\rm B} = 0\,. \tag{B.29}$$

Using the fact that the intrinsic moments, $X^{(k_{\rm A},k_{\rm B})}_{q_{\rm A}.q_{\rm B}}(\theta)$, share the same symmetry relations as for the spherical harmonic products (see Eqs. (B.3) and (B.4)), it can then be analogously stated that the Hertel-Stoll normalised moments are given as described in Chapter 7. The extrinsic moments are simply a constant multiplied by a spherical harmonic. Hence, when the two extrinsic moments are multiplied together, they form a spherical harmonic product which can be Hertel-Stoll normlalised in the same way as Eqs. (B.23) and (B.25).

B.2 Comparison to Complex Case

Now that the Hertel-Stoll normalised moments have been defined, it becomes necessary to ensure the expansion of the differential cross section in Eq. 7.30 using complex moments can be recovered from a similar expansion of the Hertel-Stoll normalised moments. Firstly, it is assumed that the scattering angular distribution can be given by

$$
\begin{aligned}
P(\theta) = \sum_{k_{\rm A}=0}^{\infty}\sum_{k_{\rm B}=0}^{\infty}(2k_{\rm A}+1)(2k_{\rm B}+1)\Bigg[\sum_{\substack{q_{\rm A}>0\\ q_{\rm B}>0}}\Bigg(&X^{\{k_{\rm A},k_{\rm B}\}}_{q_{\rm A}+,q_{\rm B}+}C^{\{k_{\rm A},k_{\rm B}\}}_{q_{\rm A}+,q_{\rm B}+} \\
&+X^{\{k_{\rm A},k_{\rm B}\}}_{q_{\rm A}-,q_{\rm B}-}C^{\{k_{\rm A},k_{\rm B}\}}_{q_{\rm A}-,q_{\rm B}-} \\
&+X^{\{k_{\rm A},k_{\rm B}\}}_{q_{\rm A}+,q_{\rm B}-}C^{\{k_{\rm A},k_{\rm B}\}}_{q_{\rm A}+,q_{\rm B}-} \\
&+X^{\{k_{\rm A},k_{\rm B}\}}_{q_{\rm A}-,q_{\rm B}+}C^{\{k_{\rm A},k_{\rm B}\}}_{q_{\rm A}-,q_{\rm B}+}\Bigg) \\
+\sum_{q_{\rm A}>0}\Bigg(&X^{\{k_{\rm A},k_{\rm B}\}}_{q_{\rm A}+,0}C^{\{k_{\rm A},k_{\rm B}\}}_{q_{\rm A}+,0} \\
&+X^{\{k_{\rm A},k_{\rm B}\}}_{q_{\rm A}-,0}C^{\{k_{\rm A},k_{\rm B}\}}_{q_{\rm A}-,0}\Bigg) \\
+\sum_{q_{\rm B}>0}\Bigg(&X^{\{k_{\rm A},k_{\rm B}\}}_{0,q_{\rm B}+}C^{\{k_{\rm A},k_{\rm B}\}}_{0,q_{\rm B}+} \\
&+X^{\{k_{\rm A},k_{\rm B}\}}_{0,q_{\rm B}-}C^{\{k_{\rm A},k_{\rm B}\}}_{0,q_{\rm B}-}\Bigg) \\
&+X^{\{k_{\rm A},k_{\rm B}\}}_{0,0}C^{\{k_{\rm A},k_{\rm B}\}}_{0,0}\Bigg]
\end{aligned}
\tag{B.30}
$$

where q_{A} and q_{B} are limited to be between $-k_{\mathrm{A}}$ and k_{A}, and $-k_{\mathrm{B}}$ and k_{B} respectively. Note that for moments and spherical harmonic products, angle dependencies have been suppressed.

The next step is to expand each product of Hertel-Stoll normalised expansion coefficients with Hertel-Stoll normalised product of spherical harmonics in terms of their complex counterparts. In what follows, the products are labelled 1-9 from top to bottom.

To break the problem down, the first four products are analysed first. The expansion of each one of these products gives 16 terms. However all terms resulting from the expansion of product 1 are reproduced identically for products 2-4, except for changes in sign. Hence, the entire expansion for products 1-4 is given by the expression in B.31. Before each term in the expansion is a bracket containing the prefactor for that term for each of products 1-4, in that order. Note that the angle dependency of individual spherical harmonics has also been suppressed here.

$$
\begin{aligned}
&\frac{1}{4}\Bigg(\\
&(1+1-1-1)X^{(k_{\mathrm{A}},k_{\mathrm{B}})}_{q_{\mathrm{A}},q_{\mathrm{B}}}C_{k_{\mathrm{A}}q_{\mathrm{A}}}C_{k_{\mathrm{B}}q_{\mathrm{B}}} \\
&(1+1+1+1)(-1)^{q_{\mathrm{A}}+q_{\mathrm{B}}}X^{(k_{\mathrm{A}},k_{\mathrm{B}})}_{q_{\mathrm{A}},q_{\mathrm{B}}}C_{k_{\mathrm{A}}-q_{\mathrm{A}}}C_{k_{\mathrm{B}}-q_{\mathrm{B}}} \\
&(1-1+1-1)(-1)^{q_{\mathrm{B}}}X^{(k_{\mathrm{A}},k_{\mathrm{B}})}_{q_{\mathrm{A}},q_{\mathrm{B}}}C_{k_{\mathrm{A}}q_{\mathrm{A}}}C_{k_{\mathrm{B}}-q_{\mathrm{B}}} \\
&(1-1-1+1)(-1)^{q_{\mathrm{A}}}X^{(k_{\mathrm{A}},k_{\mathrm{B}})}_{q_{\mathrm{A}},q_{\mathrm{B}}}C_{k_{\mathrm{A}}-q_{\mathrm{A}}}C_{k_{\mathrm{B}}q_{\mathrm{B}}} \\
&(1+1+1+1)(-1)^{q_{\mathrm{A}}+q_{\mathrm{B}}}X^{(k_{\mathrm{A}},k_{\mathrm{B}})}_{-q_{\mathrm{A}},-q_{\mathrm{B}}}C_{k_{\mathrm{A}}q_{\mathrm{A}}}C_{k_{\mathrm{B}}q_{\mathrm{B}}} \\
&(1+1-1-1)X^{(k_{\mathrm{A}},k_{\mathrm{B}})}_{-q_{\mathrm{A}},-q_{\mathrm{B}}}C_{k_{\mathrm{A}}-q_{\mathrm{A}}}C_{k_{\mathrm{B}}-q_{\mathrm{B}}} \\
&(1-1-1+1)(-1)^{q_{\mathrm{A}}}X^{(k_{\mathrm{A}},k_{\mathrm{B}})}_{-q_{\mathrm{A}},-q_{\mathrm{B}}}C_{k_{\mathrm{A}}q_{\mathrm{A}}}C_{k_{\mathrm{B}}-q_{\mathrm{B}}} \\
&(1-1+1-1)(-1)^{q_{\mathrm{B}}}X^{(k_{\mathrm{A}},k_{\mathrm{B}})}_{-q_{\mathrm{A}},-q_{\mathrm{B}}}C_{k_{\mathrm{A}}-q_{\mathrm{A}}}C_{k_{\mathrm{B}}q_{\mathrm{B}}} \\
&(1-1+1-1)(-1)^{q_{\mathrm{B}}}X^{(k_{\mathrm{A}},k_{\mathrm{B}})}_{q_{\mathrm{A}},-q_{\mathrm{B}}}C_{k_{\mathrm{A}}q_{\mathrm{A}}}C_{k_{\mathrm{B}}q_{\mathrm{B}}} \\
&(1-1-1+1)(-1)^{q_{\mathrm{A}}}X^{(k_{\mathrm{A}},k_{\mathrm{B}})}_{q_{\mathrm{A}},-q_{\mathrm{B}}}C_{k_{\mathrm{A}}-q_{\mathrm{A}}}C_{k_{\mathrm{B}}-q_{\mathrm{B}}} \\
&(1+1-1-1)X^{(k_{\mathrm{A}},k_{\mathrm{B}})}_{q_{\mathrm{A}},-q_{\mathrm{B}}}C_{k_{\mathrm{A}}q_{\mathrm{A}}}C_{k_{\mathrm{B}}-q_{\mathrm{B}}} \\
&(1+1+1+1)(-1)^{q_{\mathrm{A}}+q_{\mathrm{B}}}X^{(k_{\mathrm{A}},k_{\mathrm{B}})}_{q_{\mathrm{A}},-q_{\mathrm{B}}}C_{k_{\mathrm{A}}-q_{\mathrm{A}}}C_{k_{\mathrm{B}}q_{\mathrm{B}}} \\
&(1-1-1+1)(-1)^{q_{\mathrm{A}}}X^{(k_{\mathrm{A}},k_{\mathrm{B}})}_{-q_{\mathrm{A}},q_{\mathrm{B}}}C_{k_{\mathrm{A}}q_{\mathrm{A}}}C_{k_{\mathrm{B}}q_{\mathrm{B}}} \\
&(1-1+1-1)(-1)^{q_{\mathrm{B}}}X^{(k_{\mathrm{A}},k_{\mathrm{B}})}_{-q_{\mathrm{A}},q_{\mathrm{B}}}C_{k_{\mathrm{A}}-q_{\mathrm{A}}}C_{k_{\mathrm{B}}-q_{\mathrm{B}}} \\
&(1+1+1+1)(-1)^{q_{\mathrm{A}}+q_{\mathrm{B}}}X^{(k_{\mathrm{A}},k_{\mathrm{B}})}_{-q_{\mathrm{A}},q_{\mathrm{B}}}C_{k_{\mathrm{A}}q_{\mathrm{A}}}C_{k_{\mathrm{B}}-q_{\mathrm{B}}} \\
&(1+1-1-1)X^{(k_{\mathrm{A}},k_{\mathrm{B}})}_{-q_{\mathrm{A}},q_{\mathrm{B}}}C_{k_{\mathrm{A}}-q_{\mathrm{A}}}C_{k_{\mathrm{B}}q_{\mathrm{B}}}\Bigg)
\end{aligned}
\tag{B.31}
$$

Hence, only four terms survive to give

$$
\begin{aligned}
&\frac{1}{4}\Big(4(-1)^{q_{\mathrm{A}}+q_{\mathrm{B}}}X^{(k_{\mathrm{A}},k_{\mathrm{B}})}_{q_{\mathrm{A}},q_{\mathrm{B}}}C_{k_{\mathrm{A}}-q_{\mathrm{A}}}C_{k_{\mathrm{B}}-q_{\mathrm{B}}}+4(-1)^{q_{\mathrm{A}}+q_{\mathrm{B}}}X^{(k_{\mathrm{A}},k_{\mathrm{B}})}_{-q_{\mathrm{A}},-q_{\mathrm{B}}}C_{k_{\mathrm{A}}q_{\mathrm{A}}}C_{k_{\mathrm{B}}q_{\mathrm{B}}}+ \\
&\quad 4(-1)^{q_{\mathrm{A}}+q_{\mathrm{B}}}X^{(k_{\mathrm{A}},k_{\mathrm{B}})}_{q_{\mathrm{A}},-q_{\mathrm{B}}}C_{k_{\mathrm{A}}-q_{\mathrm{A}}}C_{k_{\mathrm{B}}q_{\mathrm{B}}}+4(-1)^{q_{\mathrm{A}}+q_{\mathrm{B}}}X^{(k_{\mathrm{A}},k_{\mathrm{B}})}_{-q_{\mathrm{A}},q_{\mathrm{B}}}C_{k_{\mathrm{A}}q_{\mathrm{A}}}C_{k_{\mathrm{B}}-q_{\mathrm{B}}}\Big).
\end{aligned}
\tag{B.32}
$$

Using the relationship given in Eq. B.3, the first four terms (including the summation over $q_{\mathrm{A}} > 0$ and $q_{\mathrm{B}} > 0$) can be rewritten as

$$\sum_{\substack{q_{\rm A}\neq 0\\ q_{\rm B}\neq 0}} \left[X^{(k_{\rm A},k_{\rm B})}_{q_{\rm A},q_{\rm B}}\right]^* C_{k_{\rm A}q_{\rm A}} C_{k_{\rm B}q_{\rm B}} \tag{B.33}$$

For products 5 and 6. With the contributions from products 5 and then 6 in order in the bracketed prefactor, the expansion gives

$$\begin{aligned}
&\frac{1}{2}\Big(\\
&(1-1)X^{(k_{\rm A},k_{\rm B})}_{q_{\rm A},0} C_{k_{\rm A}q_{\rm A}} C_{k_{\rm B}0} \\
&(1+1)(-1)^{q_{\rm A}} X^{(k_{\rm A},k_{\rm B})}_{q_{\rm A},0} C_{k_{\rm A}-q_{\rm A}} C_{k_{\rm B}0} \\
&(1+1)(-1)^{q_{\rm A}} X^{(k_{\rm A},k_{\rm B})}_{-q_{\rm A},0} C_{k_{\rm A}q_{\rm A}} C_{k_{\rm B}0} \\
&(1-1)X^{(k_{\rm A},k_{\rm B})}_{-q_{\rm A},0} C_{k_{\rm A}-q_{\rm A}} C_{k_{\rm B}0}\Big)
\end{aligned} \tag{B.34}$$

which then becomes, including the summation over $q_{\rm A} > 0$

$$\sum_{q_{\rm A}\neq 0} \left[X^{(k_{\rm A},k_{\rm B})}_{q_{\rm A},0}\right]^* C_{k_{\rm A}q_{\rm A}} C_{k_{\rm B}0}\,. \tag{B.35}$$

By symmetry, products 7 and 8 become

$$\sum_{q_{\rm B}\neq 0} \left[X^{(k_{\rm A},k_{\rm B})}_{0,q_{\rm B}}\right]^* C_{k_{\rm A}0} C_{k_{\rm B}q_{\rm B}}\,. \tag{B.36}$$

Product 9 is simply

$$\left[X^{(k_{\rm A},k_{\rm B})}_{0,0}\right]^* C_{k_{\rm A}0} C_{k_{\rm B}0}\,. \tag{B.37}$$

Inserting Eqs. (B.33), (B.35), (B.36) and (B.37) into Eq. (B.30), one can obtain

$$P(\theta) = \sum_{\substack{k_{\rm A}k_{\rm B}\\ q_{\rm A}q_{\rm B}}} (2k_{\rm A}+1)(2k_{\rm B}+1) \left[X^{(k_{\rm A},k_{\rm B})}_{q_{\rm A},q_{\rm B}}\right]^* C_{k_{\rm A}q_{\rm A}} C_{k_{\rm B}q_{\rm B}} \tag{B.38}$$

and Eq. 7.1 is regained.

B.3 Reflection Symmetry Properties of Other 4-Vector Correlations

Here the reflection symmetry properties are examined for two other possible 4-vector correlations. One in which both molecules have their molecular frame polarised, and one in which both molecules have their angular momentum polarised.

B.3.1 $\boldsymbol{r}_{\mathrm{A}} - \boldsymbol{r}_{\mathrm{B}} - \boldsymbol{k} - \boldsymbol{k}'$ correlation

If instead, both molecules have their bond axes oriented before the collision, giving a set of angles, θ_{A}, ϕ_{A}, θ_{B} and ϕ_{B} all of which have the properties of θ_{r} and ϕ_{r} as listed above, we get:

$$\begin{aligned}
\hat{\mathcal{S}} C^{\{k_A,k_B\}}_{q_A+,q_B+} &= \hat{\mathcal{S}} \left[C^{(k_A)}_{-q_A}(\theta_A,0)\, C^{(k_B)}_{-q_B}(\theta_B,0) \cos(q_A\phi_A) \cos(q_B\phi_B) \right] \\
&= C^{(k_A)}_{-q_A}(\theta_A,0)\, C^{(k_B)}_{-q_B}(\theta_B,0) \cos(-q_A\phi_A) \cos(q_B - \phi_B) \\
&= C^{(k_A)}_{-q_A}(\theta_A,0)\, C^{(k_B)}_{-q_B}(\theta_B,0) \cos(q_A\phi_A) \cos(q_B\phi_B) \\
&= C^{\{k_A,k_B\}}_{q_A+,q_B+}
\end{aligned} \tag{B.39}$$

and analogously

$$\hat{\mathcal{S}} C^{\{k_A,k_B\}}_{q_A-,q_B-} = C^{\{k_A,k_B\}}_{q_A-,q_B-} \tag{B.40}$$

$$\hat{\mathcal{S}} C^{\{k_A,k_B\}}_{q_A+,q_B-} = -C^{\{k_A,k_B\}}_{q_A+,q_B-} \tag{B.41}$$

$$\hat{\mathcal{S}} C^{\{k_A,k_B\}}_{q_A-,q_B+} = -C^{\{k_A,k_B\}}_{q_A-,q_B+} \tag{B.42}$$

$$\hat{\mathcal{S}} C^{\{k_A,k_B\}}_{0,q_B+} = C^{\{k_A,k_B\}}_{0,q_B+} \tag{B.43}$$

$$\hat{\mathcal{S}} C^{\{k_A,k_B\}}_{0,q_B-} = -C^{\{k_A,k_B\}}_{0,q_B-} \tag{B.44}$$

$$\hat{\mathcal{S}} C^{\{k_A,k_B\}}_{q_A+,0} = C^{\{k_A,k_B\}}_{q_A+,0} \tag{B.45}$$

$$\hat{\mathcal{S}} C^{\{k_A,k_B\}}_{q_A-,0} = -C^{\{k_A,k_B\}}_{q_A-,0} \tag{B.46}$$

$$\hat{\mathcal{S}} C^{\{k_A,k_B\}}_{0,0} = C^{\{k_A,k_B\}}_{0,0} \,. \tag{B.47}$$

The non-zero moments are therefore $R^{\{k_A,k_B\}}_{q_A\pm,q_B\pm}$, where if q_A or q_B is equal to zero, then it should be treated as having a positive sign.

B.3.2 $\boldsymbol{j}_{\mathrm{A}} - \boldsymbol{j}_{\mathrm{B}} - \boldsymbol{k} - \boldsymbol{k}'$ correlation

Finally, if both molecules has their angular momentum oriented before the collision, giving a set of angles, θ_{A}, ϕ_{A}, θ_{B} and ϕ_{B} all of which have the properties of θ_{j} and ϕ_{j} as listed above, we get:

$k_A + k_B$	Sign after q_A	Sign after q_B
even	$\pm$	$\pm$
odd	$\pm$	$\mp$

Table B.1: Rules for non-zero Hertel-Stoll normalised moments for the $\boldsymbol{j}_\mathrm{A} - \boldsymbol{j}_\mathrm{B} - \boldsymbol{k} - \boldsymbol{k}'$ correlation of the sort $U^{\{k_A,k_B\}}_{q_A\pm,q_B\pm/\mp}$. Note that if q_A or q_B are 0, they should be treated as having a positive sign.

$$\begin{aligned}
\hat{\mathcal{S}} C^{\{k_A,k_B\}}_{q_A+,q_B+} &= \hat{\mathcal{S}} \left[C^{(k_A)}_{-q_A}(\theta_A,0)\, C^{(k_B)}_{-q_B}(\theta_B,0) \cos(q_A\phi_A) \cos(q_B\phi_B) \right] \\
&= C^{(k_A)}_{-q_A}(\pi-\theta_A,0)\, C^{(k_B)}_{-q_B}(\pi-\theta_B,0) \cos(q_A(\pi-\phi_A)) \cos(q_B(\pi-\phi_B)) \\
&= (-1)^{k_A+q_A} C^{(k_A)}_{-q_A}(\theta_A,0)\, (-1)^{k_B+q_B} C^{(k_B)}_{-q_B}(\theta_B,0) \\
&\quad (-1)^{q_A} \cos(q_A\phi_A)\, (-1)^{q_B} \cos(q_B\phi_B) \\
&= (-1)^{k_A+k_B} C^{\{k_A,k_B\}}_{q_A+,q_B+} \qquad \text{(B.48)}
\end{aligned}$$

and analogously

$$\hat{\mathcal{S}} C^{\{k_A,k_B\}}_{q_A-,q_B-} = (-1)^{k_A+k_B} C^{\{k_A,k_B\}}_{q_A-,q_B-} \qquad \text{(B.49)}$$

$$\hat{\mathcal{S}} C^{\{k_A,k_B\}}_{q_A+,q_B-} = (-1)^{k_A+k_B-1} C^{\{k_A,k_B\}}_{q_A+,q_B-} \qquad \text{(B.50)}$$

$$\hat{\mathcal{S}} C^{\{k_A,k_B\}}_{q_A-,q_B+} = (-1)^{k_A+k_B-1} C^{\{k_A,k_B\}}_{q_A-,q_B+} \qquad \text{(B.51)}$$

$$\hat{\mathcal{S}} C^{\{k_A,k_B\}}_{0,q_B+} = (-1)^{k_A+k_B} C^{\{k_A,k_B\}}_{0,q_B+} \qquad \text{(B.52)}$$

$$\hat{\mathcal{S}} C^{\{k_A,k_B\}}_{0,q_B-} = (-1)^{k_A+k_B-1} C^{\{k_A,k_B\}}_{0,q_B-} \qquad \text{(B.53)}$$

$$\hat{\mathcal{S}} C^{\{k_A,k_B\}}_{q_A+,0} = (-1)^{k_A+k_B} C^{\{k_A,k_B\}}_{q_A+,0} \qquad \text{(B.54)}$$

$$\hat{\mathcal{S}} C^{\{k_A,k_B\}}_{q_A-,0} = (-1)^{k_A+k_B-1} C^{\{k_A,k_B\}}_{q_A-,0} \qquad \text{(B.55)}$$

$$\hat{\mathcal{S}} C^{\{k_A,k_B\}}_{0,0} = (-1)^{k_A+k_B} C^{\{k_A,k_B\}}_{0,0}\,. \qquad \text{(B.56)}$$

The non-zero moments are then given in Table B.1. The notation is chosen so as to agree with the $\boldsymbol{j}$-PDDCSs from a 3-vector correlation.

C

General Solutions to the Slice Method Simultaneous Equations

This appendix will have the general equations to solve the simultaneous equations required for the slice method described in Section 5.4.

It is assumed that the scattering distribution in the image is ϕ independent. This scattering angular distribution will be taken to be a DCS, $\mathrm{d}\sigma/\mathrm{d}\omega(\theta)$. The constants $\tilde{C}$ and S will be neglected. Hence, the intensity of any given slice i is given by

$$I_i(\theta) = \frac{\mathrm{d}\sigma}{\mathrm{d}\omega}(\theta)\left[1 + F_0^{\{2\}}(\Gamma_i)\,\rho_0^{\{2\}}(\theta) + F_{1+}^{\{2\}}(\Gamma_i)\,\rho_{1+}^{\{2\}}(\theta) + F_{2+}^{\{2\}}(\Gamma_i)\,\rho_{2+}^{\{2\}}(\theta)\right] \quad \text{(C.1)}$$

where Γ_i are the Euler angles for that slice.

If there are four slices $\{1, 2, 3, 4\}$, of which 1 and 2 are taken with laser polarisation χ_1 and 3 and 4 with laser polarisation χ_2, we define the quantities

$$D_{ij} = F_0^{\{2\}}(\Gamma_i)\,/F_0^{\{2\}}(\Gamma_j) \quad \text{(C.2)}$$

which in turn help to define

$$\begin{aligned} C_{\chi_1,\chi_2} &= \frac{F_{1+}^{\{2\}}(\Gamma_1) - D_{13}F_{1+}^{\{2\}}(\Gamma_3)}{F_{1+}^{\{2\}}(\Gamma_2) - D_{24}F_{1+}^{\{2\}}(\Gamma_4)} \\ C_{\chi} &= \frac{F_{1+}^{\{2\}}(\Gamma_1) - D_{12}F_{1+}^{\{2\}}(\Gamma_2)}{F_{1+}^{\{2\}}(\Gamma_3) - D_{34}F_{1+}^{\{2\}}(\Gamma_4)}\,. \end{aligned} \quad \text{(C.3)}$$

These then help to define

$$\begin{aligned} B_{\chi_1,\chi_2} &= F_{2+}^{\{2\}}(\Gamma_1) - D_{13}F_{2+}^{\{2\}}(\Gamma_3) - C_{\chi_1,\chi_2}\left(F_{2+}^{\{2\}}(\Gamma_2) - D_{24}F_{2+}^{\{2\}}(\Gamma_4)\right) \\ B_{\chi} &= F_{2+}^{\{2\}}(\Gamma_1) - D_{12}F_{2+}^{\{2\}}(\Gamma_2) - C_{\chi}\left(F_{2+}^{\{2\}}(\Gamma_3) - D_{34}F_{2+}^{\{2\}}(\Gamma_4)\right) \end{aligned} \tag{C.4}$$

and

$$\begin{aligned} A_{\chi_1,\chi_2} &= 1 - D_{13} - C_{\chi_1,\chi_2}(1 - D_{24}) \\ A_{\chi} &= 1 - D_{12} - C_{\chi}(1 - D_{34}) \,. \end{aligned} \tag{C.5}$$

These then allow the DCS to be found by

$$\begin{aligned} \frac{\mathrm{d}\sigma}{\mathrm{d}\omega}(\theta) = &- \frac{1}{A_{\chi_1,\chi_2} - A_{\chi}\frac{B_{\chi_1,\chi_2}}{B_{\chi}}}\left[\left(1 - \frac{B_{\chi_1,\chi_2}}{B_{\chi}}\right)I_1(\theta) - \left(C_{\chi_1,\chi_2} - D_{12}\frac{B_{\chi_1,\chi_2}}{B_{\chi}}\right)I_2(\theta)\right. \\ &\left. - \left(D_{13} - C_{\chi}\frac{B_{\chi_1,\chi_2}}{B_{\chi}}\right)I_3(\theta) + \left(C_{\chi_1,\chi_2}D_{24} - C_{\chi}D_{34}\frac{B_{\chi_1,\chi_2}}{B_{\chi}}\right)I_4(\theta)\right] \end{aligned} \tag{C.6}$$

and $\rho_{2+}^{\{2\}}(\theta)$ to be found by

$$\rho_{2+}^{\{2\}}(\theta) = \frac{I_1(\theta) - D_{13}I_3(\theta) - C_{\chi_1,\chi_2}\left(I_2(\theta) - D_{24}I_4(\theta)\right)}{\frac{\mathrm{d}\sigma}{\mathrm{d}\omega}(\theta)B_{\chi_1,\chi_2}} - \frac{A_{\chi_1,\chi_2}}{B_{\chi_1,\chi_2}} \,. \tag{C.7}$$

Now we define

$$\begin{aligned} D_{ij}^{(\mathrm{S})} &= F_{1+}^{\{2\}}(\Gamma_i)\,/F_{1+}^{\{2\}}(\Gamma_j) \\ C_{\chi_1,\chi_2}^{(\mathrm{S})} &= \frac{F_{2+}^{\{2\}}(\Gamma_1) - D_{13}^{(\mathrm{S})}F_{2+}^{\{2\}}(\Gamma_3)}{F_{2+}^{\{2\}}(\Gamma_2) - D_{24}^{(\mathrm{S})}F_{2+}^{\{2\}}(\Gamma_4)} \\ B_{\chi_1,\chi_2}^{(\mathrm{S})} &= F_{0}^{\{2\}}(\Gamma_1) - D_{13}^{(\mathrm{S})}F_{0}^{\{2\}}(\Gamma_3) - C_{\chi_1,\chi_2}^{(\mathrm{S})}\left(F_{0}^{\{2\}}(\Gamma_2) - D_{24}^{(\mathrm{S})}F_{0}^{\{2\}}(\Gamma_4)\right) \\ A_{\chi_1,\chi_2}^{(\mathrm{S})} &= 1 - D_{13}^{(\mathrm{S})} - C_{\chi_1,\chi_2}^{(\mathrm{S})}\left(1 - D_{24}^{(\mathrm{S})}\right) \end{aligned} \tag{C.8}$$

where the superscript (S), meaning 'Shifted', suggests that the subscripts of $F_{q+}^{\{k\}}(\Gamma_i)$ have been cycled in the calculation (*ie* $0 \to 1+ \to 2+ \to 0$).

$\rho_{0}^{\{2\}}(\theta)$ may then be found by

$$\rho_{0}^{\{2\}}(\theta) = \frac{I_1(\theta) - D_{13}^{(\mathrm{S})}I_3(\theta) - C_{\chi_1,\chi_2}^{(\mathrm{S})}(I_2(\theta) - D_{24}^{(\mathrm{S})}I_4(\theta))}{\frac{\mathrm{d}\sigma}{\mathrm{d}\omega}(\theta)B_{\chi_1,\chi_2}^{(\mathrm{S})}} - \frac{A_{\chi_1,\chi_2}^{(\mathrm{S})}}{B_{\chi_1,\chi_2}^{(\mathrm{S})}} \tag{C.9}$$

The final definitions required are

$$\begin{aligned} C^{(\mathrm{PS})}_{\chi_1,\chi_2} &= \frac{F^{\{2\}}_{2+}(\Gamma_1) - D_{13}F^{\{2\}}_{2+}(\Gamma_3)}{F^{\{2\}}_{2+}(\Gamma_2) - D_{24}F^{\{2\}}_{2+}(\Gamma_4)} \\ B^{(\mathrm{PS}^2)}_{\chi_1,\chi_2} &= F^{\{2\}}_{1+}(\Gamma_1) - D_{13}F^{\{2\}}_{1+}(\Gamma_3) - C^{(\mathrm{S})}_{\chi_1,\chi_2}\left(F^{\{2\}}_{1+}(\Gamma_2) - D_{24}F^{\{2\}}_{1+}(\Gamma_4)\right) \\ A^{(\mathrm{PS})}_{\chi_1,\chi_2} &= 1 - D_{13} - C^{(\mathrm{S})}_{\chi_1,\chi_2}\left(1 - D^{(\mathrm{S})}_{24}\right) \end{aligned} \tag{C.10}$$

where the subscripts (PS), meaning 'Part-Shifted', suggests a shift of the subscript as before, except for the D_{ij} quantities and (PS^2), meaning 'part-double-shifted', suggests a double cycling of the subscrpits of $F^{\{k\}}_{q+}(\Gamma_i)$, except for the D_{ij} quantities, which have no shift.

Finally, these quantities may be used to find $\rho^{\{2\}}_{1+}(\theta)$ by

$$\rho^{\{2\}}_{1+}(\theta) = \frac{I_1(\theta) - D_{13}I_3(\theta) - C^{(\mathrm{PS})}_{\chi_1,\chi_2}(I_2(\theta) - D_{24}I_4(\theta))}{\frac{\mathrm{d}\sigma}{\mathrm{d}\omega}(\theta)B^{(\mathrm{PS}^2)}_{\chi_1,\chi_2}} - \frac{A^{(\mathrm{PS})}_{\chi_1,\chi_2}}{B^{(\mathrm{PS}^2)}_{\chi_1,\chi_2}}\,. \tag{C.11}$$

References

[1] E. D. Hughes, F. Juliusburger, S. Masterman, B. Topley, J. Weiss, *Journal of the Chemical Society* **1935**, 1525–1529.

[2] E. D. Hughes, C. K. Ingold, *Journal of the Chemical Society* **1935**, 244–255.

[3] W. A. Cowdrey, E. D. Hughes, C. K. Ingold, S. Masterman, A. D. Scott, *Journal of the Chemical Society* **1937**, 1252–1271.

[4] K. Fukui, T. Yonezawa, H. Shingu, *Journal of Chemical Physics* **1952**, *20*, 722–725.

[5] K. Fukui, T. Yonezawa, C. Nagata, H. Shingu, *Journal of Chemical Physics* **1954**, *22*, 1433–1442.

[6] K. Fukui, *Science* **1982**, *218*, 747–754.

[7] R. B. Beuhler Jr., R. J.; Bernstein, *Journal of Chemical Physics* **1969**, *51*, 5305–5315.

[8] H. B. Burgi, J. D. Dunitz, J. M. Lehn, G. Wipff, *Tetrahedron* **1974**, *30*, 1563–1572.

[9] H. B. Burgi, J. D. Dunitz, E. Shefter, *Acta Crystallographica Section B-Structural Science* **1974**, *B 30*, 1517–1527.

[10] H. Pelzer, E. Wigner, *Zeitschrift Fur Physikalische Chemie-Abteilung B-Chemie Der Elementarprozesse Aufbau Der Materie* **1932**, *15*, 445–471.

[11] R. D. Levine, *Chemical Physics Letters* **1990**, *175*, 331–337.

[12] I. W. M. Smith, *Journal of Chemical Education* **1982**, *59*, 9–14.

[13] M. Born, R. Oppenheimer, *Annalen Der Physik* **1927**, *84*, 0457–0484.

[14] J. Čìžek, *Journal of Chemical Physics* **1966**, *45*, 4256–+.

[15] M. Kállay, J. Gauss, *Journal of Chemical Physics* **2005**, *123*.

[16] V. A. Rassolov, S. Garashchuk, *Chemical Physics Letters* **2008**, *464*, 262–264.

[17] J. L. G. Vallejo, C. Snowdon, R. Stocks, F. Kazemian, F. C. Y. Yu, C. Seidl, Z. Seeger, M. Alkan, D. Poole, B. M. Westheimer, M. Basha, M. de la Pierre, A. Rendell, E. I. Izgorodina, M. S. Gordon, G. M. J. Barca, *Journal of Chemical Physics* **2023**, *159*.

[18] C. Brouard, M.; Vallance, *Tutorials in Molecular Reaction Dynamics*, The Royal Society of Chemistry, Cambridge, **2010**.

[19] B. Friedrich, D. P. Pullman, D. R. Herschbach, *Journal of Physical Chemistry* **1991**, *95*, 8118–8129.

[20] F. J. Aoiz, M. Brouard, S. D. S. Gordon, B. Nichols, S. Stolte, V. Walpole, *Physical Chemistry Chemical Physics* **2015**, *17*, 30210–30228.

[21] L. Onsager, *Physical Review* **1931**, *37*, 405–426.

[22] B. Nichols, H. Chadwick, S. D. S. Gordon, C. J. Eyles, B. Hornung, M. Brouard, M. H. Alexander, F. J. Aoiz, A. Gijsbertsen, S. Stolte, *Chemical Science* **2015**, *6*, 2202–2210.

[23] C. G. Heid, V. Walpole, M. Brouard, P. G. Jambrina, F. J. Aoiz, *Nature Chemistry* **2019**, *11*, 662–668.

[24] A. J. Orr-Ewing, R. N. Zare, *Annual Review of Physical Chemistry* **1994**, *45*, 315–366.

[25] M. P. de Miranda, F. J. Aoiz, L. Bañares, V. S. Rábanos, *Journal of Chemical Physics* **1999**, *111*, 5368–5383.

[26] V. Walpole, C. G. Heid, P. G. Jambrina, F. J. Aoiz, M. Brouard, *Journal of Physical Chemistry A* **2019**, *123*, 8787–8806.

[27] W. Xu, G. Zhao, *Central European Journal of Physics* **2012**, *10*, 253–270.

[28] J. Aldegunde, M. P. de Miranda, J. M. Haigh, B. K. Kendrick, V. Sáez-Rábanos, F. J. Aoiz, *Journal of Physical Chemistry A* **2005**, *109*, 6200–6217.

[29] F. J. Aoiz, M. Brouard, P. A. Enriquez, *Journal of Chemical Physics* **1996**, *105*, 4964–4982.

[30] P. W. Atkins, R. Friedman, *Molecular Quantum Mechanics*, 5th ed., Oxford University Press, Oxford, **2011**.

[31] T. G. Heil, S. Green, D. J. Kouri, *Journal of Chemical Physics* **1978**, *68*, 2562–2583.

[32] P. G. Jambrina, J. Aldegunde, M. P. de Miranda, V. Sáez-Rábanos, F. J. Aoiz, *Physical Chemistry Chemical Physics* **2012**, *14*, 9977–9987.

[33] R. J. Beuhler Jr., R. B. Bernstein, K. H. Kramer, *Journal of the American Chemical Society* **1966**, 5331.

[34] P. R. Brooks, E. M. Jones, *Journal of Chemical Physics* **1966**, *45*, 3449–.

[35] K. H. Kramer, R. B. Bernstein, *Journal of Chemical Physics* **1965**, *42*, 767–770.

[36] C. J. Eyles, M. Brouard, C. H. Yang, J. Klos, F. J. Aoiz, A. Gijsbertsen, A. E. Wiskerke, S. Stolte, *Nature Chemistry* **2011**, *3*, 597–602.

[37] H. L. Bethlem, G. Berden, G. Meijer, *Physical Review Letters* **1999**, *83*, 1558–1561.

[38] N. Vanhaecke, U. Meier, M. Andrist, B. H. Meier, F. Merkt, *Physical Review A* **2007**, *75*.

[39] D. W. Chandler, P. L. Houston, *Journal of Chemical Physics* **1987**, *87*, 1445–1447.

[40] A. T. J. B. Eppink, D. H. Parker, *Review of Scientific Instruments* **1997**, *68*, 3477–3484.

[41] M. Brouard, *Faraday Discussions* **2024**, *251*, 666–675.

[42] G. Q. Tang, M. Besemer, S. Kuijpers, G. C. Groenenboom, A. van der Avoird, T. Karman, S. Y. T. van de Meerakker, *Science* **2023**, *379*, 1031–1036.

[43] H. W. Zhou, W. E. Perreault, N. Mukherjee, R. N. Zare, *Science* **2021**, *374*, 960–964.

[44] H. W. Zhou, W. E. Perreault, N. Mukherjee, R. N. Zare, *Nature Chemistry* **2022**, *14*, 658–663.

[45] M. H. Alexander, *Journal of Chemical Physics* **1993**, *99*, 7725–7738.

[46] M. H. Alexander, *Journal of Chemical Physics* **1982**, *76*, 5974–5988.

[47] P. E. S. Wormer, J. A. Kłos, G. C. Groenenboom, A. van der Avoird, *Journal of Chemical Physics* **2005**, *122*.

[48] M. Karplus, R. N. Porter, R. D. Sharma, *Journal of Chemical Physics* **1965**, *43*, 3259–.

[49] C. L. Russell, D. E. Manolopoulos, *Journal of Chemical Physics* **1999**, *110*, 177–187.

[50] S. Seamons, DPhil Thesis, University of Oxford, **2015**.

[51] S. J. Greaves, E. Wrede, N. T. Goldberg, J. Y. Zhang, D. J. Miller, R. N. Zare, *Nature* **2008**, *454*, 88–91.

[52] F. J. Aoiz, J. E. Verdasco, V. J. Herrero, V. S. Rábanos, M. A. Alexander, *Journal of Chemical Physics* **2003**, *119*, 5860–5866.

[53] C. M. Guo, H. Zhang, X. L. Cheng, *Journal of Physical Chemistry A* **2024**, *128*, 5435–5444.

[54] H. Chadwick, B. Nichols, S. D. S. Gordon, B. Hornung, E. Squires, M. Brouard, J. Klos, M. H. Alexander, F. J. Aoiz, S. Stolte, *Journal of Physical Chemistry Letters* **2014**, *5*, 3296–3301.

[55] P. M. Agrawal, L. M. Raff, *Journal of Chemical Physics* **1981**, *75*, 2163–2176.

[56] D. J. Garton, A. L. Brunsvold, T. K. Minton, D. Troya, B. Maiti, G. C. Schatz, *Journal of Physical Chemistry A* **2006**, *110*, 1327–1341.

[57] G. C. Groenenboom, A. J. H. M. Meijer, *Journal of Chemical Physics* **1994**, *101*, 7592–7602.

[58] M. Menéndez, J. F. Castillo, B. Martínez-Haya, F. J. Aoiz, *Physical Chemistry Chemical Physics* **2015**, *17*, 25471–25482.

[59] F. J. Aoiz, L. Banares, M. Faubel, B. MartinezHaya, L. Y. Rusin, U. Tappe, J. P. Toennies, *Chemical Physics* **1996**, *207*, 245–259.

[60] M. Menéndez, E. Garcia, M. Lara, P. G. Jambrina, F. J. Aoiz, *Journal of Physical Chemistry A* **2023**.

[61] P. Szabó', G. Lendvay, *Journal of Physical Chemistry A* **2015**, *119*, 7180–7189.

[62] Z. F. Sun, R. J. A. Scheidsbach, M. C. van Hemert, A. van der Avoird, A. G. Suits, D. H. Parker, *Physical Chemistry Chemical Physics* **2023**, *25*, 17828–17839.

[63] S. C. Althorpe, *Journal of Chemical Physics* **2001**, *114*, 1601–1616.

[64] S. C. Althorpe, *Journal of Chemical Physics* **2004**, *121*, 1175–1186.

[65] S. C. Althorpe, *Physical Review A* **2004**, *69*.

[66] J. Y. Huang, S. Liu, D. H. Zhang, R. V. Krems, *Physical Review Letters* **2018**, *120*.

[67] S. C. Althorpe, D. C. Clary, *Annual Review of Physical Chemistry* **2003**, *54*, 493–529.

[68] A. M. Arthurs, A. Dalgarno, *Proceedings of the Royal Society of London Series A: Mathematical and Physical Sciences* **1960**, *256*, 540–551.

[69] F. W. J. Olver, National Institute of Standards and Technology (U.S.), *NIST handbook of mathematical functions*, Cambridge University Press, Cambridge, **2010**.

[70] T. G. Heil, D. J. Kouri, *Chemical Physics Letters* **1976**, *40*, 375–380.

[71] F. Fernández-Alonso, R. N. Zare, *Annual Review of Physical Chemistry* **2002**, *53*, 67–99.

[72] M. Brouard, *Reaction Dynamics*, Oxford University Press, Oxford, **1998**.

[73] A. R. P. Rau, *Physics Today* **2005**, *58*, 13–13.

[74] T. de Jongh, M. Besemer, Q. Shuai, T. Karman, A. van der Avoird, G. C. Groenenboom, S. Y. T. van de Meerakker, *Science* **2020**, *368*, 626–+.

[75] J. S. Blair, *Physical Review* **1959**, *115*, 928–938.

[76] M. Faubel, *Journal of Chemical Physics* **1984**, *81*, 5559–5569.

[77] A. Ballast, A. Gijsbertsen, H. Linnartz, S. Stolte, *Molecular Physics* **2008**, *106*, 315–331.

[78] A. Semenov, D. Babikov, *Journal of Physical Chemistry Letters* **2014**, *5*, 275–278.

[79] A. Semenov, D. Babikov, *Journal of Physical Chemistry A* **2015**, *119*, 12329–12338.

[80] D. Babikov, A. Semenov, *Journal of Physical Chemistry A* **2016**, *120*, 319–331.

[81] B. Mandal, A. Semenov, D. Babikov, *Journal of Physical Chemistry A* **2018**, *122*, 6157–6165.

[82] A. Semenov, *Journal of Chemical Physics* **2018**, *148*.

[83] C. Joy, B. Mandal, D. Bostan, D. Babikov, *Physical Chemistry Chemical Physics* **2023**, *25*, 17287–17299.

[84] A. Semenov, M. L. Dubernet, D. Babikov, *Journal of Chemical Physics* **2014**, *141*.

[85] M. H. Alexander, P. J. Dagdigian, H. J. Werner, J. Klos, B. Desrousseaux, G. Raffy, F. Lique, *Computer Physics Communications* **2023**, *289*.

[86] E. H. Taylor, S. Datz, *Journal of Chemical Physics* **1955**, *23*, 1711–1718.

[87] D. R. Herschbach, *Discussions of the Faraday Society* **1962**, 149–161.

[88] Y. T. Lee, J. D. Mcdonald, P. R. Lebreton, D. R. Herschbach, *Review of Scientific Instruments* **1969**, *40*, 1402–+.

[89] A. Kantrowitz, J. Grey, *Review of Scientific Instruments* **1951**, *22*, 328–332.

[90] G. B. Kistiakowsky, W. P. Slichter, *Review of Scientific Instruments* **1951**, *22*, 333–337.

[91] E. W. Becker, K. Bier, *Zeitschrift Fur Naturforschung Section a-a Journal of Physical Sciences* **1954**, *9*, 975–986.

[92] E. W. Becker, W. Henkes, *Zeitschrift Fur Physik* **1956**, *146*, 320–332.

[93] S. Dworski, G. Alexandrowicz, P. Fouquet, A. P. Jardine, W. Allison, J. Ellis, *Review of Scientific Instruments* **2004**, *75*, 1963–1970.

[94] T. R. Sharples, T. F. M. Luxford, D. Townsend, K. G. McKendrick, M. L. Costen, *Journal of Chemical Physics* **2015**, *143*.

[95] W. E. Perreault, N. Mukherjee, R. N. Zare, *Nature Chemistry* **2018**, *10*, 561–567.

[96] H. U. Hostettler, R. B. Bernstein, *Review of Scientific Instruments* **1960**, *31*, 872–877.

[97] A. Schultz, H. W. Cruse, R. N. Zare, *Journal of Chemical Physics* **1972**, *57*, 1354–1355.

[98] L. Zandee, R. B. Bernstein, *Journal of Chemical Physics* **1979**, *71*, 1359–1371.

[99] G. Scoles, *Atomic and Molecular Beam Methods*, *Vol. 1*, Oxford University Press, New York, **1988**.

[100] E. Orunesajo, S. Abubakar, B. Oguh, S. K. Lee, W. Li, *Review of Scientific Instruments* **2024**, *95*.

[101] S. K. Lee, Y. F. Lin, S. Lingenfelter, L. Fan, A. H. Winney, W. Li, *Journal of Chemical Physics* **2014**, *141*.

[102] S. Trippel, M. Stei, R. Otto, P. Hlavenka, J. Mikosch, C. Eichhorn, U. Lourderaj, J. X. Zhang, W. L. Hase, M. Weidemüller, R. Wester, *XXVI International Conference on Photonic Electronic and Atomic Collisions* **2009**, *194*.

[103] G. Schönhense, A. Oelsner, O. Schmidt, G. H. Fecher, V. Mergel, O. Jagutzki, H. Schmidt-Böcking, *Surface Science* **2001**, *480*, 180–187.

[104] W. C. Wiley, I. H. McLaren, *Review of Scientific Instruments* **1955**, *26*, 1150–1157.

[105] A. Nomerotski, S. Adigun-Boaye, M. Brouard, E. Campbell, A. Clark, J. Crooks, J. J. John, A. J. Johnsen, C. Slater, R. Turchetta, C. Vallance, E. Wilman, W. H. Yuen, *Nuclear Instruments & Methods in Physics Research Section A: Accelerators Spectrometers Detectors and Associated Equipment* **2011**, *633*, S243–S246.

[106] A. T. Clark, J. P. Crooks, I. Sedgwick, R. Turchetta, J. W. L. Lee, J. J. John, E. S. Wilman, L. Hill, E. Halford, C. S. Slater, B. Winter, W. H. Yuen, S. H. Gardiner, M. L. Lipciuc, M. Brouard, A. Nomerotski, C. Vallance, *Journal of Physical Chemistry A* **2012**, *116*, 10897–10903.

[107] J. J. John, M. Brouard, A. Clark, J. Crooks, E. Halford, L. Hill, J. W. L. Lee, A. Nomerotski, R. Pisarczyk, I. Sedgwick, C. S. Slater, R. Turchetta, C. Vallance, E. Wilman, B. Winter, W. H. Yuen, *Journal of Instrumentation* **2012**, *7*.

[108] T. Poikela, J. Plosila, T. Westerlund, M. Campbell, M. De Gaspari, X. Llopart, V. Gromov, R. Kluit, M. van Beuzekom, F. Zappon, V. Zivkovic, C. Brezina, K. Desch, Y. Fu, A. Kruth, *Journal of Instrumentation* **2014**, *9*.

[109] M. Fisher-Levine, A. Nomerotski, *Journal of Instrumentation* **2016**, *11*.

[110] R. Ballabriga, M. Campbell, X. Llopart, *Radiation Measurements* **2020**, *136*.

[111] D. Townsend, M. P. Minitti, A. G. Suits, *Review of Scientific Instruments* **2003**, *74*, 2530–2539.

[112] J. J. Lin, J. G. Zhou, W. C. Shiu, K. P. Liu, *Review of Scientific Instruments* **2003**, *74*, 2495–2500.

[113] C. R. Gebhardt, T. P. Rakitzis, P. C. Samartzis, V. Ladopoulos, T. N. Kitsopoulos, *Review of Scientific Instruments* **2001**, *72*, 3848–3853.

[114] D. L. Smith, G. N. Gibson, *Physical Review A* **2018**, *97*.

[115] D. Chakraborty, D. S. Slaughter, S. Ptasinska, *Physical Review A* **2023**, *108*.

[116] F. Allum, R. Mason, M. Burt, C. S. Slater, E. Squires, B. Winter, M. Brouard, *Molecular Physics* **2020**.

[117] J. Aoki, H. Hazama, M. Toyoda, *Journal of the Mass Spectrometry Society of Japan* **2011**, *59*, 57–61.

[118] M. McCrea, Part II Thesis, University of Oxford, **2021**.

[119] M. Hippler, J. Pfab, *Chemical Physics Letters* **1995**, *243*, 500–505.

[120] M. N. R. Ashfold, R. N. Dixon, N. Little, R. J. Stickland, C. M. Western, *Journal of Chemical Physics* **1988**, *89*, 1754–1761.

[121] K. P. Huber, G. Herzberg, *Constants of Diatomic Molecules*, Van Nostrand Reinhold, New York, **1979**.

[122] G. Herzberg, *Spectra of Diatomic Molecules*, 2nd Edition, D. Van Nostrand, New York, **1950**.

[123] R. K. Hinkley, J. A. Hall, T. E. H. Walker, W. G. Richards, *Journal of Physics B: Atomic and Molecular Physics* **1972**, *5*, 204–212.

[124] J. M. Brown, J. T. Hougen, K. P. Huber, J. W. C. Johns, I. Kopp, H. Lefebvre-Brion, A. J. Merer, D. A. Ramsay, J. Rostas, R. N. Zare, *Journal Of Molecular Spectroscopy* **1975**, 500–503.

[125] R. N. Zare, *Angular momentum: understanding spatial aspects in chemistry and physics*, Wiley Inter-Science, **1988**.

[126] A. Timmermann, R. Wallenstein, *Optics Communications* **1981**, *39*, 239–242.

[127] C. Rist, M. H. Alexander, P. Valiron, *Journal of Chemical Physics* **1993**, *98*, 4662–4671.

[128] J. W. Simmons, W. Gordy, *Physical Review* **1948**, *73*, 713–718.

[129] G. Herrmann, *Journal of Chemical Physics* **1958**, *29*, 875–879.

[130] G. Herzberg, *Infrared and Raman Spectra of Polyatomic Molecules*, Van Nostrand Reinhold, New York, **1945**.

[131] O. Tkac, A. K. Saha, J. Onvlee, C. H. Yang, G. Sarma, C. K. Bishwakarma, S. Y. T. van de Meerakker, A. van der Avoird, D. H. Parker, A. J. Orr-Ewing, *Physical Chemistry Chemical Physics* **2014**, *16*, 477–488.

[132] L. H. Coudert, E. Roueff, *Astronomy & Astrophysics* **2006**, *449*, 855–859.

[133] K. Balasubramanian, *Journal of Chemical Physics* **1981**, *74*, 6824–6829.

[134] O. Sipilä, J. Harju, P. Caselli, S. Schlemmer, *Astronomy & Astrophysics* **2015**, *581*.

[135] V. A. Cho, PhD Thesis, University of California, Los Angeles, **1994**.

[136] K. M. Chen, E. S. Yeung, *Journal of Chemical Physics* **1978**, *69*, 43–52.

[137] S. E. Choi, R. B. Bernstein, *Journal of Chemical Physics* **1986**, *85*, 150–161.

[138] C. J. Eyles, M. Brouard, H. Chadwick, B. Hornung, B. Nichols, C. H. Yang, J. Klos, F. J. Aoiz, A. Gijsbertsen, A. E. Wiskerke, S. Stolte, *Physical Chemistry Chemical Physics* **2012**, *14*, 5403–5419.

[139] C. J. Eyles, DPhil Thesis, University of Oxford, **2010**.

[140] J. J. Kay, S. Y. T. van de Meerakker, E. A. Wade, K. E. Strecker, D. W. Chandler, *Journal of Physical Chemistry A* **2009**, *113*, 14800–14806.

[141] O. Tkác, A. J. Orr-Ewing, P. J. Dagdigian, M. H. Alexander, J. Onvlee, A. van der Avoird, *Journal of Chemical Physics* **2014**, *140*.

[142] O. Tkác, A. K. Saha, J. Loreau, Q. L. Ma, P. J. Dagdigian, D. H. Parker, A. van der Avoird, A. J. Orr-Ewing, *Molecular Physics* **2015**, *113*, 3925–3933.

[143] O. Tkác, A. K. Saha, J. Loreau, D. H. Parker, A. van der Avoird, A. J. Orr-Ewing, *Journal of Physical Chemistry A* **2015**, *119*, 5979–5987.

[144] Z. Gao, J. Loreau, A. van der Avoird, S. Y. T. van de Meerakker, *Physical Chemistry Chemical Physics* **2019**, *21*, 14033–14041.

[145] S. E. J. Kuijpers, A. J. A. van Roij, E. Sweers, S. Herbers, Y. M. Caris, S. Y. T. van de Meerakker, *Review of Scientific Instruments* **2024**, *95*.

[146] Q. L. Ma, A. van der Avoird, J. Loreau, M. H. Alexander, S. Y. T. van de Meerakker, P. J. Dagdigian, *Journal of Chemical Physics* **2015**, *143*.

[147] J. Loreau, A. van der Avoird, *Journal of Chemical Physics* **2015**, *143*.

[148] I. Kusunoki, *Journal of Chemical Physics* **1977**, *67*, 2224–2229.

[149] D. B. M. Klaassen, J. M. H. Reijnders, J. J. Ter Meulen, A. Dymanus, *Journal of Chemical Physics* **1982**, *76*, 3019–3034.

[150] D. B. M. Klaassen, J. J. Ter Meulen, A. Dymanus, *Journal of Chemical Physics* **1982**, *77*, 4972–4981.

[151] D. B. M. Klaassen, J. J. Ter Meulen, A. Dymanus, *Journal of Chemical Physics* **1983**, *78*, 767–776.

[152] H. Meyer, U. Buck, R. Schinke, G. H. F. Diercksen, *Journal of Chemical Physics* **1986**, *84*, 4976–4987.

[153] G. Ebel, R. Krohne, H. Meyer, U. Buck, R. Schinke, T. Seelemann, P. Andresen, J. Schleipen, J. J. Ter Meulen, G. H. F. Diercksen, *Journal of Chemical Physics* **1990**, *93*, 6419–6432.

[154] J. Schleipen, J. J. Ter Meulen, G. C. M. van der Sanden, P. E. S. Wormer, A. van der Avoird, *Chemical Physics* **1992**, *163*, 161–172.

[155] G. C. M. van der Sanden, P. E. S. Wormer, A. van der Avoird, J. Schleipen, J. J. Ter Meulen, *Journal of Chemical Physics* **1995**, *103*, 10001–10004.

[156] G. C. M. van der Sanden, P. E. S. Wormer, A. van der Avoird, *Journal of Chemical Physics* **1996**, *105*, 3079–3088.

[157] K. B. Gubbels, S. Y. T. van de Meerakker, G. C. Groenenboom, G. Meijer, A. van der Avoird, *Journal of Chemical Physics* **2012**, *136*.

[158] N. Bouhafs, C. Rist, F. Daniel, F. Dumouchel, F. Lique, L. Wiesenfeld, A. Faure, *Monthly Notices of the Royal Astronomical Society* **2017**, *470*, 2204–2211.

[159] J. Loreau, A. van der Avoird, *Faraday Discussions* **2024**, *251*, 249–261.

[160] K. Ohashi, T. Kasai, K. Kuwata, *Journal of Physical Chemistry* **1988**, *92*, 5954–5958.

[161] S. R. Gandhi, R. B. Bernstein, *Journal of Chemical Physics* **1987**, *87*, 6457–6467.

[162] T. D. Hain, R. M. Moision, T. J. Curtiss, *Journal of Chemical Physics* **1999**, *111*, 6797–6806.

[163] I. Szabo, *International Journal of Mass Spectrometry and Ion Processes* **1986**, *73*, 197–235.

[164] B. Nichols, Part II Thesis, University of Oxford, **2011**.

[165] J. Bulthuis, J. J. van Leuken, S. Stolte, *Journal of the Chemical Society-Faraday Transactions* **1995**, *91*, 205–214.

[166] Y.-P. Chang, F. Filsinger, B. G. Sartakov, J. Küpper, *Computer Physics Communications* **2014**, *185*, 339–349.

[167] D. H. Parker, R. B. Bernstein, *Annual Review of Physical Chemistry* **1989**, *40*, 561–595.

[168] G. Herzberg, *Electronic spectra and electronic structure of polyatomic molecules*, Van Nostrand, New York, **1966**.

[169] Autodesk Inc., Autodesk Inventor Professional 2025, **2025**.

[170] R. W. Anderson, *Journal of Physical Chemistry A* **1997**, *101*, 7664–7673.

[171] M. Kirste, H. Haak, G. Meijer, S. Y. T. van de Meerakker, *Review of Scientific Instruments* **2013**, *84*.

[172] C. M. Western, University of Bristol, PGOPHER, A Program for Simulating Rotational, Vibrational and Electronic Spectra.

[173] SIMION 2020 is a software program for performing charge particle optics simulations developed by Adaptas Solutions, LLC.

[174] M. Strutton, Part II Thesis, University of Oxford, **2023**.

[175] R. N. Zare, *Journal of Chemical Physics* **1966**, *45*, 4510–4518.

[176] M. Brouard, H. Chadwick, C. J. Eyles, B. Hornung, B. Nichols, F. J. Aoiz, P. G. Jambrina, S. Stolte, *Journal of Chemical Physics* **2013**, *138*.

[177] U. Fano, J. H. Macek, *Reviews of Modern Physics* **1973**, *45*, 553–573.

[178] K. Blum, *Density Matrix Theory and Applications*, 2nd ed., Plenum, New York, **1996**.

[179] B. Hornung, DPhil Thesis, University of Oxford, **2013**.

[180] C. J. Eyles, M. Brouard, H. Chadwick, B. Hornung, B. Nichols, C. H. Yang, J. Klos, F. J. Aoiz, A. Gijsbertsen, A. E. Wiskerke, S. Stolte, *Physical Chemistry Chemical Physics* **2012**, *14*, 5403–5419.

[181] A. G. Suits, C. K. Bishwakarma, L. Song, G. C. Groenenboom, A. van der Avoird, D. H. Parker, *Journal of Physical Chemistry A* **2015**, *119*, 5925–5931.

[182] A. Crosby, Part II Thesis, University of Oxford, **2025**.

[183] S. E. J. Kuijpers, P. Kalaitzis, E. Sakkoula, S. Y. T. van de Meerakker, T. P. Softley, D. H. Parker, *Journal of Physical Chemistry A* **2024**, *128*, 10993–11004.

[184] M. H. Alexander, *Faraday Discussions* **1999**, *113*, 437–454.

[185] M. H. Alexander, S. Stolte, *Journal of Chemical Physics* **2000**, *112*, 8017–8026.

[186] T. V. Tscherbul, J. Kłos, *Physical Review A* **2021**, *103*.

[187] HIBRIDON is a package of programs for the time-independent quantum treatment of inelastic collisions and photodissociation written by M. H. Alexander, D. E. Manolopoulos, H. Werner, B. Follmeg with contributions P. F. Vohralik, D. Lemoine, G. Corey, R. Gordon, B. Johnson, T. Orlikowski, A. Berning, A. D. Esposti, C. Rist, P. Dagdigian, B. Pouilly, G. van der Sanden, M. Yang, F. de Weerd, S. Gregurick, and J. Kłos.

[188] D. E. Manolopoulos, *Journal of Chemical Physics* **1986**, *85*, 6425–6429.

[189] M. H. Alexander, D. E. Manolopoulos, *Journal of Chemical Physics* **1987**, *86*, 2044–2050.

[190] M. H. Alexander, *Journal of Chemical Physics* **1999**, *111*, 7426–7434.

[191] B. Wen, H. Meyer, J. Klos, *Journal of Chemical Physics* **2010**, *132*.

[192] J. Kłos, G. Chalasinski, M. T. Berry, R. A. Kendall, R. Burcl, M. M. Szczesniak, S. M. Cybulski, *Journal of Chemical Physics* **2000**, *112*, 4952–4958.

[193] M. Brouard, S. D. S. Gordon, A. H. Boyle, C. G. Heid, B. Nichols, V. Walpole, F. J. Aoiz, S. Stolte, *Journal of Chemical Physics* **2017**, *146*.

[194] M. Brouard, H. Chadwick, S. D. S. Gordon, B. Hornung, B. Nichols, F. J. Aoiz, S. Stolte, *Journal of Physical Chemistry A* **2015**, *119*, 12404–12416.

[195] M. Brouard, H. Chadwick, S. D. S. Gordon, B. Hornung, B. Nichols, F. J. Aoiz, S. Stolte, *Journal of Chemical Physics* **2016**, *144*.

[196] F. J. Aoiz, J. E. Verdasco, M. Brouard, J. Klos, S. Marinakis, S. Stolte, *Journal of Physical Chemistry A* **2009**, *113*, 14636–14649.

[197] A. Gijsbertsen, H. Linnartz, C. A. Taatjes, S. Stolte, *Journal of the American Chemical Society* **2006**, *128*, 8777–8789.

[198] M. H. Alexander, *Chemical Physics* **1985**, *92*, 337–344.

[199] M. C. van Beek, J. J. ter Meulen, M. H. Alexander, *Journal of Chemical Physics* **2000**, *113*, 628–636.

[200] M. C. van Beek, J. J. ter Meulen, M. H. Alexander, *Journal of Chemical Physics* **2000**, *113*, 637–646.

[201] M. C. van Beek, PhD Thesis, Katholieke Universiteit Nijmegen, **2001**.

[202] K. Schreel, J. J. ter Meulen, *Journal of Physical Chemistry A* **1997**, *101*, 7639–7647.

[203] D. Bein, Master's Thesis, Freie Universität Berlin, **2022**.

[204] C. A. Taatjes, A. Gijsbertsen, M. J. L. de Lange, S. Stolte, *Journal of Physical Chemistry A* **2007**, *111*, 7631–7639.

[205] P. G. Jambrina, J. F. E. Croft, N. Balakrishnan, F. J. Aoiz, *Physical Chemistry Chemical Physics* **2021**, *23*, 19364–19374.

[206] D. van den Ende, S. Stolte, *Chemical Physics* **1984**, *89*, 121–139.

[207] G. Paterson, S. Marinakis, M. L. Costen, K. G. McKendrick, *Physical Chemistry Chemical Physics* **2009**, *11*, 8813–8820.

[208] W. E. Perreault, N. Mukherjee, R. N. Zare, *Nature Chemistry* **2018**, *10*, 561–567.

[209] P. G. Jambrina, J. F. E. Croft, H. Guo, M. Brouard, N. Balakrishnan, F. J. Aoiz, *Physical Review Letters* **2019**, *123*.

[210] J. F. E. Croft, N. Balakrishnan, M. Huang, H. Guo, *Physical Review Letters* **2018**, *121*.

[211] B. Mandal, J. F. E. Croft, P. G. Jambrina, H. Guo, F. J. Aoiz, N. Balakrishnan, *Physical Chemistry Chemical Physics* **2024**, *26*, 18368–18381.

[212] P. G. Jambrina, J. F. E. Croft, J. X. Zuo, H. Guo, N. Balakrishnan, F. J. Aoiz, *Physical Review Letters* **2023**, *130*.

[213] P. G. Jambrina, J. F. E. Croft, N. Balakrishnan, H. Guo, F. J. Aoiz, *Faraday Discussions* **2024**, *251*, 104–124.

[214] O. Godsi, G. Corem, Y. Alkoby, J. T. Cantin, R. V. Krems, M. F. Somers, J. Meyer, G. J. Kroes, T. Maniv, G. Alexandrowicz, *Nature Communications* **2017**, *8*.

[215] Y. Alkoby, H. Chadwick, O. Godsi, H. Labiad, M. Bergin, J. T. Cantin, I. Litvin, T. Maniv, G. Alexandrowicz, *Nature Communications* **2020**, *11*.

[216] H. Chadwick, M. F. Somers, A. C. Stewart, Y. Alkoby, T. J. D. Carter, D. Butkovicova, G. Alexandrowicz, *Nature Communications* **2022**, *13*.

[217] H. Chadwick, G. Alexandrowicz, *Faraday Discussions* **2024**, *251*, 76–91.

[218] N. F. Ramsey, *Physical Review* **1952**, *85*, 60–65.

[219] I. Hertel, W. Stoll, *Advances in Atomic and Molecular Physics* **1978**, *13*, 113–228.

[220] N. E. Shafer-Ray, A. J. Orr-Ewing, R. N. Zare, *Journal of Physical Chemistry* **1995**, *99*, 7591–7603.

[221] J. Kłos, Q. L. Ma, M. H. Alexander, P. J. Dagdigian, *Journal of Chemical Physics* **2017**, *146*.

[222] H. Chadwick, Private Communication, **2024**.

[223] M. S. Westley, K. T. Lorenz, D. W. Chandler, P. L. Houston, *Journal of Chemical Physics* **2001**, *114*, 2669–2680.

[224] T. de Jongh, T. Karman, S. N. Vogels, M. Besemer, J. Onvlee, A. G. Suits, J. O. F. Thompson, G. C. Groenenboom, A. van der Avoird, S. Y. T. van de Meerakker, *Journal of Chemical Physics* **2017**, *147*.

[225] Z. Gao, S. N. Vogels, M. Besemer, T. Karman, G. C. Groenenboom, A. van der Avoird, S. Y. T. van de Meerakker, *Journal of Physical Chemistry A* **2017**, *121*, 7446–7454.

[226] S. N. Vogels, T. Karman, J. Klos, M. Besemer, J. Onvlee, A. van der Avoird, G. C. Groenenboom, S. Y. T. van de Meerakker, *Nature Chemistry* **2018**, *10*, 435–440.

[227] Q. Shuai, T. de Jongh, M. Besemer, A. van der Avoird, G. C. Groenenboom, S. Y. T. van de Meerakker, *Journal of Chemical Physics* **2020**, *153*.

[228] C. G. Heid, I. P. Bentham, R. Gheorghe, P. G. Jambrina, F. J. Aoiz, M. Brouard, *Molecular Physics* **2022**, *120*.

[229] Q. L. Ma, J. Kłos, M. H. Alexander, A. van der Avoird, P. J. Dagdigian, *Journal of Chemical Physics* **2014**, *141*.

[230] P. C. Cross, R. M. Hainer, G. W. King, *Journal of Chemical Physics* **1944**, *12*, 210–243.